

**OBSERVING WATER VAPOUR AND OZONE
IN THE TROPICAL UTLS WITH THE MIPAS
INSTRUMENT ON ENVISAT**

Thesis submitted for the degree of
Doctor of Philosophy
at the University of Leicester

by

Harjinder Sembhi BSc MSc
Earth Observation Science Group
Department of Physics and Astronomy
University of Leicester

September 2007

UMI Number: U601130

All rights reserved

INFORMATION TO ALL USERS

The quality of this reproduction is dependent upon the quality of the copy submitted.

In the unlikely event that the author did not send a complete manuscript and there are missing pages, these will be noted. Also, if material had to be removed, a note will indicate the deletion.



UMI U601130

Published by ProQuest LLC 2013. Copyright in the Dissertation held by the Author.
Microform Edition © ProQuest LLC.

All rights reserved. This work is protected against
unauthorized copying under Title 17, United States Code.



ProQuest LLC
789 East Eisenhower Parkway
P.O. Box 1346
Ann Arbor, MI 48106-1346

© Harjinder Sembhi, September 2007

This thesis is copyright material and no quotation from it may be published without proper acknowledgement.

Declaration

I hereby declare that no part of this thesis has been previously submitted to this or any other University as part of the requirement for a higher degree. The work described herein was conducted by the undersigned except for contributions from colleagues as acknowledged in the text.

Harjinder Sembhi

September 2007

OBSERVING WATER VAPOUR AND OZONE IN THE TROPICAL UTLS WITH THE MIPAS INSTRUMENT ON ENVISAT

Harjinder Sembhi

ABSTRACT

In this thesis, the potential to observe the distribution of water vapour (H_2O) and ozone (O_3) in the tropical upper troposphere and lower stratosphere (UTLS) from an atmospheric limb sounding spectrometer is assessed. Vertical profile data retrieved operationally from observations from the Michelson Interferometer for Passive Atmospheric Sounding (MIPAS) are examined under “clear sky” and thin cloud conditions. In the tropical UTLS, the distributions of these two naturally occurring important climate gases are characterised by sharp gradients through a cold tropopause. This in combination with the high occurrence of cirrus clouds in this region, makes accurate “clear sky” satellite observations difficult to achieve.

The impact of clouds on MIPAS measurements is quantified by simulating the effects of tropical UTLS cirrus clouds into MIPAS H_2O and O_3 retrievals. It is found that clouds in the MIPAS line of sight can lead to a systematic positive bias in MIPAS H_2O measurements and an increase in random retrieval error for both H_2O and O_3 . It was also found that cloud errors can propagate into the “clear sky” profile above the cloud altitude. Recommendation for improvements to the operational cloud filtering methods of tropical MIPAS H_2O and O_3 are proposed.

Comparisons of MIPAS H_2O and O_3 screened with the proposed cloud filtering schemes, to correlative *in situ* and solar occultation data suggest that improved filtering improves the agreement. However, MIPAS H_2O and O_3 data quality remain limited by the increased retrieval uncertainty near the tropopause.

Finally, the seasonal variability of the tropical cloud filtered MIPAS H_2O and O_3 through the tropical UTLS is examined. Regional analysis reveals possible evidence of upper tropospheric O_3 enhancements and monsoon effects. The results show that MIPAS can sufficiently sound the tropical UTLS region.

ACKNOWLEDGEMENTS

First and foremost, I would like to acknowledge my supervisor, Dr. John Remedios, for giving me the opportunity to conduct this research with the Earth Observation Science group and for many insightful discussions, much appreciated guidance and encouragement for the duration of this project.

I would also like to thank the MIPAS QWG team, particularly Piera Raspollini and Ugo Cortesi who have contributed to this work through their collaboration and expertise. A special mention also goes to Reinhold Spang, Alison Waterfall, Anu Dudhia, Larry Miloshevich, the Remote Sensing group at RAL, and countless members of the SCOUT-O3 community (particularly those at the 2005 aircraft campaign in Darwin) for invaluable scientific discussion and educating me on many aspects of their work.

This project would not have been possible without UK NERC funding and provision of MIPAS data by ESA. The NASA HALOE and SHADOZ groups must also be acknowledged for instructions and provision of HALOE and SHADOZ data. Finally, thanks to Peter Minnett and Liz Williams of the University of Miami for giving me access to data collected on the Explorer of the Seas Laboratory.

The last four years have been unforgettable and despite the late nights in the office, many disagreements with IDL and countless conference shenanigans, I have enjoyed every moment! Thanks to all of the past and present members of the EOS group who have imparted their scientific (and Ph.D.-related) wisdom, guided me through Latex and trusted me with their library books (despite my reputation as the notorious EOS book-thief). Thanks also to Tina, Dave, “San-shini” and Marky for putting up with me in my writing-up days.

Finally, this thesis is dedicated to my family for their unconditional support, time and patience. Thank you.

Table of Contents

Table of Contents	I
1 Introduction	1
1.0.1 The role of H ₂ O in the atmosphere	3
1.0.2 The role of O ₃ in the atmosphere	4
1.1 The tropical UTLS	5
1.1.1 The tropical tropopause layer	7
1.1.1.1 Factors controlling tropical UTLS H ₂ O	10
1.1.1.2 Factors controlling tropical UTLS O ₃	12
1.1.1.3 Clouds in the tropical UTLS	14
1.2 Observing H ₂ O and O ₃ distributions in the tropical UTLS	16
1.2.1 <i>In situ</i> observations	16
1.2.1.1 Aircraft measurements	16
1.2.1.2 Balloon measurements	18
1.2.1.3 Ozone sondes	18
1.2.1.4 Radiosondes	21
1.2.2 Previous satellite observations	25
1.2.2.1 Satellite observations of tropical UTLS O ₃	25
1.2.2.2 Satellite observations of tropical UTLS H ₂ O	25
1.2.3 In situ vs. remote sensing	29
1.2.4 Motivation for this work	29
2 Remote sensing of the tropical UTLS region	31
2.1 Infrared limb sounding	32
2.2 Radiative transfer	34
2.2.1 Radiative transfer in a clear sky atmosphere	34
2.2.2 Radiative transfer in a cloudy atmosphere	36
2.3 Infrared spectroscopy	39
2.3.1 Theory	39
2.3.1.1 Rotation of molecules	40
2.3.1.2 Vibrations of molecules	40
2.3.2 Infrared spectroscopy of H ₂ O	41
2.3.3 Infrared spectroscopy of O ₃	42
2.3.4 Spectral line intensity	42
2.3.5 Spectral line width	43

2.3.6	The Voigt profile	44
2.4	Forward Modelling	45
2.4.1	The Oxford Reference Forward Model	45
2.4.1.1	RFM features	45
2.4.1.2	Ray Tracing	46
2.4.1.3	Atmospheric profiles	46
2.4.1.4	Spectroscopic database	48
2.4.1.5	Instrument parameters	48
2.4.2	The FM2D multiple scattering model	49
2.5	Retrieval theory	51
2.5.1	Definitions	52
2.5.1.1	The weighting function matrix	52
2.5.1.2	Maximum Likelihood estimation	53
2.5.2	Solution without <i>a priori</i>	54
2.5.3	Iterative methods	55
2.5.3.1	Retrieval convergence	56
2.5.3.2	The Gain matrix	57
2.5.3.3	The averaging kernel matrix	57
2.5.3.4	Retrieval errors	58
2.5.4	Solution with <i>a priori</i>	58
2.6	Summary	59
3	The MIPAS instrument	60
3.1	The ENVISAT Satellite	60
3.1.1	MIPAS history and concept	62
3.1.2	MIPAS Objectives	62
3.2	The MIPAS measurement geometry and instrument layout	63
3.2.1	Observational modes	64
3.2.2	Instrument design and layout	65
3.2.3	Measuring the atmosphere with the MIPAS	65
3.2.4	The MIPAS interferometer	66
3.2.5	Interferogram sampling	67
3.2.6	Detectors and spectral ranges	68
3.2.7	MIPAS electronics	69
3.3	MIPAS performance	69
3.3.1	Offset measurement	69
3.3.2	Gain measurement	70
3.3.3	Spectral calibration	70
3.3.4	Instrument Line Shape Retrieval	70
3.3.5	Line of sight calibration	71
3.3.6	MIPAS field of view	72
3.3.7	Noise Equivalent Spectral Radiance	72
3.4	MIPAS data	72
3.4.1	MIPAS Level 1B data	74
3.4.2	MIPAS Level 2 data	75

3.5	The Level 2 Retrieval	75
3.5.1	General Retrieval Features	76
3.5.1.1	Microwindows	76
3.5.1.2	Global Fitting	77
3.5.1.3	Sequential retrieval	78
3.5.1.4	Level 2 Retrieval Procedure	78
3.5.2	The Optimised Forward Model	79
3.5.3	Convolution of spectra	79
3.5.4	Convergence criterion	80
3.5.5	Retrieval Requirements	80
3.5.5.1	Spectroscopic database	80
3.5.5.2	Reference atmosphere database	81
3.5.6	Retrieval Assumptions	81
3.5.6.1	Horizontal homogeneity	81
3.5.6.2	Non-local thermodynamic equilibrium	82
3.6	Characterisation of MIPAS Level 2 profiles	82
3.7	MIPAS Level 2 errors	82
3.7.0.3	Calibration errors	83
3.7.0.4	Forward model errors	84
3.7.1	Level 2 H ₂ O and O ₃ errors in the tropical UTLS	84
3.7.2	The new “Reduced Resolution” mode	85
3.8	Studying the tropical UTLS with the MIPAS instrument	87
3.9	Summary	88
4	Investigating cloud contamination in Level 2 MIPAS data	89
4.1	Cloud signatures in MIPAS L1B spectra	90
4.1.1	MIPAS cloud detection	92
4.1.2	Limitations of the cloud detection methodology	93
4.1.3	Modelling clouds in limb infrared spectra	94
4.2	Investigating cloud contamination in MIPAS L2 H ₂ O and O ₃ profiles	95
4.2.1	Objectives	97
4.2.2	Methodology	98
4.2.2.1	Step 1. Representative scenarios for cloud	99
4.2.2.2	Step 2. Representing real cloud in MIPAS L1B spectra	101
4.2.2.3	Step 3. Estimating cloud extinction	102
4.2.2.4	Step 4. Verifying simulations of MIPAS cloud microwindows	103
4.2.2.5	Step 5. Simulating nominal microwindows for H ₂ O and O ₃	104
4.2.2.6	Step 6. Retrieving cloudy L2 H ₂ O and O ₃ with the ORM	105
4.2.2.7	Step 7. Relating the CI-A to retrieved H ₂ O and O ₃	106
4.3	Results	107
4.4	Case study: cloud at 12 km	107
4.4.1	Simulated <i>cloudy</i> spectra	108

4.4.1.1	Retrieved cloudy and clear-sky H ₂ O and O ₃ profiles .	110
4.4.1.2	Deviations in retrieved H ₂ O profiles	112
4.4.1.3	Deviations in retrieved O ₃ profiles	114
4.4.2	Investigating the impact of random noise on 12 km retrievals .	114
4.5	Case study: cloud at 18 km	117
4.5.0.1	Simulated <i>cloudy</i> spectra	118
4.5.0.2	Compensating for the O3_0001 offset	123
4.5.0.3	Retrieved profiles of H ₂ O and O ₃	125
4.5.0.4	Deviations in retrieved H ₂ O profiles	125
4.5.0.5	Deviations in retrieved O ₃ profiles	128
4.5.1	Investigating the impact of random noise on 18 km retrievals .	128
4.6	Discussion	130
4.6.1	Investigating the relationship between the CI-A and scattering	132
4.6.2	FM2d comparisons with RFM for thin clouds	133
4.6.2.1	Cloud spectral simulations with FM2D	134
4.7	Definition of a cloud index for tropical H ₂ O and O ₃	140
4.7.1	Cloud index thresholds for H ₂ O and O ₃ at 12 and 18 km . . .	141
4.8	Summary	142
5	Comparisons of tropical UTLS MIPAS L2 H₂O and O₃ with HALOE and <i>in situ</i> instruments	145
5.0.1	Previous inter-comparison of MIPAS L2 H ₂ O and O ₃ profiles	146
5.0.2	Intercomparison methodologies	148
5.0.2.1	<i>Accuracy, bias and precision determination</i>	149
5.1	Inter-comparison strategy	150
5.1.1	Coincidence criteria	151
5.1.2	Analysis of results	151
5.1.2.1	Application of MIPAS averaging kernels	153
5.1.2.2	Application of tropical cloud detection schemes for MIPAS H ₂ O profiles	153
5.2	Inter-comparison of MIPAS H ₂ O and O ₃ with HALOE	154
5.2.1	The Halogen Occultation Experiment	155
5.2.2	Sources of errors in HALOE data	155
5.2.3	MIPAS H ₂ O and O ₃ offline data comparisons with HALOE H ₂ O and O ₃	158
5.2.3.1	<i>Coincidence criteria</i>	159
5.2.3.2	<i>Results of H₂O inter-comparisons</i>	160
5.2.3.3	<i>Mean profiles</i>	162
5.2.3.4	<i>Results of O₃ inter-comparisons</i>	166
5.2.3.5	<i>Mean profiles</i>	166
5.2.4	Discussion	168
5.3	Inter-comparison of MIPAS O ₃ with SHADOZ O ₃	172
5.3.0.1	Electrochemical concentration cell ozone sondes . . .	173
5.3.1	ECC ozone sonde errors	174
5.3.2	MIPAS O ₃ comparisons with SHADOZ O ₃	175

5.3.2.1	<i>Coincidence criteria</i>	176
5.3.2.2	<i>Results of O₃ inter-comparisons</i>	176
5.3.2.3	<i>Mean profiles</i>	177
5.3.3	Discussion	179
5.4	Inter-comparison of MIPAS H ₂ O with Vaisala radiosondes	182
5.4.1	Sources of errors and corrections for Vaisala radiosondes	183
5.4.1.1	<i>Coincidence criteria</i>	185
5.4.1.2	<i>Application of Vaisala corrections</i>	186
5.4.1.3	<i>Results of H₂O inter-comparisons</i>	188
5.4.1.4	<i>Mean profiles</i>	188
5.4.2	Discussion	190
5.5	Summary	193
5.5.0.1	H ₂ O	193
5.5.0.2	O ₃	194
6	Tropical UTLS averages of MIPAS H₂O and O₃	196
6.0.0.3	Methodologies for seasonal averages	198
6.0.0.4	Cloud top pressure, occurrence frequency, and “tropopause” temperatures	200
6.1	Operational and improved cloud cleared MIPAS averages	204
6.1.1	Tropical cloud filtering schemes for H ₂ O and O ₃	207
6.1.2	Impact of cloud filtering improvements on tropical UTLS H ₂ O and O ₃	209
6.1.2.1	Scheme A and B for H ₂ O	209
6.1.2.2	Scheme A and B for O ₃	210
6.1.3	Longitudinal resolution effects	214
6.1.4	Seasonal analysis of H ₂ O and O ₃	217
6.1.4.1	Seasonal H ₂ O	217
6.1.4.2	Seasonal O ₃	221
6.1.5	Regional analysis of MIPAS H ₂ O and O ₃	225
6.1.6	Investigating the South Atlantic O ₃ enhancement	225
6.1.7	Evidence of monsoon signatures in MIPAS H ₂ O	233
6.1.8	Summary	237
7	Conclusions and future work	240
7.1	Summary of conclusions	240
7.2	Recommendations for future work	244

List of Figures

1.1	The Earth's Atmosphere	2
1.2	The Earth's radiation budget.	3
1.3	Stratosphere - troposphere exchange.	7
1.4	Temperature and O ₃ vertical profiles in the TTL	8
1.5	Schematic of deep convection in the tropics	13
1.6	Seasonal patterns of convection in the tropics.	15
1.7	Schematic of an Electrochemical Concentration Cell ozone sonde. . .	20
1.8	Vertical profiles of O ₃ measured at the tropical locations of San Cristobal (0.9°S,89.6°W) and the west Pacific (2°S, 157°W) using ozone sondes. Source: Vomel et al. [2002]	20
1.9	Zonal O ₃ distribution from the SHADOZ network	21
1.10	An example of an RS92 Vaisala radiosonde	22
1.11	Vertical profiles of H ₂ O measured in the tropics	24
1.12	Seasonal climatological tropospheric O ₃ column	26
1.13	215 mb H ₂ O measured by the MLS instrument	27
1.14	Zonal mean H ₂ O as measured by the HALOE instrument	28
1.15	The stratospheric H ₂ O tape recorder measured by the MLS and HALOE instruments	28
2.1	Limb sounding of the atmosphere. Source: Stephens [1994]	32
2.2	Vibrational and rotational modes of H ₂ O and O ₃ molecules	42
2.3	Maximum, minimum and mean Equatorial climatological profiles of H ₂ O, O ₃ and temperature from the Standard Atmosphere climatology	47
3.1	Instruments onboard the ENVISAT module. Source: ESA [2007] . . .	61
3.2	Observational geometry of the MIPAS instrument. Source: ESA [2007]	64

3.3	Schematic of the MIPAS MIO layout. Source: ESA [2007]	66
3.4	The MIPAS Interferometer. Source: ESA [2007]	67
3.5	MIPAS NESR on ground and in-flight performance. Source: Kleinert et al. [2007]	73
3.6	Block diagram of MIPAS data processing. Source: ESA [2007]	74
3.7	Averaging kernels for MIPAS H ₂ O and O ₃ calculated for April at 10°S, between the altitudes of 12 and 68 km.	83
3.8	Systematic and random error profiles for equatorial offline MIPAS H ₂ O and O ₃ profiles. The total error is shown by the black line in each figure.	86
4.1	MIPAS L1B spectra in bands A, AB, B, C and D under varying cloud influence.	91
4.2	MIPAS cloud detection microwindows. Source: Greenhough et al., [2005]	92
4.3	MIPAS H ₂ O for June 2003. Data corresponding to tropics/subtropics are shown between 50°N and 50°S only	96
4.4	MIPAS O ₃ for June 2003. Data corresponding to tropics/subtropics are shown between 50°N and 50°S only	97
4.5	Creating a cloud box	102
4.6	Simulated 12 km cloud indices and <i>a priori</i> extinction profile	107
4.7	Cloudy to clear sky 12 km spectra generated for the MIPAS cloud and nominal O ₃ and H ₂ O microwindows.	109
4.8	The 12 km mean radiance in the MIPAS cloud and nominal O ₃ and H ₂ O microwindows against MIPAS CI-A	111
4.9	H ₂ O and O ₃ profiles retrieved in clear sky and cloudy conditions with a cloud present at 12 km.	113
4.10	Deviations in H ₂ O concentrations from expected clear-sky concentrations at 12 km and 15 km and the 12 and 15 km deviations <i>root-sum-squared</i> with Oxford systematic errors against 12 km CI	115
4.11	Deviations in O ₃ concentrations from expected clear-sky concentrations at 12 km and 15 km and the 12 and 15 km deviations <i>root-sum-squared</i> with Oxford systematic errors against 12 km CI	116
4.12	Deviations in H ₂ O concentrations from expected clear-sky concentrations at 12 km and 15 km with varying random seeds.	118

4.13	Deviations in O ₃ concentrations from expected clear-sky concentrations at 12 km and 15 km with varying random seeds.	119
4.14	Simulated 18 km cloud indices and <i>a priori</i> extinction profile	119
4.15	18 km cloudy to clear sky spectra generated for the MIPAS cloud and nominal H ₂ O and O ₃ microwindows.	120
4.16	The mean radiance in each nominal H ₂ O and O ₃ microwindow against the MIPAS CI-A	122
4.17	Scaling the radiance in O3_0001 at 18 km	124
4.18	H ₂ O and O ₃ profiles retrieved in clear sky and cloudy condition.	126
4.19	Deviations in H ₂ O concentrations from expected clear-sky concentrations at 18 km and 21 km and 18 and 21 km deviations <i>root-sum-squared</i> with Oxford systematic errors against 18 km CI-A.	127
4.20	Deviations in O ₃ concentrations from expected clear-sky concentrations at 18 km and 21 km. 18 and 21 km deviations <i>root-sum-squared</i> with Oxford systematic errors against 18 km CI-A.	129
4.21	Deviations in H ₂ O concentrations from expected clear-sky concentrations at 18 km and 21 km with varying random seeds.	130
4.22	Deviations in O ₃ concentrations from expected clear-sky concentrations at 18 km and 21 km with varying random seeds.	131
4.23	FM2D, RFM and real MIPAS spectra for the 12 km case	135
4.24	The CI-A vs mean radiance with the 12 km FM2D-generated cloud spectra plotted over the real and RFM spectra in each microwindow	136
4.25	FM2D, RFM and real MIPAS spectra for the 18 km case	138
4.26	The CI-A vs mean radiance with the 18 km FM2D-generated cloud spectra plotted over the real and RFM spectra in each microwindow at 18 km	139
5.1	Example of HALOE sunset and sunrise events in a single UARS orbit	156
5.2	Locations of matched HALOE and MIPAS profiles	160
5.3	Examples of matched MIPAS and HALOE H ₂ O profiles	161
5.4	Ensemble of operational cloud filtered MIPAS H ₂ O profiles compared to HALOE H ₂ O	162

5.5	Mean MIPAS versus. HALOE H ₂ O profiles with varying cloud filtering schemes	164
5.6	Longitudinal variation of RD between MIPAS and HALOE H ₂ O . . .	165
5.7	Examples of matched MIPAS and HALOE O ₃ profiles	167
5.8	Ensemble of operationally filtered MIPAS and HALOE O ₃ matched profiles	168
5.9	Mean MIPAS versus. HALOE O ₃ profiles with varying cloud filtering schemes	169
5.10	Longitudinal variation of RD between MIPAS and HALOE O ₃	171
5.11	SHADOZ measurement sites. Source: www.croc.gsfc.nasa.gov/shadoz	173
5.12	Locations of matched SHADOZ and MIPAS profiles	177
5.13	Examples of matched MIPAS and SHADOZ O ₃ profiles	178
5.14	Ensemble of operationally cloud filtered MIPAS O ₃ and SHADOZ profiles with and without MIPAS averaging kernels	179
5.15	Mean MIPAS versus. SHADOZ O ₃ profiles with varying cloud filtering schemes	180
5.16	Longitudinal variation of RD between MIPAS and SHADOZ	181
5.17	Locations of matched Explorer and MIPAS profiles	187
5.18	Examples of matched MIPAS and Vaisala H ₂ O profiles	189
5.19	Ensemble and mean MIPAS and VAISALA H ₂ O matched profiles . .	190
5.20	Mean MIPAS versus. Vaisala H ₂ O profiles with varying cloud filtering schemes	191
6.1	Seasonal mean CPT for 2003	202
6.2	Seasonal mean COF for 2003	204
6.3	Seasonal 100 mb “tropopause” temperatures	205
6.4	68 mb and 215 mb H ₂ O for DJF with operational cloud filtering . . .	207
6.5	68 mb and 215 mb O ₃ for DJF with operational cloud filtering	208
6.6	H ₂ O averaged concentrations and estimated grid box error filtered with scheme A.	211
6.7	H ₂ O averaged concentrations and estimated grid box error filtered with scheme B.	212

6.8	O ₃ averaged concentrations and estimated grid box error filtered with scheme A.	213
6.9	O ₃ averaged concentrations and estimated grid box error filtered with scheme B.	214
6.10	JJA H ₂ O with varying longitude averaging.	216
6.11	DJF H ₂ O at 68 mb, 100 mb and 215 mb	219
6.12	JJA H ₂ O at 68 mb, 100 mb and 215 mb	220
6.13	DJF O ₃ at 68 mb, 100 mb and 215 mb	223
6.14	JJA O ₃ at 68 mb, 100 mb and 215 mb	224
6.15	Brazil and Africa O ₃ concentrations shown with the zonal wave-one regions of the South Atlantic and Pacific oceans	227
6.16	Longitude-Altitude cross section of O ₃ from Equator to 20° South. . .	228
6.17	Vertical structure of SH O ₃ in DJF	230
6.18	Vertical structure of SH O ₃ in MAM	230
6.19	Vertical structure of SH O ₃ in JJA	231
6.20	Vertical structure of SH O ₃ in SON	231
6.21	Global maps of MOPITT CO at 150 and 250 mb for SON 2003 . . .	232
6.22	H ₂ O and O ₃ at 68 mb and 100 mb in JJA over the North American and Summer Monsoon regions	235
6.23	Vertical structure of NH H ₂ O in JJA	236
6.24	Vertical structure of NH O ₃ in JJA	236
7.1	H ₂ O and O ₃ retrieved by the ORM with and without a cloud at 12 km	246

List of Tables

1.1	Field campaigns in which in situ tropical UTLS H ₂ O and O ₃ measurements have been made in MIPAS operation lifetime	24
2.1	Limb sounding instruments in operation during MIPAS mission . . .	33
3.1	MIPAS detectors and spectral regions	69
3.2	Spectral lines and intervals used for MIPAS ILS and spectral calibration	71
3.3	NESR requirements for MIPAS spectral bands	73
3.4	Nominal microwindows used by the MIPAS L2 retrieval	77
3.5	List of systematic error sources for MIPAS L2 retrievals	85
4.1	Cloud index thresholds used in MIPAS bands A,B and D	93
4.2	Percentage of various CI-A values in December, January and February 2002/2003	99
4.3	Percentage of various CI-A values in March, April and May 2003 . . .	99
4.4	Percentage of various CI-A values in June, July and August 2003 . .	99
4.5	Percentage of various CI-A values in September, October and November 2003	100
4.6	Setup for retrieval of particle extinction and L2 profile retrieval . . .	103
4.7	Microwindow regions and interfering absorbers	105
5.1	Total error estimates for HALOE O ₃ in percent. Source: Bruhl et al. [1996]	157
5.2	Total error estimates for HALOE H ₂ O in percent. Source: Harries et al. [1996]	158
5.3	Number of matches found between July 2002 and March 2004 for the chosen criteria.	159

5.4	Summary of MIPAS and HALOE H ₂ O comparison with varying cloud filters. The numbers in brackets next to each MRD represents the number of points in each comparison.	163
5.5	Summary of MIPAS and HALOE O ₃ comparison with varying cloud filters. The numbers in brackets next to each MRD represents the number of points in each comparison.	170
5.6	SHADOZ measurement sites.	173
5.7	Number of matches found between July 2002 and March 2004 for the chosen criteria.	176
5.8	Summary of MIPAS and SHADOZ O ₃ comparison with varying cloud filters. The numbers in brackets next to each MRD represents the number of points in each comparison.	182
5.9	Number of matches found between July 2002 and March 2004 for the chosen criteria.	186
5.10	Summary of MIPAS and Vaisala H ₂ O comparison with varying cloud filters. The numbers in brackets next to each MRD represents the number of points in each comparison.	192
6.1	UARS Pressure levels for the UTLS region.	199
6.2	Approximate co-ordinates of tropical regions featured in this chapter	200

Chapter 1

Introduction

The atmosphere is an important part of the Earth's climate system and is composed primarily of nitrogen (78%), oxygen (20%) and argon (0.8%), with concentrations of trace gases including water vapour (H_2O), carbon dioxide (CO_2) and ozone (O_3). Additional components present in the Earth's atmosphere are conglomerates of water and ice crystals in the form of clouds and particulate and aerosol particles. Particular layers in the atmosphere are identifiable by their thermal structure, that varies with altitude as shown by Figure 1.1. The region that is of primary interest to the work in this thesis is the upper troposphere and lower stratosphere (UTLS), that provides the connection between the Earth's troposphere and stratosphere.

The troposphere is a turbulent layer that is characterised by strong eddy (circular air currents) and convective activity, high concentrations of H_2O , and meteorological weather systems. In the troposphere, the temperature decrease with increasing altitude until a temperature inversion, or a tropopause is reached. The tropopause effectively acts as a lid to convection and is usually characterised by a distinct temperature minimum. The height of the tropopause tends to vary with latitude from approximately 16 km (100 mb in terms of atmospheric pressure) in the tropics to around 8 km in the poles. In the stratosphere, radiative heating is the dominant process due to absorption of solar radiation by O_3 .

The Earth's climate system is chiefly driven by incoming solar radiation of approximately 342 Wm^{-2} [Kiehl and Trenberth, 1997] as illustrated in Figure 1.2, part of which is reflected by clouds, aerosol, and surface albedo (i.e. surface reflectivity), and the remaining energy is absorbed by the Earth's surface and the atmosphere. At the

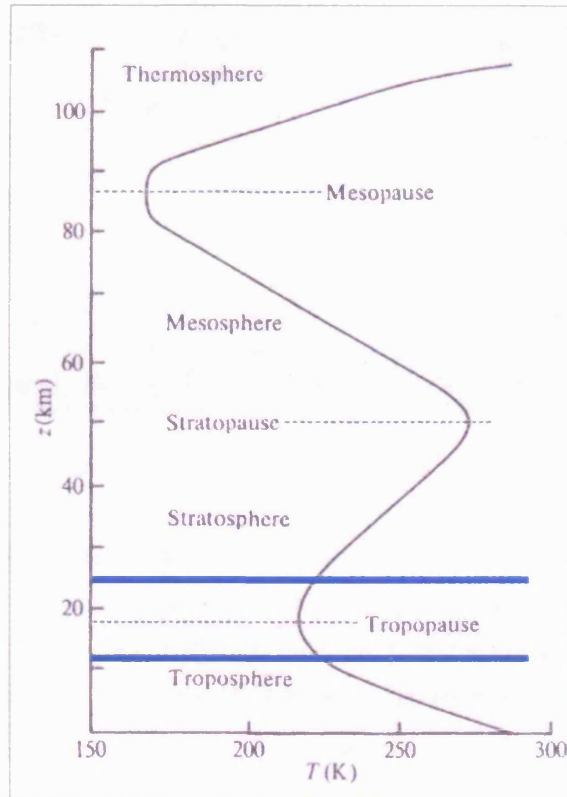


Figure 1.1: The Earth's Atmosphere. Source: Wayne [2000]. The variation in temperature characterises the different layers in the atmosphere. The approximate location of the UTLS (the region that is of interest to this thesis) lies between the blue lines.

same time, the Earth acts like blackbody in which case it emits infrared or *longwave* radiation some of which is absorbed by infrared absorbing atmospheric constituents, mainly H_2O , CO_2 and O_3 . These gases play a significant role in the atmosphere as they are naturally-occurring greenhouse gases because they possess the ability to absorb and re-radiate longwave radiation and give rise to the so called "greenhouse" effect.

Quantification of greenhouse gas distributions near the tropopause, including the distributions of H_2O and O_3 are important for estimating the climate response due to these gases on the Earth's atmosphere. Shine and Sinha [1991] and Forster and Shine [1997] showed that the climate response due to these gases, in terms of a H_2O feedback and a radiative forcing for O_3 , are most sensitive to perturbations that occur close to the tropopause. Furthermore, knowledge of the distribution of these gases is particularly important for Global Climate Models (GCMs) that are required to

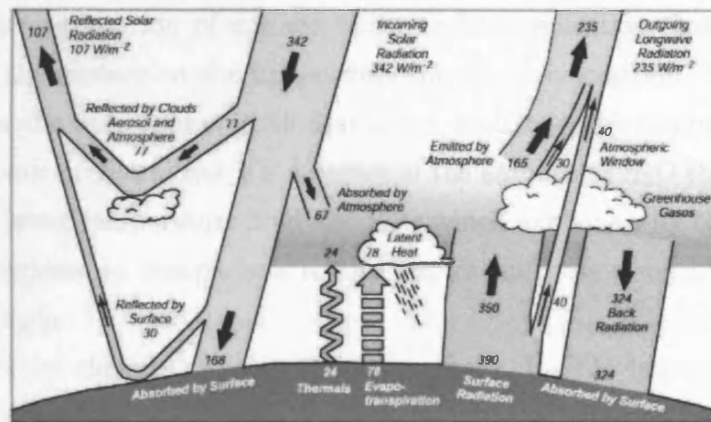


Figure 1.2: The Earth's radiation budget as depicted by Kiehl and Trenberth [1997].

forecast the impact of changing greenhouse gas concentrations on the Earth's climate system. Observing the variations in greenhouse gas concentrations in the tropical UTLS represents a particular challenge because this region is characterised by: a) a lack of ground based measurement, as most measurement networks are restricted to equatorial continental landmasses, b) the persistence of clouds that make remote measurements difficult, and c) cold tropopause temperatures and generally sharp gradients of H_2O and O_3 across the tropical tropopause.

1.0.1 The role of H_2O in the atmosphere

First and foremost a natural greenhouse gas, H_2O , is the most abundant and effective greenhouse gas in the troposphere. The largest and most variable concentrations, ranging from hundreds to thousands of parts per million per volume (ppmv) are found near the surface and reduce gradually with increasing altitude. Concentrations reduce to no more than a few ppmv near the tropopause resulting in a H_2O feature typically referred to as the "hygropause" [Kley et al., 1979]. This occurs due to the "freeze drying" of moist airmasses that pass through the "cold trap" or tropopause. In the stratosphere, concentrations increase to approximately 5 to 6 ppmv.

In terms of its importance as a greenhouse gas, Kiehl and Trenberth [1997] found that in clear sky conditions, H_2O can contribute to at least 60% of the total radiative forcing in comparison to 26% from CO_2 . H_2O also has a crucial role in the Earth's hydrological cycle, in which it is transferred throughout the climate system, and plays a role in the formation of clouds and precipitation. It is supplied to the atmosphere

primarily from evaporation of surface water and transpiration from plants. It is uplifted from the surface to the upper troposphere by convection. The amount of H_2O that is in the atmosphere is, to first order, controlled by temperature and the saturation vapour pressure that is a measure of the amount of H_2O that air can hold. Air parcels of lower temperature hold less H_2O which explains why there is less H_2O in the polar regions, in comparison to the tropics and less atmospheric H_2O with increasing altitude.

In terms of its chemical role in the atmosphere, H_2O is important for several reasons. H_2O is a source of hydroxyl radicals (OH) in the troposphere and the stratosphere (from the reaction of excited oxygen with H_2O to produce 2OH molecules in the presence of O_3 and UV radiation of less than 340 nm [Lelieveld et al., 2004]). OH is known to act as an atmosphere “cleanser” in that it is involved in the removal of many reactive chemical species in the atmosphere (such as methane (CH_4) and carbon monoxide (CO)). In the stratosphere, H_2O concentrations increase (to 5 - 6 ppmv) as a primary product from the oxidation of methane CH_4 .

1.0.2 The role of O_3 in the atmosphere

In contrast to H_2O , O_3 is found in high concentrations in the stratosphere with a maximum close to 25 km. Typically, O_3 concentrations are close to 10 ppmv near the maximum in the stratosphere. In the upper troposphere, concentrations are typically less than 0.1 ppmv. According to the Intergovernmental Panel on Climate Change [Houghton et al., 2001], O_3 in the upper troposphere is the third most important greenhouse gas after CO_2 and CH_4 .

In the stratosphere, O_3 absorbs incoming UV radiation between the wavelengths of 240 - 290 nm and it is this absorption of radiation that heats the stratosphere leading to an increase in temperature with increasing altitude. Without O_3 , much of this radiation would reach the ground and due to its ability to destroy the biological makeup of plants and animals, can be lethal to living organisms on Earth. Hence, it has a critical role in the atmosphere and for surface biology. About 90 % of atmospheric O_3 exists in the stratosphere. Its concentration in the stratosphere is governed by three body reactions and by a series of photochemical reactions that involve the photo-dissociation of molecular oxygen (O_2) by UV radiation (in Schumann-Runge UV bands (175-200 nm) and the Herzberg continuum (242 nm)), and by photolysis of

O₃ itself [Wayne, 2000]. Its concentration is also balanced by several catalytic cycles involving reactive species that result in a removal of odd-oxygen O_x (O₃ and O) thus, resulting in a loss of many O₃ molecules. Reactive species such as HO_x (OH + HO₂), NO_x (NO₂ + NO), ClO_x (Cl + ClO) and BrO_x (Br + BrO) species are responsible for the catalytic removal of O₃ in the stratosphere.

Around 10 % of O₃ resides in the troposphere and its *in situ* formation in the upper troposphere is governed by the photolysis of O₃ precursors (chemicals that induce O₃ formation) in particular NO_x, Volatile Organic Compounds (VOCs) including CH₄ and non-methane hydrocarbons, and other biogenic compounds.

1.1 The tropical UTLS

The tropical upper troposphere and lower stratosphere or UTLS, from approximately 200 to 40 mb (12 to 21 km) altitude, is a region in the atmosphere where the variability in the distribution of H₂O and O₃ is influenced by the coupling of the upper troposphere and lower stratosphere through dynamical, chemical and radiative processes. The tropical UTLS region can be thought of as a transition region that connects a convection-dominated, turbulent troposphere with a radiatively-controlled, stable stratified stratosphere.

In the tropics, Hadley circulation cells, in which air rises vertically from the surface to the troposphere, are driven by solar radiation incident upon the tropical atmosphere causing air at low latitudes to heat and rise. The vertically rising air eventually cools and sinks and while doing so, transports heat and momentum in a poleward direction following a series of circulatory cells. In the tropics, this upward motion is responsible for the uplift of moisture in the low pressure region of the Intertropical Convergence Zone (ITCZ) that is characterised by a belt of convective mesoscale cloud systems [Barry and Chorley, 1998]. The outer regions of the Hadley cells near 30°N and 30°S are characterised by semi-permanent, high pressure, anticyclonic systems. In northern hemisphere summer, the ITCZ shifts northward over India during the monsoon season and over the northern sector of South America and Equatorial Africa. In northern hemisphere winter, the ITCZ shifts to the southern regions of south America and Africa and passes over Northern Australia.

The tropical UTLS region is significant also for the global middle atmosphere because the general circulation of the Earth's atmosphere is driven from the tropical troposphere. It is generally accepted that air enters the global mean circulation from the tropical troposphere as first envisaged by Brewer [1949]. He postulated that air enters the atmosphere at the equator followed by an upward and poleward motion, more formally known as the Brewer-Dobson circulation. An important aspect of the UTLS region is how air mass is exchanged through this region. Air, rich in source gases but low in O_3 can be transported from the troposphere into the stratosphere. Similarly, air rich in O_3 but poor in H_2O can be transported from the stratosphere into the troposphere and collectively these processes are termed stratosphere - troposphere exchange (STE) [Holton et al., 1995]. Fujiwara et al. [2001] found that waves that propagate eastwards along the equator with no meridional velocity component, otherwise known as Kelvin waves, were one mechanism for STE that "opened" the tropopause for downward transport displacing dry, O_3 -rich stratospheric air into the upper troposphere. A schematic of the global mean meridional circulation and exchange processes is shown in Figure 1.3 from Stohl et al. [2003], that is an adaptation of the original proposed global circulation view by Holton et al. [1995]. In the diagram, the troposphere is separated from the stratospheric "overworld" by the tropopause that is represented by the 380 K potential temperature surfaces, or isentropes, (defined as the temperature possessed by an unsaturated dry air parcel if were adiabatically compressed to the 1000 mb pressure level) shown by the thick black line. In the tropics, this surface is located at approximately 100 mb or 16 km that slopes down to roughly 310 K or 8 km in the polar regions. Large-scale ascent transports air through the tropopause into the stratosphere where it is carried towards the mid-latitudes and finally descends through large scale subsidence in the polar regions. The upward motion of air is thought to be driven non-locally by eddy motions in the extratropical stratosphere and mesosphere indicating a downward control exerted on the troposphere. Over time, the eddy effects of breaking planetary-scale waves that have horizontal wavelengths up to thousands of kilometres (also called Rossby waves) can "add up" and gradually draw air upwards from the tropical stratosphere thereby inducing a mechanically wave driven circulation [Holton et al., 1995].

Ultimately, all large and small scale transport processes between the tropical upper troposphere and lower stratosphere, that can re-distribute H_2O , O_3 and its precursors,

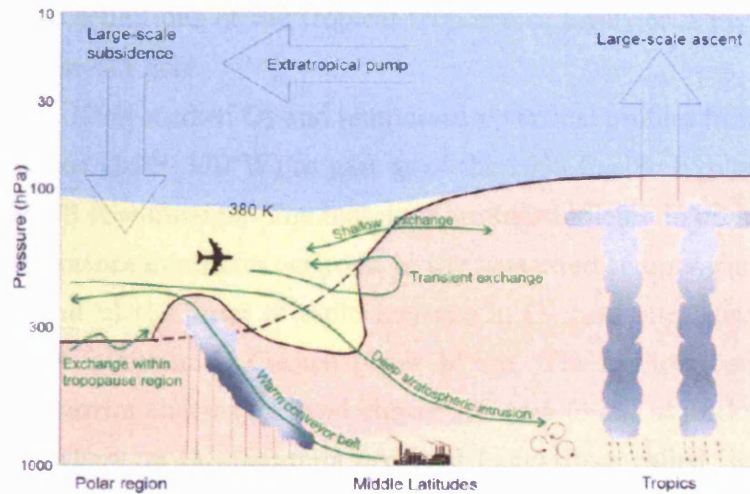


Figure 1.3: Stratosphere - troposphere exchange. Source: Stohl et al. [2003]. See text for explanation.

must pass through the tropical tropopause region. However, the definition, location and characteristics of the tropical tropopause is currently under debate and some of the properties of this region, in relation to H_2O and O_3 are discussed below.

1.1.1 The tropical tropopause layer

The tropical tropopause region has become the focus of much attention in recent years as observations of temperature and trace gas profiles suggest that the definition of the tropical tropopause deviates from the traditional view of a simple boundary between the troposphere and the stratosphere [Highwood and Hoskins, 1998]. Conventionally, the tropopause boundary is characterised by the altitude at which the temperature lapse rate is 2 K/km [Roe and Jasperson, 1980; Reid and Gage, 1981]. It has also been defined as the layer at which the minimum temperature, or the cold point temperature (CPT), is observed. This tropopause is usually called the cold point tropopause [Highwood and Hoskins, 1998]. However, in recent years it has been suggested that the tropical tropopause can be thought of as a transition zone between the troposphere and the stratosphere as opposed to a sharp boundary. This transition layer is thought to lie approximately between 150 and 50 mb (approximately 14 to 18 km) that connects a moist, convection-dominated upper troposphere to a dry, radiatively-active, stable lower stratosphere [Gettelman and de Forster, 2002a].

Currently, many definitions of the tropical tropopause layer, or TTL exist, some of which are summarised here.

Folkins et al. [1999] studied O_3 and temperature vertical profiles from ozone sondes launched at Samoa (14°S , 170°W) as part as of the 1999 Pacific Exploratory Mission (PEM) TROPICS A campaign. The measured profiles indicated two key features; a) a distinct temperature minimum occurred in the measured temperature profiles near 16 and 17 km and b) the onset of rapid increase in O_3 concentrations above 14 km with a distinctive minimum in O_3 just below 14 km. The authors postulated that a vertical mixing barrier that suppressed convection was found at 14 km. The region between 14 km where an O_3 minimum occurred (sometimes called the chemopause) and the CPT tropopause (around 17 km) was considered to be a transition zone (see Figure 1.4).

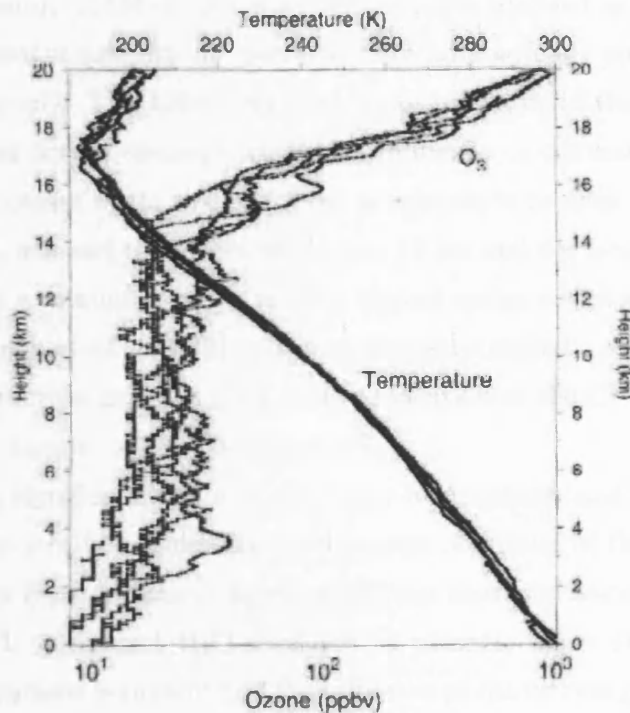


Figure 1.4: Temperature and O_3 vertical profiles in the TTL. Source: Folkins et al. [1999]. Note the location of the cold point tropopause, indicated by the minimum in the temperatures profiles, at 17 km.

Sherwood and Dessler [2000] describe the region between the level of neutral buoyancy (close to 150 mb, 14 km) and the absolute maximum height that convection can

influence (close to 50 mb, 19 km) as the region enclosing the TTL. By simulating the tropical UTLS environment using a model of convective and advective transport in the TTL region, their model results showed that: a) TTL air is mixed by overshooting convection then undergoes slow large-scale ascent until it reaches the stratosphere, b) a persistent layer of thick cirrus clouds occurs at 140 mb, c) an O₃ minimum occurs just below the TTL and d) a H₂O minimum is evident just above the TTL. Gettelman and de Forster [2002a] envisaged the TTL as a ‘transition’ layer between the upper troposphere and lower stratosphere with focus on the fact that the influence of convection decreases with increasing height. They used the cold point tropopause to define the upper boundary of the TTL that occurs at 16 km in Global Telecommunications Systems (GTS) and National Centres for Environmental Prediction (NCEP) radiosonde temperature soundings. For the base of the TTL, the authors identified the lapse rate minimum (LRM) in potential temperature (defined as the temperature possessed by an unsaturated dry air parcel if were adiabatically compressed to the 1000 mb pressure level). The LRM was used as an indicator of the stability as the height at which this occurs displays where the influence of convection is dominant before radiative processes begin to control the temperature profiles. This altitude or the base of the TTL is found to be between 10 and 12 km and the location of the LRM was consistent with a minimum in O₃ volume mixing ratios and strongly coupled to convection. Gettelman et al. [2002b] indicated that stratospheric stability influences the temperature structure near the CPT and the location of the CPT is found 1 to 2 km below a H₂O minimum or the “hygropause”.

Despite being a significant sector of the lower atmosphere, and attracting much attention from the scientific community, no universal definition of the TTL currently exists. The findings reported above agree on certain characteristics so far as to say that above the TTL, a distinct H₂O minimum is present; below the TTL, a minimum in O₃ concentrations is present and the influence of convection gradually reduces with increasing height. In essence, this region is thought to share characteristics of both troposphere and stratosphere [Thuburn and Craig, 2002] and it is imperative that the community reaches consensus on its definition. Characterising the concentrations and the variations of both H₂O and O₃ can aid in better definition of this region. Most specifically whether it can be considered to be a separate region in its own right, or whether it is simply a transition region that shares some tropospheric

and stratospheric characteristics and has no boundaries. Nevertheless, it is a region in which coupling of transport and chemical regimes can affect the distribution of upper tropospheric greenhouse gases. Some of the factors that control H₂O and O₃ concentrations here are discussed below.

1.1.1.1 Factors controlling tropical UTLS H₂O

One of the reasons that the TTL has become the focus of attention, particularly for several dedicated measurement campaigns, is the puzzling aspect of how air masses travel through the TTL and where in the TTL H₂O concentrations are reduced before air parcels get into the stratosphere. This process that involves the removal of H₂O from air masses is usually termed “dehydration” and there are several theories as to where and how this is caused. Much of the debate focussing on this subject surrounds two possible factors that could cause dehydration, namely air passage through the regions of the coldest tropical temperatures or the cold trap region, or by ice formation and precipitation associated with convective clouds [Read et al., 2004].

Newell and Gould-Stewart [1981] examined global 100 mb temperatures, taken as a representative of the tropopause, and proposed that air entered the stratosphere, from the tropopause, at particular times of the year where the tropopause was colder than average, in regions they termed the “stratospheric fountain”. The western Pacific Ocean, northern Australia and Indonesia, in November to March and the Bay of Bengal and India during the Monsoon season were proposed fountain regions. This was considered to be the case until Sherwood [2000] examined tropopause wind fields over Indonesia and found that within the maritime continent, the mean mass flux was in fact downwards and that no such fountain region was recognised. He proposed that cool air entered the tropopause region through irreversible mixing in overshooting turrets associated with towering convective clouds in the tropics. Since then several mechanisms have emerged as key factors that could play a role in the dehydration of air as it passes through the TTL. One is that tropical deep convection is dominating factor in controlling H₂O mixing ratios. Deep convective systems provide a source of H₂O to the tropical upper troposphere where they eventually, in the presence of wind shear, create anvils that cover a large horizontal [Jensen et al., 1996]. Earlier, Danielsen [1982] had postulated that air is rapidly dehydrated within these tropical deep convective clouds, or “dehydration engines” and that it is fully dehydrated before

it vertically ascends into the stratosphere [Sherwood and Dessler, 2000, 2001, 2003].

Conversely, it is believed that air undergoes fast horizontal advection through cold trap regions, such as the west Pacific and is subsequently dehydrated as it reaches the lower stratosphere [Hartmann et al., 2001; Holton and Gettleman, 2001]. The proposed mechanism is that air parcels, from warmer longitudes pass quasi-horizontally through the maritime continent where the tropopause temperatures are coldest (often less than 190 K) resulting in depletion of H₂O from moist air that reaches the lower stratosphere. Recently, transport pathways into the TTL and lower stratospheric region have been investigated using 3-d trajectory analysis [Bonazzola and Haynes, 2004; Fueglistaler et al., 2004] and the western pacific region appears to play a crucial role for all air parcels travelling from the tropical troposphere to stratosphere (TST). Fueglistaler et al. [2004] performed trajectory calculations of air passing through the TTL using wind and temperature fields from the European Centre for Medium-Range Weather Forecasts (ECMWF) and found that a large proportion of the trajectories (approximately 80%) passed through the TTL over the western Pacific region in northern hemisphere winter and summer, and often travelled distances much greater than 5000 km with residence times in the TTL close to 13 days, before they enter the stratosphere and encounter their minimum H₂O mixing ratio. H₂O mixing ratios assumed after TST were found to be in range between 1.6 ppmv and 3.7 ppmv depending on season. Other regions that were found to contribute to TST were over the Indian ocean, the Tibetan Plateau and the Caribbean.

In addition to transport processes, the primary factor that controls H₂O in the tropical tropopause region is tropopause temperatures. H₂O mixing ratios in the lower stratosphere were found to be closely related to the seasonal cycle of the tropical tropopause temperatures. As air parcels pass through these cold region they retained a memory, like a magnetic tape, of the conditions of the tropical tropopause before they entered the stratosphere. Lower stratospheric H₂O concentrations and their connection to tropical tropopause temperatures were investigated by Mote et al. [1996] who used several satellite instruments from the Upper Atmosphere Research Satellite (UARS) to investigate the propagation of a H₂O signal imprinted onto upwardly advected air entering the stratosphere. The authors found that air entering the stratosphere with ascent rates varied from $0.2 \times 10^{-3} \text{ m s}^{-1}$ to $0.4 \times 10^{-3} \text{ m s}^{-1}$, driven by extra-tropical wave pumping action that draws the air upward, retaining a

memory of the tropopause conditions for up to 18 months.

1.1.1.2 Factors controlling tropical UTLS O₃

The distribution of O₃ in the TTL is influenced by dynamical and chemical processes of which deep convection, STE, lightning within tropical thunderclouds and biomass burning are the most significant [Lelieveld and Dentener, 2000].

An important source of O₃ precursors in the tropics is from tropical biomass burning [Hao and Liu, 1994]. Smoke from biomass burning is laden with trace gases and particulates including CO, CH₄, NO_x [Andreae, 1990] that can lead to the formation of O₃ through cyclic reactions involving the photolysis of NO_x and through the oxidation of CO, CH₄ (and other hydrocarbons). Wayne [2000] states that each molecule of CO generates one molecule of tropospheric O₃ and one molecule of CH₄ produces one 3.5 molecules of tropospheric O₃. Such O₃ formation is a result of the efficiency of vertical exchange, usually within deep convective systems, and the emitted precursors [Andreae et al., 2001]. Biomass burning constitutes the burning of forests, and savannah for the purpose of deforestation, clearing of agricultural residue and shifting cultivation. Burning usually occurs over Central and South Africa, South America, South Asia and Australia. Burning seasons are usually identified as “wet” and “dry” seasons for which January/February and May to October are the dry seasons for Brazil and South Africa respectively [Kirchhoff et al., 1996].

The presence of deep convective cumulonimbus clouds are another contributor to O₃ enhancements in the upper troposphere. Deep tropical convection can redistribute pollutants from the surface or boundary layer directly into the UTLS region [Dickerson et al., 1987]. If taking place near regions of active biomass burning, deep convection can rapidly inject boundary layer air containing CO and NO_x into the upper troposphere contributing to O₃ formation. An additional factor that is related to deep convective clouds and also leads to O₃ formation is from NO_x produced as a consequence of lightning in such clouds. Thompson et al. [1997] estimates that 20 - 30 % of O₃ enhancement observed over the south Atlantic basin was attributed to a combination of deep convective uplift of biomass burning pollution and lightning (See Figure 1.5 for schematic of deep convection). Alternatively, convection can also lead to a reduction of O₃ in the tropical upper troposphere near 200 mb. Ozone sonde observations in various tropical locations including stations located in the southeast

Pacific (Galapagos, Samoa) have indicated reduced near-zero O_3 concentrations and it is postulated that these occur due to the uplift of clean, pollutant-free boundary layer air [Folkins et al., 2002; Solomon et al., 2005].

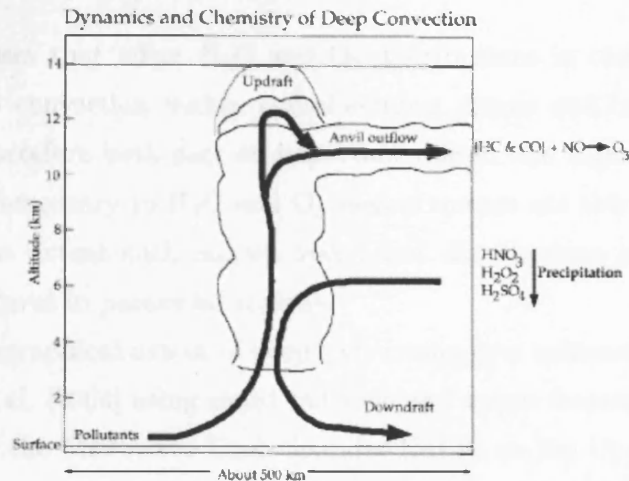


Figure 1.5: Schematic of deep convection in the tropics. Source: Thompson et al. [1997]. O_3 precursors are uplifted from the boundary layer into the upper troposphere within convective clouds.

Transport processes affecting O_3 in the UTLS region are not only upwards. Suhre et al. [1997] observed O_3 -rich air of stratospheric origin in upper tropospheric air measurements obtained from aircraft flying near 12 km. Some of the O_3 rich signal was observed near regions of cumulus anvil clouds and the downward transport of stratospheric O_3 was attributed to either 1) downward transport of O_3 -rich air in falling ice particles following overshooting anvil reaching the lower stratosphere or 2) quasi-isentropic transport of O_3 -rich air entering convective regions near the aircraft.

Occasionally mid-latitude intrusions can be associated with filamentations that break away from subtropical high-pressure systems. Intrusions of such stratospheric O_3 -rich air from the mid-latitude can directly transport ozone into the tropical troposphere [Cooper et al., 2005]. Intrusions are also associated with breaking Rossby waves [Waugh and Polvani, 2000] that result in the infiltration of subtropical air deep into the tropics. As well as intrusion from the extratropical regions, intrusions from the tropical stratosphere, penetrate the tropical upper troposphere with stratospheric O_3 concentrations. Thus, downwelling air from the stratosphere can penetrate the

TTL and directly inject O₃ into the upper troposphere; however, it is still not clear how much air enters the TTL from upward convective processes and how much from downward transport.

1.1.1.3 Clouds in the tropical UTLS

Some of the processes that affect H₂O and O₃ distributions in the tropical UTLS region involve deep convection within cumulonimbus clouds and interactions with cirrus clouds and therefore both play an important role in this region. Observations of the clouds complementary to H₂O and O₃ measurements are therefore important to establish to what extent such factors may affect distributions and furthermore validate certain features in particular regions.

Recently the geographical extent of deep convection, over seasonal timescales was studied by Jiang et al. [2004] using cloud radiance and upper tropospheric humidity measurements from the Microwave Limb Sounder (MLS) on the Upper Atmosphere Research Satellite (see section 1.2.2 for further reference to the MLS). They found that near the bottom of the TTL, regions of cold temperature and pronounced convective activity from the south Indian Ocean to the West Pacific occurred in December - March, with temperatures displaced slightly westwards (downwind) from convective centres. Within the TTL, close to 100 mb layer, they observed the lowest H₂O mixing ratios towards the north of convection and towards the top of the TTL and near 68 mb, convective influence dropped by 2% but primarily over the west Pacific. In July to September the most distinctive regions where cloudiness and the coldest temperatures are observed tend to be localised over the regions of the North America and South Asia/Tibet in association with anti-cyclonic activity associated with the monsoons (See Figure 1.6). Similarly, Liu and Zipser [2005] used 5 year precipitation radar data measured by the Tropical Rainfall Measuring Mission (TRMM) to investigate overshooting convection and found that no more than 1 % convection reached higher than 14 km.

Other clouds that persist in the UTLS region are high altitude cirrus clouds often termed Ultra-Thin Tropopause Cirrus (UTTC) or Sub-visible cirrus (SVC) [Luo et al., 2003]. Cirrus clouds in the tropical UTLS are formed by two mechanisms, either from anvil dissipation from the tops of convective towers or from *in situ* formation that depends on the right combination of temperature and relative humidity [Jensen et al.,

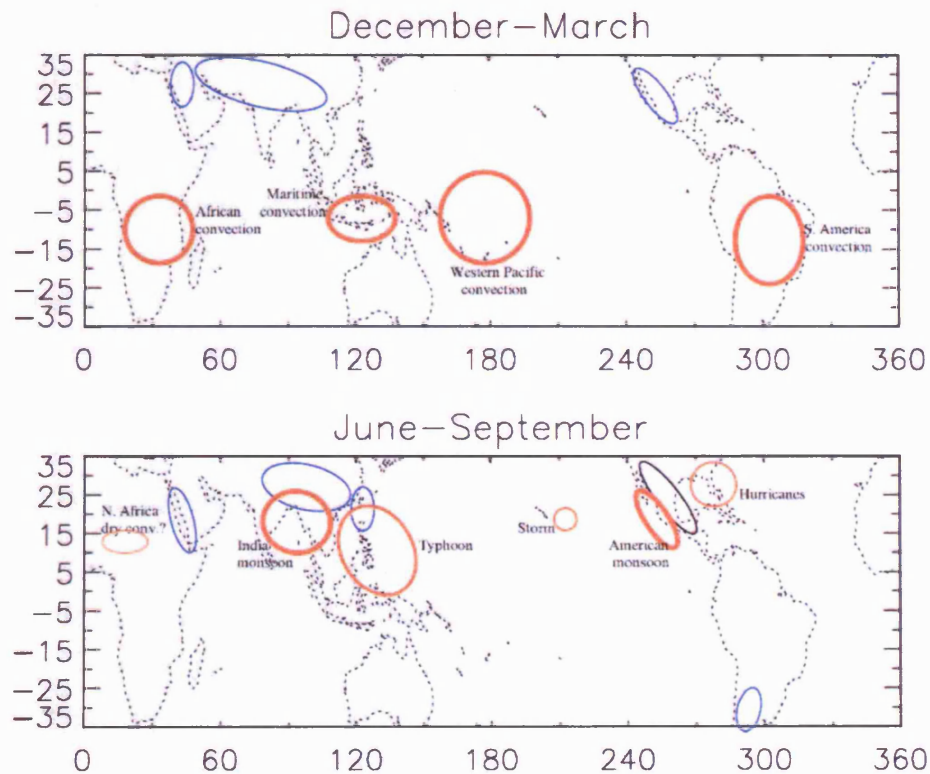


Figure 1.6: Seasonal patterns of convection in the tropics. Source: Jiang et al. [2004]. Note distinct regions of convection over the Western Pacific and African convection. Blue circles denote topography related disturbances. Top panel indicates SH and bottom panel indicates NH summers.

1996]. The interactions of ice particles from these clouds with moist or ozone-rich air can alter concentrations of these gases in the TTL. Jensen and Pfister [2004] reported that clouds in the TTL region can deplete H_2O from vertical and horizontally advected air in this region.

The presence of clouds in the UTLS/TTL region can compromise the quantity and quality of *in situ* and remote observations of this region. In the following section, some of methods that have been used to observe this region are described with reference to UTLS H_2O and O_3 observations made by some of the instruments.

1.2 Observing H₂O and O₃ distributions in the tropical UTLS

As might be expected from the preceding descriptions, both H₂O and O₃ have variable concentrations in the tropical UTLS. Since the discovery of the airidity of the lower stratosphere, H₂O observations close to the tropopause region have increased with much attention given to regional variations and determination of stratospheric entry concentrations. The three primary methods used for observations of the atmosphere are instruments on ground-, air- and space-based platforms.

1.2.1 *In situ* observations

Measurements of H₂O and O₃ in the tropical UTLS have conventionally been acquired from instruments on ground or air-borne platforms. Instruments on these platforms are termed *in situ* as they are within the region of interest and make a direct measurement as opposed to a remote measurement. Historically, most *in situ* measurements of the upper troposphere were made over the Northern Hemisphere landmasses with poor sampling in the tropics. In the cases when tropical measurements were made, they often did not reach upper tropospheric altitudes meaning that this region has not always been well represented.

The earliest archived *in situ* tropical upper tropospheric data-sets, consisting of radiosonde and radar measurements dating back to the 1940s, are owned by the World Meteorological Organisation (WMO). Since the work of Brewer [1949] and the growing interest in the tropical UTLS, the frequency of *in situ* measurements in this region have increased. In the last 30 years or so, the position and composition of the TTL has increasingly become the focus of many long-term measurement programs and *in situ* field campaigns. The different methods and kinds of measurements being made in the tropical UTLS are discussed below.

1.2.1.1 Aircraft measurements

In situ UTLS data are obtained primarily from one of two platforms: aircraft and balloons. The use of aircraft to sound the UTLS is a convenient and operationally flexible method to obtain *in situ* data. The major advantage of using small light

aircraft is that it is easily adaptable in that the speed and altitude of the aircraft can be changed to meet the requirements of the instruments onboard. It allows point and transect analysis of regions so that small-scale processes can be measured and has the important advantage of being able to avoid cloud layers should it need to. A particular downside to using aircraft is that measurements are short-term and not usually continuous so atmospheric probing can only be performed for up to a few months. Other factors that could be seen as detrimental are the costs to fund aircraft campaigns which depends on duration, and the location of the aircraft flights which is determined by flying permissions that influence the planning of the aircraft campaigns. Aircraft used to sound the atmosphere generally do not reach the tropopause but can reach the upper troposphere such as the DLR FALCON and Grob 520T Egrett aircraft that reach maximum cruise altitudes near 12 km. An exception to this is the Russian M55 Geophysica aircraft that reaches a maximum altitude of 20 km making it a suitable platform for TTL-related studies. These aircraft recently flew in the dedicated scientific tropical aircraft campaign called SCOUT-O3 that took place in Darwin, Australia 2005. Aircraft are an integral part of tropical field campaigns that rely on these platforms to sample the UTLS atmosphere. Several tropical *in situ* field campaigns that have measured UTLS H₂O and O₃ during MIPAS's lifetime are given in table 1.1.

Alternatively, instruments can be carried onboard selected commercial jets that take part in measurement programmes specially instigated to provide more continuous coverage. Two such programmes are the Measurement of Ozone and Water Vapour by Airbus In-Service Aircraft (MOZAIC) and a European consortium called the Civil Aircraft for the Regular Investigation of the Atmosphere Based on an Instrument Container (CARIBIC) [Brenninkmeijer et al., 2005]. The passenger jets are equipped with instruments that directly sample middle and upper tropospheric air whilst the commercial jet is in flight. Measurements of H₂O, O₃, aerosol and other trace gases are made using an automated sensors and atmospheric probes that have direct contact with the atmosphere. For example, commercial jets involved in the MOZAIC program [Marengo et al., 1998] are equipped with Vaisala humidity sensors and dual-beam UV absorption instruments to measure humidity and O₃, respectively. Measurements from commercial jets are made at aircraft cruise altitudes of 9 to 12 km meaning that the UTLS is not efficiently sampled in the tropics.

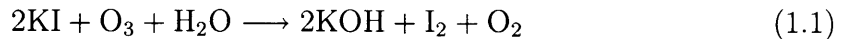
1.2.1.2 Balloon measurements

In situ measurements of H_2O and O_3 are also obtained from light weight instruments carried on balloons that are released from the ground and continuously sense the atmosphere until the balloon bursts at an altitude near the upper troposphere. Using balloons to measure the atmosphere is one of the earliest methods of *in situ* sounding with the first balloon measurements made more than sixty years ago. Instruments carried on meteorological balloons essentially make vertical profile measurements at a location. They are relatively cost-effective and can sample the air directly with a high time and altitude resolution which allows them to capture fine-scale structure in the atmosphere.

1.2.1.3 Ozone sondes

Typically balloon measurements of O_3 are made by three kinds of ozone sondes which are the Brewer Mast, the Electrochemical Concentration Cell and the Japanese ozone sonde. An ozone sonde has four basic components that collectively consist of a pump, an ozone sensor cell, and an electronics and transmitting module to transmit the ozone measurements to a ground based unit, all tethered to a meteorological balloon. Ozone sondes are usually launched from the ground or alternatively dropped from aircraft (drop sondes). Most ozone sondes use the same basic principles that require a redox reaction involving potassium iodide where the current generated by the redox reaction is proportional to the ozone flow rate through the cell.

An Electrochemical Concentration Cell (ECC) ozone sensor is a device that measures the vertical distribution of ozone in the atmosphere by means of a redox reaction between O_3 and iodide. The instrument was designed by William Komhyr at the National Oceanographic Atmospheric Administration (NOAA) in Colorado and has provided high resolution ozone data from the ground level to approximately 30 km. The ECC sondes use an iodometric wet method in which O_3 -rich air is forced into a cathode chamber where the O_3 reacts with iodide leading to the production of iodine (I_2) [Komhyr et al., 1995]. Both electrodes are immersed in aqueous potassium solution and as the iodine molecule converts back to iodide, electrons flow through the cell's external circuit.



This external current is proportional to the rate at which ozone enters the sensor. If the pump flow rate, cell current and the temperature are known, the partial pressure of ozone P_{O_3} , can be obtained using Equation 1.2:

$$P_{O_3} = 4.306 \times 10^{-4} (I - I_{BG}) T_p T_{100} * (PCF) \quad (1.2)$$

where I is the ozone current, I_{BG} is the background or ‘no O_3 ’ current, T is the temperature of the sonde pump in kelvin, and T_{100} is the reciprocal of the flow rate in seconds per 100 cm^{-3} of airflow. The PCF term is the pump flow rate correction factor that is equivalent to $1/\text{efficiency}$. The PCF term adjusts for a decrease in the pump’s efficiency with increasing altitude. The ozone partial pressure (in mb) is converted to volume mixing ratios using equation 1.3.

$$ozone[vmr] = P_{O_3} * \frac{1000}{pressure(mb)} \quad (1.3)$$

There are five different kinds of ECC ozone sondes: the SPC 3A, 4A, 5A, 6A and the 1Z model that are currently manufactured by the Science Pump Corporation and the EN-SCI Corporation [Johnson et al., 2002]. An illustration of an ECC ozone sonde is given in Figure 1.7.

Ozone sondes allow the opportunity to determine the vertical distribution of O_3 in the tropics. Recently, Vomel et al. [2002] measured O_3 in the tropical upper troposphere and lower stratosphere over Ecuador, Brazil and the west Pacific and observed O_3 concentrations characteristic of deep convective uplift of upper tropospheric low- O_3 air over the convective west Pacific region (see Figure 1.8). Often most balloon borne measurements of O_3 are made during specialised measurement campaigns and therefore do not provide long-term or continuous measurements of O_3 in the tropics.

To overcome the fact that measurements of the tropical atmosphere can be sparse, the Southern Hemisphere Additional Ozonesonde (SHADOZ) network was set up to make regular and timely measurements of O_3 over a wide range of tropical latitudes [Thompson et al., 2004]. Since 1998, the SHADOZ network has continuously acquired vertical O_3 profiles and has provided an alternative view of the distribution of O_3 in the tropics (Figure 1.9). Although it is restricted to the southern hemisphere tropics,

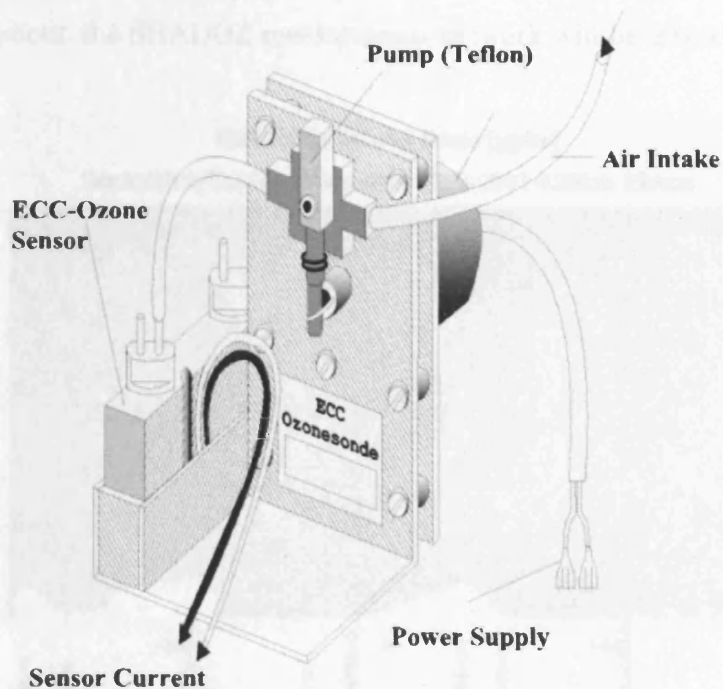


Figure 1.7: Schematic of an ECC ozone sondes. Source: <http://www.fz-juelich.de>

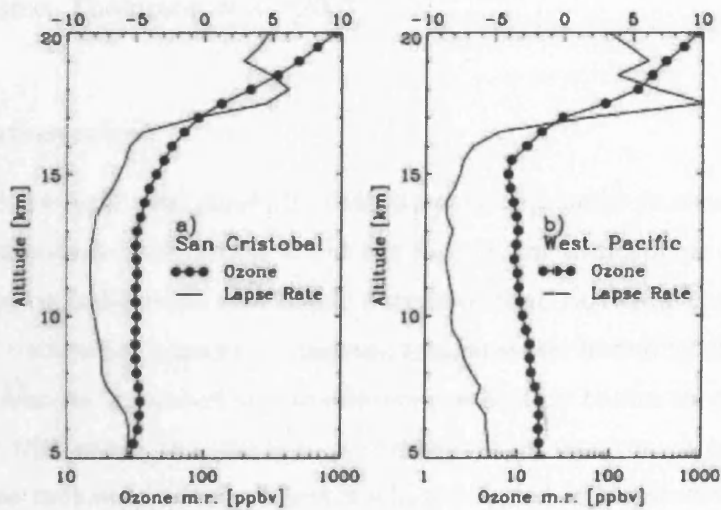


Figure 1.8: Vertical profiles of O_3 measured at the tropical locations of San Cristobal ($0.9^\circ\text{S}, 89.6^\circ\text{W}$) and the west Pacific ($2^\circ\text{S}, 157^\circ\text{W}$) using ozone sondes. Source: Vomel et al. [2002]

the SHADOZ network is an important provider of O_3 measurements in the tropics. More details about the SHADOZ measurement network will be given in chapter five of this thesis.

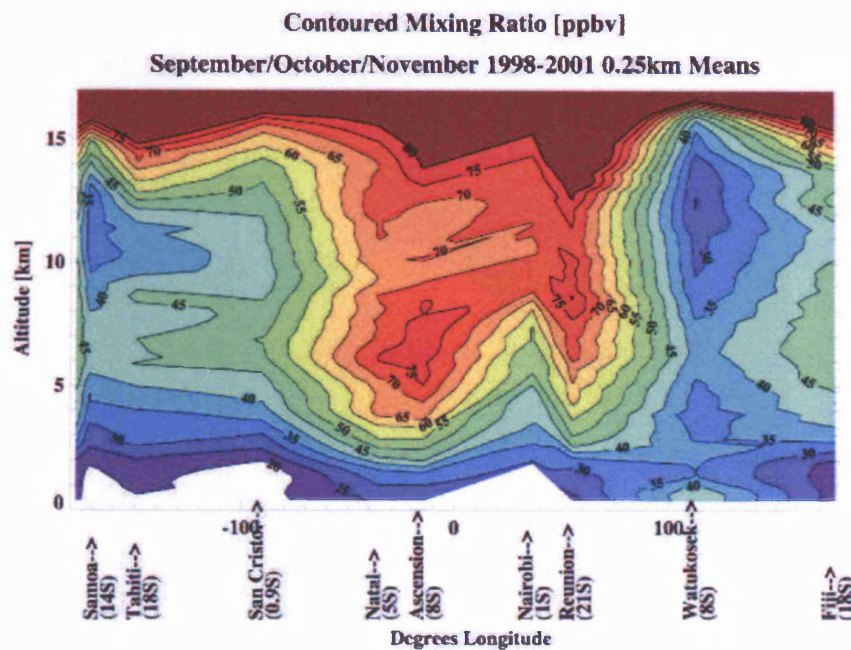


Figure 1.9: Longitudinal O_3 distribution from the surface to approximately 15 km measured by the SHADOZ network. SHADOZ station locations are highlighted below the figure Source: Thompson et al. [2003]

1.2.1.4 Radiosondes

Radiosondes have been used since the 1940s to routinely make *in situ* humidity measurements from which information about the H_2O in the atmosphere can be derived. In basic terms, a radiosonde is a small container that carries a thermometer, hygrometer and barometer, sensors to measure temperature, humidity and air pressure, respectively. Also incorporated into the device is a battery to run the instrument and a transmitter that sends the signal to a corresponding receiver. Measurements are recorded as the radiosonde device ascends whilst coupled to a meteorological weather balloon. Historically, radiosondes are one of the most well established meteorological instruments and were first produced and distributed in 1936 by Finnish Professor Vilho Vaisala, who modified the originally designed radiosonde by Russian meteorologist Pavel Molchanov [Michelsen, 2006]. Since then many types of radiosondes have

been produced and in this section, the Vaisala radiosondes, that are the oldest and most popular kind of radiosonde, will be described.



Figure 1.10: An example of an RS92 Vaisala radiosonde. Source:www.vaisala.com

Radiosonde measurements are some of the longest running atmospheric measurements with a global radiosonde network as part of the World Meteorological Organisation (WMO) making regular, usually twice daily atmospheric measurements at more than a thousand “upper air” stations. The two most commonly used radiosondes are the carbon hygistor and the thin film capacitors [Kley et al., 2000]. Carbon hygristors are radiosondes that contain polystyrene strips coated with carbon hygroscopic film whose electrical resistance increases with increasing relative humidity. However, the carbon hygristors do not perform so well at low temperatures (less than -40°C) and can therefore be unreliable in the upper troposphere [Kley et al., 2000].

The most commonly used and longest established radiosondes are Vaisala radiosondes from which relative humidity (RH) measurements are made. RH is a quantity that describes the amount of H_2O that is present in the atmosphere as a percentage of the maximum amount of H_2O the air can hold. RH sensors are based

on a carbon humidity element that is made from a glass or plastic substrate that swells with increasing humidity. One kind of humidity sensor is the thin-film capacitor, usually called a Humicap sensor, that consists of a thin hydrophilic polymer layer on a glass substrate. The dielectric constant of the polymer varies with ambient H₂O pressure. H₂O molecules are captured on binding sites on the polymer and the number of molecules is proportional to the capacitance measured by the radiosonde [Miloshevich et al., 2001]. The more molecules measured, the higher the H₂O concentration. A radiosonde system is flown attached to a natural or synthetic rubber balloon that expands with ascent with an eventual burst at some pressure. They provide information on pressure, geopotential height, temperature, relative humidity, temperature, wind direction and wind speed. The measurements are continuously transmitted to a ground-based receiving system until the measurements cease when the balloon bursts usually at an altitude around 25 km. Typical ascent rates for the sondes are around 5 m/s with a sampling rate of approximately 2 seconds producing a vertical resolution near 10 - 50 m.

Currently there are two main kinds of Vaisala radiosondes in operation. RS80-A radiosondes were developed in the 1980s and later the RS80-H radiosonde was introduced in 1992 and remains one of the most commonly used radiosondes at present. The “A” and “H” in their names indicate the two different polymer materials, where the A-type polymer was the initial design and in the early part of the current decade one of the most common used radiosonde type at measurement sites world wide. The H-type polymer, that was developed in the later 80’s is more efficient in taking up water molecules and more stable against hysteresis at higher humidities. RS80 sondes measure over a RH range of 0% to 100% with a 1% RH resolution. The RS90 (and RS92) radiosondes are the most recently developed Vaisala radiosondes, introduced in 2000 and 2003, respectively [Miloshevich et al., 2004] and use a thinner and smaller H-type polymer. Both RS90 and RS92 have dual sensors that are heated alternately to overcome sensor icing and are therefore considered to be more accurate than RS80 sondes. The RH measurement range for RS90 sondes are 0 to 100% RH with a 1% RH resolution.

For tropical H₂O, balloon borne measurements usually incorporate measurements from radiosondes although, similar to the O₃ cases, observations in the tropical regions were sparse. Some of the earliest measurements of H₂O vertical profiles have been

made in dedicated tropical measurements campaigns such as those performed by Kley et al. [1979] in Brazil where H₂O mixing ratios as low as 2.6 ppmv were observed and more recently, Vomel et al. [2002] made balloon measurements of H₂O over Brazil, Ecuador and West Pacific where dehydrated air with H₂O mixing ratios close to 2 ppmv were observed (See Figure 1.11).

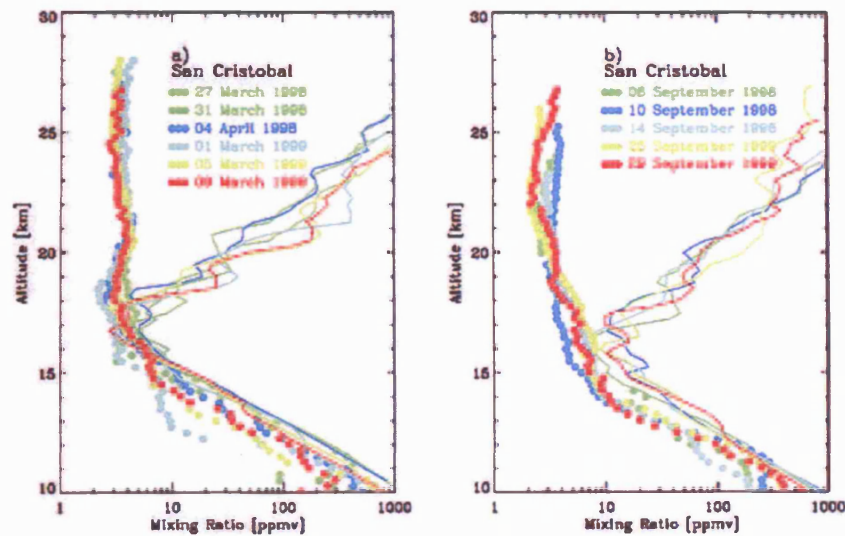


Figure 1.11: Vertical profiles of H₂O measured in the tropics made from balloon-borne observations incorporating radiosondes. Source: Vomel et al. [2002]

Campaign	Location	Dates	Platform
TROCCINOX I	Sao Paulo, Brazil	31/01/04 - 15/03/04	Falcon aircraft, MIR-SAOZ long duration balloon
TROCCINOX II	Bauru, Brazil	18/01/05 - 09/03/05	Falcon and Geophysica aircraft
SCOUT-O3	Darwin, Australia	16/11/05 - 05/12/05	Falcon and Geophysica aircraft
ACTIVE	Darwin, Australia	07/11/05 - 09/12/05, 16/01/06 - 17/02/06	Dornier and Egrett aircraft, Ozone sonde balloon
AMMA	Niger, Africa	31/07/06 - 18/08/06	Geophysica aircraft, ozone sondes

Table 1.1: Field campaigns in which in situ tropical UTLS H₂O and O₃ measurements have been made in MIPAS operation lifetime. Only the TROCCINOX I campaign overlapped with a few days worth of MIPAS nominal full resolution data.

The alternative method of observing the tropical UTLS is of course, remotely.

The distributions of H₂O and O₃ measured previously by satellites are discussed in the following section.

1.2.2 Previous satellite observations

To overcome the inability of *in situ* instruments to be able to make large-scale and continuous measurements of H₂O and O₃ in the tropical UTLS, instruments onboard satellite platforms provide an ideal opportunity to make near-global and continuous measurements of H₂O and O₃ in this region.

1.2.2.1 Satellite observations of tropical UTLS O₃

Some of the first indications of the distribution of O₃ in the tropical latitudes came from nadir viewing instruments on board Earth observing satellites such as the Total Ozone Mapping Spectrometer (TOMS) and the Solar Backscatter Ultraviolet (SBUV) onboard the National Aeronautical Space Administration (NASA) Nimbus-7 satellite from which total O₃ columns could be inferred. Longterm measurements of total column O₃ from the TOMS instrument, combined with longterm O₃ measurements from the Stratospheric Aerosol and Gas Experiment I (SAGE I) to remove the stratospheric O₃ signal, provided insight into the distribution of tropospheric O₃ [Fishman et al., 1990]. From integrated columns of tropospheric O₃, it was found that the highest concentrations occurred over the Atlantic Ocean to the west of the African coast, usually maximised between July and October. Later, Fishman and Brackett [1997] observed the seasonal cycle of TOMS and SAGE I derived tropospheric O₃ and found that it followed a distinctive seasonal cycle, as shown in Figure 1.12. Although this method using the TOMS highlighted important O₃ features in the tropics, it is unable to provide information about the vertical structure of O₃ particularly regions of distinctive layering within the tropospheric O₃ signal.

1.2.2.2 Satellite observations of tropical UTLS H₂O

Satellites also provided the first view of the distribution of H₂O in the tropics. One satellite that provided layer information about H₂O down to 316 mb (close to 9 km) with an effective vertical resolution close to 3 km [Read et al., 2001], was the

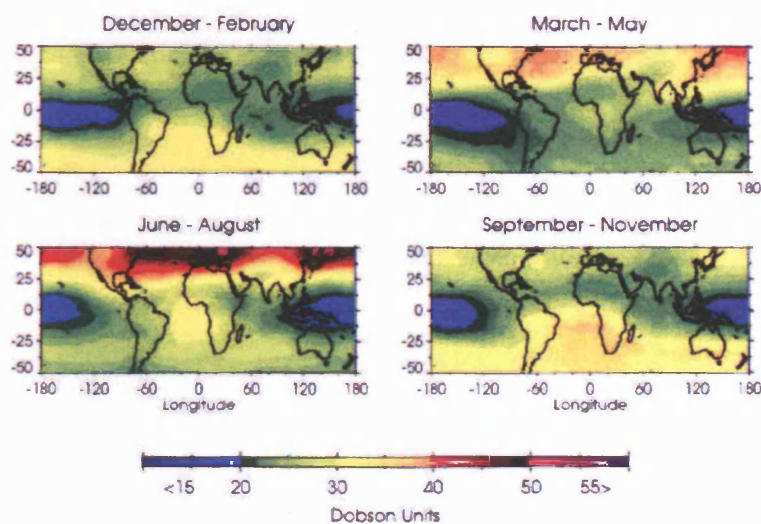


Figure 1.12: Seasonal climatological tropospheric O₃ residual column, measured in Dobson units, derived from the TOMS and SAGE I and SAGE II measurements (1 DU = 1 Dobson unit that is equivalent to 2.69×10^{16} molecules of O₃ per square centimetre). Source: Fishman and Brackett [1997]

Microwave Limb Sounder (MLS) onboard the UARS satellite launched in 1991. Because it observes the atmosphere in the microwave region, MLS measurements are relatively transparent to cirrus and aerosol, although its measurements are still affected by thick cirrus. Even in so called clear sky scenes, interpretation of these data can be affected by cirrus presence [Read et al., 2001]. The MLS instrument has been used to study the seasonality, and distribution of H₂O in the tropical UTLS at in terms of separate layers and zonal distributions [Clark et al., 1998; Chen et al., 1999; Pumphrey et al., 2000; Clark et al., 2001]. Features such as high H₂O mixing ratios at 215 mb over southeast Asia and low mixing ratios over Indonesia were found with concentrations often higher than 170 ppmv at 215 mb. At 68 mb, low mixing ratios of 2.95 to 3.10 ppmv were observed over Indonesia and the West Pacific, indicating dehydration processes in this region. Stone et al. [2000] investigated the seasonal distribution of H₂O in the upper troposphere using MLS measurements with SAGE II H₂O measurements. Over the tropical latitudes, MLS H₂O showed regions of variability with concentrations ranging from 10 to 200 ppmv throughout the year (See Figure 1.13).

Other satellite instruments that have measured distributions of the H₂O in the

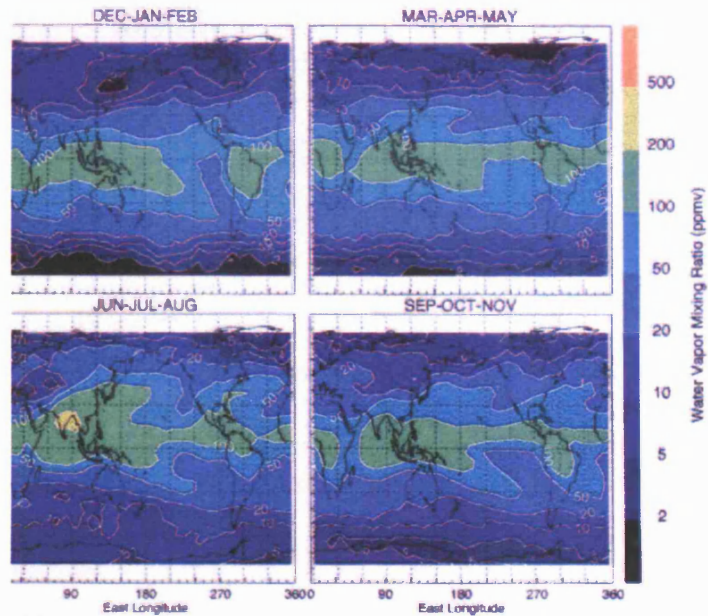


Figure 1.13: H₂O at 215 mb measured by the MLS instrument. Source: Stone et al. [2000]. MLS upper tropospheric H₂O measurements indicate regions of variability in the tropics with concentrations close to 200 ppmv over South Asia in northern hemisphere summer

tropical UTLS include HALOE and SAGE II that observe through the atmosphere, however with coverage limited to particular latitude bands (see section 2.1). Data from these instruments have been used to examine the seasonal cycle of H₂O entering the stratosphere [Dessler and Kim, 1999] as well as derivation of regional variations and trends in H₂O distributions. For example, Randel et al. [2001] observed the seasonal cycle of H₂O in the lower stratosphere measured by HALOE in a nine year climatology and found localised variations such as H₂O maxima over the South Asian region in northern hemisphere summer and regions of dehydrated air over the west Pacific (See Figure 1.14).

Mote et al. [1996] used H₂O measurements from the UARS satellite to determine the seasonal cycle of H₂O entering the stratosphere. The H₂O “tape recorder” as measured by the MLS and HALOE instruments are shown in Figure 1.15. Details about each section are given in figure caption, but essentially the figure shows the distinct seasonal cycle of H₂O entering the stratosphere, consistent with the seasonal

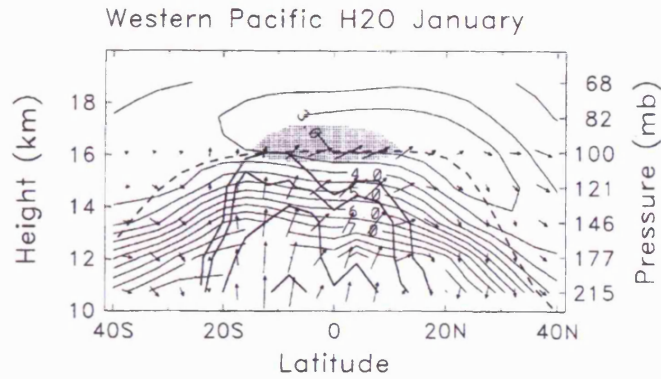


Figure 1.14: Zonal mean H₂O as measured by the HALOE instrument. Source: Randel et al. [2001]. Note the location of a “hygropause” at 17 km.

cycle of the tropopause temperatures (that is colder and higher in northern hemisphere winter). The air driven upwards by the extratropical suction pump retains the information about the tropical tropopause conditions it encountered during the previous 18 months.

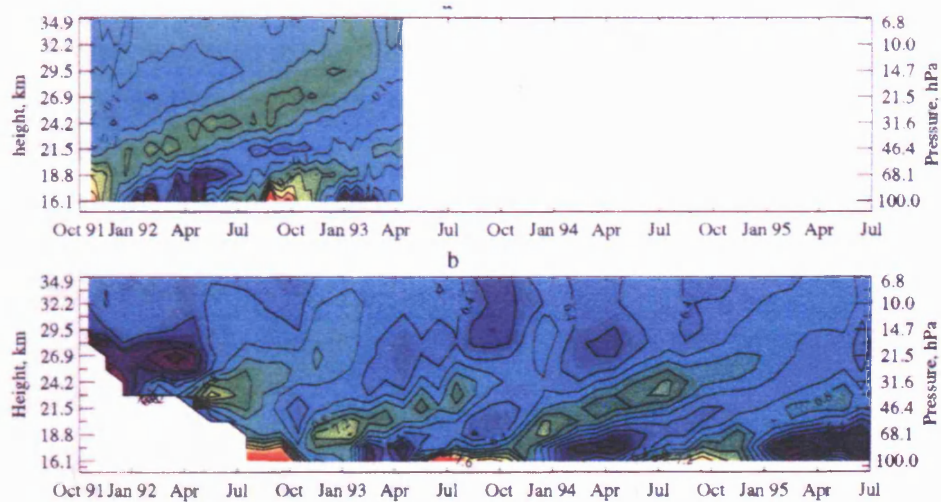


Figure 1.15: The stratospheric H₂O tape recorder measured by the MLS and HALOE instruments adapted from Mote et al. [1996]). The figure shows the time-height cross sections of H₂O anomalies between 12°N and 12°S from the MLS (section a) and HALOE total hydrogen (section b). Note the successive maxima and minima of H₂O entering the stratosphere in July - September and January - April, respectively.

1.2.3 In situ vs. remote sensing

UTLS measurements obtained from aircraft instruments can make point and wider scale measurements making them highly adaptable and suitable for making long range measurements. This flexibility allows aircraft to easily measure at a particular location whereas satellite measurements of a particular location of interest depends purely on when the satellite orbit passes over that location. On the other hand, factors such as creating flight plans and obtaining flying permits can be time consuming and problematic in which case satellite measurements are more convenient.

In situ measurements obtained from balloon instruments are cheap in comparison to aircraft and satellite instruments and can be directly accessed. This means that balloon instruments can be launched directly into a region of interest such as a biomass burning plume or into the outflow of a thunderstorm as soon as such events begin. Balloon measurements are best operated in light meteorological conditions as severe meteorological conditions would lead to sondes drifting and becoming damaged. Balloon instruments require a constant uplink to a GPS computer system and accurate calibration methods as all instruments do. A potential source of error is human error in launching sondes and inaccurately recording information such as time and date. Ground based methods are usually sporadic and often only operate on a campaign basis.

Satellite measurements can provide a useful tool to obtain a vast coverage over the tropical region and this has been demonstrated by some of the satellite examples shown above. However, satellite measurements can also be limited in terms of their vertical resolution, measurement technique and often inability to measure accurately in the presence of cloud.

1.2.4 Motivation for this work

In the sections above, the role of H_2O and O_3 in the tropical UTLS and some of the factors that can influence their distributions were discussed. The requirement for continuous observations of lower stratospheric H_2O and O_3 in the tropical tropopause has been noted. Takashima and Shiotani [2007] noted the need for increased observations of the distribution of O_3 in the UTLS region to quantify dynamical factors that may cause variability in this region. Similarly, Rosenlof et al. [2001] and Randel

et al. [2006] noted changes in the trend of H₂O entering the stratosphere for which regular global monitoring is important. Satellite instruments are well suited for such requirements and can provide large-scale observations from the stratosphere to the lower atmosphere although they are limited by their vertical resolution.

In this thesis, remotely sensed tropical UTLS H₂O and O₃ measurements are considered. The Michelson Interferometer for Passive Atmospheric Sounding (MIPAS) instrument is a high resolution spectrometer that measures infrared emission spectra using the limb sounding technique. The infrared measurements of the MIPAS instrument can be used to investigate the simultaneous distributions of both H₂O and O₃ and with some indication of cloud presence, also allows quantification of “clear sky” and thin cloud measurements. For example, MIPAS can provide a better representation of “clear sky” measurements, compared to those of MLS. Although MLS looks *through* cirrus clouds, it can be difficult to distinguish concentrations of H₂O in “clear sky” and thin cloud measurements. In terms of comparison to the solar occultation instruments, the advantage of MIPAS is that it can measure more profiles globally than the average of 30 profiles per day achieved by instruments such as HALOE and SAGE II.

The structure of the remainder of this thesis is as follows: in chapter two, the theory of atmospheric radiation and the techniques used to capture H₂O and O₃ signatures in the atmosphere are followed by an introduction to remote sensing and retrieval techniques. In chapter three, a description of the MIPAS instrument and the data processing is given. In chapter four, the impact of the cloud on MIPAS H₂O and O₃ data is analysed with particular focus on how cloud errors can propagate into the data, lowering data quality, and how these effects can be identified and removed. In chapter five, inter-comparison experiments of MIPAS H₂O and O₃ with existing independent measurements obtained from satellite and *in situ* instruments are performed. Chapter six presents some seasonal distributions of H₂O and O₃ in the tropical UTLS followed by final and suggestions for further work will follow in chapter seven.

Chapter 2

Remote sensing of the tropical UTLS region

Remote sensing of the Earth's land, sea or atmosphere is the practise of deriving information using some part of the electromagnetic spectrum to measure the radiation that is emitted or reflected from the Earth's surface or atmosphere [Campbell, 1996]. Instruments carried onboard a spaceborne platform provide an ideal platform to obtain thousands of measurements on a large-scale of some atmospheric property. Satellite instruments can provide global coverage in a few days which is particularly advantageous for areas that are inadequately monitored by ground- and air-based instruments. Such instrument can also provide long-term, near-continuous atmospheric measurements such as NASA's Total Ozone Spectrometer, the measurements of which are ideal for generating climatological datasets. Satellite instruments typically make radiance measurements that require some form of mathematical inversion and manipulation to convert the *raw* radiance signal into an atmospheric property such as a temperature or trace gas concentration value. To obtain such information, specially designed, mathematical, retrieval algorithms that take into account the instrument's measurement geometry and measurement technique as well as the state of the real atmosphere, are used to *retrieve* atmospheric quantities. In this chapter, a discussion of the infrared limb sounding methods used to observe H₂O and O₃ in the tropical atmosphere is presented. The following sections describe the principles of limb sounding and radiative transfer, and the infrared spectroscopy of H₂O and O₃. Finally, the fundamentals of retrieval theory are discussed.

2.1 Infrared limb sounding

Satellite instruments usually sound the Earth's atmosphere using nadir or limb sounding techniques. Nadir sounders observe the atmosphere at 90° to the surface and provide measurements from which mainly total columns of trace gases can be inferred. The limb sounding technique works by observing the Earth's atmosphere "horizontally" at the horizon (also called the Earth's limb). In doing so, it measures the emission of the atmosphere with a cold space background or alternatively the absorption of the atmosphere with the sun as a background source. This latter method is called the occultation method in which stars (stellar) and the moon (lunar) can also be used as an illumination source. Table 2.1 lists limb sounding instruments that have measured tropical H_2O and O_3 whilst MIPAS has been in operation.

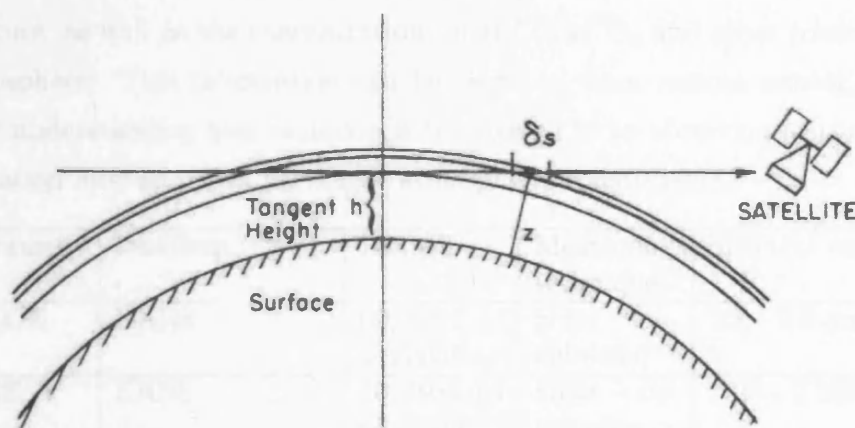


Figure 2.1: Limb sounding of the atmosphere. Source: Stephens [1994]

The limb geometry is shown in figure 2.1 where h is tangent height and z is the actual height at a segment of the atmosphere, ds . The limb sounding technique is suitable for vertical profiling of the atmosphere because it can provide a vertical resolution of the atmosphere of 3 km or better. This is relatively high compared to the vertical resolution achieved by nadir sounding instruments (usually > 5 km). By scanning the instrument's view vertically through the atmosphere, measurements at consecutive tangent altitudes can be obtained. The radiation that is measured at each tangent height is not influenced by any radiation below the measurement and the signal comes solely from the radiation at h , and typically the altitudes above, weighted by the decrease in atmospheric density and gas vmr with height. Due to

the measurement geometry of limb sounders, the emission from the atmosphere is measured along a relatively long horizontal path even at the tangent point (> 500 km) and this allows greater sensitivity to constituents with low mixing ratios. This feature can be exploited to measure both major (H_2O and O_3) and minor atmospheric constituents such as HCFC-22 [Moore, 2005] and C_2H_6 [von Clarmann et al., 2007].

The limb sounding geometry and instrument pointing must be known precisely so that potentially retrievable quantities can be accurately determined. The measurement range can extend from the mesosphere to as low as 5 - 6 km although, in the upper troposphere, limb measurements can be affected by the presence of clouds. Thick opaque clouds act as blackbodies and can remove the sensitivity to trace gas concentrations at the cloud altitude and below. The thermal radiation that is measured by limb sounders such as MIPAS, carries information about the atmospheric temperature, as well as the concentrations of H_2O and O_3 and other constituents in the atmosphere. This information can be retrieved from remote sensing measurements by understanding how radiation is transferred to an observing instrument and how radiation interacts with particular atmospheric constituents.

Instrument	Platform	Launch	Measurement technique	Spectral range
HALOE	UARS	09/1991 to 11/2005	Solar occultation	2.8 - 9.6 μm
SAGE II	ERBS	10/1984 to 08/2005	Solar occultation	1.02 - 0.382 μm
SAGE III	Meteor-3M	10/2001 to 03/2006	Solar occultation	280 - 1040 nm
TES	AURA	07/04 to present	Limb emission	3.2 - 15.4 μm
EOS-MLS	AURA	07/2004 to present	Limb emission	118 - 2250 GHz
ACE-FTS	SCISAT	08/2003 to present	Solar Occultation	2.2 - 13.3 μm
ODIN-SMR	OSIRIS	02/2001 to present	Limb emission	485 - 580 GHz

Table 2.1: Limb sounding instruments in operation during MIPAS mission. HALOE = Halogen Occultation Experiment; SAGE = Stratospheric Aerosol and Gas Experiment; TES = Tropospheric Emission Spectrometer; ACE-FTS = Atmospheric Chemistry Experiment - Fourier Transform Spectrometer; ODIN-SMR = Odin Sub Millimetre Radiometer.

2.2 Radiative transfer

To interpret atmospheric measurements obtained from remote sensing instruments, an understanding of how atmospheric matter interacts with radiation can be obtained from radiative transfer theory [Liou, 2002]. Imagine a radiation beam being sensed by a remote sensing instrument. The radiation that arrives at the observing instrument is that which is emitted directly by trace gases or scattered by clouds and aerosols into the beam of radiation. In the case of limb occultation, the total radiation also consists of background, or source radiation that passes through the atmosphere and then enters through the field of view of the instrument. The radiation is simultaneously modified by absorption processes and by scattering out of the beam of radiation. The monochromatic intensity or radiance, in a given direction, is a measure of intensity of this radiance in units of energy per cross sectional area per time per wavelength and per steradian.

2.2.1 Radiative transfer in a clear sky atmosphere

A beam of monochromatic radiation interacts with atmospheric matter in two ways. Firstly, extinction processes such as absorption and scattering, result in a reduction in intensity of the radiation beam and secondly, emission and scattering processes result in an increase in intensity of the radiation beam [Liou, 2002]. If the beam of radiation, of wavelength λ , passes through an absorbing medium and crosses a path, ds , the net decrease in radiation will be:

$$dL_\lambda = -k_\lambda n_a L_\lambda ds \quad (2.1)$$

where L_λ is the radiance, n_a is the number density of the absorbing molecules, and k_λ is the extinction coefficient. The negative sign denotes that there is a loss of radiation from the beam.

For the same beam of radiation, an increase due to emission and multiple scattering along the path, ds , is given by;

$$dL_\lambda = j_\lambda n_a ds \quad (2.2)$$

where j_λ is the source function coefficient. By combining equations 2.1 and 2.2, the net change in radiation can be written as:

$$dL_\lambda = -k_\lambda n_a L_\lambda ds + j_\lambda n_a ds \quad (2.3)$$

Rearranging 2.3 and defining the source function, J_λ as $J_\lambda = j_\lambda/k_\lambda$, the formal equation for radiative transfer known as Schwarzschild's equation can be found by:

$$\frac{dL_\lambda}{k_\lambda n_a ds} = -[L_\lambda - J_\lambda] \quad (2.4)$$

Consider the path taken by a beam of radiation from point s_0 to point s_1 . The monochromatic optical thickness of the atmosphere (τ_λ) between these points is written as:

$$\tau_\lambda = \int_{s_0}^{s_1} k_\lambda n_a ds \quad (2.5)$$

The intensity of radiation at point s_1 can be found by integrating equation 2.4 and multiplying by a factor $e^{-\tau_\lambda(s_1, s_0)}$ to give:

$$L_\lambda = L_\lambda(s_0)e^{-\tau_\lambda(s_1, s_0)} + \int_{s_0}^{s_1} J_\lambda(s)e^{-\tau_\lambda(s_1, s)} ds \quad (2.6)$$

where the transmissivity of the atmosphere is given by:

$$T(s_1, s_0) = \exp\left(-\int_{s_0}^{s_1} k_\lambda n_a ds\right) = \exp(-\tau_\lambda) \quad (2.7)$$

In the case that the atmosphere is in local thermodynamic equilibrium (LTE) and scattering is negligible, the source function, J_λ is given by the Planck function that is:

$$B_\lambda(T) = \frac{2hc^2}{\lambda^5 \left(e^{\frac{hc}{\lambda T}} - 1\right)} \quad (2.8)$$

where h and k are the Planck and Boltzmann constant's equal to 6.626×10^{-34} J s and 1.3806×10^{-23} J K⁻¹ respectively. T is the temperature in kelvin and c is the speed of light.

In the absence of scattering, k_λ is now the absorption coefficient and the solution to the radiative transfer equation becomes:

$$L_\lambda = L_\lambda(s_0)e^{-\tau_\lambda(s_1, s_0)} + \int B_\lambda(T)e^{-\tau_\lambda(s_1, s)} ds \quad (2.9)$$

Equation 2.6 can be used to determine the intensity of radiation along a path, as long as the absorption coefficients and the number density distributions of absorbing molecules are known. The first term in the equation describes the absorption or attenuation of radiance by the atmosphere and the second term describes the emission contribution from the atmosphere.

The radiance that is observed by a limb sounding instrument for a nonscattering atmosphere in LTE is given by:

$$L_{\lambda}(s_1) = \int_{s_0}^{s_1} B_{\lambda} \frac{dT_{\lambda}(s)}{ds} ds \quad (2.10)$$

where s_1 is the observation point and s_0 is the cold background against which the emission from the atmosphere is measured. Usually the assumption of an LTE atmosphere is coupled with a plane parallel assumption meaning that any variations in atmospheric parameters such as temperature, pressure and trace gases only occur in the vertical direction. The derivative term from Equation 2.10 is an important theoretical quantity called a weighting function, W , that indicates the contribution to the intensity due to the emission from a layer at distance, s , and is given by:

$$W(s_1, s_0) = \frac{dT_{\lambda}(s)}{ds}(s_1, s_0) \quad (2.11)$$

The weighting functions for the limb sounding geometry can give an indication of which altitude is sensitive to which part of the atmosphere. If the intensity at a single tangent height measurement is integrated over altitude z the intensity is given by:

$$I(h) = \int_h^{\infty} B(z) \frac{dT_{\lambda}(s, \infty)}{ds} \frac{ds}{dz} dz \quad (2.12)$$

2.2.2 Radiative transfer in a cloudy atmosphere

In the thermal infrared region, clouds scatter, emit and absorb radiation. Some of the radiant energy that is incident on ice crystals and water droplets within the clouds, will be re-directed to a new direction (that is the scattering component), as well as absorbed and emitted by the ice crystals. The degree of scattering is dependent on the ice crystal shape and size. In a cloudy atmosphere, the radiation measured by a limb sounding instrument is a combination of the radiation that is emitted by atmospheric

constituents, radiation emitted by the cloud and radiation that is scattered into the FOV from below the cloud [Stephens, 1994]. The radiative transfer equation that was derived earlier for a non-scattering clear-sky atmosphere must be modified to account for the scattering and emission from clouds. For a beam of radiation along a path, ds , emission as well as scattering processes will lead to an increase in radiation along that path.

The scattering and absorption coefficients associated with the scattering and absorption of radiation by cloud particles are defined here as β_s and β_a , respectively. Similarly, the extinction coefficient that describes the amount of radiation that has been attenuated by an ice crystal when radiation is incident on the particle can be defined as β_e . The units for these coefficients are per distance and are usually expressed in units of km^{-1} . The β_s and β_e coefficients can be used to calculate the single scattering albedo, ω_o that is a measure of the ratio of the scattered radiation to the total attenuated radiation and is given by:

$$\omega_o = \frac{\beta_s}{\beta_e} \quad (2.13)$$

For the calculation of the optical properties of the cloud particles, some prior knowledge of a typical size distribution of the particles is required. If the particles have a distribution $n(r)$, the volume β_e can be calculated using:

$$\beta_e = \int_0^{\infty} n(r)\pi r^2 Q_e dr \quad (2.14)$$

where Q_e is the extinction efficiency factor and r is the radii of the particles. The term $n(r)$ describes the distribution of the particles with radii between r and $r+dr$. A typical distribution that is often used to represent ice particle or water droplet distributions is the log-normal distribution which is given by:

$$n(r) = \frac{N}{\sqrt{2\pi}} \frac{1}{S} \frac{1}{r} \exp\left[-\frac{(\ln(r) - r_m)^2}{2S^2}\right] \quad (2.15)$$

where N is the number of particles per unit volume, r_m is the mode radius and S is the spread of the distribution [Kerridge et al. 2004a].

In a scattering medium the source function is equal to J_λ , that is the scattering source function. The non-scattering radiative transfer equation defined earlier now becomes:

$$\frac{dL_\lambda}{ds} = -\beta_a(L_\lambda - B_\lambda) - \beta_s(L_\lambda - J_\lambda) = -\beta_e(L_\lambda - S_\lambda) \quad (2.16)$$

S_λ is the source function associated with scattering *and* absorption and is a weighted mean of the absorption and scattering coefficients. It is defined as:

$$S_\lambda = \frac{(\beta_a B_\lambda - \beta_s J_\lambda)}{\beta_e} \quad (2.17)$$

where β_e is the extinction coefficient. Equation 2.17 can be re-defined by incorporating the single scattering albedo:

$$S_\lambda = (1 - \omega_o)B_\lambda + \omega_o J_\lambda \quad (2.18)$$

In the thermal infrared, J_λ (that is associated with scattering only) takes into account multiple scattering processes that occur in an azimuth independent component written as:

$$J_\lambda = \frac{1}{2} \int_{-1}^1 P(\mu, \mu') L_\lambda(\mu, \mu') d\mu' \quad (2.19)$$

where $\mu = \cos(\theta)$ and θ represents the zenith angle. The angles that correspond to the direction from which the radiation is scattered *from* are denoted with a 'prime'. The quantity, P , is called the scattering phase function that indicates the angular distribution of scattered energy as a function of direction. P is given in terms of spherical coordinates and is a function of the scattering angle, $\cos(\Theta)$, and the azimuth angle, ϕ , and now becomes:

$$P(\mu, \mu') = \frac{1}{2\pi} \int_0^{2\pi} P \cos(\Theta) d\phi' = \frac{1}{2\pi} \int_0^{2\pi} P(\mu, \phi; \mu', \phi') d\phi' \quad (2.20)$$

In reality, scattering by ice crystals (and atmospheric particulates) can be highly forward peaked, and this must be taken into account when multiple scattering processes are represented in the radiative transfer problem. To calculate the strength of forward scattering, the asymmetry parameter g that is indicative of the ratio of forward to backward scattering, can be defined as:

$$g = \frac{1}{2} \int_0^\pi P(\Theta) \cos\Theta \sin\Theta d\Theta \quad (2.21)$$

The phase function can then be approximated by the Henyey-Greenstein analytical function incorporating g [Yang et al., 2001]. This is given by:

$$P_{HG}(\Theta) = \frac{1 - g^2}{(1 + g^2 - 2g\cos\Theta)^{3/2}} \quad (2.22)$$

2.3 Infrared spectroscopy

The MIPAS instrument is sensitive to radiation emitted in the mid infrared region between 4.15 and 14.5 microns. Knowledge of how terrestrial emitted radiation in this region interacts with H₂O and O₃ molecules is required so that emission spectra belonging to each of these species can be accurately modelled in an atmospheric forward model. The importance of forward modelling and its contribution to retrieval theory will be discussed later.

At terrestrial temperatures of approximately 255 K, the Planck function that is a function of wavelength and temperature, peaks at approximately 11 microns where strong spectral signatures of atmospheric constituents are observed [Goody, 1995]. Therefore, this part of the spectrum contains a unique spectral fingerprint for many atmospheric constituents including H₂O and O₃ that are both important absorbers in this region.

2.3.1 Theory

The observed atmospheric emission spectrum of the Earth's atmosphere is composed of a large number of emission lines that belong to atmospheric constituents that have sufficiently strong features to be detected. Energy is radiated only when an molecule makes a transition from one quantum state to another during which a photon, that carries a quantum of energy, $h\nu$, is either absorbed or emitted in the transition. Emission of a photon occurs when an atom or molecule transits from an excited to a lower energy state and each transition that occurs between fixed energy levels result in an emission line. Conversely, an absorption spectrum arises when a photon is absorbed by an atom or molecule resulting in a transition from the ground state to an excited state. An allowed radiative transition can only occur when the transition dipole moment is non-zero. Molecules can primarily possess three types of discrete quantised energies: a) *electronic energy* that is the energy change due to a change in the energy states of the electrons within the molecule, b) *rotational energy* that is the energy associated with the rotating or revolving of a molecule about its centre

of mass and c) *vibrational energy* that is the energy due to molecular vibrations about their equilibrium positions. Rotational energy changes are usually around the order of 1 cm^{-1} therefore purely rotational transitions generally only occur at wavenumbers smaller than 10 cm^{-1} , in the far-infrared and microwave regions [Liou, 2002]. However, vibrational energy changes are usually greater than 600 cm^{-1} and are much larger than rotational energy changes. In the mid-infrared region, molecular emissions are a result of combined vibrational and rotational transitions. Both H_2O and O_3 are radiatively active gases that have permanent dipole electric moments due to their asymmetric charge distributions. In the infrared region, both molecules are involved with vibrational and rotational molecular transitions [Banwell, 1972].

2.3.1.1 Rotation of molecules

Molecules can rotate about their centre of mass and therefore possess a moment of inertia about some internal axis. The moment of inertia for each axis is usually written as I_A , I_B and I_C with $I_A \leq I_B \leq I_C$. Different types of molecules possess specific moments of inertia that depend on the geometry of the molecule. Molecules can be divided into four classes that correspond to:

1. Linear molecules such as CO_2 or N_2O which are triatomic molecules that have two equal moments of inertia $I_B = I_C$ whilst I_A is zero.
2. Symmetric top molecules usually have two equal moments of inertia and a third moment that is not equal to zero. An example of a symmetric top molecule is the NH_3 molecule that has moments of inertia $I_A < I_B = I_C$.
3. Spherical top molecules such as CH_4 have three equal moments of inertia that follow the rule $I_A = I_B = I_C$. These are the simplest class of molecules and they possess no allowed pure rotational spectrum.
4. Asymmetric top molecules such as have H_2O and O_3 have three unequal moments of inertia where $I_A \neq I_B \neq I_C$.

2.3.1.2 Vibrations of molecules

Vibrational transitions occur when a molecular vibration produces an oscillating dipole moment. The quantised energy levels for harmonic vibrations are given by:

$$E_v = h\nu(v_k + 1/2) \quad (2.23)$$

where ν is the frequency and v_k is the vibrational quantum number.

The number of fundamental vibrations for molecules are determined by the number of atoms, N , in the molecule. The motion of each atom in the molecule can be specified in the x , y , and z coordinate system and are said to possess $3N$ degrees of freedom. In general, the number of allowed internal vibrations for H_2O and O_3 molecules follows the rule $3N - 6$. For linear molecules, the number of vibrational degrees of freedom follows the rule $3N - 5$. Both H_2O and O_3 are complex radiatively active molecules that display emission and absorption features in particular regions of the infrared spectrum. Figure 2.2 illustrates the three fundamental vibrations of the H_2O and O_3 molecules.

2.3.2 Infrared spectroscopy of H_2O

The H_2O molecule is a triatomic asymmetric top molecule that has three fundamental modes of vibration given by: ν_1 mode (*symmetric stretching*), ν_2 (*symmetric bending*) and the ν_3 mode (*antisymmetric stretch*). These motions are said to be the normal vibrations of the molecules as all of the atoms move in phase with each other and at the same frequency.

H_2O displays a distinct infrared absorption band in the $6.3 \mu\text{m}$ region, from 1200 to 2000 cm^{-1} , that corresponds to the ν_2 fundamental mode. This band is called a vibration-rotation band. The ν_1 and ν_3 fundamental modes of H_2O molecules are found close together in the $2.7 \mu\text{m}$ spectral region. In the 900 to 40 cm^{-1} range, the pure rotational spectrum of H_2O can be found.

In addition to strong emission lines, H_2O also possesses a distinct less structured “continuum” absorption in the infrared spectral region. This continuous absorption that occurs over all infrared regions but exceeds line absorption in the infrared atmospheric window region, has been thought to be caused by a water dimer and from the self-broadening contribution (displacements of more than 25 cm^{-1} from the line centre often called far wing region) in the wings of H_2O lines [Goody and Yung, 1989]. In recent times, the H_2O continuum has been investigated using sophisticated [Ma and Tipping, 1999] and semi-empirical line shape models [Clough et al., 1989]. Although

the far wing line absorption of H₂O is thought to be the dominating cause, the dimer nature of the continuum has not been discounted [Paynter et al., 2007].

2.3.3 Infrared spectroscopy of O₃

The O₃ molecule is an asymmetric top molecule that has a dipole moment in its electronic ground state and possesses three fundamental modes of vibration that are: the ν_1 mode that is the most active located at 1103 cm⁻¹, a weak ν_2 mode emits at 14.15 μm in a region close to the 15 μm emission of CO₂, and the ν_3 located at 1042 cm⁻¹. In the 9.6 μm spectral region, the ν_3 fundamental mode combines with the ν_1 mode leading to the generation of the O₃ vibration-rotation band [Goody and Yung, 1989]. In addition to these regions, O₃ molecules also have absorption features for electronic bands in the visible, and ultraviolet bands around 0.255 μm although these are not the focus of this thesis.

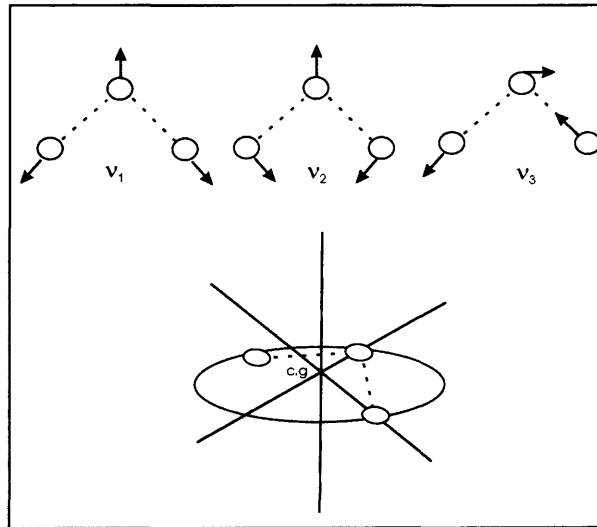


Figure 2.2: Vibrational and rotational modes of H₂O and O₃ molecules. c.g. is centre of mass. Source: [Liou, 2002]

2.3.4 Spectral line intensity

Not all molecular transitions occur with the same probability. The spectral line that is produced following a molecular transition, in a vibration-rotation band, is characterised by a certain spectral line *intensity* and *width* that depends on the properties of the molecule and the atmospheric state. The spectral line strength

is proportional to the probability that a photon will be emitted (or absorbed) for a particular transition and the spectral width or shape depends on the distribution of the transmitted or emitted radiance with frequency.

The intensity (S) or strength of a spectral line depends on the number of molecules that are available to make a particular transition and the absorption coefficient associated with a particular transition between energy levels of that gas:

$$S = \int k_\nu d\nu \quad (2.24)$$

where k_ν is the absorption coefficient. The integrated absorption coefficient over a line is related to the Einstein coefficients for absorption and stimulated emission of a transition from state i to state j. The integrated intensity of a vibration - rotation line in cgs units is given by:

$$S_{line} = \frac{8\pi^3}{3hc} \left[\frac{N}{Q} \right] \tilde{\nu}_{ji} \exp\left(\frac{-E_i}{kT}\right) \left[1 - \exp\left(\frac{-hc\tilde{\nu}_{ij}}{kT}\right) \right] S_{ij} \quad (2.25)$$

where N is the overall density of molecules, T is the temperature in kelvin and Q is the internal partition function (which also depends on T). E_i is the energy of the lower state and S_{ij} is the transition line strength that is defined as the square of the transition moment relative to an axis fixed in space.

2.3.5 Spectral line width

Spectral lines are not infinitely narrow but possess a natural shape that is characteristic of the species and the wavelength region [Lopez-Puertas, 2001]. Lines can be naturally broadened in the atmosphere, however, two external forms of line broadening that can occur in the atmosphere are *pressure broadening* and *Doppler broadening*.

Pressure broadening: Spectral lines can be broadened by instantaneous collisions between absorbing molecules and between absorbing and non-absorbing molecules. Due to the pressure effect this is usually significant at altitudes below 40 km. The shape of these lines is given by a Lorentz profile.

Doppler broadening: Lines are also broadened by the Doppler effect from the difference of the thermal velocities of atoms and molecules. Usually this type of broadening occurs in the upper atmosphere. Along any path, a range of thermal

velocities are observed that induce a range of Doppler shifts resulting in a broadening of lines.

In practise, Lorentz lines are more intense in the line wings in comparison to the Doppler lines. In the altitude range of 20 to 50 km, both Doppler and pressure broadening influence the effective line shapes and both depend on the mass and structure of a molecule and atmospheric temperature and pressure. At standard temperature and pressure, the Lorentzian line width of common atmospheric gases is at least two orders of magnitude larger than Doppler widths which can be neglected, meaning that the spectral line shape can be calculated using just the simple Lorentz line shape and width at the Earth's surface.

2.3.6 The Voigt profile

To calculate accurately the spectral lines of various gases in the mid-infrared, for example, in a radiative transfer model that require modelling of spectral lines, the mechanisms that can affect emission lines in the real atmosphere must be considered. In regions where both Doppler and pressure-broadening can impact spectral line shapes, the two line shapes can be convolved to produce a hybrid line shape that accounts for these effects. This is called the Voigt profile and is given by:

$$k(\nu - \nu_o) = \frac{S}{\alpha_D \sqrt{\pi}} \frac{y}{\pi} \int_{-\infty}^{\infty} \frac{e^{-t^2} dt}{y^2 + (x - t)^2} \quad (2.26)$$

Where $y = \alpha_L/\alpha_D$ is ratio of Lorentz broadening to Doppler broadening and $x = (\nu - \nu_o)/\alpha_D$. S represents the integrated line intensity.

The absorption coefficients of various gases in the atmosphere can be obtained from laboratory-based spectroscopy experiments that measure the absorption cross-sections and line spectra of gases under conditions of varying pressure and temperature for specific wavenumber regions. A radiative transfer model is a key component of satellite retrieval algorithms that requires these spectroscopic measurements of trace gases to accurately model atmospheric spectra. Inaccurate measurements of the spectral properties of these gases lead to incorrect modelled spectra that inevitably project onto the retrieved parameters. The following section describes how atmospheric spectra can be modelled using radiative transfer calculations.

2.4 Forward Modelling

A radiative transfer model can be used to calculate atmospheric limb radiances for various atmospheric conditions. A forward model must contain the relevant physics of the atmosphere as well as incorporate information about the observing instrument. The model should be optimised and numerically efficient so that it can handle large arrays and provide high-resolution accurately-calculated emission/transmittance spectra. To model emission radiance spectra, detailed calculations of the transmittance of individual spectral lines are required and therefore line by line calculations are performed. Spectral line information, and for heavy molecules such as halocarbons, cross section files must be supplied to the model. For optimisation and temporal efficiency, often assumptions about atmospheric variability and processes must be made. The following section describes a state of the art forward model that is used to simulate MIPAS radiances in chapter four.

2.4.1 The Oxford Reference Forward Model

The Oxford Reference Forward Model (RFM) is a line by line radiative transfer code that solves the radiative transfer equation for the measurement scenario of the MIPAS instrument. It is based on the GENLN2 code [Edwards, 1996] and it was designed to model atmospheric radiances observed by the MIPAS instrument although it can be used for many more applications. The model requires a driver table through which a user defined atmosphere can be specified. The driver must contain information about the measuring instrument such as its altitude above the Earth's surface and its instantaneous field-of-view (IFOV) as well as its spectral resolution. The model must be supplied with some estimate of the atmospheric parameters (such as pressure, temperature and mixing ratios) that contribute to the radiance observed in specific wavelength regions [Dudhia, 1997].

2.4.1.1 RFM features

The RFM calculates the radiances observed by an instrument by calculating the transmittance for each gas that contributes to the spectral region of interest. The atmosphere state is sub-divided into atmospheric layers, implemented as concentric shells by the RFM, and assuming a constant radius of curvature for each ray path

that can be defined in terms of elevation angle, geometric or refracted altitudes.

Spectral calculations are performed using a two-pass system that first calculates lines on a coarse 0.5 cm^{-1} grid followed by an triangular interpolation of the line wings onto a fine mesh grid of 0.0005 cm^{-1} resolution. This ensure that the narrowest lines are adequately sampled although a user defined irregular grid can also be defined. All spectral calculations are performed at a user defined resolution and a wavenumber range. Options to include Lorentz, Doppler and Voigt line shapes are also a component of the RFM. The continuum broadband absorption, or arbitrary grey *background* absorption, is an important component of the absorption in the atmospheric window region. It can be included in the radiance calculations for particular gases including H_2O and CO_2 . The version 4.26 RFM model uses the “MT-CKD v1” for H_2O continuum. The default model setting is to assume that the atmosphere is in local thermodynamic equilibrium (LTE) and flags can be enabled for non-LTE processes.

2.4.1.2 Ray Tracing

Each ray trajectory through the atmosphere requires the knowledge on the lower boundary altitude and the local zenith angle at the lower boundary altitude and this is determined using Snell’s law. Once the ray paths (l) are defined, layer related slant path column amounts ($U_{g,l}$) for each species, g, can be used to determine the Curtis - Godson weighted mean temperature T_{CG} and pressure P_{CG} for each layer [von Clarmann et al., 2003]. The $P_{CG,g}$ and $T_{CG,g}$ are assumed to be constant within the layers and are given by equations 2.28 and 2.29.

$$U_{g,l} = \int_l \rho_g(l) dl \quad (2.27)$$

$$P_{CG,g} = \frac{\int_l \rho_g(l) p(l) dl}{U_{g,l}} \quad (2.28)$$

$$T_{CG,g} = \frac{\int_l \rho_g(l) T(l) dl}{U_{g,l}} \quad (2.29)$$

2.4.1.3 Atmospheric profiles

The RFM requires atmospheric profiles of pressure in millibars, temperature in kelvin, and gas concentration profiles of all atmospheric constituents that are to be used in the

radiance calculations. These profiles can be taken from seasonally and zonally averaged climatological database such as the v3.1 MIPAS Reference Atmosphere database that has two components; the standard atmospheres and the Initial Guess 2 (IG2) climatology [Remedios et al., 2007]. The standard atmospheres characterise mean equatorial, mid-latitude day and night, and polar summer and winter atmospheric states. Maximum, minimum and one sigma profiles are also included to capture extreme atmospheric conditions. The database contains profiles of temperature, pressure and thirty six species that are represented on a 0 - 120 km grid of 1 km spacing. The standard atmosphere profiles are constructed primarily from the UARS Reference Atmosphere Project (URAP) from which stratosphere trace gas observations from instruments onboard the UARS satellite are used. For H_2O and O_3 , the URAP climatology are combined with ECMWF and SAGE II observations and the 3D CTM model, MOZART, for tropospheric ozone distributions. The second component that is the IG2 climatology provide a zonal mean and seasonal climatology that encapsulates greater atmospheric variability. More details on the IG2 climatology are given in Chapter three.

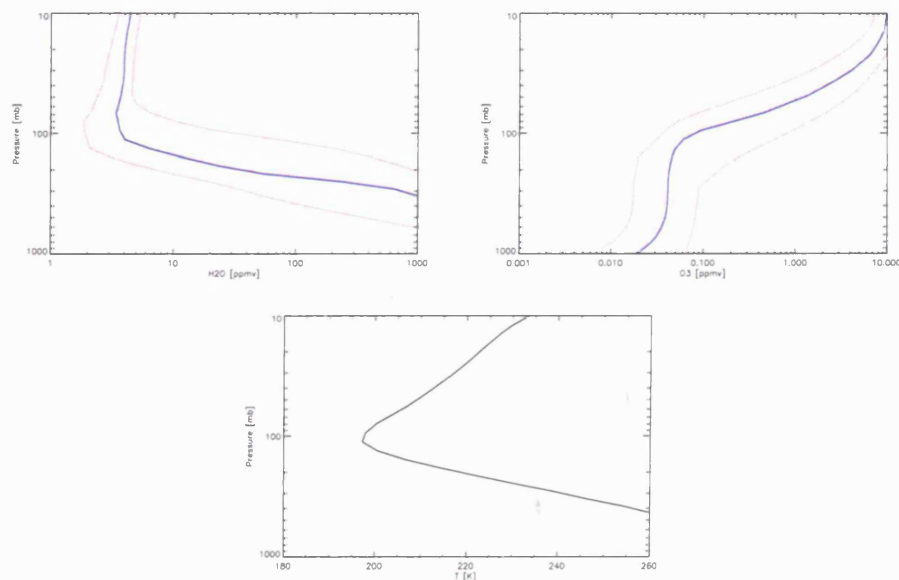


Figure 2.3: Maximum, minimum and mean Equatorial climatological profiles of H_2O , O_3 and temperature from the Standard Atmosphere climatology

2.4.1.4 Spectroscopic database

The line and cross section data must be supplied in the form of a spectral database or specific cross section files. The RFM uses spectroscopic line information from standard databases such as the GEISA, HITRAN but also a specific MIPAS database (see chapter three). Databases such as the HITRAN database [Rothman et al., 2005] contain data of more than 1 million spectral lines for 37 molecules. For aerosol and heavy molecules, cross section data files that contain the absorption coefficients for the absorbing molecules at varying temperature and pressures and for specific wavenumber ranges, must be supplied. These files can usually be downloaded from the HITRAN website (<http://www.hitran.com>). Usually any appropriate database is sufficient for use with the RFM but it must be converted to binary format. Alternatively, the same line and cross section data can be supplied in the form of compressed Singular Value Decomposition (SVD) look up tables. These tables contain pre-tabulated absorption coefficients for all absorbers in a specific spectral range.

2.4.1.5 Instrument parameters

To simulate MIPAS radiances, the instrument characteristics such as the field-of-view (FOV) and the spectral response, or instrument line shape (ILS) for MIPAS must be supplied (see chapter three). To accurately model radiances, the viewing geometry of the instrument must be taken into account. The MIPAS FOV can be defined in terms of altitude or elevation angle and only a single FOV file is required for all spectral regions and altitudes as the FOV function is an independent instrument parameter. An instrument parameter that is dependent upon the spectral region is the ILS that is the spectral response of the instrument. The ILS functions for each spectral channel must be defined in separate files with which the model calculated spectra are convolved.

The RFM was recently part of a forward model inter-comparison experiment under the AMIL2DA project [von Clarmann et al., 2003]. The RFM radiance output was compared to other radiative transfer models including the Rutherford Appleton Laboratory's Two-Dimensional Forward Model (FM2D) and the Optimised Forward Model (OFM) that is the model used to simulate MIPAS radiances for data processing. Radiance spectra was simulated under various cases that were set up to test the

model output at infrared spectral regions at tangent altitudes of 10, 15, 40 and 100 km. Line mixing, ILS and continuum effects for these region with the inclusion of various species, were examined. It was found that the RFM performed well in the comparison with the other models; relatively small spectra differences, often of the order of 0.1 nW, were found between the models. For reference, typical signals for H₂O and O₃ are of the order of 1000 nW at 12 km in the regions near 808 cm⁻¹ and 765 cm⁻¹, respectively, which are of interest in this thesis. The RFM is a zero-scattering model that does not incorporate multiple scattering processes, meaning that it does not compute the scattering source function but rather the Planck function only. The following section describes a multiple scattering code that serves the purpose of calculating cloud radiances in the sub-millimetre and infrared spectrum.

2.4.2 The FM2D multiple scattering model

The Two Dimensional Forward Model (FM2D) that was developed at the Rutherford Appleton Laboratory is a line by line radiative transfer model capable of calculating radiances in the 1-D (assuming atmosphere is spherical symmetrical) and 2-D vertical and horizontal modes [Kerridge et al. 2004a]. The FM2D model was originally designed for calculations at sub-millimetre wavelengths although it has recently been extended to include the mid infrared region. A major component of the FM2D model is that it calculates the multiple scattering source function for limb line of sights.

The scattering component in FM2D is based on an extended version of the multiple scattering code from the GOMETRAN model [Rozanov et al., 1997]. The GOMETRAN model was originally designed for the UV-Visible region at the University of Bremen. The model calculates the scattering source function for rays traced through an approximated plane parallel atmosphere. The scattering source function, in the FM2D is calculated using Equation 2.30:

$$J_{\lambda}(\mu, \theta, \phi) = \frac{1}{4\pi} \int_0^{2\pi} \int_0^{\pi} P(\mu, \theta', \phi', \theta, \phi) \sin(\theta') d\theta' d\phi' \quad (2.30)$$

where $P(\mu, \theta', \phi', \theta, \phi)$ is the scattering phase function that describes the fraction of intensity from a beam of radiation from a direction θ', ϕ' scattered into a direction θ, ϕ that can be normalised to:

$$\int_0^{2\pi} \int_0^\pi P(\mu, \theta', \phi', \theta, \phi) \sin(\theta') d\theta' d\phi' = 4\pi \quad (2.31)$$

The scattering radiative transfer equation is solved using a finite difference method that involves three key steps: First, the phase function is expanded in terms of a Fourier series expansion and for the infrared region only the 0th order term in the series is considered (as scattering in the infrared region is isotropic) and secondly, the calculations are performed as azimuth independent equations for which the view direction is selected as a number of streams or elevation angles. A greater number of streams corresponds to greater accuracy.

The scattering phase function is calculated as a function of altitude, wavenumber and scattering angle and the angular dependence of the phase function is based on two input parameters that are: a) the Henyey-Greenstien asymmetry parameter, g , that is a single number that defines the complete phase function in terms of forward and backward scattering and b) the Rayleigh Function, R , that is used to define the Rayleigh phase function P_R term that contributes to the overall phase function that is calculated using Equation 2.32:

$$P(s, \Theta, \nu) = R(s, \nu)P_R(s, \Theta) + (1 - R)(s, \nu)P_{HG}(g(s, \nu), \Theta)P(s) \quad (2.32)$$

To activate scattering in the FM2D model, four parameters must be defined by the user are: the wavelength of the spectral region, the cloud altitude and thickness, the effective radius R_E , and the ice water content (IWC) that is a measure of the amount of ice water in a certain volume and is measured in units of gm^{-3} , must be defined by the user. The scattering component in the FM2D model utilises a particle size distribution table based on *in situ* observations of microphysical cloud properties [Kerridge et al. 2004a]. Once defined, the R_E are interpolated onto the internal particle size distribution which come from a set of nine particle size distributions based on a state-of-the-art aggregate particle shape model by Anthony Baran of the UK Meteorological Office (UKMO). Definition of these properties allows the bulk optical properties, namely the scattering and absorption coefficients to be calculated.

The FM2D model is initialised by two driver tables that can be thought of as the *sensor* and *atmosphere* driver tables that take into account the defined atmosphere as well as the characteristics of the observing instrument. The sensor driver table

requires information on: the altitude and the view (limb or nadir) of the instrument; the instrument spectral response or the ILS; the retrieval grid, the tangent altitudes of the measurements and the spectral range of interest and the spectral resolution required for the calculations.

Similarly, the atmosphere driver table requires information on pressure and temperature for which a climatological profile such as those from the Standard Atmospheres, described earlier, would be suitable; the number and full list of interfering absorbers; assumed line shapes, or continuum files for the interfering gases; spectroscopic and cross section information on target and interfering gases such as those from the HITRAN spectroscopic database. Finally, if including scattering, the wavelength of the region being simulated with information about the IWC and an effective size of ice particles must also be defined.

2.5 Retrieval theory

The radiance measurements obtained by satellite instruments can be used to estimate the concentrations of atmospheric constituents, pressure and temperature. A retrieval methodology that takes into account the state of the atmosphere and the characteristics of the measurement and the associated errors, can be used to *infer* such information by solving some approximated form of appropriate physics equations. The problem of retrieving an atmospheric profile from an indirect measurement, such as that from a remote sensing satellite, is often ill-posed and ill conditioned. For example, due to the ill-posed nature of the retrieval problem, the retrieval of an atmospheric temperature profile may possess more than one solution of which some may not be consistent with what is observed in the “real” atmosphere [Thompson et al., 1986]. Clearly, the retrieval problem requires some method to distinguish what the actual solution may be. Most real inversion problems are non-linear and do not possess an unique solution in which case, a solution, from a number of possible solutions, can be found by constraint or extra information. Usually, the solution has to be inferred from a set of finite atmospheric measurements that represent continuous parameters in the atmosphere such as concentration profiles. The following section introduces retrieval theory which largely follows the theory described in Rodgers [2000] and Carlotti et al. [2001] for the methods used to retrieve constituent profiles from the atmosphere.

2.5.1 Definitions

The measurement of a parameter that provides information about the atmosphere (for example, atmospheric radiance spectra) can be defined as the *measurement vector* or \mathbf{y} . The *state vector* that describes the state of the atmosphere is defined as \mathbf{x} . The quantity \mathbf{y} , that has m elements, is related to \mathbf{x} , that has n elements, by the *forward function*, $\mathbf{f}(\mathbf{x}, \mathbf{b})$. The forward function describes the relationship between the measurement and state vectors and \mathbf{b} is the *forward function parameters* a set of quantities, such as interfering gases, atmospheric pressure and temperature, that affect the measurement but are not known exactly. All instruments possess an error and for the quantity, y , an associated error that represents the measurement error or random noise in the measurement is given by ϵ .

The general equation that describes the retrieval scenario and relates all of the above parameters is given by;

$$\mathbf{y} = \mathbf{f}(\mathbf{x}, \mathbf{b}) + \epsilon \quad (2.33)$$

In practise, the forward function is represented by a forward model $\mathbf{F}(\mathbf{x})$ that approximates the physics of the atmosphere and the instrument. Equation 2.33 can be written as:

$$\mathbf{y} = \mathbf{F}(\mathbf{x}) + \epsilon \quad (2.34)$$

The forward model requires knowledge of how the instrument observes the atmosphere as well as how the measured quantities relate to desired quantity such as how radiance relates to a temperature profile.

2.5.1.1 The weighting function matrix

As explained above, the retrieval problem is often non-linear. One way to approach this problem is to linearise the forward model about some reference state, \mathbf{x}_o , in which case the information content of a measurement can be more easily sought. This is shown by Equation 2.35:

$$\mathbf{y} - \mathbf{F}(\mathbf{x}_o) = \frac{\partial \mathbf{F}(\mathbf{x})}{\partial \mathbf{x}} (\mathbf{x} - \mathbf{x}_o) \quad (2.35)$$

In which case, the first term on the left hand side can be written as:

$$\mathbf{K} = \frac{\partial \mathbf{F}(\mathbf{x})}{\partial \mathbf{x}} \quad (2.36)$$

\mathbf{K} is a weighting function matrix of $m \times n$ elements and represent the partial derivative's of the state vector element's in the forward model. The weighting function gives information about the sensitivity of each element of \mathbf{F} to each state element and is also known as the Jacobian matrix or sensitivity kernel. In the case that there are more measurements than unknowns (so $m > n$) the retrieval problem is said to be over-constrained or over-determined and conversely, when there are fewer measurements than unknowns, the retrieval is said to ill-posed or under-constrained.

2.5.1.2 Maximum Likelihood estimation

The aim of a satellite retrieval is to find the *best* solution, or estimate of the desired state, given an atmospheric measurement \mathbf{y} . Often, a Bayesian approach is used that allows a number of possible states to be defined using the information about the measurement, the forward model and all associated errors. Using this information and for mathematical simplicity, assuming a normal Gaussian distribution of the all states, a probability density function for all possible states can be defined. In practise, only a single state from a range of possible states is required and this is essentially is the “solution” to the retrieval problem. If $\mathbf{P}(\mathbf{x})$ is a probability density function (*pdf*) of the state, \mathbf{x} , and $\mathbf{P}(\mathbf{y})$ is the *pdf* of the measurement \mathbf{y} , a conditional pdf of \mathbf{x} given \mathbf{y} can be defined as $P(\mathbf{x}|\mathbf{y})$. The most likely state (i.e. the mean state averaged over the *pdf*) from an ensemble of all possible states or *pdf* corresponds to:

$$\hat{\mathbf{x}} = \int \mathbf{x}P(\mathbf{x}|\mathbf{y})d\mathbf{x} \quad (2.37)$$

where $P(\mathbf{x}|\mathbf{y})$ is the *pdf* and $\hat{\mathbf{x}}$ is the “solution”. Assuming a gaussian *pdf*, the mean state averaged over the pdf corresponds to the solution and the width, or variance of the *pdf*, is an estimate of the associated error.

The *best* solution can be found using a non-linear least square fitting technique that consists of fitting a simulation using a forward model to the real observations. One way is to use the maximum likelihood estimation (MLE) theory that looks for a solution by minimising some function, χ^2 , that is defined as the square summation of the differences between observations and simulations weighted by the measurement

error.

An alternative method that is used to find a solution can be using some prior knowledge of the unknown continuous quantity. If the best solution is found using prior knowledge, then the *maximum a posteriori* (MAP) solution is used that is based on finding a state that maximises the posterior *pdf*. An *a priori* profile is one that provides the best independent estimate of the quantity being measured and is used alongside the measurement itself to obtain a best estimate of the solution. Typically, the *a priori* corresponds to either a climatological profile and variance profile of the desired quantity or a previous measurement of the quantity.

2.5.2 Solution without *a priori*

Given that $\tilde{\mathbf{x}}$ is an assumed profile of the desired quantity, and that the simulation corresponding to a measurement \mathbf{y} is $\mathbf{F}(\mathbf{p}, \tilde{\mathbf{x}})$, the vector that defines the difference between the simulation and the measurement is \mathbf{R} and is given by:

$$\mathbf{R} = \mathbf{y} - \mathbf{F}(\mathbf{p}, \tilde{\mathbf{x}}) \quad (2.38)$$

If \mathbf{S}_y is the noise covariance matrix associated with the measurement, \mathbf{y} , the χ^2 function that is to be minimised with respect to the unknown \mathbf{x} is:

$$\chi^2 = \mathbf{R}^T \mathbf{S}_y^{-1} \mathbf{R} \quad (2.39)$$

As the retrieval problem is not linear, and assuming that the χ^2 function is well approximated by a quadratic form, χ^2 can be expanded in a Taylor series and now becomes:

$$\chi^2(\mathbf{x}) = \chi^2(\tilde{\mathbf{x}}) + \nabla \chi^2 \mathbf{d} + \frac{1}{2} \mathbf{d}^T \nabla^2 \chi^2 \mathbf{d} \quad (2.40)$$

Where \mathbf{d} is $\mathbf{x} - \tilde{\mathbf{x}}$ that is the correction to be applied to the assumed value in order to obtain the correct value, $\hat{\mathbf{x}}$. ∇ and ∇^2 are the gradient and the Hessian of the χ^2 function respectively. Writing Equation 2.40 in terms of \mathbf{K} , the Jacobian matrix:

$$\chi^2(\mathbf{x}) = \chi^2(\tilde{\mathbf{x}}) - 2(\mathbf{K}^T \mathbf{S}_y^{-1} \mathbf{R})^T \mathbf{d} + 2\mathbf{d}^T (\mathbf{K}^T \mathbf{S}_y^{-1} \mathbf{K} - \frac{\partial \mathbf{K}}{\partial \mathbf{x}} \mathbf{S}_y^{-1} \mathbf{R}) \mathbf{d} \quad (2.41)$$

If the problem is linear, then the value of \mathbf{d} that minimises the χ^2 function corresponds to the Gauss-Newton solution is given by:

$$d = (\mathbf{K}^T \mathbf{S}_y^{-1} \mathbf{K})^{-1} \mathbf{K}^T \mathbf{S}_y^{-1} \mathbf{R} \quad (2.42)$$

In which case, the solution $\hat{\mathbf{x}}$ is equal to $\hat{\mathbf{x}} = \mathbf{d} + \tilde{\mathbf{x}}$. If the problem is not linear which is often the case in the atmospheric retrieval problem, then an iterative procedure is used to find $\hat{\mathbf{x}}$ where the vector $\hat{\mathbf{x}} = \mathbf{d} + \tilde{\mathbf{x}}$ provides a better estimate of $\hat{\mathbf{x}}$.

In a linear retrieval method, the objective is to obtain a state, from an ensemble of states, that satisfies some degree of optimality and is within some experimental error. Non-linear problems can be linearised about some point with some optimisation criterion to be satisfied. Such problems do not possess an explicit expression for optimality therefore the solution to such problems must be found numerically and iteratively. Two iterative methods that can be used to obtain the best solution from a non-linear problem are the Newtonian iteration and the Levenberg- Marquardt iterative method described below.

2.5.3 Iterative methods

For a non-linear problem, the Newtonian iterative method describes a way of obtaining the zero gradient of the cost function. The Newtonian iteration that is used to obtain a solution for $\hat{\mathbf{x}}$ is given by:

$$\mathbf{x}_{iter} = \mathbf{x}_{iter-1} + (\mathbf{K}_{iter-1}^T \mathbf{S}_y^{-1} \mathbf{K}_{iter-1})^{-1} \mathbf{K}_{iter-1}^T \mathbf{S}_y^{-1} \mathbf{R}_{iter-1} \quad (2.43)$$

Where \mathbf{x}_{iter} is the new estimate of \mathbf{x} and \mathbf{x}_{iter-1} is the result of the previous iteration. $\mathbf{K}_{iter-1} = \frac{\partial \mathbf{F}(\mathbf{p}, \mathbf{x}_{iter-1})}{\partial \mathbf{x}_{iter-1}}$ and is the Jacobian relative to the previous iteration and $\mathbf{R}_{iter-1} = \mathbf{y} - \mathbf{F}(\mathbf{p}, \mathbf{x}_{iter-1})$ and is the residual term between the simulation and the measurement. After each iteration, χ^2 (cost function) value can be evaluated under some convergence criterion.

To establish when a value that is close enough to minimum of χ^2 is reached, some *convergence* criteria are required. This method is usually only sufficient for processes with weak nonlinearities. If the χ^2 value is far from the minimum, the calculated correction factor could be far from the minimum in which case the residual could increase.

Sometimes in a Newtonian iterative process, the true solution can be far from the current iteration and in fact further iterations do not change the residual (or could in fact make the residual larger). In such a case, a Levenberg-Marquardt iterative retrieval can be used. For Levenberg-Marquardt procedures, a constant term can be incorporated into the iterative process that is evaluated after each iteration to aid convergence of the retrieval. The term, λ is chosen after each iteration in order to minimise the cost function and reduce the amplitude of the parameter correction vector. The Gauss-Newton iteration now becomes:

$$\mathbf{x}_{iter} = \mathbf{x}_{iter-1} + (\mathbf{K}_{iter-1}^T \mathbf{S}_y^{-1} \mathbf{K}_{iter-1} + \lambda \mathbf{I})^{-1} \mathbf{K}_{iter-1}^T \mathbf{S}_y^{-1} \mathbf{R}_{iter-1} \quad (2.44)$$

where \mathbf{I} is the unit matrix and the term λ is initialised by the user that increases or decreases depending on whether χ^2 increases or decreases. If λ is increased, then the step direction tends to the steepest descent and the step size between the current and previous iteration tends to zero. The optimal solution that maximally reduces the cost function is found as λ decreases from infinity. For computational efficiency, the λ value can be evaluated and updated at each iteration step, either increasing or decreasing after each step. The expectation value of χ^2 is given by $(n - m)$ and the standard deviation is given by $\sqrt{(n - m)}$. Using these, the quality of the retrieval can be found by:

$$Quality_{Retr} = \frac{\chi^2}{n - m} \quad (2.45)$$

If this value deviates largely from unity then it can indicate errors in the assumptions used in the retrieval.

2.5.3.1 Retrieval convergence

The Gauss-Newton or Levenberg iterations stop once some suitable convergence criteria is reached. Usually, the difference between the current iteration and the previous iteration is a good indicator of the retrieval convergence. Often the variation of the values can be compared to some threshold value. For instance, the χ^2 value of the current iteration can be compared to the previous iteration and if it falls below some pre-defined threshold t_1 , the retrieval converges as shown in Equation 2.46.

$$\left| \frac{\chi^2(\mathbf{x}_{iter-1}) - \chi^2(\mathbf{x}_{iter})}{\chi^2(\mathbf{x}_{iter})} \right| < t_1 \quad (2.46)$$

Another method of reaching retrieval convergence is to allow the iteration index, iter, or number of iterations to reach some pre-defined threshold number t_2 where:

$$iter \leq t_2 \quad (2.47)$$

2.5.3.2 The Gain matrix

The measurement gain or \mathbf{G} describes how the solution is affected by a change in the *measurement*, \mathbf{y} , and is given by:

$$\mathbf{G} = \frac{\partial \hat{\mathbf{x}}}{\partial \mathbf{y}} \quad (2.48)$$

The gain is also known as the contribution function and relates the unknowns to all of the measured quantities. It is given by:

$$\mathbf{G} = (\mathbf{K}^T \mathbf{S}_y^{-1} \mathbf{K})^{-1} \mathbf{K}^T \mathbf{S}_y^{-1} \quad (2.49)$$

In terms of \mathbf{G} , the solution $\hat{\mathbf{x}}$ is essentially equal to:

$$\hat{\mathbf{x}} = \mathbf{G}\mathbf{y} \quad (2.50)$$

2.5.3.3 The averaging kernel matrix

The sensitivity of the retrieval to the *true* state, \mathbf{x} is described by the averaging kernel matrix :

$$\mathbf{A} = \frac{\partial \hat{\mathbf{x}}}{\partial \mathbf{x}} \quad (2.51)$$

In terms of the contribution function and the Jacobian matrix, \mathbf{A} is given by:

$$\mathbf{A} = \mathbf{G}\mathbf{K} \quad (2.52)$$

The solution $\hat{\mathbf{x}}$ can be found in terms of the true atmospheric state \mathbf{x} and by expanding \mathbf{A} about a generic atmospheric state \mathbf{x}_o :

$$\hat{\mathbf{x}} - \hat{\mathbf{x}}_o = \mathbf{A}(\mathbf{x} - \mathbf{x}_o) + \mathbf{S}_x \quad (2.53)$$

$$\hat{x} = \mathbf{A}\mathbf{x} + \hat{\mathbf{x}}_o - \mathbf{A}\mathbf{x}_o + \mathbf{S}_x \quad (2.54)$$

Where $\hat{\mathbf{x}}_o \approx \mathbf{A}\mathbf{x}_o$. The averaging kernel provides a description of how the observing instrument modifies the true state of the atmosphere. The rows of the averaging kernels can be regarded as smoothing functions that generally tend to peak at particular tangent heights representing the tangent height from which the state information comes from. The half-width of the averaging kernels represents the spatial resolution of the instrument and the area, that should be less than one indicates how much of the retrieval comes from the real data and how much is influenced by the a priori. In an ideal retrieval method, the averaging kernel matrix would be:

$$\mathbf{A} = \mathbf{I} \quad (2.55)$$

2.5.3.4 Retrieval errors

The error that is associated with the solution is found by mapping the experimental uncertainty, that is essentially the instrument noise, into the retrieved parameter. This is characterised by the variance covariance matrix given by:

$$\mathbf{S}_x = \mathbf{G}\mathbf{S}_y\mathbf{G}^T = (\mathbf{K}^T\mathbf{S}_y^{-1}\mathbf{K})^{-1} \quad (2.56)$$

The quantity \mathbf{S}_x indicates several things about the retrieval: as well as providing the estimated standard deviation of the retrieved parameter, the square root of the diagonal elements of \mathbf{S}_x is the *root-mean-square* error of the corresponding retrieved parameter. The off-diagonal elements of the matrix \mathbf{S}_x , that is s_{xij} , can be normalised to the square root of the product of the two diagonal elements s_{xii} and s_{xjj} and provides a correlation coefficient between parameters i and j that is essentially the correlation coefficient between the adjacent tangent layers.

2.5.4 Solution with *a priori*

If *a priori* information of the unknown parameters is available then \mathbf{x}_a is the a priori profile and its associated covariance is given by \mathbf{S}_a . The cost function to be minimised

in this case is given by:

$$\chi^2 = (\mathbf{x} - \mathbf{x}_a)^T \mathbf{S}_a^{-1} (\mathbf{x} - \mathbf{x}_a) + \mathbf{R}^T \mathbf{S}_y^{-1} \mathbf{R} \quad (2.57)$$

The Gauss-Newton iteration and the variance covariance matrix of the retrieved parameters now become:

$$\mathbf{x}_{iter} = \mathbf{x}_{iter-1} + (\mathbf{K}_{iter-1}^T \mathbf{S}_y^{-1} \mathbf{K}_{iter-1} + \mathbf{S}_a^{-1})^{-1} (\mathbf{K}_{iter-1}^T \mathbf{S}_y^{-1} \mathbf{R}_{iter-1} + \mathbf{S}_a^{-1} (\mathbf{x}_{iter-1} - \mathbf{x}_a)) \quad (2.58)$$

$$\mathbf{S}_x = (\mathbf{K}^T \mathbf{S}_y^{-1} \mathbf{K} + \mathbf{S}_a^{-1})^{-1} \quad (2.59)$$

2.6 Summary

In this chapter, the principles of the infrared limb sounding technique were described, with a description of the processes involved in the interaction of radiation with atmospheric matter in clear sky and cloud conditions. The principles relating to the spectroscopy of H₂O and O₃ in the infrared spectrum to measure the spectral features of both gases in an emission spectrum were described.

An absorption only radiative transfer model and a multiple scattering forward model, both capable of modelling atmospheric emission spectra, and used later in this thesis were described. These two models will be used in chapter four to model emission spectra measured by the MIPAS instrument.

Finally, the methods used to *invert* a infrared emission spectral measurements from a limb sounding satellite into a meaningful concentration profile were reported. The retrieval scheme that is described in this chapter relate to the methods used by the operational MIPAS processor and other scientific algorithms employed by the MIPAS community. Details of the operational retrieval scheme will be given in the following chapter with a description of the MIPAS instrument.

Chapter 3

The MIPAS instrument

3.1 The ENVISAT Satellite

On March 1st 2002, the ENVironmental SATellite (ENVISAT) mounted onboard an European Space Agency (ESA) Ariane-5 rocket, was successfully launched into a polar sun-synchronous orbit from Kourou, French Guiana. ENVISAT carries a suite of instruments dedicated to monitoring of the Earth's atmosphere, land, sea and ice, making it Europe's largest earth-observing satellite. In essence, the ENVISAT mission is a continuation of the multidisciplinary first and second European Remote Sensing Satellites (ERS -1 and ERS-2) that were consecutively launched in 1991 and 1995. Although there will be a diminishing fuel supply, the ENVISAT mission should remain active until 2010 and possibly longer with extended lifetime scenarios being actively investigated by ESA at the current time. This is at least five years longer than the design of a five year mission lifetime.

ENVISAT encompasses a payload module and a separate service module, that contains the satellite support systems (attitude and orbit control, power generation, thermal control and data handling systems). It has a total mass of 8.2 tonnes of which 2.1 tonnes belongs to the payload instruments. A solar panel, located in the sun direction, supplies an average of 2 kilowatts of power to the instruments. The ENVISAT orbits the earth at a mean altitude of 799.8 km with an orbital speed of 7.45 km/second and an orbit period of 100.59 minutes. This results in 14.3 orbits per day and a repeat orbit cycle, that is the time taken for an orbit to pass over a specific location, that takes 35 days. An orbit inclination of (98.55°) maintains a

constant position in relation to the sun and allows ENVISAT to pass the equator at the same local time, otherwise known as the Mean Local Solar Time (MLST), of 10 a.m. in the descending (southwards) node and 10 p.m. in the ascending (northward) node.

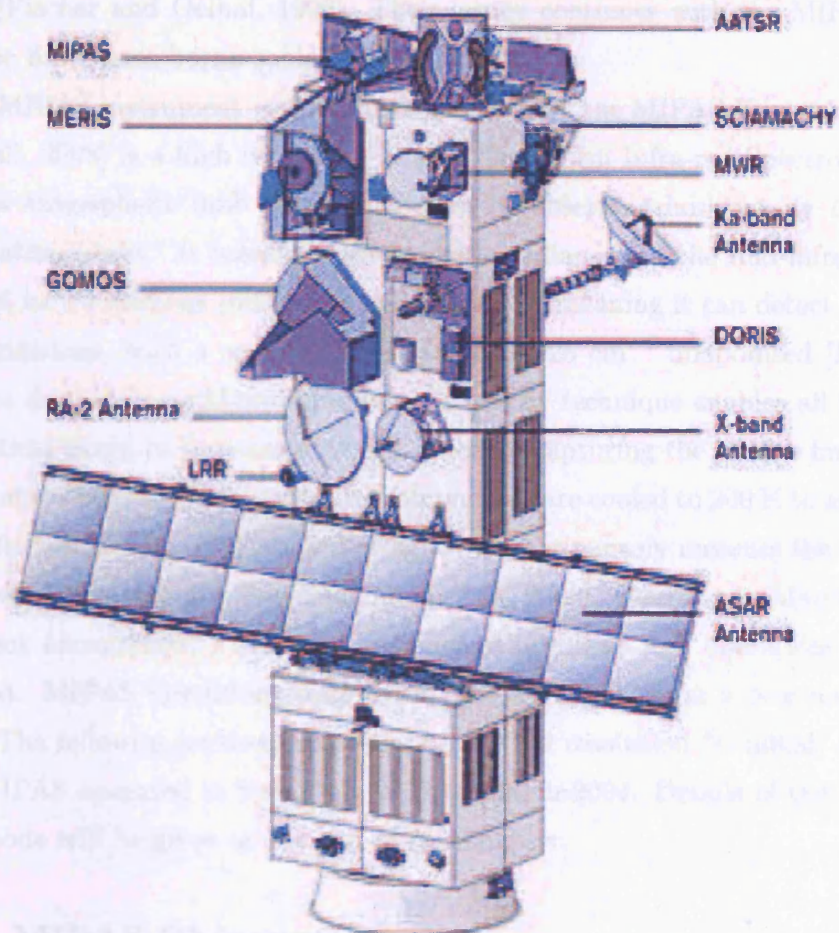


Figure 3.1: Instruments onboard the ENVISAT module. Source: ESA [2007]

Collectively, the ENVISAT payload consists of instruments specifically selected to observe the complete Earth system over a wide range of wavelengths in the electromagnetic spectrum. The payload constitutes three atmosphere-observing instruments, a synthetic aperture radar, two instruments designed to measure surface properties of the land and sea, a radar and microwave radiometer and two ENVISAT position tracking instruments. The following section will describe the MIPAS instrument, from concept, design and operation to the calibration and data retrieval.

3.1.1 MIPAS history and concept

Since the early 1980s, the Institut für Meteorologie und Klimaforschung (IMK) have developed ground, balloon and aircraft versions of the MIPAS instrument that have successfully measured high quality, high-spectral resolution atmospheric emission spectra [Fischer and Oelhaf, 1996]. Their legacy continues with the MIPAS instrument; the first space-borne cooled interferometer.

The MIPAS instrument (sometimes referred to as the MIPAS-E instrument) [Fischer et al., 2008] is a high resolution Fourier Transform Infra-red Spectrometer that measures atmospheric limb emission spectra by observing horizontally *through* the Earth's atmosphere. It measures atmospheric radiances in the mid-infrared region from 14.6 to 4.5 microns (685 cm^{-1} to 2410 cm^{-1}), meaning it can detect in day and night conditions, with a spectral resolution of 0.025 cm^{-1} unapodised [Endemann, 1999]. Its dual-slide rapid-scanning interferometric technique enables all frequencies in its optical range to be scanned simultaneously capturing the unique fingerprint of up to 25 atmospheric constituents. Its components are cooled to 200 K to achieve high radiometric sensitivity. MIPAS was designed to continuously measure the Earth's radiance over a five year lifetime [Endemann et al., 2000]. However, in March 2004, the instrument encountered a series of mechanical problems and operations temporarily ceased. MIPAS operations resumed in January 2005 under a new measurement regime. The following sections will describe the full resolution "nominal" mode with which MIPAS operated in from July 2002 to March 2004. Details of the new observation mode will be given at the end of this chapter.

3.1.2 MIPAS Objectives

MIPAS observations of the Earth's atmosphere have and will continue to contribute to a number of key scientific topics. The primary objective for the MIPAS instrument is to study the dynamics and chemistry of the upper troposphere, stratosphere, mesosphere and lower thermosphere [Fischer et al., 2008]. The MIPAS instrument can provide global, day and night observations for application towards studying the following scientific domains:

1. Stratospheric chemistry: in particular, ozone depletion, the role of chlorofluorocarbons (CFCs) in the lower stratosphere, OH radical chemistry

2. Atmospheric dynamics, stratosphere - troposphere exchange: the processes involved in re-distributing trace gases globally and from the troposphere to the stratosphere (and the reverse).
3. Upper troposphere and lower stratosphere studies, transport of natural and anthropogenic greenhouse gases between the regions. The impact of biomass burning and industry on tropospheric O₃ and other trace gases.
4. Polar stratospheric clouds (PSCs) and cirrus clouds: the distribution and occurrence frequency of clouds as well as the top height, temperature and formation of the clouds can be studied.
5. Upper atmosphere studies, with focus on the upper atmosphere dynamics and temperature structure.
6. Climatological study and weather forecasting.

In support of these broad objectives, data from MIPAS have successfully provided measurements of non-operational species. Recently, Fischer et al. [2008] reported of some of the first spaceborne measurements of some important tropospheric species such as Peroxyacetyl Nitrate (PAN) as well as other species such as ethane (C₂H₆) and carbon monoxide (CO) retrieved from MIPAS indicating that it has successfully fulfilled some of its scientific requirements.

In the following sections, a description of the MIPAS instrument, from design to measurement principles and data are presented that are based largely on Fischer et al. [2008] and the official ESA MIPAS product handbook [ESA, 2007], any deviation from these sources are stated within the text.

3.2 The MIPAS measurement geometry and instrument layout

The MIPAS instrument is located on the anti-sun side of ENVISAT (next to the AATSR instrument) and this position ensures that its optical components are masked from any earthshine. In full spectral resolution “nominal” mode, it collects radiance from its rearward or anti-flight pointing instantaneous field of view (IFOV) of 3 km

x 30 km and samples atmospheric profiles with a 3 km vertical resolution at tangent heights 6 km to 42 km, 5 km resolution from 42 km to 52 km and 8 km resolution from 52 km to 68 km. The distance of MIPAS from the limb tangent point is approximately 3000 km. Each vertical profile is measured approximately 500 km (about 5°) along-track and between 100 km and 800 km across track. The MIPAS instrument has a second FOV of 3 km x 35 km that points sideways, in an anti-sun direction and is used when the instrument enters a “special” mode. One complete elevation scan measurement is achieved in approximately 76 seconds with each tangent height or sweep being measured in 4.45 seconds. This geometry allows the instrument to obtain 75 profiles per orbit which correspond to around 31080 profiles per month when MIPAS was in daily operation.

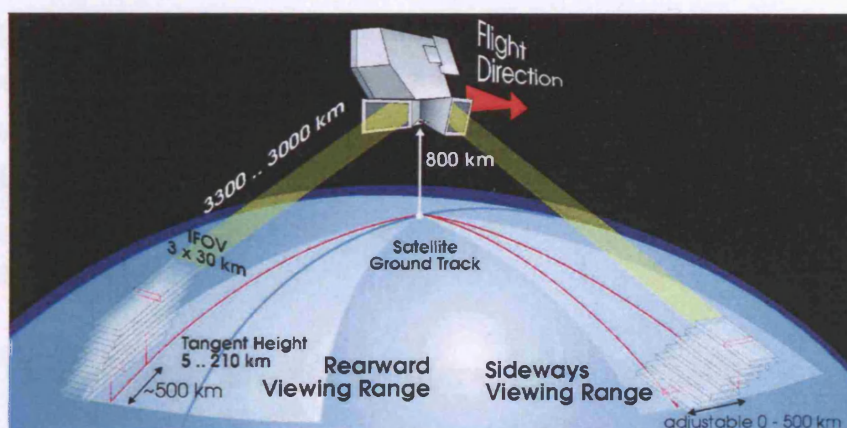


Figure 3.2: Observational geometry of the MIPAS instrument. Source: ESA [2007]

3.2.1 Observational modes

The MIPAS operates in the nominal mode for 80 % of the time; the remaining 20 % operation time is distributed to the special modes where the vertical sampling and altitude range is modified to make specific measurements of certain regions in the atmosphere. In this thesis, only measurements from the full spectral resolution nominal mode are investigated in order to study the behaviour of the H₂O and O₃.

3.2.2 Instrument design and layout

The MIPAS has a compact design, with dimensions of 1.36 m in the flight direction and 0.74 m in the nadir direction and weighs about 170 kg. The instrument is divided into two main sections: the MIPAS Optics module or the MIO (located in the anti-sunward direction) and the MIPAS Electronics module or the MIE (located on the anti-flight direction).

The MIO is a multi-layer insulated subsystem that contains the main components of the MIPAS instrument: 1) The Front-End Optics that hold the input telescope and mirrors, 2) the Interferometer section and 3) the Focal Plane subsystem that houses the MIPAS detectors. All optical components are cooled to 205 K by a large radiator to ensure the instrument's self-emission does not contribute significantly to the detected signal from the atmosphere. Radiation enters the instrument through two tilted rear-pointing and side-pointing baffles, tilted to restrict any incident stray light, that are located below the MIO. The rearward-pointing baffle is used in MIPAS full resolution nominal mode with the side baffle only being used for special mode observations. The following section describe how the MIPAS instrument measures the Earth's atmosphere.

3.2.3 Measuring the atmosphere with the MIPAS

Thermal radiation enters through the rear baffle located at the bottom-end of the instrument. It passes through the Azimuth and Elevation scan units (ASU and ESU) that collectively select the Line Of Sight (LOS). The ASU contains a flat steering mirror that rotates about an axis parallel to the nadir to direct light into the instrument. The ESU mirror selects the actual limb height of the measurement by tilting over a 3° angle in the vertical plane. This small angle is sufficient to select limb tangent heights from 6 km to 68 km as well as a 250 km view for a deep space calibration scene. In the nominal mode, the MIPAS measures at 17 tangent heights and each elevation scan measurement begins at the top tangent altitude. The radiation proceeds to the instrument's anamorphic telescope where it is collimated to match the input optical dimensions of the interferometer.

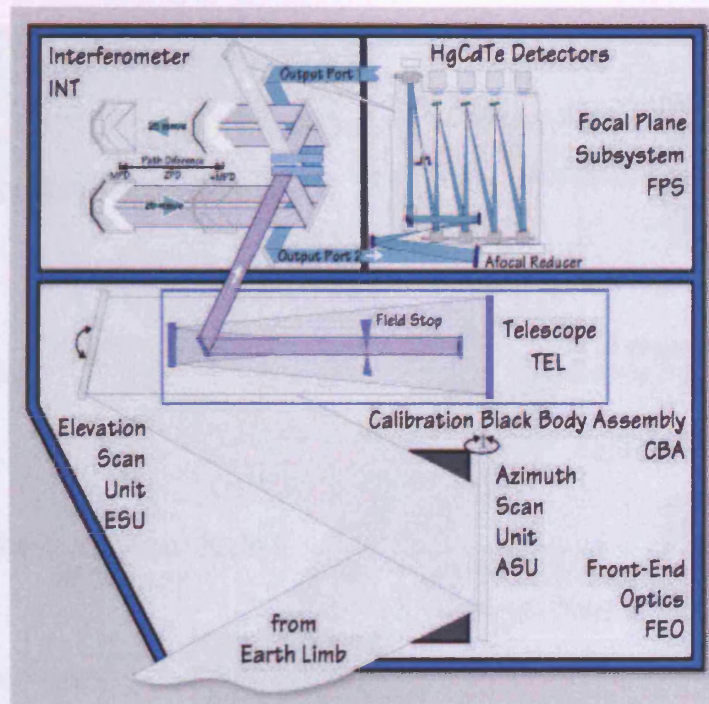


Figure 3.3: Schematic of the MIPAS MIO layout. Source: ESA [2007]

3.2.4 The MIPAS interferometer

The MIPAS interferometer is based on the principles of the classic Michelson-Morley interferometer with some modifications made to fulfil the radiometric and spectroscopic, continuity and size requirements for the MIPAS instrument. The interferometer has two input and output ports, to increase the detected signal-to-noise ratio and provide redundancy, and two sliding corner cube reflectors that each move over a physical path of 10 cm. This achieves a total maximum path difference (MPD) of 20 cm to fulfil the 0.025 cm^{-1} spectral resolution requirement.

Once in the interferometer, the radiation hits a beamsplitter that transmits approximately 50 % of the incident radiation and reflects the remaining 50 % toward two sliding corner cube reflector mirrors. The cube-corner mirrors are designed so that any incident and reflected rays do not overlap as they travel to and from the beamsplitter. The cube-corner slides are guided by dry-lubricated mechanical ball bearings, that are driven by a force generated by magnetic actuators in two Interferometer Drive Units (IDU). Also within the interferometer, is an Optical-Path Difference Sensor that is a built-in circularly-polarised 1.3 micron laser interferometer. It is used to control

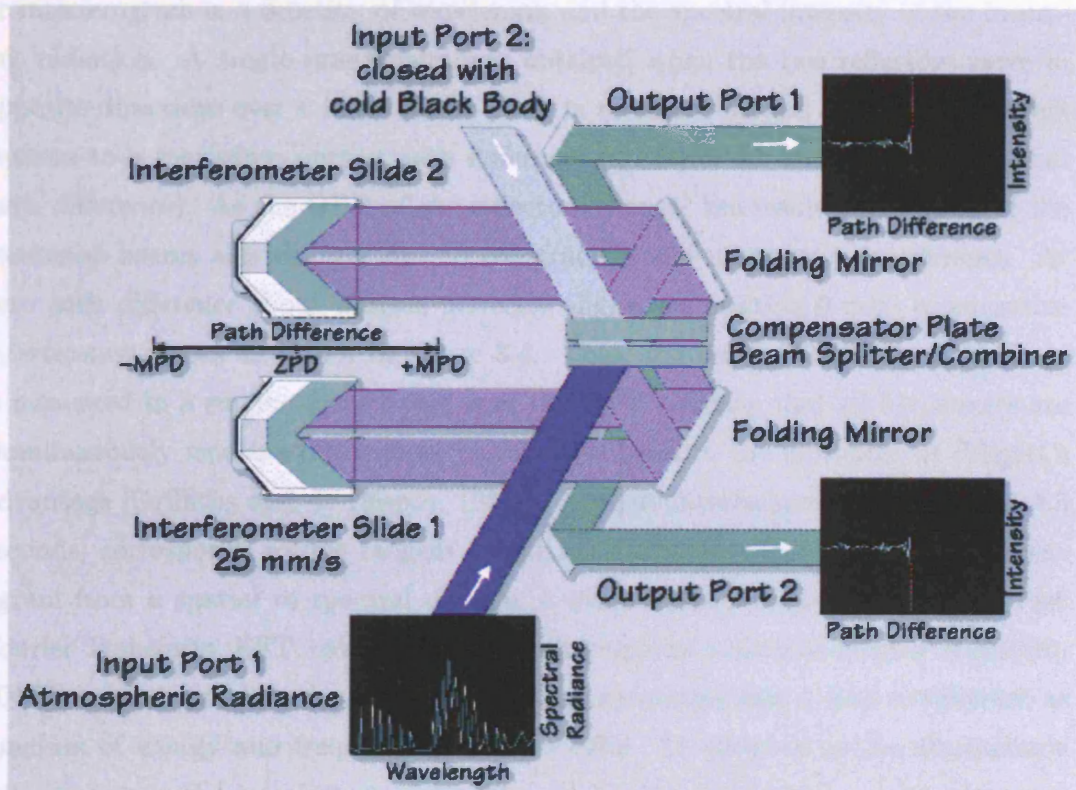


Figure 3.4: The MIPAS Interferometer. Source: ESA [2007]. Atmospheric radiation enters through the input port, passes through the interferometer from which it is directed towards to output ports containing MCT detectors. Note the interferogram pattern at each output port (See text for detail)

the slide velocity with an error of less than 1 % rms. The laser is injected into the interferometer via optical fibres and triggers the sampling of the atmospheric signal, at precise increments along the optical path with a required sampling accuracy of 30 nm. The split radiation beams are reflected back to the beamsplitter where they recombine and constructively or destructively interfere. The recombined signal is directed through two outport ports where eight Mercury Cadmium Telluride (HgCdTe or MCT) detectors record the variation in the interference pattern.

3.2.5 Interferogram sampling

The intensity of the interference pattern is controlled by the optical path difference between the moving retro-reflectors. The interference pattern produced by the beams,

or interferogram is a function of wavelength and the spectral intensity of the incoming radiation. A single interferogram is obtained when the two reflectors move in opposite directions over a 10 cm path. Thus, in total, the motion of the two reflectors equates to a maximum optical path difference (OPD) of 20 cm (twice the physical path difference). As the OPD of the reflectors change, the resulting intensity of the combined beams also changes due to constructive and destructive interference. At zero path difference (both mirrors perfectly aligned at position 0 mm) constructive interference occurs as shown by figure 3.4. Thus, the entire MIPAS spectral range is measured in a single mirror sweep over the OPD meaning that all frequencies are simultaneously measured in a short period (this leads to the multiplex or Fellgett's advantage [Griffiths and de Haseth, 1986]). A single interferogram, measured in 4.5 seconds, corresponds to one tangent height measurement. To convert this interferogram from a spatial to spectral domain, a computational algorithm called a Fast Fourier Transform, FFT, can be performed that applies a discrete Fourier Transform (DFT) to each point in the interferogram thus reconstructing it into a spectrum as function of energy and frequency [Griffiths, 1975]. In addition to the atmospheric measurements, the interferograms are also used in the calibration modes which are described further in the sections below.

3.2.6 Detectors and spectral ranges

The MIPAS detectors are arranged with four detectors at each outport port. This provides redundancy for 3 of the channels if a detector fails as well as increasing the signal to noise ratio. The MIPAS wavelength range is split into five bands and all detectors are optimised to detect specific spectral bands. Photo-conductive HgCdTe (PC-CMT) detectors are used to detect the long-wave (14.6 to 7 microns) spectral range and photovoltaic HgCdTe detectors cover the short-wave (7 to 4 microns) range. A temperature of 70 K is maintained by two Stirling cycle coolers and reduces any internal noise contribution from the detectors.

The output signal of the MCT detectors have been shown to display a non-linear behaviour in relation to the input photon flux, that is dependent on the detector material, age, and temperature. The response of the detectors were tested pre-launch in a specialised thermal chamber to calculate detector scaling factors that are used to

Band	Detector	Spectral range (cm ⁻¹)
A	A1 A2	685-970
AB	B1	1020-1170
B	B2	1215-1500
C	C1 C2	1570-1750
D	D1 D2	1820-2410

Table 3.1: MIPAS detectors and spectral regions

characterise the non-linearity of the detectors and the incident photon flux. The characterised non-linear behaviour is cross-checked with in-flight data, and comparisons of the on-ground and in-flight data have shown that the accuracy of the corrections, when applied to the calibrated scene spectra are to within a few percent.

3.2.7 MIPAS electronics

The MIPAS electronics module is comprised of the signal processing electronics (SPE) that digitises the signals, and generates formatted data packets that are then sent to the platform bus in preparation for transmission to the ground. The operation of the MIPAS instrument such as recording of instrument events, monitoring the equipment and processing of MIPAS housekeeping data are performed by the adjoining Instrument Control Unit (ICE).

3.3 MIPAS performance

Any emission arising from noise sources within the detectors or thermal emission from the optical components will contribute to the instrument signal. The radiometric calibration characterises the instrument self-emission and is performed in two steps in which MIPAS measures “cold” and “warm” targets. Each interferometer sweep that corresponds to a calibration measurement is performed at a low spectral resolution (1/10th the nominal spectral resolution) taking 0.4 seconds and requires an ensemble of measurements that are co-added to increase the signal to noise ratio.

3.3.1 Offset measurement

A deep space measurement, in which radiance is measured at a tangent altitude of 250 km constitutes the offset calibration and accounts for the instruments self-emission.

These measurements are performed once every 4 elevation scans amounting to 20 offset measurements per orbit, and account for temperature variations along the orbit. They consist of several low resolution interferometer sweeps in the forward and backward direction. The “cold” deep space observation provides a scene of negligible radiance from which the instrument overall thermal emission is determined and is subtracted from each atmospheric measurement. The offset measurement requires a total of 600 interferometer sweeps and takes approximately 16.15 seconds.

3.3.2 Gain measurement

The gain calibration is performed once per week and requires the instrument to make a deep space and internal blackbody observation. The internal blackbody has an emissivity greater than 99.6 % and when heated to 250 K is used to test the instruments response in each channel at a temperature corresponding to high radiance emissions. The deep space measurements in the gain measurement are performed explicitly to correct the blackbody measurements and in total, 600 deep space and 600 blackbody measurements are required for the gain calibration. The radiometric gain stability has been found to be better than 1.5 % per week and one of the contributors to the changing gain is ice contamination of the detectors.

3.3.3 Spectral calibration

Spectral calibration requires several radiometrically - calibrated atmospheric limb measurements from which the positions of reference spectral lines (see Table 3.2) are retrieved to appropriately assign wavenumbers to the measured spectra. These are compared to well known peak positions in accordance with the reference spectral lines, in each of the MIPAS spectral bands. The correct spectral location is obtained by appropriately shifting the measured spectra to match the theoretical spectra. This calibration is performed every four limb sequences, or 320 s.

3.3.4 Instrument Line Shape Retrieval

The instrument line shape or ILS, is a function that describes the instrument response when measuring a spectral line of negligible width. The ILS is directly related to the MPD of an instrument, as the greater the MPD, the narrower the instrument

Band	Target gas	Peak position (cm ⁻¹)	Spectral interval (cm ⁻¹)	Tangent altitude (km)	Number of coad-conditions	Used in ILS cali-bration	Used in spectral calibra-tion
A	O ₃	802.5074	802.40 - 802.62	30	1	yes	yes
AB	O ₃	1125.2085	1125.10 - 1125.30	30	1	yes	no
B	H ₂ O	1409.9686	1409.85-1410.08	50	1	yes	yes
C	H ₂ O	1672.4750	1672.40 - 1672.55	50	1	yes	yes
D	H ₂ O	1966.2615	1966.00 - 1966.50	50	1	yes	yes

Table 3.2: Spectral lines and intervals used for MIPAS ILS and spectral calibration. Source [ESA, 2007]

lineshape arising from the boxcar truncation and the finer the maximum spectral resolution attained. The ILS retrieval is performed by selecting specific wavenumbers that contain a single peak of some reference species and fitting some theoretical spectra to the reference lines. The ILS retrieval is performed once per week and is provided in the MIPAS Level 1B product (discussed later). The reference spectra that are used for the ILS retrieval and spectral calibration are shown in Table 3.2.

3.3.5 Line of sight calibration

The line of sight measurement is performed once a week to determine the pointing error required to correct elevation angles and pointing biases. The trajectory of stars passing through the IFOV are compared to the expected time of star passing calculated by taking into the account the orbital position of the satellite. Any differences between the expected and measurement in time of star passing indicates pointing errors that are then appropriately determined using a model characterising the ENVISAT position along the orbit. Kiefer et al. [2007] investigated the pointing performance of MIPAS by analysing the retrieved altitudes from MIPAS data with the engineering altitudes that are characterised by the position of the ENVISAT

satellite. The MIPAS engineering altitudes have been discovered to be too high by 0 - 1.8 km [Kiefer et al., 2007] and there is a systematic pointing difference between the tropics and poles of 1.5 to 2 km.

3.3.6 MIPAS field of view

The MIPAS FOV response and the co-alignment of the detector channels has been characterised in pre and post-launch modes to determine the response pattern and associated variation in each channel. This is acquired by scanning the MIPAS line of sight across an infrared bright source from which the response of the individual detectors as a function of elevation and azimuth offset can be obtained from the spectrally integrated signals from each channel. Kleinert et al. [2007] reports that there is generally good agreement between pre-flight and post launch FOV widths and the co-alignment of the detectors, with only minor deviations in the FOV response due to thermal perturbations.

3.3.7 Noise Equivalent Spectral Radiance

The radiometric sensitivity of MIPAS measurements is determined by the Noise Equivalent Spectral Radiance (NESR) that quantifies the noise observed in the spectra, in terms of incident radiance, and is dependent on the spectral range, channel and profile. The pre-flight required NESR, for each MIPAS band, is shown in Table 3.3 and Figure 3.5. Recently, [Kleinert et al., 2007] reported that the NESR has not degraded in any systematic way since MIPAS has been in orbit and has remained well within the required limits. However, the only factor to compromise the NESR is due to accumulation of ice on the detectors that can temporarily degrade the NESR by up to 20 % with respect to an ice free detector. Typically, the NESR ranges between 50 nW/[cm⁻² sr cm⁻¹] and 3 nW/[cm⁻² sr cm⁻¹] across bands A to D and remains well within the requirements.

3.4 MIPAS data

The detector signals undergo some on board processing, such as digitisation, numerical filtering and decimation, and compressed into source packets that are received

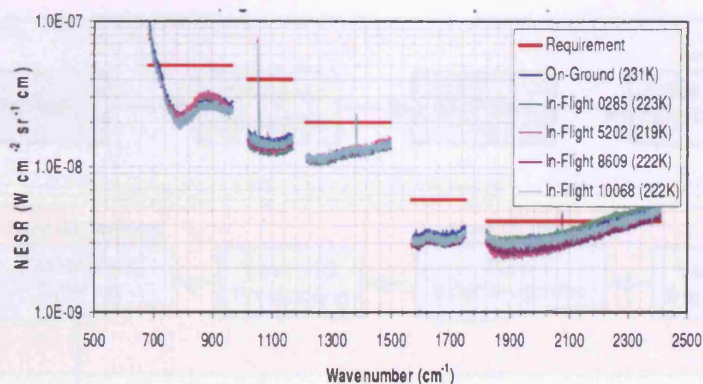


Figure 3.5: MIPAS NESR on ground and in-flight performance. Source: Kleinert et al. [2007]

MIPAS band	NESR (nW/cm^{-2} sr cm^{-1})
A	50
AB	40
B	20
C	6
D	4.2

Table 3.3: NESR requirements for MIPAS spectral bands

by the ground stations in Kiruna (Sweden) and Esrin (Italy) as the MIPAS Level 0 data set. Data packets are then extracted and sorted into time sequenced atmospheric measurement interferograms and calibration measurement interferograms by the Level 1A (L1A) data processing. The data processing flowchart is shown in Figure 3.6. A description of the data processing is given in the following sections.

The two operational data products from the MIPAS instrument are:

1. Level 1B data that are geo-located, spectrally and radiometrically calibrated radiance spectra for each tangent height measurement in consecutive elevation scans. These spectra are an intensity measurement as a function wavenumber and the units are $\text{nW}/[\text{cm}^2 \text{sr cm}^{-1}]$.
2. Level 2 data that are vertical profiles of temperature (T), pressure (P) and six target species: water vapour (H_2O), ozone (O_3), methane (CH_4), nitric acid (HNO_3), nitrogen dioxide (NO_2), and nitrous oxide (N_2O).

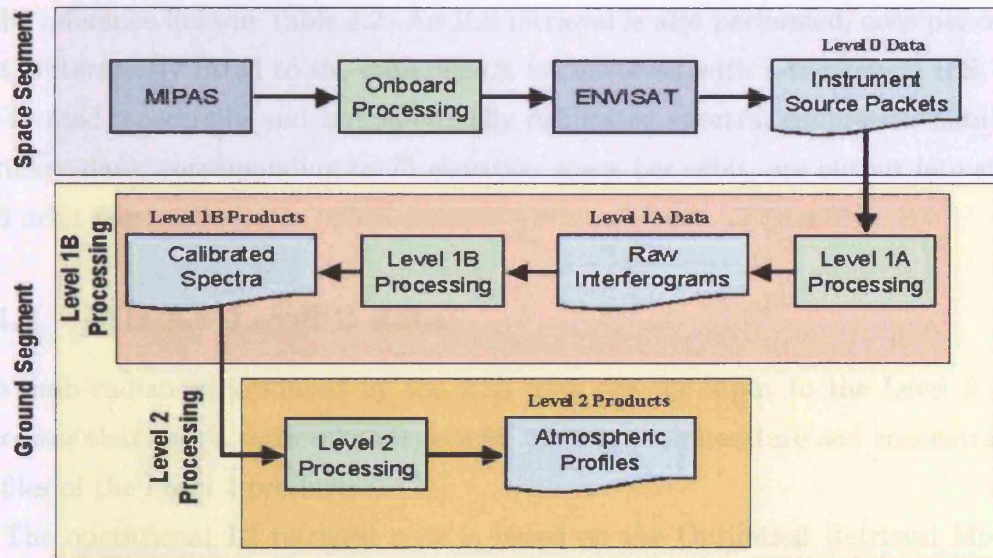


Figure 3.6: Block diagram of MIPAS data processing. Source: ESA [2007]

3.4.1 MIPAS Level 1B data

The primary requirement of the Level 1B (L1B) data processing are to radiometrically, spectrally calibrate and geo-locate MIPAS atmospheric measurements [Kleinert et al., 2007]. The processing begins with the L1A output where interferograms are appropriately grouped into atmosphere, deep space and calibration blackbody measurements. All measurements have a unique time-stamp for measurement identification. L1B processing requires auxiliary files that contain information about the instrument status, timing and position of the measurements. These files also contain calibration and characterisation data that are used in each calibration step in the L1B processing. Specific functions are applied to the data in the following order: an offset calibration function is applied to produce a group of calibrated offsets followed by a gain calibration function that outputs the radiometric gain calculated from the blackbody and deep space interferograms. The gain measurement is approved once per week before it is used in the L1B processing. The scene calibration function is then applied that computes the tangent height, latitude and longitude of the measurement, along with the NESR. Functions that detect and correct any fringe count errors, co-add the interferograms to increase the signal to noise ratio and correct for detector non-linearity are applied before each of the above calibrations are performed. A spectral calibration factor is applied every four elevation scans using the positions

of the reference lines in Table 3.2. An ILS retrieval is also performed, once per orbit, that is iteratively fitted to the data once it is convolved with a theoretical ILS. The geo-located, spectrally and radiometrically calibrated spectra, calibration data and auxiliary data, corresponding to 75 elevation scans per orbit, are output into single L1B orbit files.

3.4.2 MIPAS Level 2 data

The limb radiances produced by the L1B data are the input to the Level 2 (L2) processor that uses a retrieval code to infer pressure, temperature and concentration profiles of the Level 2 products.

The operational L2 retrieval code is based on the Optimised Retrieval Module (ORM), designed by an international consortium led by ESA for the Near Real-Time (NRT) processing of retrieved L2 products within three hours of the measurement [Ridolfi et al., 2000; Raspollini et al., 2006]. The code is required to process a large amount of data and to retrieve atmospheric states from the atmospheric spectral radiance measurements made at each tangent altitude. For re-analysis of MIPAS data, an extended version of the NRT code is used for offline (OL) processing using a relaxed processing time of six hours for each profile retrieval. The L2 processor is based on a non-linear least squares fitting of a parameterised forward model to the measured MIPAS spectra. Data were nominally processed in the NRT mode from July 2002 until March 2004 when the MIPAS instrument was switched off due to mechanical problems. The OL processing has been used to re-process all data from July 2002 to March 2004.

3.5 The Level 2 Retrieval

The L2 processor retrieves its target species based on the principles of a non-linear least squares global fit of a theoretical model to the observations. A theoretical model $\mathbf{F}(\mathbf{p}, \mathbf{x})$ simulates each limb radiance observation, \mathbf{y} , using a set of known instrumental, geophysical and spectral parameters \mathbf{p} to retrieve the unknown quantity \mathbf{x} . The “best” solution is obtained using a Gauss-Newton iterative method modified by the Levenberg-Marquardt criterion that evaluates a cost function or χ^2 after each iteration. A solution is obtained by minimisation of the χ^2 value within pre-defined

convergence bounds [Raspollini et al., 2006]. The retrieval theory predominately follows that which was described in chapter two and the main features of the L2 retrieval, including the forward model, the assumptions, and optimisations made in the processor are described below.

3.5.1 General Retrieval Features

A number of key optimisations were made in the L2 retrieval code to allow computational and temporal efficiency. The three most significant optimisations are: a) the use of “microwindows”, b) global fitting and c) a sequential retrieval.

3.5.1.1 Microwindows

“Microwindows” are narrow spectral regions, typically up to three wavenumbers width, that contain the “best” information about each MIPAS target gas. Each microwindow is pre-selected by computing the combination of a high target gas information content and a low total error propagation, i.e. the minimisation of the sum of all systematic and random errors [Dudhia et al. 2002a].

The total error is given by Equation 5.7:

$$\mathbf{S}_x^{Total} = \mathbf{S}_x + \sum_i \mathbf{S}_x^i \quad (3.1)$$

Where \mathbf{S}_x is the random measurement error and each \mathbf{S}_x^i element corresponds to an independent forward model error (discussed later).

Microwindows are two dimensional arrays that are set in altitude and wavenumber domains in which the propagation of each error through the microwindow is evaluated. For each error, and error spectrum is calculated by differencing the modelled radiance expected with the nominal values for the error parameter with radiances derived from the parameters when they are perturbed by 1σ . The error spectrum for each error source is δy_i is related to the variance covariance matrix of the forward model by Equation 3.2.

$$\mathbf{S}_y^i = (\delta \mathbf{y}_i)(\delta \mathbf{y}_i)^T \quad (3.2)$$

The final microwindows are chosen when the information content cannot increase further or when the maximum 3 wavenumber width is reached. The microwindows

Microwindow label	Spectral Range cm^{-1}	Altitude Range (km)
H ₂ O Retrieval		
H2O_002	807.85 - 808.45	12.0 to 18.0
H2O_022	946.65 - 947.70	6.0 - 18.0
H2O_007	1645.525 - 1646.20	27.0 - 60.0
H2O_001	1650.025 - 1653.025	15.0 - 68.0
O ₃ Retrieval		
O3_021	763.375 - 766.375	6.0 - 68.0
O3_013	1039.375 - 1040.325	52.0 - 68.0
O3_001	1122.800 - 1125.8	6.0 - 68.0

Table 3.4: Nominal microwindows used by the MIPAS L2 retrieval

are additionally used to retrieve the atmospheric continuum or background emission signal for each tangent height measurement. This allows the retrieval of each target species to be based on the amplitude of the line structure rather than the absolute magnitude of the line. However, this joint continuum retrieval approach can make retrievals of heavier molecules such as N₂O₅ difficult. During the L2 retrieval procedure, the L2 processor uses a pre-selected set of microwindows optimised for maximum target gas information and minimum CPU cost. The microwindows used for the H₂O and O₃ retrieval are shown in table 3.4.

3.5.1.2 Global Fitting

The L2 retrieval uses a global-fitting technique [Carlotti, 1988] that requires that all altitudes in the profile, i.e. a complete elevation scan is fitted simultaneously. Using the Levenberg-Marquardt method described in Chapter 2, the vector residual term (Equation 3.3) is the difference of the observations and the simulations from all altitudes in the MIPAS elevation scan measurement.

$$\mathbf{R} = \mathbf{y} - \mathbf{F}(\mathbf{p}, \hat{\mathbf{x}}) \quad (3.3)$$

Carlotti [1988] compared two O₃ concentration profiles retrieved using a non-linear least square fitting retrieval technique incorporating either global fitting or an onion peeling method. It was found that the estimated standard deviation (ESD) of the profile retrieved using global fitting was significantly smaller throughout the profile, than the onion peeling method. This profile also exhibited a strong correlation

between consecutive retrieval altitudes and a more consistent profile in comparison to the profile retrieved separately. In the onion peeling approach, any retrieval error encountered at higher altitudes can propagate into lower layer retrievals meaning increased uncertainty at the UTLS region. Global fitting takes into account the interdependence of concentrations at subsequent layers from which the correlation between consecutive altitudes can be evaluated.

3.5.1.3 Sequential retrieval

The adopted strategy performs a sequential retrieval of the L2 species as follows: pressure and temperature are retrieved simultaneously, in the “pT” retrieval using the hydrostatic assumption relating pressure, temperature and geometric altitude. This is followed by a sequential retrieval of H₂O, O₃, CH₄, HNO₃, NO₂, and N₂O and lastly a retrieval of continuum-like emission effects and the zero-level offset. Any uncertainty in the pT retrieval will propagate into the corresponding VMR retrieval and are characterised by a pT variance covariance matrix (VCM). This pT error is microwindow dependent therefore must be calculated for each microwindow selection. The pT error displays a latitude and seasonal dependence that can be accounted for using pre-defined values [Raspollini and Ridolfi, 2000]. Currently, the pT error is accounted for in the systematic error estimates that are explained later in this chapter. A sequential approach is adopted as the computer memory required for simultaneous processing of large matrices (proportional in size to the product of the number of unknown parameters and the number of observations) is too large.

3.5.1.4 Level 2 Retrieval Procedure

The retrieval begins with a Level 2 pre-processor that assesses the quality of a chosen L1B elevation scan using a quality indicator or PCD flag. Any corrupt L1B data are flagged as “false” and not used in any part of the L2 retrieval. A cloud detection algorithm, incorporated into the operational retrieval since July 2003 [Raspollini et al., 2006] is used to identify cloud-corrupted L1B data. The cloud detection methodology will be discussed in detail in chapter four, however, at this point it can be noted that this algorithm simply distinguishes between cloudy and non-cloudy measurement scenes using a cloud indicator defined for MIPAS bands A, B and D. If the L1B is flagged as cloudy, it is removed from the analysis and the profile retrieval begins from

the tangent height above the cloud-corrupted measurement.

3.5.2 The Optimised Forward Model

The good-quality, cloud-flagged spectra are simulated by a stand-alone code called the Optimised Forward Model (OFM) incorporated within the ORM. Firstly, for the target parameter being retrieved, spectra corresponding to the “best” microwindows are selected and linearly interpolated onto a fine (0.0005 cm^{-1}) spectral grid, irregularly sampled. A fine grid is required to resolve the range of lines and features observed in emission spectra through the atmosphere vertical range measured. A set of discrete layers are defined for all spectra taking into account the refractive index along the ray paths. Once the retrieval is set up in the spectral and altitude domains, absorption cross sections of the relevant absorbers for each microwindow are calculated using singular value decomposition (SVD) look-up tables (LUT) [Dudhia et al. 2002b]. These tables consist of pre-calculated absorption coefficients of all absorbers contributing to each microwindow at a range of pressures and temperatures. Comparisons of the LUT and line by line method by Dudhia et al. [2002b] show that differences between the two methods is less than the NESR level for each microwindow. Using LUTs gives the advantage of increasing temporal and computational memory efficiency making this highly desirable for an optimised operational retrieval code such as that used for MIPAS operational analysis.

3.5.3 Convolution of spectra

As the real MIPAS spectra are obtained with a finite spectral resolution and a finite FOV, the simulated spectra must be convolved with appropriate functions to resemble the way in which MIPAS observes continuous atmospheric spectra. This constitutes the convolution of the ILS that is acquired from the L1B processor with the L2 apodisation function.

Secondly, each altitude-dependent spectrum is convolved with an IFOV that describes the MIPAS finite IFOV “shape”. For MIPAS, this function is a pre-tabulated pattern distribution that resembles a four-point trapezium shape [ESA, 2007]. The mid-point of the MIPAS FOV is the point at which the tangent altitude measurement is obtained.

3.5.4 Convergence criterion

The L2 retrieval process requires the minimisation of a χ^2 value (Equation 3.4) that is evaluated against some convergence criteria after each iteration.

$$\chi^2 = \mathbf{n}_{iter}^T \mathbf{S}_n^{-1} \mathbf{n}_{iter} \quad (3.4)$$

\mathbf{n}_{iter} is the vector “residuals” at the iteration “iter” and \mathbf{S}_n is the variance covariance matrix. The retrieval process stops when the convergence criteria is fulfilled. The convergence criteria are based on three conditions:

1. The maximum relative difference of the χ^2 value from the previous iteration to the current χ^2 value must be below some threshold T1. Raspollini et al. [2006] state typical T1 values of less than 0.02 for OL processing.
2. The maximum relative difference of the fitted parameters between two consecutive iterations must be below some threshold T2. In OL processing T2 is found to be less than 0.2 [Raspollini et al., 2006].
3. The maximum number of allowed iterations is 8. Typically, convergence is reached with 3 to 6 iterations.

3.5.5 Retrieval Requirements

For the OFM to realistically model the real atmosphere, it requires accurate estimates of global geophysical parameters, spectral line and absorption cross-section information on all or most atmospheric constituents that contribute the signal observed by the MIPAS.

3.5.5.1 Spectroscopic database

The L2 processor utilises a spectroscopic database containing spectral line information and infrared cross section measurements of up to 37 atmospheric constituents, constructed originally from the High-Resolution Transmission molecular absorption database or HITRAN (www.hitran.com). The MIPAS dedicated database, `mipas_pf3.1`, was built starting from HITRAN 1996, and contains updated and improved spectral data of six molecules including O_3 with the most significant improvement to the

HNO₃ molecule. This database replaces the original mipas_pf2.0 and has been used operationally since July 2003 for the NRT and OL processing (re-processing).

3.5.5.2 Reference atmosphere database

The reference atmosphere database [Remedios et al., 2007], as explained in chapter two, has two components that are the standard and the initial guess (IG2) profiles. The L2 processor utilises the IG2 profiles as an initial guess of the species to be retrieved and also as representative profiles of interfering species. The IG2 profiles are mostly based on satellite data from instruments onboard the UARS satellite and some CTM model data primarily from the MOZART and SLIMCAT models. The IG2 database covers seasonal variability with trace gas profiles for January, April, July and October atmospheric conditions representing the four seasons. Each set of seasonal profiles vary latitudinally over six bands that are 0 - 20°, 20 - 65° and 65 - 90° for both hemispheres. For the initial guess of each target species, a weighted mean profile that is comprised of a) the IG2 profile of the target species, b) an ECMWF profile, and c) the previous retrieved profile from the previous iteration. In addition to the IG2 profiles, the standard profiles are used for error analysis and generation of the best microwindows for each target species.

3.5.6 Retrieval Assumptions

As modelling of all atmospheric effects is computationally expensive and time consuming, the L2 retrieval assumes that the atmosphere is horizontally homogenous and in local thermodynamic equilibrium.

3.5.6.1 Horizontal homogeneity

Although the long horizontal path length attained in the limb geometry allows good sensitivity to many trace gases with weak spectral signatures, the measurement signal can be thought of as an average of the atmosphere over this path length. The L2 processor assumes that the atmosphere measured over these long path lengths are horizontally homogeneous. Real horizontal structures that are not represented in the forward model, can potentially introduce an error as the real atmosphere does not display such homogeneity. For this reason, associated errors are estimated in the final

MIPAS error budget and are discussed in the next section.

3.5.6.2 Non-local thermodynamic equilibrium

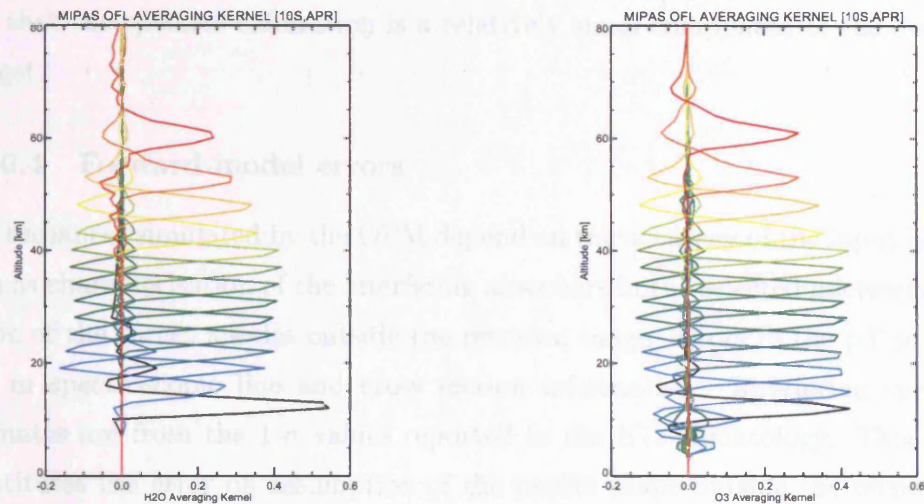
Modelling and representing all non-LTE processes requires extensive coding and computational power that is not suitable for the operational L2 retrieval requirements. Such processes are considered to be weak in the stratosphere, where MIPAS measurements are mostly concentrated and therefore, the atmosphere is assumed to be in Local Thermodynamic Equilibrium (LTE) by the MIPAS forward model. By testing the response of the retrieval to perturbed synthetic non-LTE and LTE spectra, the errors due to the exclusion of non-LTE effects are considered in the total error budget of the retrieved profiles. For the retrieval of target species, the best microwindows are selected where emission is in the thermodynamic equilibrium.

3.6 Characterisation of MIPAS Level 2 profiles

MIPAS averaging kernels are not produced for each retrieved MIPAS profile and standard averaging kernels can be obtained for temperature and each retrieved species [Ceccherini, 2004]. For NRT and OL products, averaging kernels have been calculated using a perturbation method in which the state vector is perturbed by some small amount and the delta-function response due to this perturbation at each element of the state can be calculated as the change in the retrieval that arises from this small perturbation. For the calculation of MIPAS H₂O and O₃ averaging kernels, H₂O was perturbed by 1 ppmv and O₃ (and the remaining trace species) is perturbed by 5 % of the maximum VMR.

3.7 MIPAS Level 2 errors

The MIPAS L2 profiles are affected by a combination of radiometric noise and discrepancies in representing the instrument and the atmosphere in the forward model. The measurement error equates to the *random* error component and is due to the mapping of the random radiometric noise onto the retrieved profiles (or the variance covariance matrix, VCM). This is calculated taking the noise estimate or the NESR that is reported in the L1B files. The *systematic* errors take into account



(a) Tropical Averaging kernels for MIPAS H₂O

(b) Tropical Averaging kernels for MIPAS O₃

Figure 3.7: Averaging kernels for MIPAS H₂O and O₃ calculated for April at 10°S, between the altitudes of 12 and 68 km.

discrepancies in the forward model input, uncertainties in the instrument parameters and the forward model assumptions. These factors are all taken into account in the total error budget provided by the Atmospheric, Oceanic and Planetary Physics (AOPP) MIPAS group at Oxford University and can be found at <http://www.atm.ox.ac.uk/group/mipas/err/>. Error sources are briefly described below.

3.7.0.3 Calibration errors

Incorrect scaling of spectra in the spectral calibration, and inaccurate characterisation of the radiometric gain and the apodised instrument line shape (AILS) width, can have a direct affect on the retrieved profiles. If spectra are incorrectly scaled in the altitude and frequency domains, these will project onto the relative radiances and

further into the retrieved profiles. Similarly, spectra assigned with a large error in the L1B processing, can affect the L2 retrieval and corresponding χ^2 values. Raspollini et al. [2006] report that the radiometric accuracy is well within the requirements and that the spectral calibration is a relatively small component of the overall error budget.

3.7.0.4 Forward model errors

The radiances simulated by the OFM depend on the accuracy of the input parameters such as characterisation of the interfering absorbers in the selected microwindows, the shape of the target species outside the retrieval range, errors in the pT propagation and in spectroscopic line and cross section information. Interfering species error estimates are from the $1-\sigma$ values reported in the IG2 climatology. This error also constitutes the error on assumption of the profile shape outside the retrieval range. The propagation of the pT error into the retrieved profiles is affected by pointing biases as uncertainty in the MIPAS pointing means the retrieved tangent pressures will also possess an error. Finally, the errors associated with the forward model assumptions of horizontal homogeneity and LTE are included in the final error budget for MIPAS L2 data. Table 3.5 lists the error value assumed for each error source in MIPAS L2 retrievals.

3.7.1 Level 2 H₂O and O₃ errors in the tropical UTLS

For the tropical UTLS region, the total error estimated from the Oxford University clear sky errors are: for H₂O at 12 km, 15 %; H₂O at 15 km, 47.9 % and at 18 km, 39.8 %. For O₃ at 12 km, the total error is 53.4%; at 15 km, 69.6 %; and at 18 km, 46.3%. The largest contributors to the total error is due to the assumption of horizontal homogeneity, followed closely by radiometric uncertainty and spectroscopic database errors. The total and individual error components affecting H₂O and O₃ retrievals are given in the table below.

Figure 3.8(a) shows the contribution of each systematic error source affecting retrieved L2 H₂O profiles in the tropics. In the tropical UTLS, the random errors are largest at 15 km and 18 km (approximately 25 %). Systematic errors vary from 13.5 % to 40 % from 12 km to 21 km and are dominated by uncertainties caused

Name	Description	1 sigma
NONLTE	Error from the assumption that atmosphere is in LTE in OFM	Modelled value
SPECDB	Errors in line strength, shape and position in the spectroscopic database	assumed 1 sigma accuracy
GAIN	Error in Radiometric gain	$\pm 2\%$
SPREAD	Error in width of the AILS	$\pm 2\%$
SHIFT	Uncertainty in spectral calibration	$\pm 0.001\text{cm}^{-1}$
CO2MIX	Error from neglecting CO2 line mixing in forward model	Modelled
CTMERR	Uncertainty in gaseous continua	$\pm 25\%$
GRA	Error from assumption of horizontal gradient effects	$\pm 1\text{K}/100\text{km}$
HALT	Uncertainty in high altitude column	Calculated during retrieval
PT	Propagation of PT error in VMR retrievals	pT VCM
SPECIES	Uncertainty in interfering species	Climatological 1σ

Table 3.5: List of systematic error sources for MIPAS L2 retrievals

by assuming horizontal homogeneity and LTE, and in the spectral and radiometric calibration.

Figure 3.8(b) displays the total error budget for tropical retrieved L2 MIPAS O₃ profiles. Random errors are as large as 57 % at 15 km and the most dominant source of systematic errors are from assuming a horizontal homogeneous atmosphere, and from errors in the spectroscopic database and AILS retrieval.

The total error budget for MIPAS L2 H₂O and O₃ shows that the errors in the tropical UTLS are strongly dominated by forward model deficiencies followed by spectroscopic database and calibration uncertainties.

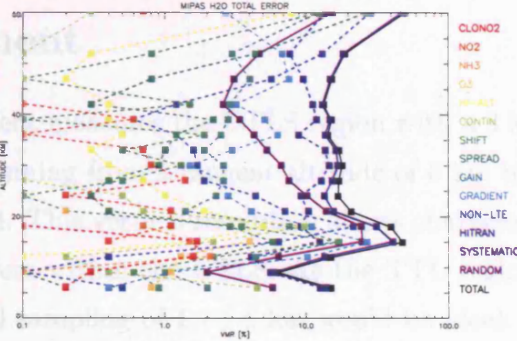
3.7.2 The new “Reduced Resolution” mode

In March 2004, due increasing data anomalies caused by problems with the motion of the retroreflectors in the interferometer, the MIPAS instrument was switched off. Following on-ground investigations a measurement set up called the “reduced resolution” (RR) mode was proposed. From January 2005 onwards, the RR mode has performed atmospheric measurements with a duty cycle of 40 % that corresponds to

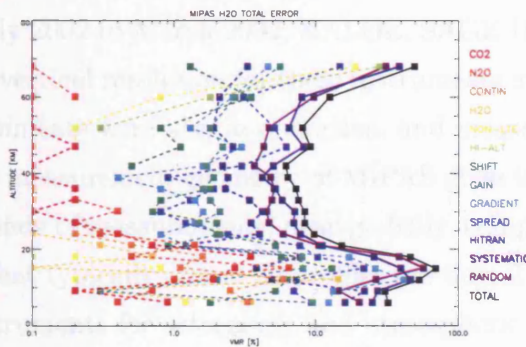
3.8 Studying the tropical UTLS with the MIPAS

Instrument

The MIPAS instrument is designed to study the UTLS region from 0 to 80 km altitude. It is a Fourier transform spectrometer (FTS) that provides a spectral resolution of 0.0625 cm⁻¹ and a vertical resolution of 1.5 km. The instrument is mounted on the Space Shuttle Challenger during the STS-52 mission in 1992. The MIPAS instrument is designed to study the UTLS region from 0 to 80 km altitude. It is a Fourier transform spectrometer (FTS) that provides a spectral resolution of 0.0625 cm⁻¹ and a vertical resolution of 1.5 km. The instrument is mounted on the Space Shuttle Challenger during the STS-52 mission in 1992.



(a) Mean equatorial MIPAS H₂O error profiles



(b) Mean equatorial MIPAS O₃ error profiles

Figure 3.8: Systematic and random error profiles for equatorial offline MIPAS H₂O and O₃ profiles. The total error is shown by the black line in each figure.

a spectral resolution of 0.0625 cm⁻¹ produced by a maximum optical path difference of 8.2 cm, and a vertical sampling of 1.5 km in the UTLS. A single interferometer sweep takes 1.64 seconds and this reduced measurement time allows more full elevation scans to be obtained. The profiles are now oversampled with a 1.5 km resolution in the UTLS, within the 3 km IFOV. The RR mode operates initially in short periods and “on request” during *in situ* or ground based measurement campaigns. The RR data-sets are currently in the validation stage.

3.8 Studying the tropical UTLS with the MIPAS instrument

The MIPAS instrument measures the UTLS region with a 3 km vertical resolution in the UTLS region spanning from a tangent altitude of 6 km to the lower stratosphere at 21 km and beyond. This vertical resolution allows characterisation of H₂O, O₃ and clouds in several layers within the UTLS. As the TTL region is at most 2 or 3 km thick, a finer vertical sampling of 1 - 1.5 km would be ideal. However, as this is not the case for the full resolution mode, MIPAS data from July 2002 to March 2004 can potentially provide information on the base of the TTL, one averaged layer within the TTL and perhaps the outflow/exchange from the top of the TTL.

In the period July 2002 to March 2004, HALOE, SAGE II, ACE-FTS and ODIN-SMR (approximate vertical resolution for these instruments are between 2 and 4 km), limb sounding instruments were also in operation, and measured H₂O and O₃ in the tropical UTLS. The measurement geometry of MIPAS gives it the advantage of being able to make thousands of measurements, near-globally, compared to SAGE II, ACE-FTS and HALOE that typically obtain 30 profiles per day. The ODIN-SMR satellite carries onboard instruments for astronomy and atmospheric measurements meaning that the measurement time is divided between the two disciplines. This means it measures less profiles in comparison to the MIPAS instrument.

Although the ENVISAT orbit allows MIPAS to make measurements over the whole globe, this does not necessarily mean that there is a retrieved vmr profile at every point observed. Due to the high presence of clouds in the tropical UTLS, all infrared remote-sensing instrument that encounter clouds in the instruments FOV, will suffer contaminated data-points and this limits the global coverage advantage of these techniques. The next chapter discusses the cloud detection methodology and presents an investigation of how clouds can affect retrieved profiles and how the cloud detection methodology can be improved to optimise the quality and quantity of tropical MIPAS H₂O and O₃.

3.9 Summary

In this chapter, the operation and measurement principles of the MIPAS instrument were described with details on how the instrument profiles the UTLS region. A description of the measurement geometry of the instrument as well as the core components of the MIPAS instrument, including the interferometer and the detectors were given.

The process of converting the raw atmospheric interferograms into emission spectra and furthermore into concentration profiles was detailed in section 3.5 describing how MIPAS measurements are processed into MIPAS geophysical data.

The data that are used in this thesis are from full spectral resolution nominal MIPAS measurements retrieved by the operational L2 processor that provides concentration profiles of H_2O and O_3 . The following chapters will describe two investigations that examine the effect of UTLS cloud on this data and furthermore how this data compares to pre-existing independent UTLS measurements.

Chapter 4

Investigating cloud contamination in Level 2 MIPAS data

Tropical UTLS measurements from limb sounding instruments, such as MIPAS, will suffer some contamination by cloud. This in turn can affect the performance of satellite retrieval algorithms and furthermore the accuracy of the products that they produce. If an optically thick cloud is in the MIPAS FOV any atmospheric constituents information will be masked by the grey body emission of the cloud. Thus satellite measurements of tropical UTLS trace gases can be difficult to interpret without the ability to deduce how the effect of cloud has propagated into the retrieved concentrations. Clearly, it is imperative to distinguish between cloudy and non-cloudy radiances, to reduce the *uncertainty* of retrieved tropical H₂O and O₃ concentrations.

To overcome such limitations, a cloud detection methodology is an important component of a satellite retrieval algorithm. From a retrieval perspective, a cloud detection method should be able to successfully distinguish between a clear-sky atmospheric radiance that contains only the contributions from a target gas and additional trace gas absorbers, and a radiance measurement that has been produced by additional particles belonging to cloud or aerosols hence resulting in a decrease of the trace gas information.

Usually any unexplained behaviour or anomalies in retrieved concentrations from satellite data near the tropical tropopause tend to be attributed to undetected cloud corruption. However, so far, no specific study of the anomalies due to cloud corruption on operationally processed MIPAS data has been performed in detail, meaning that

any other potential anomalies (such as retrieval algorithm or instrument affects that are unaccounted for) may be mistaken for cloud contamination. In this chapter, the direct effect of clouds on the *retrieved* MIPAS H₂O and O₃ data are examined.

4.1 Cloud signatures in MIPAS L1B spectra

Figures 4.1(a) to 4.1(e) show three tropical 12 km radiance measurements observed by the MIPAS instrument on the 30th July 2003 in orbit 07386. The figures correspond to MIPAS detection bands A, AB, B, C and D respectively. The spectra shown for each band correspond to a clear sky measurement, a thin cloud in the MIPAS LOS and an optically thick cloud in the MIPAS LOS.

The two most significant features observed in the optically thick cloudy conditions (blue spectra) is a distinct broadband offset and the loss of trace gas spectral features. The radiance offset is more than doubled in band A and similar offsets of at least two to three times larger than clear sky values are seen in bands AB, B and D. Significant spectral offsets are also produced when a thin cloud enters the MIPAS LOS as shown by the red spectra although the spectra appear to retain the absorber line shapes. This does not necessarily mean that all trace gas information is comprehensible. The most noteworthy changes between cloudy and clear-sky spectra occur in the regions of 685 cm⁻¹ to 750 cm⁻¹ in band A, 1060 cm⁻¹ to 1170 cm⁻¹ in band AB, 1215 cm⁻¹ to 1251 cm⁻¹ in band B and 1820 cm⁻¹ to 2050 cm⁻¹ in band D. In band C, no distinctive offsets are observed because of trace gas line opacity. Clearly, increased cloud presence, or cloud optical thickness, has a predominant effect on the atmospheric window region between 800 cm⁻¹ and 970 cm⁻¹ in band A.

It is postulated that there is potential to retrieve trace gas profiles from spectra that are only affected weakly by thin cloud [Spang and Remedios, 2003]. This issue, particularly how weak an offset from a thin cloud can be tolerated and what the accuracy of profiles retrieved in the presence of thin cloud is addressed in this investigation. It is evident from the spectra shown in Figures 4.1(a) to 4.1(e) that for optically thick clouds, trace gas spectral features are not discernable and concentration profile retrievals are not possible. Although this is a limitation in obtaining trace gas information in the tropical UTLS, cloudy spectra are enriched with cloud microphysical information meaning that cloud retrievals from MIPAS are also possible.

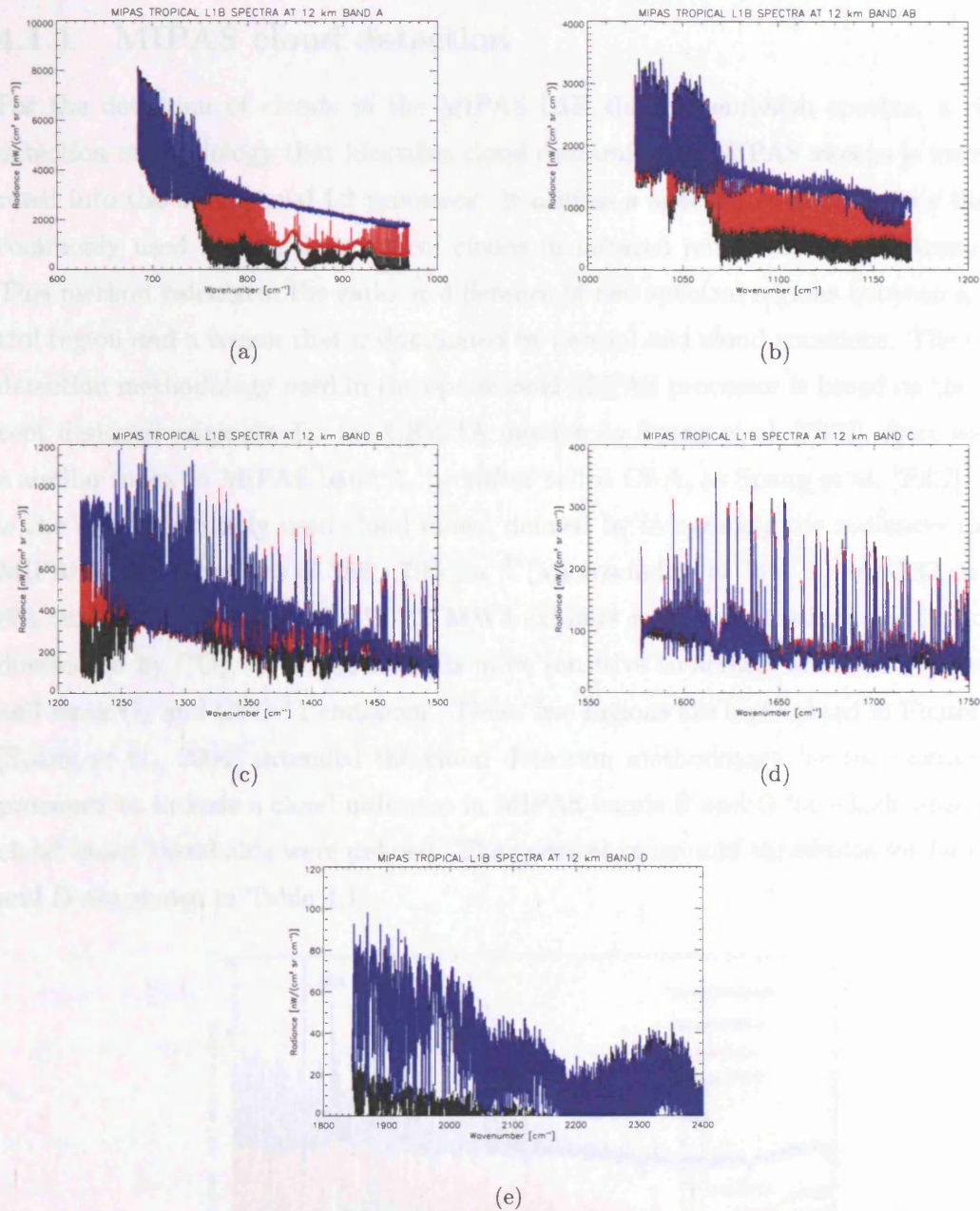


Figure 4.1: MIPAS L1B spectra under varying cloud influence for (a) MIPAS band A; (b) MIPAS band AB ; (c) MIPAS band B; (d) MIPAS band C and (d) MIPAS band D. Black spectra correspond to non-cloudy conditions, red spectra to optically thin cloud conditions and blue spectra to optically thick cloud conditions in the MIPAS FOV.

This potential will be discussed later in this chapter.

4.1.1 MIPAS cloud detection

For the detection of clouds in the MIPAS L1B thermal emission spectra, a cloud detection methodology that identifies cloud contaminated MIPAS sweeps is incorporated into the operational L2 processor. It utilises a spectral ratio technique that is commonly used for the detection of clouds in infrared remote sensing instruments. This method calculates the ratio or difference of two spectral regions between a control region and a region that is dominated by aerosol and cloud emissions. The cloud detection methodology used in the operational MIPAS processor is based on the concept designed originally for the CRISTA mission by Spang et al. [2002]. Here we use a similar index in MIPAS band A, hereafter called CI-A, as Spang et al. [2002], that is the most commonly used cloud index, defined by integrating the radiances in the MIPAS spectral regions of $788 - 796 \text{ cm}^{-1}$ (Microwindow or MW 1) and $832 \text{ cm}^{-1} - 834 \text{ cm}^{-1}$ (microwindow or MW 2). MW1 exhibits weak O_3 emissions and is mostly dominated by CO_2 . MW2 however, is more sensitive to aerosol and cloud emissions and weak O_3 and CFC-11 emissions. These two regions are highlighted in Figure 4.2. [Spang et al., 2004] extended the cloud detection methodology for the operational processor to include a cloud indicator in MIPAS bands B and D for which additional cloud index thresholds were defined. The spectral range and thresholds for bands B and D are shown in Table 4.1.

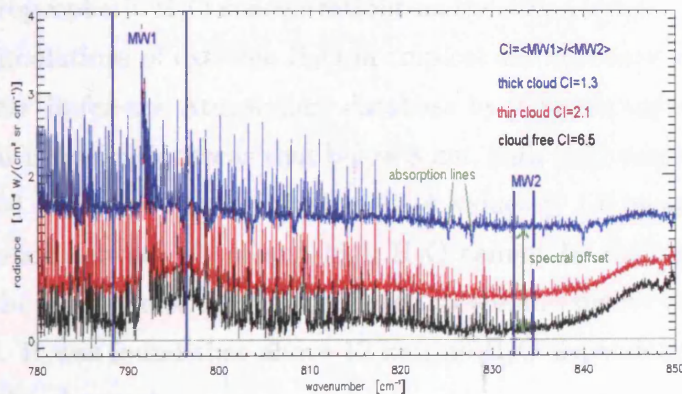


Figure 4.2: MIPAS cloud detection microwindows. Source: Greenhough et al., [2005]

Typical values for CI-A [Spang et al., 2004] are found to be close to unity when

Cloud Index MIPAS Band	MW1 (cm ⁻¹)	MW2 (cm ⁻¹)	CI thresh- old	Altitude range [km]
CI-A	788.20 - 796.25	832.3 - 834.4	1.8	12 - 40
CI-B	1246.3 - 1249.1	1232.3 - 1234.4	1.2	12 - 40
CI-D	1929.0 - 1935.0	1973.0 - 1983.0	1.8	12 - 30

Table 4.1: Cloud index thresholds used in MIPAS bands A,B and D

an optically thick cloud is present and CI-A is large (CI-A > 4.0) for a clear sky line of sight (in non polar regions). The values between 2.0 and 4.0 were found to correspond to the transition from optically thick to optically thin cloud presence or when a cloud only partially fills the MIPAS FOV.

For operational processing of MIPAS data, the nominal cloud detection scheme uses CI-A values to identify cloud contaminated sweeps. However, if band A is not available then the detection algorithm uses a sequence that utilises bands B and D depending on the availability of the spectra in these bands. In the operational processing of MIPAS data, a “cloud threshold” of CI-A = 1.8 is used in operational cloud detection where any value ≤ 1.8 is deemed cloudy and removed from the L1B dataset before it enters L2 processing.

4.1.2 Limitations of the cloud detection methodology

One of the most important limits on the utility of the cloud index is the effect of extreme upper tropospheric H₂O concentrations on the cloud index. This was tested, for CI-A using simulations of extreme H₂O in tropical and mid-latitude atmospheres using the Leicester Reference Atmosphere database by [Greenhough et al., 2005]. A key result in their investigations was that below 8 km, high H₂O concentrations could produce enhanced radiances that resulted in CI-A values ≤ 1.8 meaning that below 8 km, the difference between cloud and high H₂O cannot be distinguished. Above 8 km however, the CI-A index can be attributed to enhancements due to cloud and aerosol presence. It was found that above 12 km, no H₂O dependence on calculated CI-A values can be observed.

4.1.3 Modelling clouds in limb infrared spectra

The cloud index detection system serves two purposes: as well providing a method in which cloud contaminated L1B radiances are removed from L2 analysis, the cloudy spectra contain a wealth of information about the cloud itself. The cloud radiances contain information about the ice water content, ice particle sizes and distribution as well as cloud top temperature and height. Such information can potentially be retrieved from MIPAS data, however, such retrievals depend on accurate and detailed modelling cloud microphysical and optical properties.

Opaque clouds in the MIPAS line-of-sight do not only generate tremendous radiance offsets but some limb radiances also show evidence of scattering of radiation from below clouds in the form of H₂O absorption features [Hopfner et al., 2002]. Scattering of radiation occurs when the size of the scattering particle is larger than or equal to the detection wavelength. Absorption lines can also be produced in strong CO₂ and O₃ emission/absorption features if a warm cloud is observed through a colder overlaying layer.

Several cloud modelling studies have demonstrated the importance of including scattering processes in the simulations of MIPAS cloud radiances. Some radiative transfer models consider the single scattering properties of cloud particles such as the Karlsruhe Optimised and Precise Radiative Transfer Algorithm (KOPRA) that can model single scattering schemes in homogenous atmospheric layers. Alternatively models can consider scattering in multiple directions such as the Atmospheric Radiative Transfer Simulator (ARTS) model and the Rutherford Appleton Laboratory's 2-Dimensional Forward Model (FM2D) model. The Oxford RFM model is a zero scattering scheme.

Hopfner and Emde [2005] compared KOPRA and ARTS radiance output of several cloud scenarios including opaque, optically thin, and polar stratospheric clouds (PSCs) in a recent model inter-comparison study. It was found that in the modelling of optically thin clouds such as PSCs and subvisible clouds, single scattering schemes were sufficient to model these radiances better than zero scattering schemes that often had errors as large as 40 %. In some cloud cases, single scattering schemes were found to be sufficient and often there was little difference between the single and multiple scattering model outputs, although in some cases, single scattering schemes underestimated cloud radiances. Recently, some multiple scattering schemes have been

developed especially to model MIPAS cloud affected radiances and have been shown to perform well in comparisons with real MIPAS cloud data. Two such schemes are the Oxford Monte Carlo scattering Forward Model (McClouds_FM) model ([Ewen et al., 2005]) and the Spherical Atmospheric Radiative Transfer code (SARTre) code ([Mendrok et al., 2007]). Both models showed that features in MIPAS cloud spectra such as H₂O absorption lines and strong continuum offsets can be well reproduced by multiple scattering models. Ewen et al. [2005] found that single scattering schemes can potentially underestimate a large percent of cloud radiance in agreement with Hopfner and Emde [2005], who found that clouds with large single scattering albedo were not modelled well by single scattering schemes and that inclusion of multiple scattering processes is more suitable. However, for thin clouds ($4 > \text{CI-A} > 1.8$), in which absorption is the dominant process and scattering is small, zero scattering schemes may be sufficient to model cloud spectra. This thesis proceeds under this assumption. Scattering considerations are tested in section 4.6.1.

4.2 Investigating cloud contamination in MIPAS L2 H₂O and O₃ profiles

It is clear that clouds add a significant complication in the interpretation of MIPAS H₂O and O₃ retrievals. Both H₂O and O₃ exhibit steep gradients in the tropical UTLS and vary greatly due to changes in local dynamical processes and from chemical influences from natural and anthropogenic sources in the tropics. Thus it is difficult to distinguish whether the variability in their concentrations are features produced naturally in the atmosphere or from undetected cloud influence. The actuality is that methods of interpreting cloud effects on MIPAS retrievals of concentration profiles have not yet been deduced. Instinctively, one would expect that increased radiance produced by cloudy spectra would result in increased concentrations of H₂O and O₃ particularly for H₂O because of the enhanced continuum line effects of the cloud. However, observations of the real MIPAS data do not only show anomalously high concentrations. Figures 4.3 and 4.4 show a subset of L2 version 4.61 and 4.62 quality-flagged and operationally cloud-flagged H₂O and O₃ data at 100 mb (approximately 16 km). Data are gridded into 5° by 5° grid boxes. The figures show significant pixel to pixel variability and with H₂O concentrations as high as 10 ppmv and as low as

0.5 ppmv over tropical latitudes, and variations in O_3 concentrations near India of greater than 1.25 ppmv.

Although a CI-A threshold of 1.8 is used for MIPAS cloud detection, there is no evidence to prove that clouds with higher indices do not affect the retrieved H_2O and O_3 concentrations. During this thesis work, Glatthor et al. [2006] investigated cloud effects in MIPAS ozone profiles retrieved from the IMK MIPAS processor and concluded that for their retrieval a cloud index higher than 4.0 is necessary to remove the effects of contaminating clouds in MIPAS O_3 profiles. So far, studies have noted effects on retrievals at the cloud altitude but not at the altitude above.

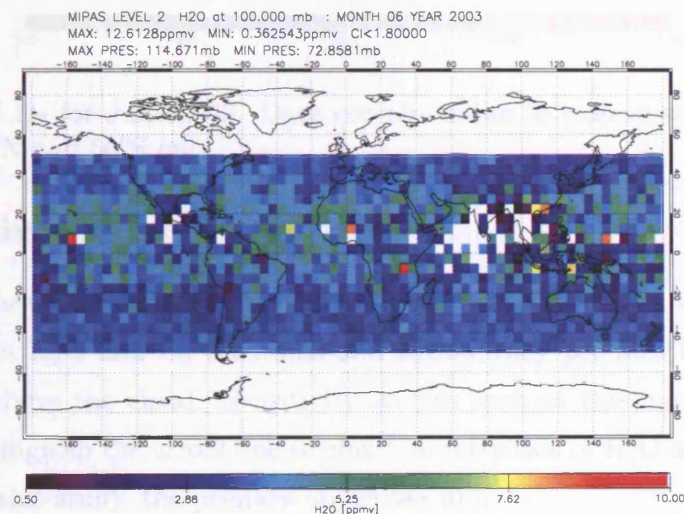


Figure 4.3: MIPAS H_2O for June 2003. Data corresponding to tropics/subtropics are shown between $50^\circ N$ and $50^\circ S$ only

In this chapter, the direct impact of cloud on MIPAS L2 retrievals of H_2O and O_3 are investigated with focus on the tropics between $30^\circ N$ and $30^\circ S$ and on the MIPAS tangent heights that correspond to 12 km, 15 km and 18 km to characterise the UTLS region. In this investigation, cloud indices that cover the full transition from cloudy to non-cloudy conditions, and the altitude dependence of clouds, on retrieved H_2O and O_3 concentrations, are analysed.

4.2.2 Methodology

To determine the error due to cloud in the retrieved MIPAS H₂O and O₃ profiles, knowledge of *how* a cloud modifies the retrieved concentrations from a typical clear-sky scenario is required. One way of isolating the effect purely due to cloud (or aerosol) would be to retrieve H₂O and O₃ concentration profiles from clear-sky spectra and then to retrieve H₂O and O₃ from the *same* spectra that now has a cloud added to the spectra. The difference between the retrieved profiles from both sets of spectra would represent the projection of the cloud from radiances into retrieved H₂O and O₃ concentrations. Such an analysis can be achieved using a simulation approach in which H₂O and O₃ profiles are retrieved from synthetic cloudy and clear-sky spectra that are treated as MIPAS observations by the L2 processor. Several factors must be taken into account for this kind of analysis to work. Firstly, the cloudy and clear-sky simulated spectra must be representative of the spectra that are measured by MIPAS in real situations. Secondly, the clear-sky and cloudy spectra must be calculated using the same input atmosphere files. Any form of variability other than that produced by the cloud will not allow the cloud error to be easily segregated.

In this investigation, a simulation approach is employed to relate the CI-A (that is derived from L1B radiance spectra) to the L2 retrieved concentrations of H₂O and O₃. This approach is chosen because: 1) No explicit validation of cloud effects in operational L2 MIPAS data exists or could be performed for full resolution MIPAS data. Such a study would require hundreds of coincidences with validating instruments in order to distinguish a relationship between the CI-A and retrieved concentrations of H₂O and O₃; 2) Using real MIPAS retrieved concentrations and the CI-A cannot allow a distinction of cloud effects as the data for both species are so variable in which case statistics for the deviations from climatological profiles would be difficult to interpret. Thus, the most suitable way of isolating the *cloud error* on the operational L2 H₂O and O₃ profiles is to use a simulation approach.

The simulation approach that is used in this investigation is to produce synthetic cloudy and clear sky MIPAS H₂O and O₃ spectra and then to relate the differences in the retrieved profiles to the CI-A. In order to produce *realistic* MIPAS cloudy spectra, a particle extinction coefficient profile is retrieved from real MIPAS spectra and this retrieved extinction forms the basis for all of the cloudy synthetic spectra produced in this analysis. Each step in this investigation will be described below.

4.2.2.1 Step 1. Representative scenarios for cloud

To select a well-qualified cloudy case for a cloud extinction retrieval and examine the variation of CI-A values, cloud index statistics are calculated from MIPAS cloud index files that have been generated at Leicester University. The frequency of cloud index occurrence is shown in tables 4.2 to 4.5. The frequencies are calculated for three month intervals for the altitudes of 12, 15 and 18 km between 30°N and 30°S. The CI-A data are sorted into bins corresponding to: a) measurements with CI-A < 1.8 b) Measurements with a CI-A between 1.8 and 6.0 and c) Measurements with CI-A > 6.0. These analysis are used to distinguish how often opaque clouds, thin clouds and clear sky scenarios are observed in MIPAS measurements.

Altitude of CI-A [km]	(a) CI-A ≤ 1.8 [%]	(b) 1.8 ≥ CI-A ≤ 6.0 [%]	(c) CI-A ≥ 6.0 [%]	Number of points
12 km	19.26	38.71	42.02	20442
15 km	10.17	9.60	80.21	20521
18 km	1.77	7.55	90.71	20539

Table 4.2: Percentage of various CI-A values in December, January and February 2002/2003

Altitude of CI-A [km]	(a) CI-A ≤ 1.8 [%]	(b) 1.8 ≥ CI-A ≤ 6.0 [%]	(c) CI-A ≥ 6.0 [%]	Number of points
12 km	26.91	58.51	14.56	17401
15 km	13.56	11.92	74.50	17628
18 km	4.26	6.88	88.85	17722

Table 4.3: Percentage of various CI-A values in March, April and May 2003

Altitude of CI-A [km]	(a) CI-A ≤ 1.8 [%]	(b) 1.8 ≥ CI-A ≤ 6.0 [%]	(c) CI-A ≥ 6.0 [%]	Number of points
12 km	28.05	55.52	16.42	21018
15 km	16.38	21.15	62.46	21546
18 km	6.60	10.93	82.46	21726

Table 4.4: Percentage of various CI-A values in June, July and August 2003

In each table, the total number of points in the tropics are given alongside the CI-A percentages in the three chosen scenarios. Unfortunately, not all L1B (and L2 datafiles) were re-processed at the time of this study therefore not all orbit files are available for all months. However, for the files that are available, some consistent

Altitude of CI-A [km]	(a) CI-A \leq 1.8 [%]	(b) 1.8 \geq CI- A \leq 6.0[%]	(c) CI-A \geq 6.0 [%]	Number of points
12 km	16.65	34.84	48.49	24819
15 km	7.20	11.03	81.77	25170
18 km	0.14	1.87	97.98	25384

Table 4.5: Percentage of various CI-A values in September, October and November 2003

behaviour throughout the year can be highlighted. The statistics show two distinctive patterns. The changes from 12 km to 18 km show that the greatest percentage of scenario (a) can be observed at 12 km, and this percentage drops with increased altitude throughout the year. In terms of changes in percentages over the different scenarios, scenario (b) has the greatest frequency at 12 km. The percentages show that the 12 km measurements are most likely to be affected by clouds (with a 1.8 definition) as would be expected. At 18 km, thick opaque clouds occur very infrequently as shown by *in situ* measurements, clouds at this altitude are likely to be optically thin cirrus clouds. Since these clouds can occur up to 10% of the time, it is important to quantify, if possible, the effects of these colder clouds on the retrieved H₂O and O₃ concentrations.

In this analysis, particular spectra are selected for the retrieval of a realistic estimate of cloud extinction. It is assumed that the cloud top is at 12 km, representing an upper tropospheric cloud and 18 km to represent a high altitude cloud. For the retrieval of cloud particle extinction, only single cloud altitudes are used for the modelling and retrieval of cloud as modelling and representing clouds at more than one tangent layer can be complicated. By observing the effect of a single cloud layer only, better interpretation and understanding of the propagation of cloud effects through the retrieved profiles can be investigated.

All L1B spectra used in this analysis must meet certain requirements. Therefore only L1B spectra that have corresponding operationally retrieved quality-flagged H₂O and O₃ profiles are used. The CI-A calculated from these spectra should possess a CI-A $<$ 1.8 as this is how clouds are currently defined in the operational processor. The bottom altitude of the retrieved particle extinction profiles (and the corresponding L2 profiles) is defined at the cloud altitude. To test the effect of a cloud at a single altitude only, the profiles with a clear-sky measurement immediately above the cloudy altitude is used. As the cloud index relies on the sensitivity of cloud MW2, the particle

extinction is retrieved from this microwindow only. All retrievals are performed on apodised spectra and the particle extinction profile is retrieved at the same tangent heights as the original spectra. The following sections describe retrieval procedure after which the results for each investigation are presented separately for a 12 km and 18 km cloud.

4.2.2.2 Step 2. Representing real cloud in MIPAS L1B spectra

Due to the ubiquitous nature of clouds, it can be difficult to differentiate how much of the radiance observed at MIPAS is due to cloud only. If a cloud completely fills the FOV, the cloud must have a large horizontal extent and a vertical thickness approximately three kilometres or more. Alternatively, if a cloud partially fills the FOV, the horizontal extent of the cloud may not be large enough or part of the cloud may be outside the MIPAS FOV. These scenarios are difficult to model therefore, a simplistic approach is used for the representation of the particle extinction *a priori*, assuming that the cloud is of large horizontal extent completely filling the MIPAS FOV. As the chosen cloud scenarios are all clear-sky ($CI-A \geq 6.0$) above the cloudy tangent height, the cloud top must be contained within the FOV of the cloudy tangent height. Hence, the shape of the *a priori* extinction profile does play an important role in defining the retrieval and must take into account the upper bounds of the MIPAS FOV.

The MIPAS FOV is a four point trapezium of base 4 km and top 2.4 km. The tangent heights used to define the *a priori* particle extinction profile is extracted directly from the cloud index profile. To create a “cloud box”, additional altitudes are required near the cloudy MIPAS tangent heights to which the *a priori* extinction can be extended to. A FOV calculation is performed to obtain the upper and lower overlap limits of the MIPAS FOV around the cloudy altitude. A schematic of the FOV set-up is shown in the figure 4.5 below. The red profile in the figure shows an *a priori* extinction profile defined at the measurement tangent altitudes. The intrusion of cloud radiance into the FOV above the cloud is clearly visible and is not representative of the real situation. The *a priori* shape used in this investigation correspond to the aqua profile on the right hand side of figure 4.5. The accuracy of the extinction retrieval is highly dependent on making realistic assumptions about the real situation and the cloud index profiles are invaluable for this process. An

unrealistic representation of the cloud situation, for example, if the cloud radiance impinges on the FOV above, could result in the radiances above the cloudy altitude being overestimated.

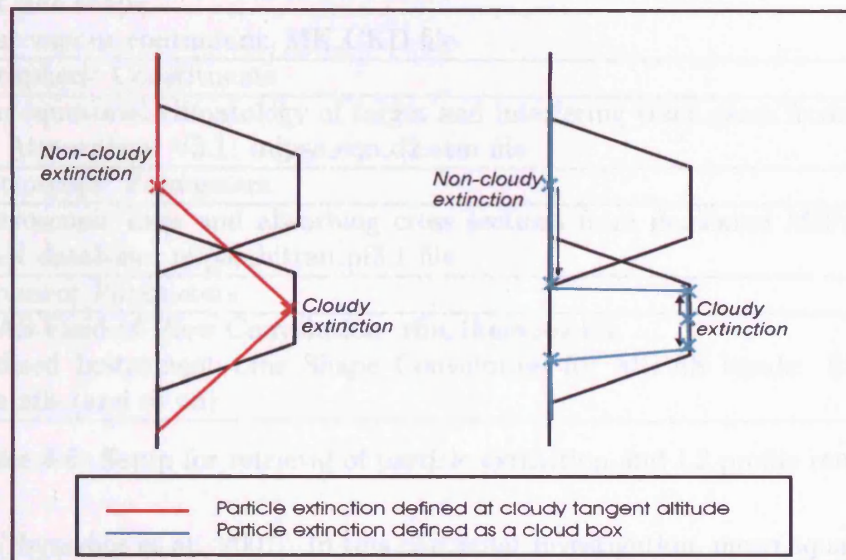


Figure 4.5: Creating a cloud box

The *a priori* extinction profiles used in these analysis are based on cloud index look up tables that have been generated using climatological extinction profiles retrieved from measurements obtained from the HALOE instrument and the standard maximum, mean and minimum equatorial atmospheres for MIPAS.

4.2.2.3 Step 3. Estimating cloud extinction

A simple retrieval methodology based on an optimal estimation technique was found to be sufficient to retrieve particle extinction. As the objective of this investigation is to test the response of the L2 processor, the retrieval and simulation setup must be consistent with the operational MIPAS L2 processor. Hence, the spectroscopic and instrument parameters that are used for the retrieval of particle extinction, and furthermore the simulation of the operational microwindows, are identical to those used by the operational L2 processor (see Table 4.6). The spectroscopic line and cross section information comes from the dedicated MIPAS spectroscopic database used operationally by the MIPAS L2 processor and atmospheric parameters used in the retrieval come from the MIPAS Reference Atmosphere, Standard atmospheres

RFM Setup
Spectral grid: 0.0005 cm ⁻¹ Spectral resolution: 0.025 cm ⁻¹ Refraction of ray paths Voigt line shape Water vapour continuum: MK_CKD file
Atmospheric Constituents
Mean equatorial climatology of target and interfering trace gases from Reference Atmosphere V3.1: mipas_eqn_d2.atm file
Spectroscopic Parameters
Spectroscopic lines and absorbing cross sections from dedicated MIPAS HITRAN database: mipas_hitran_pf3.1 file
Instrument Parameters
MIPAS Field of View Convolution: rfm_1km5.fov file Apodised Instrument Line Shape Convolution for MIPAS bands: files mipas_a_ails (and so on)

Table 4.6: Setup for retrieval of particle extinction and L2 profile retrieval

dataset [Remedios et al., 2007]. In this particular investigation, mean equatorial profiles are used for the representation of the mean tropical atmosphere. These are the only profiles used in the particle extinction retrieval and microwindow simulations and no real MIPAS data are used to ensure that no additional variability (or errors) are introduced into the retrieval. The Oxford RFM is employed to simulate the MW2 radiances from the cloud altitude (either 12 or 18 km) to 40 km. The retrieval method uses an Gauss-Newton iterative process, modified by the Levenberg-Marquardt criterion and requires a suitable particle extinction *a priori* profile that is discussed in the following section. A solution is found when the retrieval reaches convergence by the minimisation of the cost function. Generally, convergence is reached within 4 - 6 iterations. The retrieval setup used for the particle extinction retrieval and H₂O and O₃ simulations is shown in Table 4.6.

4.2.2.4 Step 4. Verifying simulations of MIPAS cloud microwindows

To verify that the retrieved cloud extinction coefficient represents the cloudy spectra used in this analysis, the RFM is used to simulate microwindow MW1 and MW2 with the *retrieved* cloud extinction profile. A simulation of the cloud spectra from 12 km to 68 km is performed using the setup described in table 4.6 and the CI-A is calculated from the simulated spectra and compared to the real CI-A. A comparison

of the simulated spectra is performed by: 1) comparing the actual radiances of the full radiance spectra in the cloud microwindows to real spectra and 2) comparing the mean radiances of both the simulated and real spectra against CI-A in microwindows MW1 and MW2. In the operational L2 processor, the cloud detection was incorrectly incorporated in that the upper limit of MW1 was defined as 799 cm^{-1} instead of 796 cm^{-1} . For consistency with this, all CI-A values calculated in this investigation use 799 cm^{-1} as the upper limit for MW1. Note that the importance of this step is to verify reasonable behaviour of the selected cloud scenario rather than absolute accuracy in matching radiances.

4.2.2.5 Step 5. Simulating nominal microwindows for H₂O and O₃

After confirming that the retrieved cloud extinction coefficient is a reasonable representation of the cloud radiance in the cloud microwindows, the nominal H₂O and O₃ microwindows used for operational MIPAS processing are simulated using the RFM with the retrieved extinction profile. Spectra are simulated from 12 km to 68 km to represent the full MIPAS elevation scan that is used in this analysis. The simulated radiances are compared to the real spectra in all microwindows as well as the mean calculated radiances against the CI-A calculated from the cloud microwindows. This is to verify that simulated spectra agree with the real MIPAS cloud data, using the retrieved cloud extinction and furthermore, highlight whether the cloud exhibits any wavelength dependency in the H₂O and O₃ microwindows.

Once the accuracy of the spectra in the nominal microwindows is verified, the same set of H₂O and O₃ spectra are simulated using modified versions of the retrieved cloud extinction profiles. The extinctions are perturbed in steps of - 5 to -10 % to produce a range of extinctions and CI-A values that represent the transition from clear-sky spectra to cloudy spectra. The values of the cloud indices produced cover a CI-A range from < 1.8 to > 6.0 where the clear sky conditions are produced using an extinction profile of $1 \times 10^{-6}\text{ km}^{-1}$. The spectral regions for the cloud and nominal H₂O and O₃ microwindows used in this analysis, and the interfering absorbers used in each region are given in Table 4.7.

Microwindow name	wavenumber range cm^{-1}	Interfering Absorbers
MW1	788.2 - 799.25	H ₂ O CO ₂ CH ₄ HNO ₃ N ₂ O NO ₂ O ₃ C ₂ H ₆ N ₂ O ₅ CCl ₄ ClONO ₂ O ₂ CFC-11 CFC-12 HCFC-22 CFC-113
MW2	832.3 - 834.4	SAME AS MW1
H2O_0001	1650.025 - 1653.025	H ₂ O CH ₄ HNO ₃ N ₂ O NO ₂ O ₃ NH ₃ O ₂
H2O_0022	946.65 - 947.7	H ₂ O CO ₂ HNO ₃ N ₂ O O ₃ NH ₃ COF ₂ SF ₆ CFC-113
H2O_0002	807.85 - 808.45	H ₂ O CO ₂ HNO ₃ NO ₂ O ₃ NH ₃ COF ₂ ClO C ₂ H ₆ CCl ₄ HNO ₄ ClONO ₂ HCFC-22 CFC-113
O3_0021	763.375 - 766.375	H ₂ O CO ₂ HNO ₃ NO ₂ O ₃ NH ₃ COF ₂ C ₂ H ₂ CCl ₄ HCN CH ₃ Cl ClONO ₂ N ₂ O ₅
O3_0001	1122.8 - 1125.8	H ₂ O N ₂ O O ₃ CH ₄ SO ₂ NH ₃ CFC-12 CFC-13 HCFC-22 CFC-113 CFC-114 CFC-115

Table 4.7: Microwindow regions and interfering absorbers

4.2.2.6 Step 6. Retrieving cloudy L2 H₂O and O₃ with the ORM

The ORM, that is the prototype code of the L2 processor (Chapter three, section 3.5) is used in this analysis for the retrieval of L2 H₂O and O₃ profiles for each of the simulations. The RFM - generated spectra are treated as MIPAS observations by the OFM that simulates the spectra starting from the same climatological profiles used for the particle extinction retrieval. The true profile is represented by the climatological profiles that are perturbed by -15 % away from the original climatological values. Random noise, corresponding to the NESR for each consecutive band is added to all spectra and the same random seed is applied to the clear sky and all cloudy tests performed. All spectra are convolved with the AILS function and IFOV function that is used operationally by the L2 processor. Profiles are retrieved with the same convergence criterion used operationally that require the χ^2 value to be below some threshold values and the maximum number of iterations is set to 6 (see chapter 3 for a description of the L2 retrieval). A systematic difference will exist between the ORM and RFM generated spectra because the particle extinction retrieval grid near the cloud altitude is not the same as the retrieval grid used by the ORM.

4.2.2.7 Step 7. Relating the CI-A to retrieved H₂O and O₃

As the primary objective of this investigation is to examine how cloud presence deviates the retrieved profiles away from expected clear-sky profiles, all profiles are compared to the clear-sky profiles retrieved by the ORM. This allows a direct comparison of a cloud affected profile to what MIPAS would “see” in terms of concentrations, in a typical clear-sky retrieval. To investigate the effect of increased particle extinction in the cloud, H₂O and O₃ microwindows, the relationship between the CI-A and *radiances* in all microwindows and furthermore, the relationship between the CI-A and the *retrieved concentrations* of H₂O and O₃ can be deduced. This relationship can be used to indicate: 1) whether the limit where the extinction due to cloud or aerosol in the MIPAS FOV will not affect the retrieved concentrations of H₂O and O₃ and 2) If the variability in the tropical UTLS is not explained by cloud effects then this investigation can highlight systematic factors other than clouds that cause variability in the retrieved concentrations. For all cloud case studies investigated the results will be presented in the following order.

1. Information about the retrieved particle extinction will be given and the spectra for each CI-A will be presented.
2. The retrieved profiles and the operational random retrieval errors for the cloudy and clear-sky cases will be presented.
3. The relationship between the retrieved concentrations and the CI-A is investigated by calculating the deviation of the retrieved *cloudy* concentration from the expected *clear-sky* concentration using equation 4.1.

$$Dev_{VMR} = \left(\frac{VMR_{CLD} - VMR_{CLEAR}}{VMR_{CLEAR}} \right) * 100 \quad (4.1)$$

The units for Dev_{VMR} are given in percent (%). The corresponding operational random retrieval error is also presented, in percentage terms using equation 4.2.

$$Error = \left(\frac{ERR_{CLOUD}}{VMR_{CLEAR}} \right) * 100 \quad (4.2)$$

Where the terms VMR_{CLOUD} , VMR_{CLEAR} and ERR_{CLOUD} correspond to the

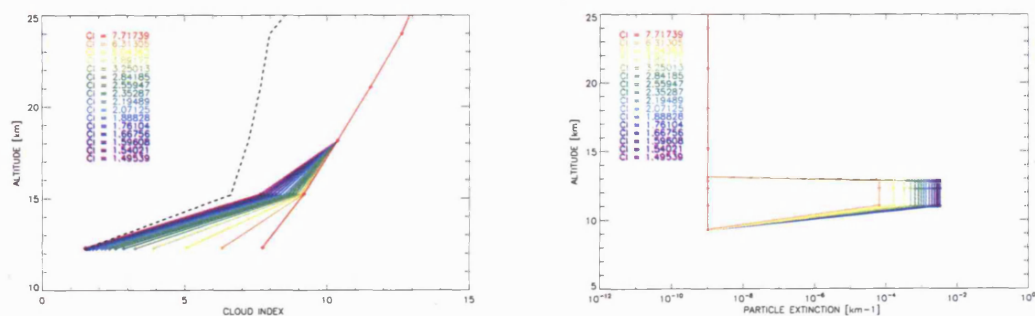
retrieved cloudy, retrieved clear-sky and the cloudy random retrieval error, respectively.

4.3 Results

The following sections present the results of 12 km and 18 km cloud cases on MIPAS H₂O and O₃ retrievals, beginning with the 12 km cloud case study.

4.4 Case study: cloud at 12 km

To investigate how an upper tropospheric cloud affects MIPAS retrievals, a scenario is defined in which a cloud with CI-A < 1.8 occurs at 12 km and all tangent heights above are non-cloudy. A real MIPAS radiance profile that appears to correspond to this scenario was found in orbit 07386 and scan number 5 corresponding to a latitude and longitude of 1.98°N and 152.9°E respectively. The cloud index profile for the real case, with a CI-A = 1.49 at 12 km, is shown (black dotted line) in Figure 4.6(a) along with the cloud index profiles for all simulations. The particle extinction profiles used in each simulation is shown in Figure 4.6(b). The retrieved cloud extinction in these cases can be thought of as an effective total particle extinction, combining the resultant effects of the absorption and scattering coefficients cannot be deduced here.



(a) 12 km cloud index profiles

(b) 12 km particle extinction profiles

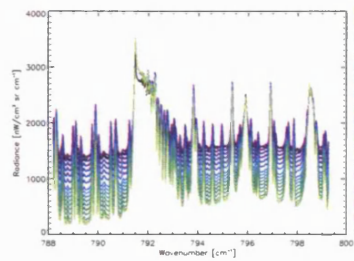
Figure 4.6: Simulated 12 km cloud indices and *a priori* extinction profile. Note the shape of the extinction profiles in which each profiles is assumed to fill the cloudy tangent height FOV completely.

4.4.1 Simulated *cloudy* spectra

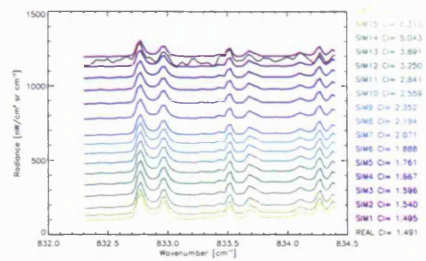
Figures 4.7(a) to 4.7(g) show each set of simulated cloudy and clear sky spectra plotted against the chosen real MIPAS spectra (black spectra). Each figure is labelled with the corresponding microwindow name and the CI-A value for each set of spectra (calculated from the mean radiances in MW1 and MW2) is colour-coded shown alongside each figure. The relationship between the cloud index and the spectral offset is evident as the CI-A undergoes a transition from cloudy to non-cloudy values. The simulation of the *real* MIPAS spectra in the cloud microwindows, in figures 4.8(a) and 4.8(b) show that the simulated cloudy spectra compare well to the real MIPAS spectra giving confidence that a realistic representation of cloud using the retrieved extinction is achieved. Some dissimilarity is observed in MW1 where the CO₂ peak around 791.5 cm⁻¹ is slightly higher than that observed in the real MIPAS data. This is a small difference relative to the total observed radiance in this region. The simulated spectra for the H₂O microwindows are shown in figures 4.7(c) to 4.7(e) and the figures show that the radiance tends to be overestimated in the H₂O peaks at 1652.6 cm⁻¹ and 808.15 cm⁻¹. This overestimation is believed to be due to the mean equatorial reference atmosphere H₂O profile, which as shown by Remedios et al. [2007], is typically higher than the mean L2 MIPAS profiles retrieved from full resolution L2 data. In the two O₃ microwindows, region O3_0021 is in better agreement with the real MIPAS cloud spectra than region O3_0001 where a constant offset of approximately 100 nW/(cm²sr cm⁻¹) can be observed. As the concentrations of the absorbers used for this simulation are identical to those used operationally, the cause of this offset may be an underestimation in the concentrations of some of the heavier gases in this region such as CFC-113, HCFC-22 and CFC-12.

Another diagnostic of the representation of the cloud cases simulated can be produced by examining the variation of radiance in each microwindow with CI-A as noted previously. The mean radiance in each simulated microwindow is plotted against CI-A (green diamonds) and is shown in figures 4.8(a) to 4.8(g). These are compared to the variations observed in real MIPAS radiances shown in each figure as black diamonds using 25 days worth of real MIPAS L1B data (from 1st August to 25th August 2003). This equates to approximately 3500 MIPAS data points in each microwindow.

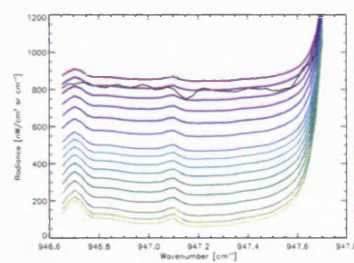
In cloud MW2, the mean simulated radiances capture the behaviour of the real data where the mean radiances decrease with increasing CI-A value. The real mean



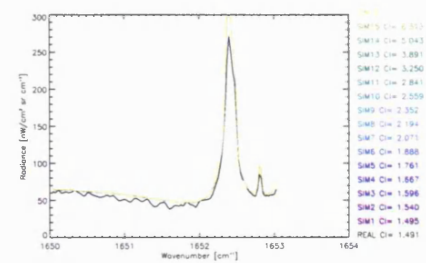
(a) MW1 for 12 km cloud



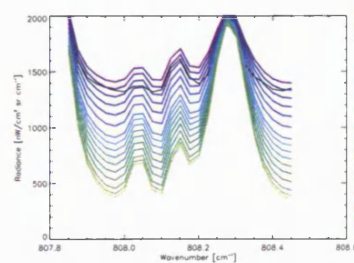
(b) MW2 for 12 km cloud



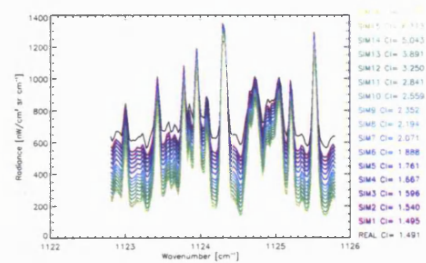
(c) H2O_0022 for 12 km cloud



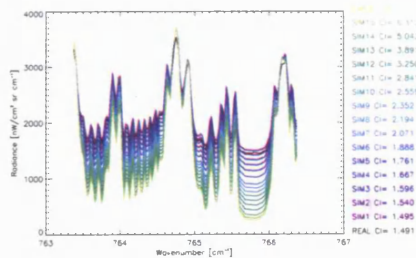
(d) H2O_0001 for 12 km cloud



(e) H2O_0002 for 12 km cloud



(f) O3_0001 for 12 km cloud



(g) O3_0021 for 12 km cloud

Figure 4.7: Cloudy to clear sky 12 km spectra generated for the MIPAS cloud and nominal O₃ and H₂O microwindows.

radiances show a neat, compact relationship with decreasing CI-A value and the mean simulated radiance values lie within this compact range of radiance values. A similar pattern is observed in cloud MW1 although the variability of the real data is not as compact as that observed in cloud MW2. It is noteworthy that very high radiances are observed at low CI-A in the real spectra. It is not the objective of this thesis to model these data as they are opaque enough to clearly cause problems for trace gas retrievals. The plots in Figure 4.8 substantiate the reasonableness of the simulated spectra for each CI-A as a good representation of the radiance variation with the CI-A value observed in the real data.

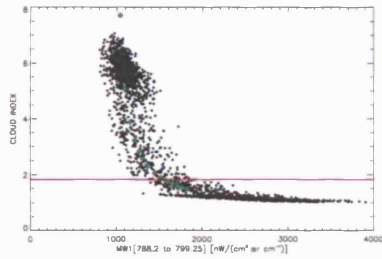
In the H₂O microwindows, the simulated spectra lie well within the mean radiance variability of the real data. The spectra in H2O_0001 are different in behaviour because the H₂O line and continuum effects mean the window is close to saturation. Hence, with increasing CI-A, the saturated H₂O peak is not affected greatly with changing cloud influence although this set of spectra is on the higher edge of the variation in this microwindow.

For O₃, the simulated radiance and CI-A variation compares well with the variations observed in the real data in the band A O3_0021 microwindow. In the O3_0001 microwindow, that is a band C microwindow, the RFM spectra are on the lower edge of the variability in the real data and this clearly relates to the offset observed in this region. The mean radiances calculated from the real data show some low radiances that tend to be near-zero. Some interesting behaviour can be observed in both O₃ microwindows and region H2O_0001 where bands of low mean radiance deviate away from the main mean radiance curve. These points are nominally disregarded here as they occur at low CI-A values produced by opaque clouds. However, these scenarios may prove to be interesting in retrievals of cloud properties from MIPAS.

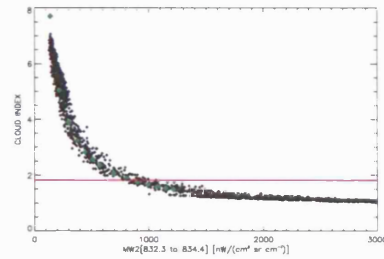
4.4.1.1 Retrieved cloudy and clear-sky H₂O and O₃ profiles

Figures 4.9(a) to 4.9(d) show the ORM retrieved profiles of H₂O and O₃ with and without cloud at 12 km. The figures are arranged so that the top two figures show H₂O and O₃ profiles for the cloudy (CI-A = 1.49) vs. clear-sky. The bottom two figures (Figures 4.9(c) and 4.9(d)) show all the cloudy and clear-sky H₂O and O₃ profiles investigated. The CI-A corresponding to each profile is plotted alongside.

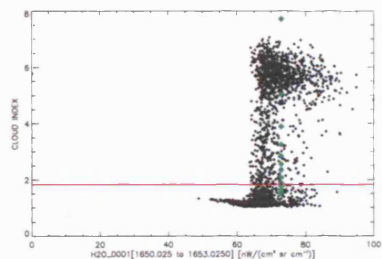
When 12 km cloudy spectra are included in the retrieval of H₂O, the retrieved



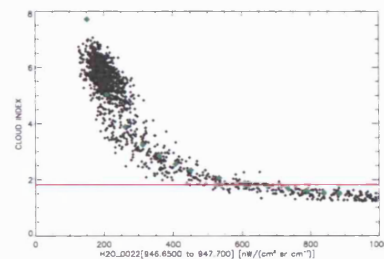
(a) CI-A vs. MW1



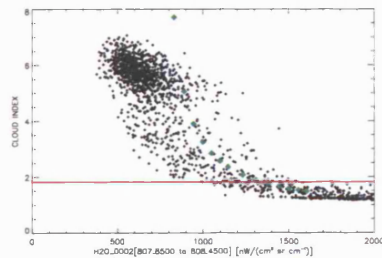
(b) CI-A vs. MW2



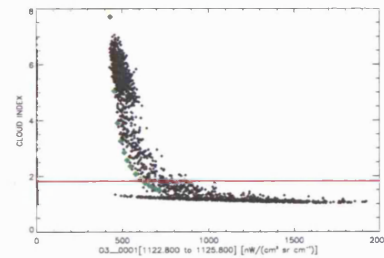
(c) CI-A vs. H2O_0001



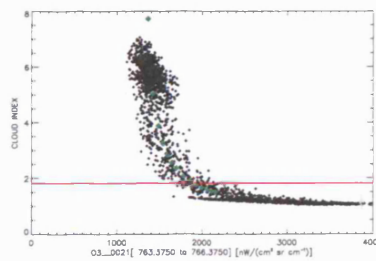
(d) CI-A vs. H2O_0022



(e) CI-A vs. H2O_0002



(f) CI-A vs. O3_0001



(g) CI-A vs. O3_0021

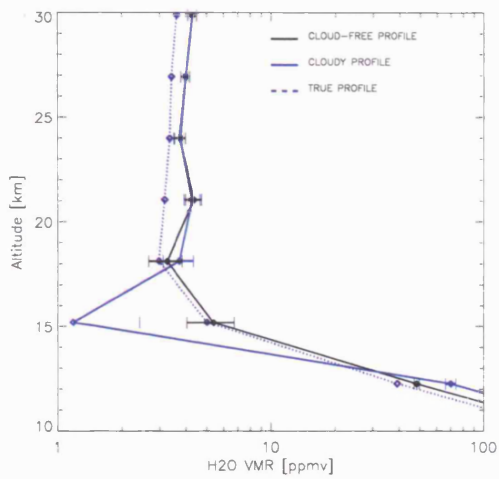
Figure 4.8: The 12 km mean radiance in the MIPAS cloud and nominal O₃ and H₂O microwindows against MIPAS CI-A

concentrations are higher at 12 km and lower at 15 km compared to the cloud-free H₂O profile 4.9(a). The concentration profiles in figure 4.9(c) shows that as cloud influence increases (i.e. CI-A becomes smaller and cloud becomes optically thicker) the concentrations at 12 km are positively biased with a *simultaneous* negative bias at 15 km. For O₃, the retrieved concentrations at the cloud altitude are lower than the cloud-free profile when a cloud is present at 12 km. Above the cloud, the concentrations appear to become higher than the clear-sky profile 4.9(b). The figure shows that the retrieved cloud-free O₃ profile itself deviates quite significantly from the 'true' profile used indicating that in cloud-free conditions, O₃ retrievals are problematic. This is because of a combination of low tropopause temperatures and low O₃ signal at this altitude. In this case, these factors in addition to a 3 km retrieval grid produces a negative bias in the retrieved concentration at 15 km. It is expected that the retrieval grid in the new reduced resolution mode will improve O₃ retrievals around the tropopause region. Also for O₃ we find the cloudy profile is coincidentally better matched to the true profile because of the increased signal from cloud compensating the low O₃ signal for this region. The profiles retrieved in the presence of varying cloud (Figure 4.9(d)) appear to increase and decrease at the cloud altitude with what appears to be an anti-correlation between the 12 km and 15 km altitudes. However, no distinctive behaviour can be deduced from the concentrations.

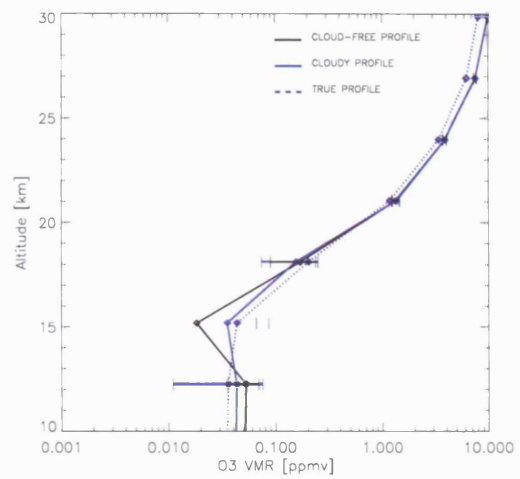
4.4.1.2 Deviations in retrieved H₂O profiles

The deviations from expected clear-sky concentrations, produced at 12 km and 15 km, by a 12 km cloud are shown in more detail in figures 4.10(a) and 4.10(b). Details are given in the figure captions. These results highlight two significant cloud effects: firstly, the deviations in the profiles appear to increase systematically with decreasing cloud index (and therefore increasing cloud influence), and secondly, that increasing cloud presence always increases the random retrieval error. The negative deviation at 15 km can be significantly larger than the random retrieval error at 15 km with increasing cloud influence at 12 km. In addition, note that the H₂O clear sky profiles also possess a small positive bias compared to the true profile used by the ORM. Although the bias for H₂O is relatively small at the cloud altitude, it is higher than the true profile at higher altitudes.

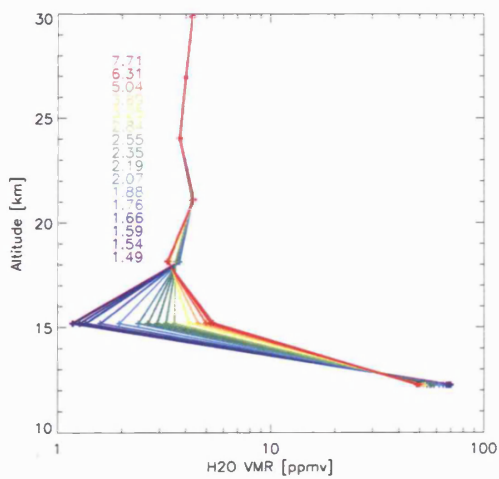
In principle, the systematic cloud error can be calculated from both the 12 km and



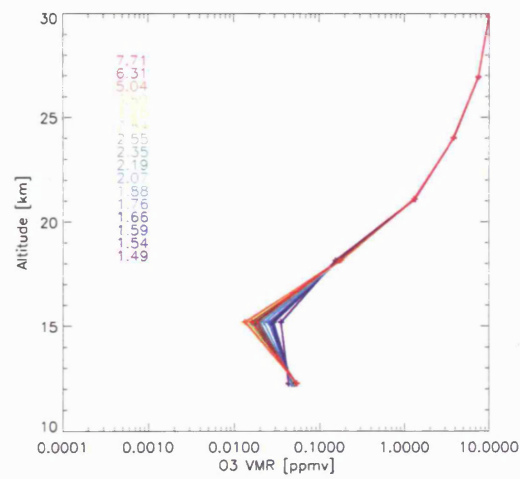
(a) Cloudy (CI-A = 1.49) vs. clear-sky H₂O profiles



(b) Cloudy (CI-A = 1.49) vs. clear-sky O₃ profiles



(c) All cloudy H₂O profiles



(d) All cloudy O₃ profiles

Figure 4.9: H₂O and O₃ profiles retrieved in clear sky and cloudy conditions with a cloud present at 12 km.

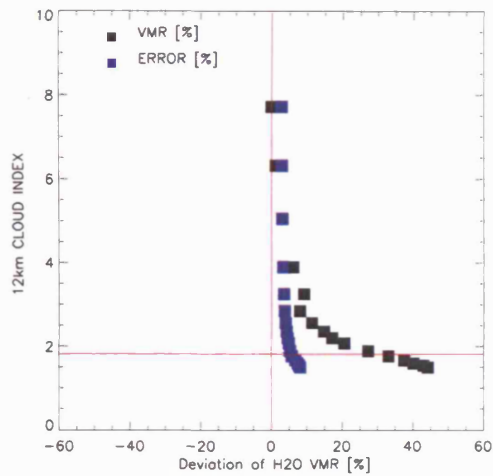
the 15 km deviations from clear sky profile as produced by the 12 km cloud. These are *root-sum-squared* with the 12 and 15 km Oxford clear sky systematic errors and are shown in figures 4.10(c) and 4.10(c). On the same figures the Oxford estimated clear sky random error (dotted red line) and the random retrieval error (solid red line) from each retrieved profile are also plotted. As shown by the solid and dotted blue lines in figure 4.10(c), the estimated systematic error increases by almost 40 % for a $CI-A \leq 1.8$. For this particular case, the 12 km random retrieval error is lower than the estimated Oxford error for 12 km and although it increases with increased cloud influence, it is not as significant as the change in the systematic errors. Figure 4.10(c) shows that the impact on the random retrieval error at 15 km is not as significant as the change in the 15 km systematic error.

4.4.1.3 Deviations in retrieved O₃ profiles

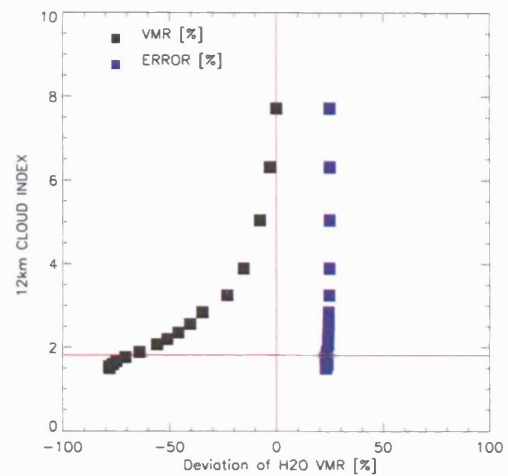
The 12 km and 15 km deviations produced by a cloud at 12 km on the O₃ profiles are shown in figures 4.11(a) and 4.11(b). As cloud presence is varied, the deviation of the retrieved cloudy concentration from the cloud-free concentrations can be positive or negative. What is clear from the 12 km results is that the change in random retrieval error is far more significant compared to the apparent systematic deviation at 12 km. In this particular case, the random retrieval error for the clear-sky case is larger than the Oxford estimates but more importantly increases greatly with increasing cloud influence. Above the cloud altitude, at 15 km, the errors are clearly larger than the deviations produced by the cloud below. Given the greater random error, it is difficult to infer a systematic cloud error despite the results of Figure 4.11, a point which is returned to later in the discussion.

4.4.2 Investigating the impact of random noise on 12 km retrievals

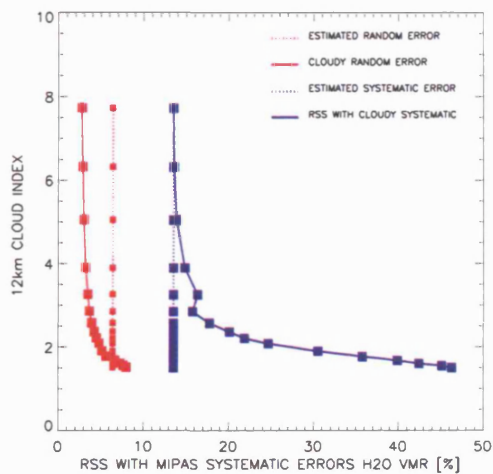
All retrieved profiles shown in the 12 km analysis were retrieved by fulfilment of the operational L2 convergence criteria (section 3.5.4) so that the experiment is consistent with the current operational L2 retrieval settings. The O₃ retrieved profiles in particular, demonstrated that near the tropopause, where concentrations are small, the



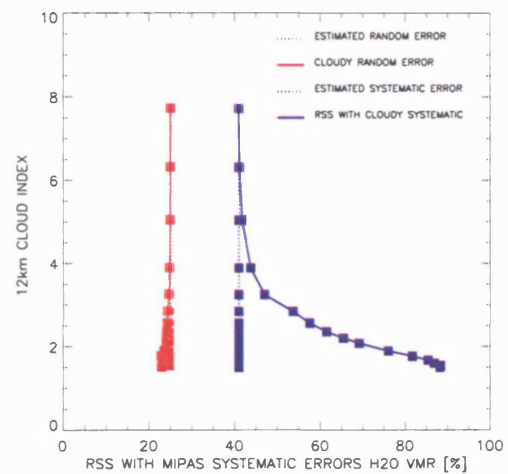
(a) Deviation in 12 km H₂O concentration with a 12 km cloud



(b) Deviation in 15 km H₂O concentration with a 12 km cloud

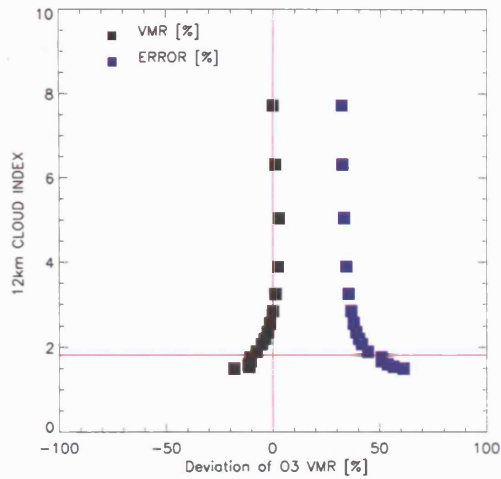


(c) RSS of 12 km deviation with H₂O estimated systematic errors

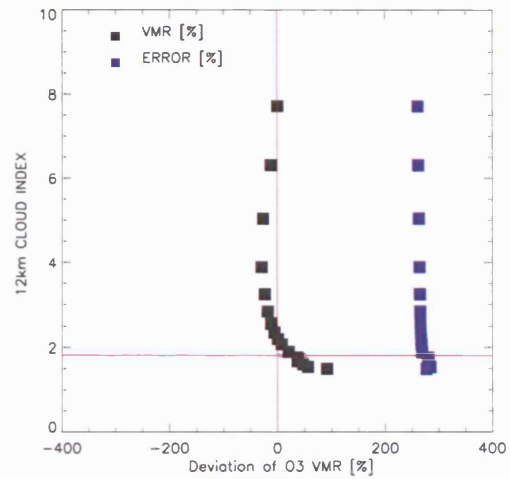


(d) RSS of 15 km deviation with H₂O estimated systematic errors

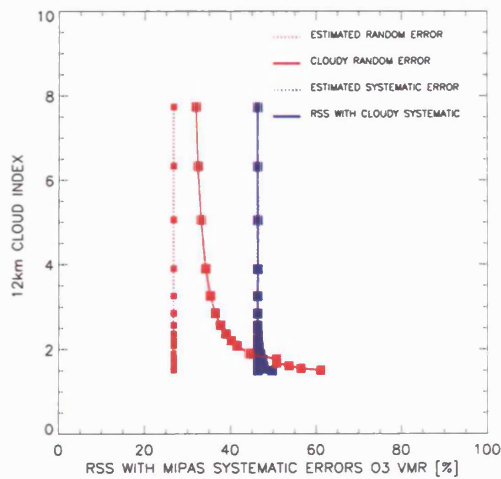
Figure 4.10: Deviations in H₂O concentrations from expected clear-sky concentrations at 12 km and 15 km and the 12 and 15 km deviations *root-sum-squared* with Oxford systematic errors against 12 km CI. Deviations can be almost 50 % greater than cloud-free 12 km concentrations and at least 80% lower than cloud-free conditions at 15 km. The corresponding retrieval errors are also shown in the figures to show how they compare to the retrieved concentrations.



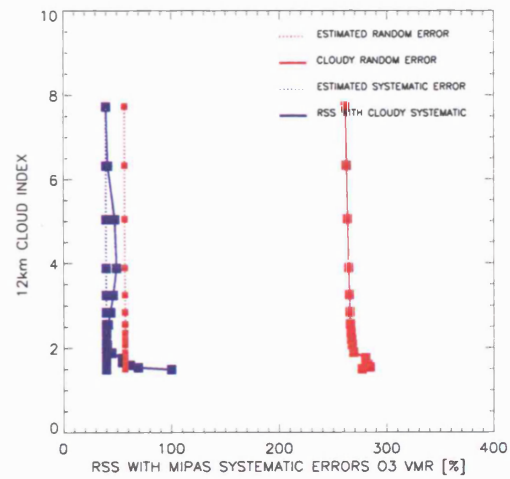
(a) Deviation in 12 km O₃ concentration with a 12 km cloud



(b) Deviation in 15 km O₃ concentration with a 12 km cloud



(c) RSS of 12 km deviation with O₃ estimated systematic errors



(d) RSS of 15 km deviation with O₃ estimated systematic errors

Figure 4.11: Deviations in O₃ concentrations from expected clear-sky concentrations at 12 km and 15 km and 12 and 15 km deviations *root-sum-squared* with Oxford systematic errors against 12 km CI-A. As the figures show, the tend to larger values for lower CI-A values and can be as large as 50 % for CI-A > 1.8

propagation of measurement noise at these altitudes is the dominating factor controlling the retrieved concentrations. As a result of this, no conclusive systematic cloud effect on O_3 retrievals could be determined. To investigate what the effect of random noise propagation into the retrieved concentrations and the corresponding retrieval error are, the impact of adding varying random noise seeds into the retrievals was evaluated. For selected CI-A values obtained in the analysis above, the H_2O and O_3 retrievals at 12 km were repeated using three varying random noise seeds.

The CI-A values that were chosen for the noise sensitivity tests were: a) CI-A = 1.8 to represent a definite cloud; b) CI-A > 6.0 to represent a definite cloud-free case; c) CI-A = 4.0 as this has been suggested by Glatthor et al. [2006] and Spang et al. [2004] to be onset of cloud-free measurements; d) CI-A = 3.0 as this was chosen to be a general cloud index by Sembhi et al. [2007]; e) 2.5 which allows a modest 20% deviation at 12 km and changing the systematic error by 5%.

The results for the cloud at 12 km are presented in Figures 4.12(a) to 4.12(f) for H_2O at 12 and 15 km and Figures 4.13(a) to 4.13(d) for O_3 at 12 and 15 km. The H_2O deviations remain larger than the random error for all seeds although the propagation into the altitude above does tend to change slightly for CI-A < 1.8. The random retrieval error always increases with increasing cloud influence with all random noise seeds tested. For O_3 , the deviations tend to not change significantly in each random noise tested and in all cases, the random error at 12 km is more significant than the deviations.

4.5 Case study: cloud at 18 km

A similar cloud case has been studied for 18 km using the real MIPAS radiance profile from orbit 07963 and scan number 9 where the 18 km tangent height has a CI-A < 1.8 and all tangent altitudes above are non-cloudy. The chosen CI profile is based at a tropical latitude and longitude of 16.49°N and 49.43°W respectively. Although the statistics show that there is not a large fraction of clouds using the 1.8 definition (less than 6%), there are more potential clouds that correspond to CI-A between 1.8 and 6.0 (up to 10 % in some cases) that may affect retrievals. The cloud index profile for the real case, with a CI-A = 1.72 at 18 km is shown (black dotted line) in Figure 4.14(b) along with the cloud index profiles for all simulations. The corresponding

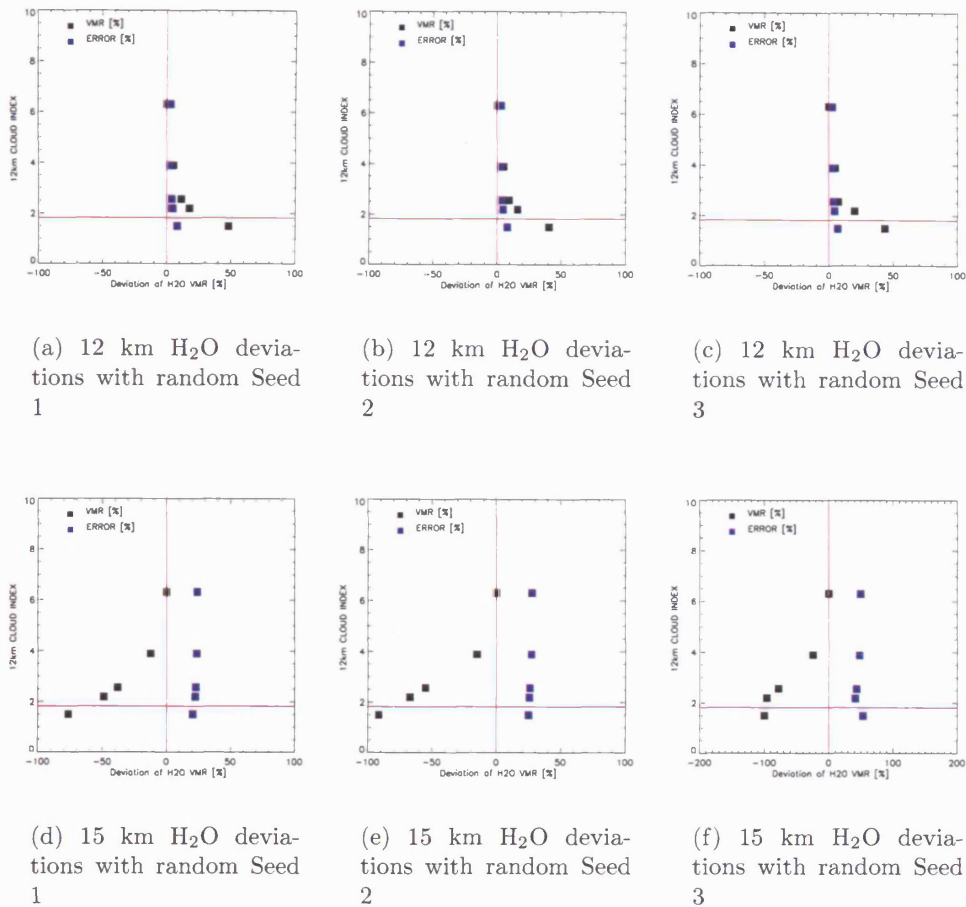


Figure 4.12: Deviations in H₂O concentrations from expected clear-sky concentrations at 12 km and 15 km with varying random seeds.

particle extinction profiles used in each simulation are shown in Figure 4.14(a). The cloud box for the 18 km cloudy case was created using the method illustrated in Figure 4.5 and similarly to the 12 km case, the cloud box is assumed to fill a large part of the cloudy tangent height FOV completely.

4.5.0.1 Simulated *cloudy* spectra

The spectra simulated for the 18 km cloud and nominal O₃ and H₂O microwindows are shown in figures 4.15(a) to 4.15(g). The match of the real data (black spectra) and the simulation of the real data (labelled "sim 1" in each figure) confirm that the retrieved cloud extinction coefficient is a reasonably accurate representation of the

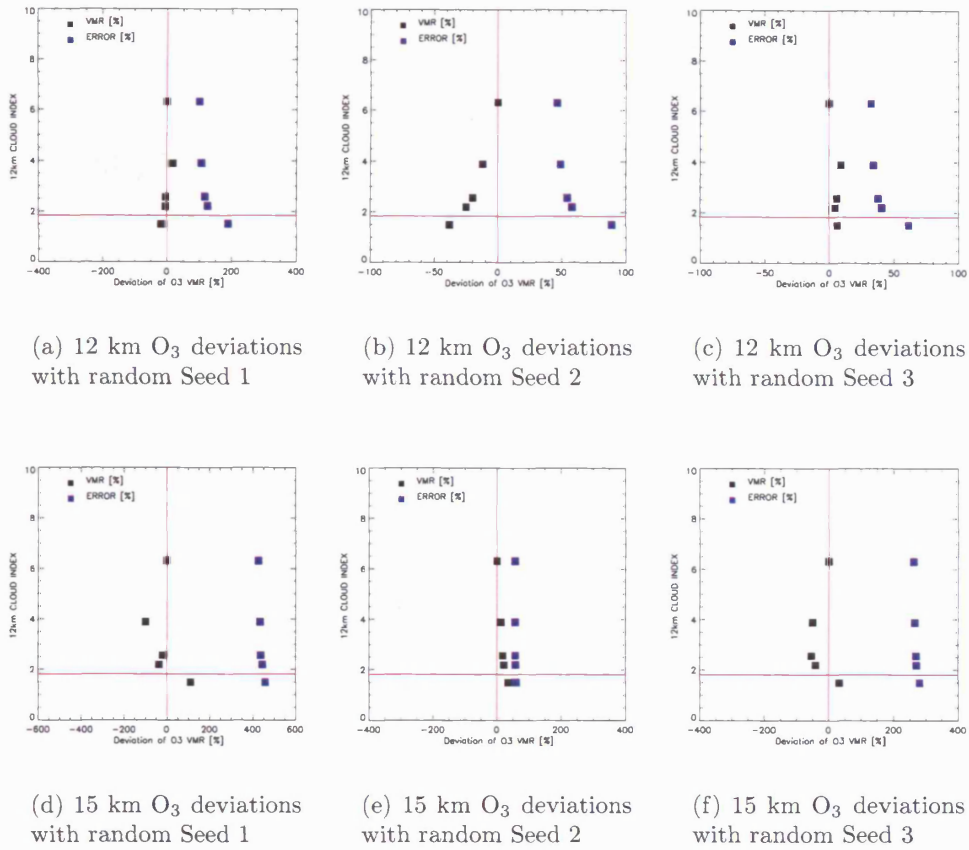


Figure 4.13: Deviations in O₃ concentrations from expected clear-sky concentrations at 12 km and 15 km with varying random seeds.

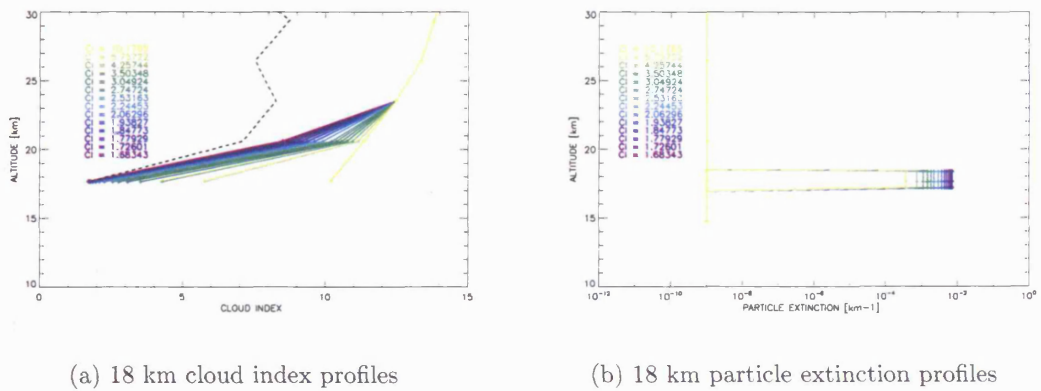
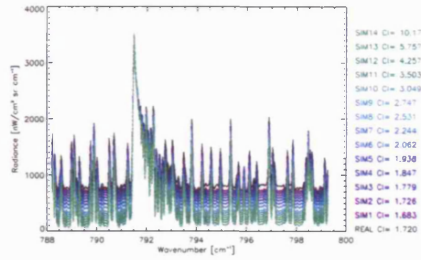
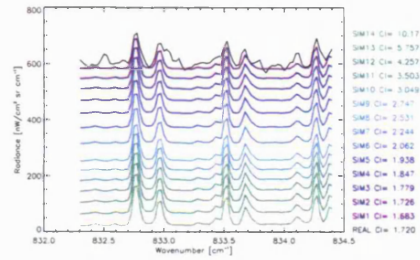


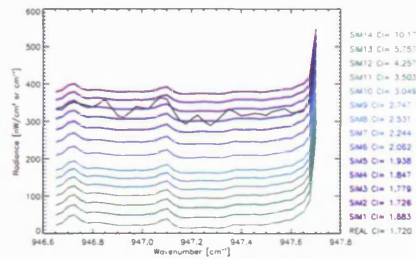
Figure 4.14: Simulated 18 km cloud indices and *a priori* extinction profile



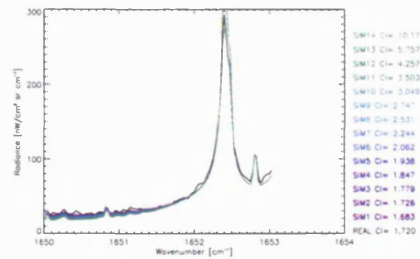
(a) MW1 for 18 km cloud



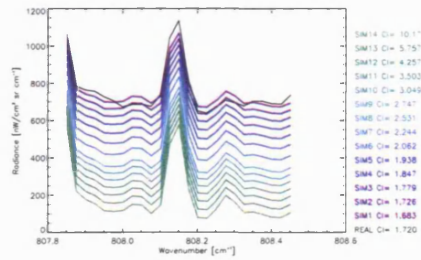
(b) O3_0021 for 18 km cloud



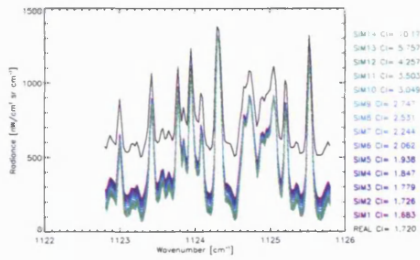
(c) H2O_0022 for 18 km cloud



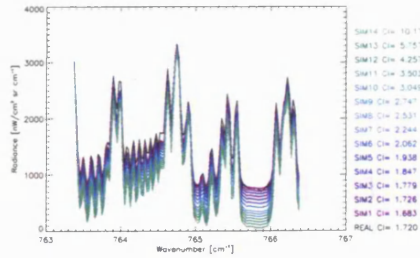
(d) H2O_0001 for 18 km cloud



(e) H2O_0022 for 18 km cloud



(f) O3_0001 for 18 km cloud



(g) O3_0021 for 18 km cloud

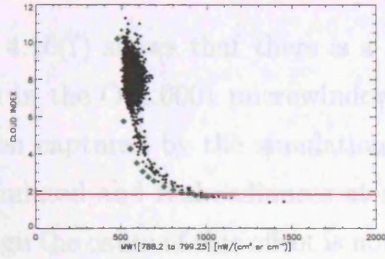
Figure 4.15: 18 km cloudy to clear sky spectra generated for the MIPAS cloud and nominal H₂O and O₃ microwindows.

real cloudy spectra used in this analysis. In the H₂O microwindows, the spectra match well, similar to the 12 km cloud case, although a noticeable offset of approximately 50 nW/(cm²sr cm⁻¹) appears in the H₂O_0001 microwindow. The simulated spectra in region O3_0021 agree well with the real data however, in the O3_0001 microwindow, the simulated spectra are smaller than the real MIPAS data by approximately 250 nW/(cm²sr cm⁻¹). It appears that the cirrus cloud at this altitude does not exhibit the same spectral response at all wavenumber regions indicating that perhaps this effect is due to a wavelength dependency of cirrus in the infrared region [Yang et al., 2001]. The inadequacy of the retrieved particle extinction to match the real MIPAS radiance in microwindow O3_0001 is investigated further below.

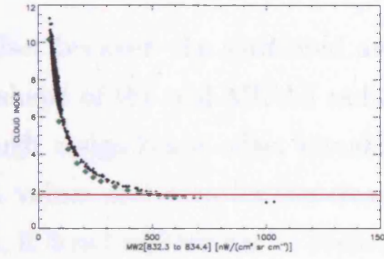
In figures 4.16(a) to 4.16(g), the mean radiance in each MIPAS microwindow of the simulated spectra is plotted against CI-A with the mean radiance of the real MIPAS data, similar to the 12 km case. The figures display that at this altitude and for the range of real MIPAS data chosen, only a small percentage of the real data falls below the 1.8 CI-A threshold and that there is a large sampling of points with CI-A > 6. The simulated radiances appear to be slightly underestimated in all microwindows except for region O3_0001, in comparison to the real MIPAS data. However, for the CI-A range investigated, the transition from cloudy to non-cloudy radiances has been fully captured by the simulated spectra. Clearly there is a significant underestimation in microwindow O3_0001, also shown in Figure 4.15(f) for which there could be three possible reasons: 1) Some problem with this particular band AB microwindow, 2) the climatological profiles of some of the absorbers used in this region are too low, or 3) the zero-scattering RFM model is not able to fully capture the radiance produced by a high altitude cloud, assumed to be formed mostly of small ice crystals, in this particular microwindow. Factors 1 and 2 can be ruled out mainly because, in the 12 km cloud case, the simulated radiances match reasonably well in this microwindow using the same climatological profiles. The evidence suggests that the effect observed this microwindow occurs only in the presence of a high altitude cloud. The possibility that some additional absorbers that may be important in the lower stratosphere such as H₂SO₄ aerosol, but are not included in the simulation of this microwindow, cannot be ruled out.

4.5.9.2 - Compensating for the O₃_0001 offset

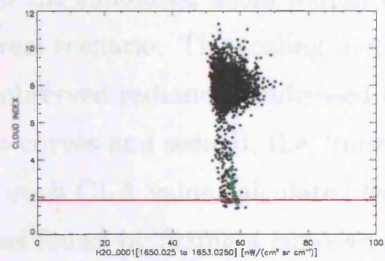
Figure 4.16 shows that there is a large offset between the mean radiance in the nominal H₂O and O₃ microwindows. The offset has been captured by the statistical approach used in the CI-A. Although the CI-A is not a perfect fit, it does capture the general trend of the data. The CI-A is a statistical fit to the data, and it is not clear from the figure whether the CI-A is a good fit to the data.



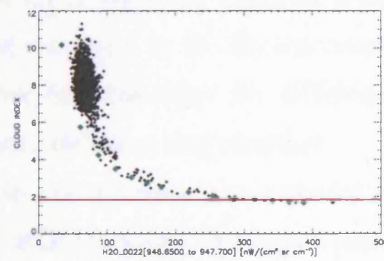
(a) CI-A vs. MW1



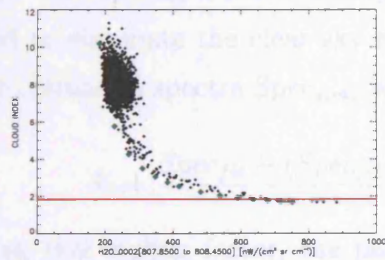
(b) CI-A vs. MW2



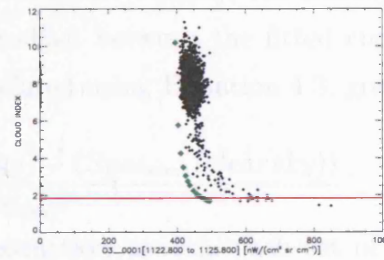
(c) CI-A vs. H2O_0001



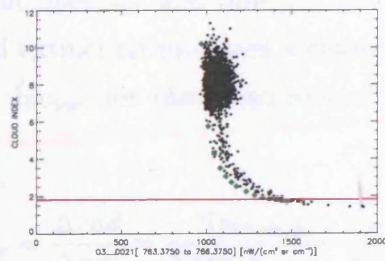
(d) CI-A vs. H2O_0022



(e) CI-A vs. H2O_0002



(f) CI-A vs. O3_0001



(g) CI-A vs. O3_0021

Figure 4.16: The mean radiance in each nominal H₂O and O₃ microwindow against the MIPAS CI-A

4.5.0.2 Compensating for the O3_0001 offset

Figure 4.16(f) shows that there is a large offset between the simulated and the real spectra in the O3_0001 microwindow. The shape of the real MIPAS radiance curve has been captured by the simulations although a significant offset remains between the simulated and real radiances at all CI-A values and even for the clear sky case. Although the cause of this offset is not known, it is not representative of cloud affected spectra used in this analysis therefore an attempt to modify the simulated spectra so that they are closer to the real MIPAS behaviour is made. A scaling method is used to scale up the simulated mean radiances at low CI-A values to be more representative of the real scenario. The scaling method that was used to fit the simulated radiance to the observed radiances addressed two issues; first the clear sky difference between the two curves and second, the “missing” cloud radiance contribution.

For each CI-A value calculated from the simulated data, the *expected* mean radiance was found by fitting a curve to the real MIPAS data. The curve that fitted the real MIPAS data was found to resemble a function that combined a linear fit through CI-A values between 10 and 4 and a hyperbolic fit through CI-A values between 4 and 1.6. The scaling method was split into two parts; firstly, the scaling factor S_1 required to eliminate the clear sky radiance offset between the fitted curve $Spec_{fit}$ and the simulated spectra $Spec_{sim1}$ was calculated using Equation 4.3, given by:

$$S_1 = \frac{Spec_{fit} - (Spec_{fit}(clearsky) - (Spec_{sim1}(clearsky)))}{Spec_{sim1}} \quad (4.3)$$

Using this scaling factor, the particle extinction used in each set of simulated spectra was multiplied by S_1 and a second set of O3_0001 spectra called $Spec_{sim2}$ and cloud extinction coefficients were obtained. The difference between radiance and extinction coefficients from $Spec_{sim1}$ and $Spec_{sim2}$ provides information about the how a change in the cloud extinction produces a change in the radiance. Using this knowledge, the Jacobian, Jac_{aer} , for these two sets of spectra was calculated using Equation 4.4:

$$Jac_{aer} = \frac{\Delta rad}{\Delta aer} = \frac{Spec_{sim2} - Spec_{sim1}}{Extinc_{sim2} - Extinc_{sim1}}, \quad (4.4)$$

where $Spec_{sim2}$ and $Extinc_{sim2}$ are the simulated spectra and the extinction of spectra 2 and $Spec_{sim1}$ and $Extinc_{sim1}$ are the simulated spectra and the extinction for spectra 1

1. As Jac_{aer} indicates how a change in cloud extinction relates to a change in cloud radiance, the expected change in extinction required between the fitted radiance and $Spec_{sim1}$, Δaer_2 was calculated rearranging Equation 4.4. Thus the cloud extinction that would be required to produce the radiance observed in the fitted spectra was found to be the sum of $Extinc_{sim2}$ and Δaer_2 . A new scaling factor was obtained from the ratio of the expected cloud extinction to the original cloud extinction. The results of this scaling process are shown in Figure 4.17. Despite the clear sky offset, the results show that the radiances are now closer to real spectra in terms of radiance, than the radiances observed in the original case. The figure shows the original spectra and the new scaled spectra (with a clear sky offset). At low CI-A values the shape of the radiance curve is not reproduced at all indicating that perhaps for clouds at this altitude, that are likely to a large number of small scattering ice crystals, a zero scattering scheme such as the RFM is not sufficient. It is clear that the extinction retrieved from the MW2 region does not produce the expected radiances in O3_0001 and that some wavelength dependent behaviour can be observed in this case. Certainly it appears that certain spectral regions respond differently to the same cloud extinctions. In the “real” case, the ratio between the original extinction coefficient and that used to scale the O3_0001 region is found to be 4.6 times greater compared to that retrieved from the MW2 region. However, this factor is still not sufficient enough to simulate the real radiance.

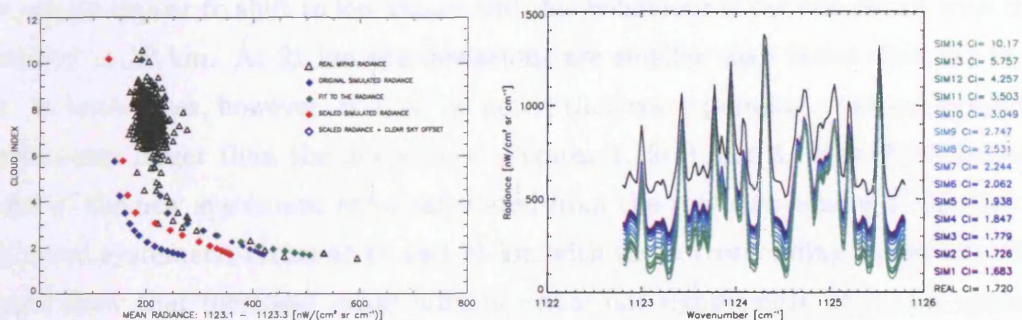


Figure 4.17: Scaling the radiance in O3_0001 at 18 km

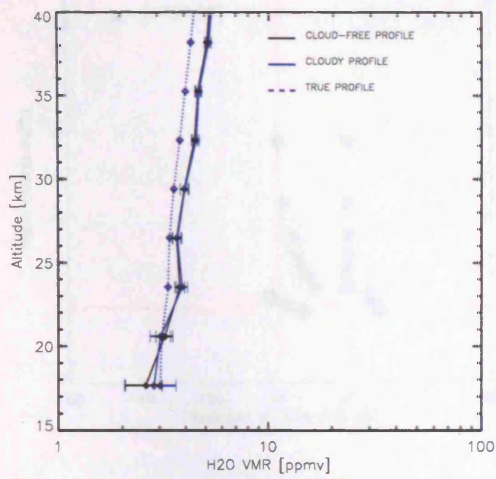
4.5.0.3 Retrieved profiles of H₂O and O₃

Figures 4.18(a) and 4.18(b) show the retrieved profiles of H₂O and O₃ with and without a cloud at 18 km. The figures show that the clear sky H₂O profile is lower compared to the true profile used in this case and that the cloudy profile is closer to the true profile. At these altitudes near the tropopause where the H₂O concentrations and the temperatures become increasingly low, the figure shows that retrievals at this altitude will be negatively biased. Comparing the cloudy profile to the clear sky shows that at 18 km, the cloud produces a positive bias in concentrations retrieved in the presence of cloud.

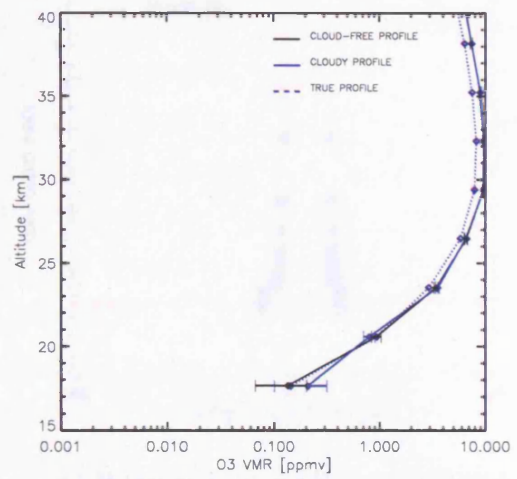
At 18 km, the clear sky O₃ compares well to the true profile used in this analysis showing that the retrieval of O₃ at 18 km performs better than the performance at 12 km. This would be expected because O₃ concentrations begin to increase above the tropopause region. Comparing the cloudy profile to the clear sky shows that a cloud at 18 km results in an increase in the retrieved concentration at this altitude. Figures 4.18(c) and 4.18(d) show all profiles retrieved with varying cloud presence.

4.5.0.4 Deviations in retrieved H₂O profiles

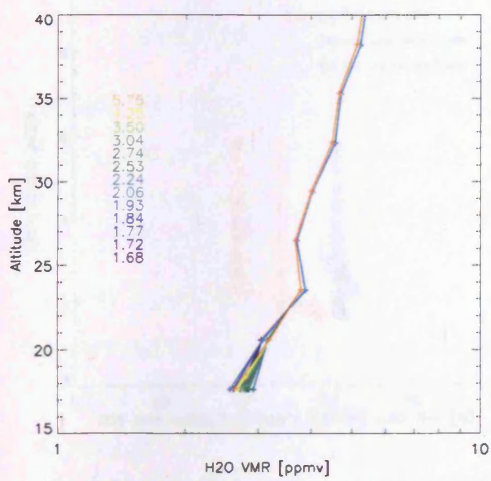
The deviations of the 18 km and 21 km cloudy concentrations from the expected clear sky concentrations are shown in figures 4.19(a) to 4.20(b). With increasing cloud influence, the deviations increase to 20% for CI-A near 2.2. Below this CI-A value, the deviations appear to shift to low values and this behaviour is not consistent with that observed at 12 km. At 21 km the deviations are smaller than those observed at 18 km. In both cases, however, it must be noted that corresponding retrieval errors are significantly larger than the deviations. Figures 4.19(c) and 4.19(d) show the estimates of the new systematic error calculated from the *root-sum-square* of the Oxford estimated systematic errors at 18 and 21 km with the corresponding deviations. The figures show that increased cloud influence does not significantly affect the systematic errors 18 and 21 km and that the effect of cloud on the corresponding random retrieval error, that increases with increased cloud influence, is more significant. The deviations at 18 km are significant smaller than those observed at 12 km.



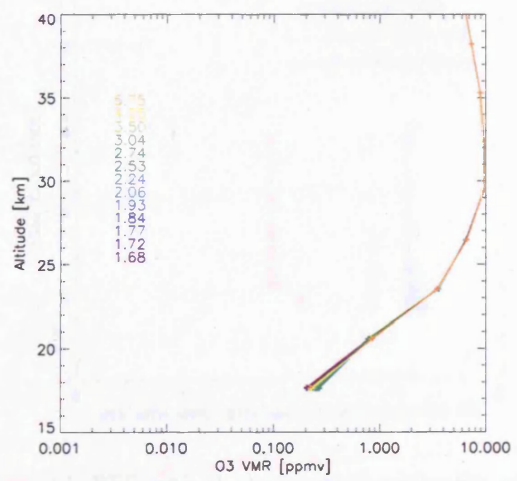
(a) Cloudy vs. clear-sky H₂O profiles



(b) Cloudy vs. clear-sky O₃ profiles



(c) All cloudy H₂O profiles

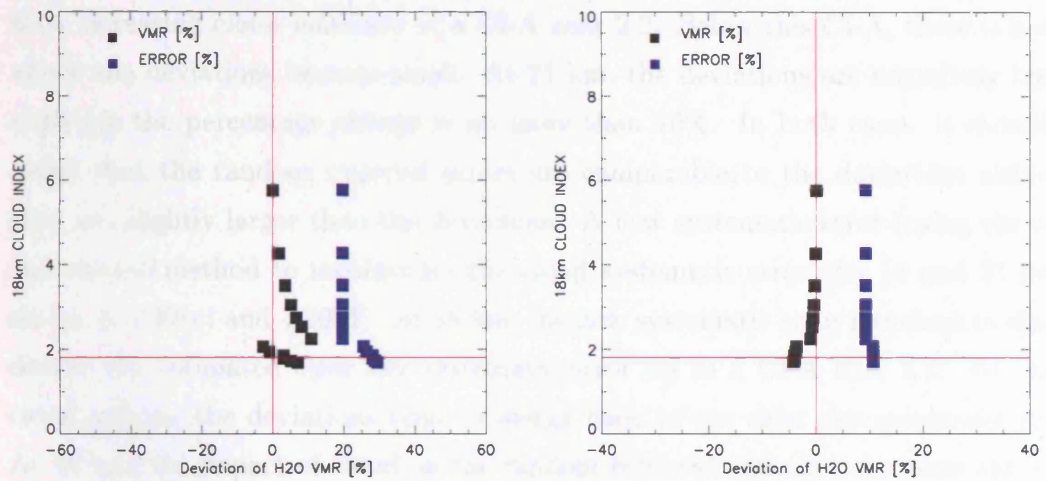


(d) All cloudy O₃ profiles

Figure 4.18: H₂O and O₃ profiles retrieved in clear sky and cloudy condition.

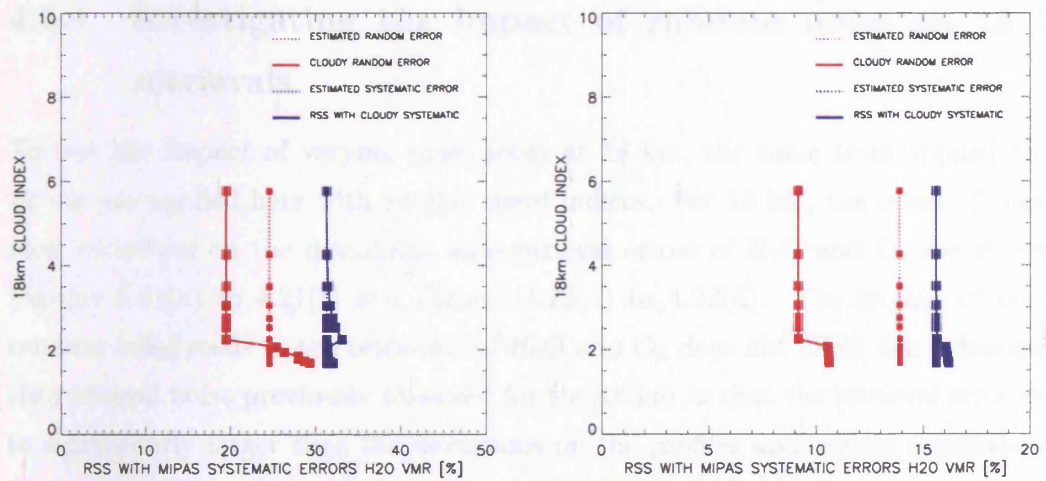
4.5.3 Deviations in retrieved H_2O profiles

Figure 4.19(a) and (b) show the deviations in H_2O concentration from the expected clear-sky concentrations. The deviations are shown as a function of the 18 km cloud index.



(a) Deviation in 18 km H_2O concentration

(b) Deviation in 21 km H_2O concentration



(c) RSS with H_2O estimated systematic errors

(d) RSS with H_2O estimated systematic errors

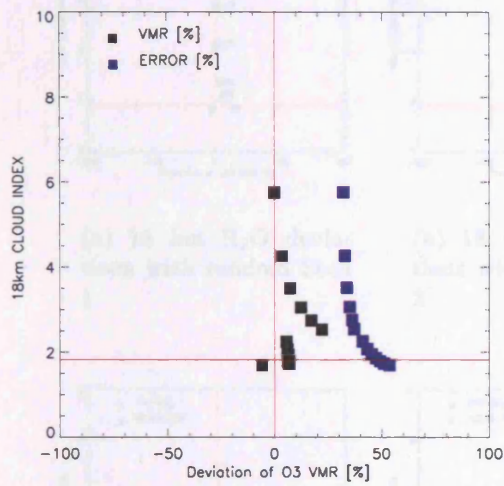
Figure 4.19: Deviations in H_2O concentrations from expected clear-sky concentrations at 18 km and 21 km and 18 and 21 km deviations *root-sum-squared* with Oxford systematic errors against 18 km CI-A.

4.5.0.5 Deviations in retrieved O₃ profiles

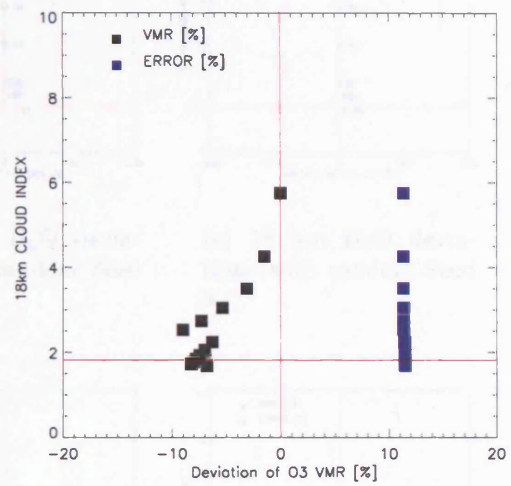
Figures 4.20(a) and 4.20(b) show the deviations in the 18 and 21 km O₃ concentrations from the expected clear sky concentrations. The deviations increase to almost 20% with increasing cloud influence at a CI-A near 2.2. Below this CI-A, there is a shift where the deviations become small. At 21 km, the deviations are negatively biased although the percentage change is no more than 10%. In both cases, it should be noted that the random retrieval errors are comparable to the deviations although they are slightly larger than the deviations. A new systematic error (using the *root-sum-square* method to incorporate the cloud systematic error) for 18 and 21 km is shown in 4.20(c) and 4.20(d). At 18 km, the new systematic error increases to almost double the estimated clear sky systematic error up to a CI-A near 2.2. For lower cloud indices, the deviations tend to merge back to the clear sky systematic error. At 18 km, the impact of cloud on the random retrieval error is to increase the error with increasing cloud influence. At both, 18 and 21 km, the O₃ deviations are just as significant as the changes in the random errors.

4.5.1 Investigating the impact of random noise on 18 km retrievals

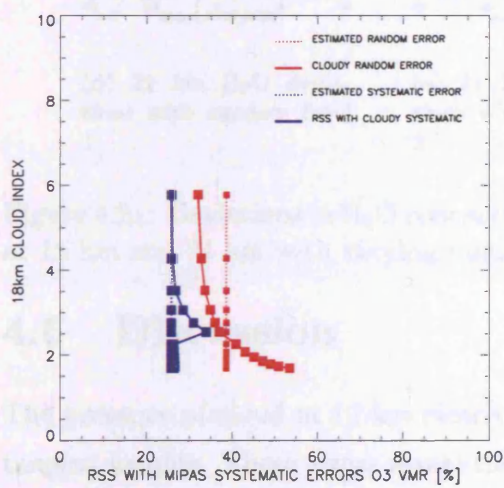
To test the impact of varying noise seeds at 18 km, the same tests applied to the 12 km are applied here with similar cloud indices. For 18 km, the effect of random seed variations on the deviations and retrieval errors of H₂O and O₃ are shown in Figures 4.21(a) to 4.21(f) and Figures 4.22(d) to 4.22(d). The impact of varying random noise seeds in the retrievals of H₂O and O₃ does not affect the behaviour of the retrieval noise previously observed for the 18 km in that the retrieval error tends to significantly larger than the deviations on the profiles and always increases with decreasing CI-A value. Similarly, the propagation of cloud effects into the 21 km retrieved concentrations tends to have an effect on the deviations of 21 km H₂O and O₃ concentrations that is smaller than the retrieval errors at this altitude.



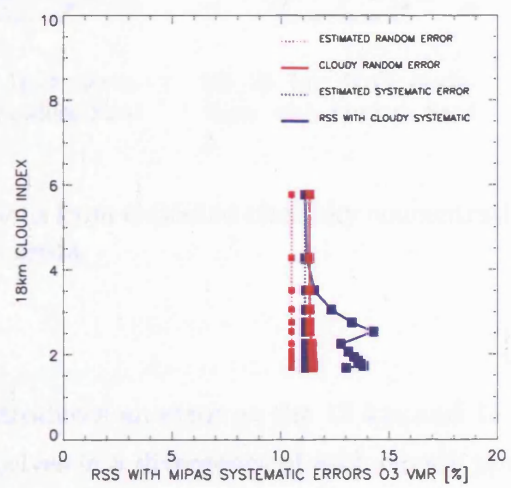
(a) Deviation in 18 km O₃ concentration



(b) Deviation in 21 km O₃ concentration

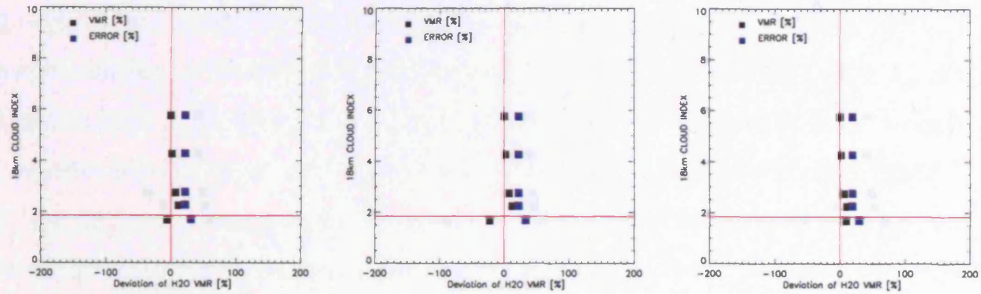


(c) RSS with 18 km O₃ estimated systematic errors



(d) RSS with 21 km O₃ estimated systematic errors

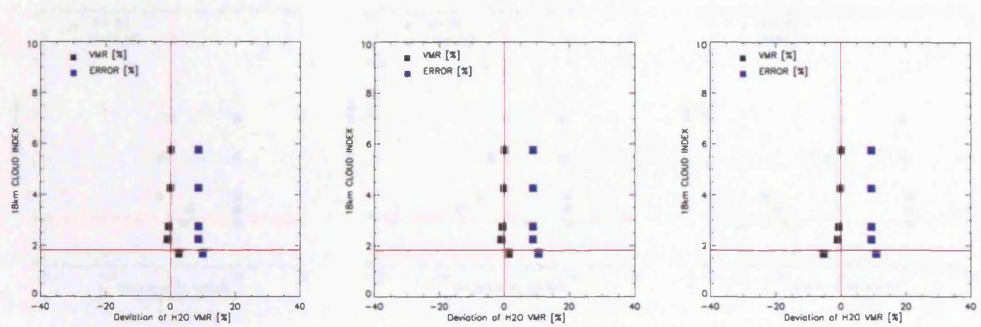
Figure 4.20: Deviations in O₃ concentrations from expected clear-sky concentrations at 18 km and 21 km. 18 and 21 km deviations *root-sum-squared* with Oxford systematic errors against 18 km CI-A.



(a) 18 km H₂O deviations with random Seed 1

(b) 18 km H₂O deviations with random Seed 2

(c) 18 km H₂O deviations with random Seed 3



(d) 21 km H₂O deviations with random Seed 1

(e) 21 km H₂O deviations with random Seed 2

(f) 21 km H₂O deviations with random Seed 3

Figure 4.21: Deviations in H₂O concentrations from expected clear-sky concentrations at 18 km and 21 km with varying random seeds.

4.6 Discussion

The presence of cloud at 12 km clearly introduces an error at the 12 km and 15 km tangent heights. These errors reveal themselves in a divergence of each cloudy profile and corresponding retrieval errors from the *expected* clear sky profile and retrieval errors. The observed deviations in concentrations are also a result of the anti-correlation between the cloudy altitude and the altitude above. This anti-correlation appears to be related to oscillations in the profiles and the observed behaviour suggests that the cloud presence introduces retrieval instabilities thereby enhancing profile oscillations. In both H₂O and O₃, the estimated standard deviation of the retrieved profiles, shown by the random retrieval error, increases with decreasing CI-A indicating that cloud

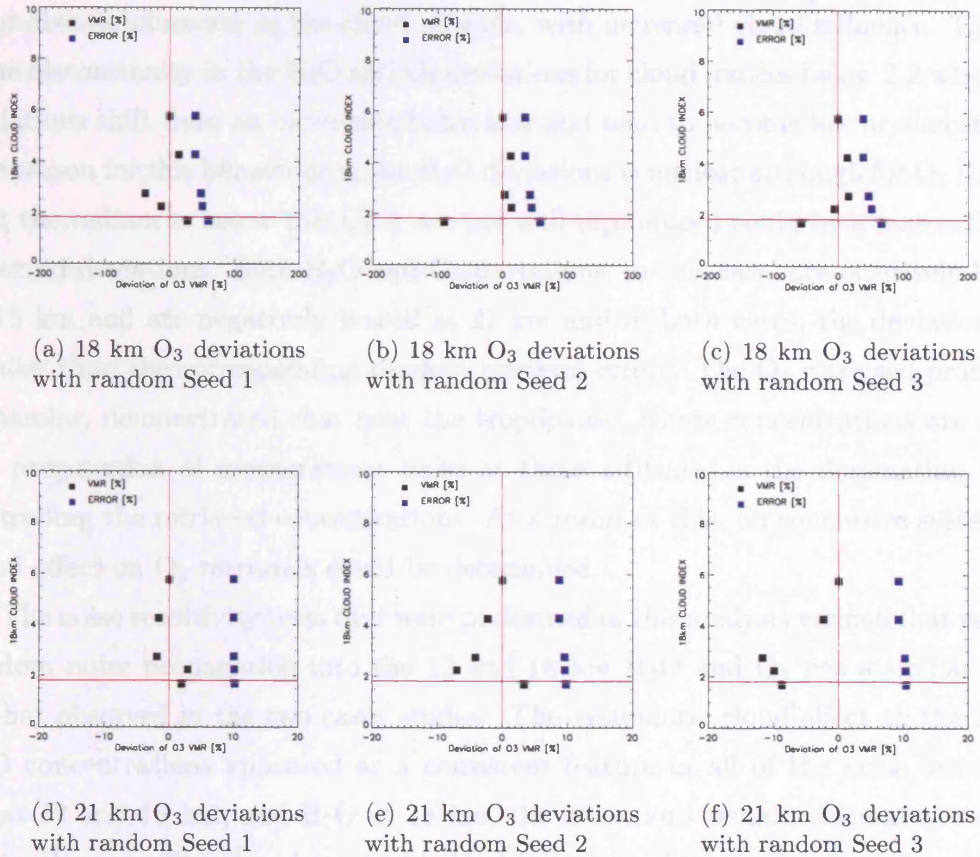


Figure 4.22: Deviations in O₃ concentrations from expected clear-sky concentrations at 18 km and 21 km with varying random seeds.

presence results in a loss of information about the target species and make the retrieval uncertainty increase (in other words, the precision decreases). The deviation behaviour indicates that the current cloud detection threshold is not high enough to remove the effects of cloud although the results also indicate that there may always be some particle influence in the retrieved profiles. A combination of low radiance signal (from temperature and O₃) and a coarse retrieval grid means that cloud-free O₃ profiles can in fact be underestimated near the tropopause. The systematic deviations for O₃ are not as significant as the effect on the random retrieval errors that tend to increase with increasing cloud influence for O₃ (and H₂O) at 12 km and 15 km.

For 18 km, the analysis have shown that a cloud at 18 km will impact the retrieved concentrations and the random retrieval error at and above 18 km. A feature that is

consistent with the observations of cloud effects at 12 km is that the random retrieval error always increases, at the cloud altitude, with increased cloud influence. There is some discontinuity in the H₂O and O₃ deviations for cloud indices below 2.2 where the deviations shift from an increasing behaviour and tend to become low or almost zero. The reason for this behaviour in the H₂O deviations is unclear although for O₃ the fact that the radiances below this CI-A are not well reproduced could be a reason for the observed deviations. Both H₂O and O₃ deviations, in this case, are positively biased at 18 km and are negatively biased at 21 km and in both cases, the deviations are smaller than the corresponding random retrieval errors. The O₃ retrieved profiles in particular, demonstrated that near the tropopause, where concentrations are small, the propagation of measurement noise at these altitudes is the dominating factor controlling the retrieved concentrations. As a result of this, no conclusive systematic cloud effect on O₃ retrievals could be determined.

The noise sensitivity tests that were performed in this analysis verified that varying random noise propagation into the 12 and 18 km H₂O and O₃ has a similar effect to that observed in the two cases studies. The systematic cloud effect on the 12 km H₂O concentrations appeared as a consistent feature in all of the noise tests. For O₃ at 12 and 18 km, and H₂O at 18 km, the deviations remained smaller than the retrieval error. The tests have highlighted that near the tropopause region, MIPAS retrievals of the H₂O and O₃ do not perform so well due to the combination of cold tropopause temperatures and the steep gradients of both gases, particularly where the concentrations become small. As well as these natural factors, the retrieved quantities are affected by larger random and systematic errors as shown by the Oxford University MIPAS errors estimates for H₂O and O₃ in this region.

4.6.1 Investigating the relationship between the CI-A and scattering

So far, the impact of scattering has been assumed to be negligible in all radiance calculations performed with the RFM. The L2 processor's OFM model also does not include scattering in its calculations of the real MIPAS spectra and in some atmospheric situations, zero scattering schemes can potentially lead to an underestimation in the radiance calculation. For clouds with a large amount of scattering (i.e. a

high single scattering albedo that is the ratio of the scattering to the extinction coefficients), radiances can be underestimated by up to 40 % and may be unable to simulate absorption features in the spectra as shown by Hopfner and Emde [2005]. Clearly such a discrepancy can affect the calculated CI-A value because the CI-A value has a distinct relationship with mean radiances in MIPAS spectra. In this section, the impact of scattering on the calculated CI-A values is investigated using the multiple scattering FM2D cloud model.

4.6.2 FM2d comparisons with RFM for thin clouds

The 12 and 18 km MIPAS spectra used in the analysis above are simulated using the FM2D model that is set up identically to the RFM (see Table 4.6). A clear sky comparison test of the two models showed that all microwindow regions (except for H₂O_0002 and H₂O_0001) compared well with negligible difference between RFM and FM2d spectral output. For the two H₂O microwindows mentioned, a difference of less than 80 nW/(cm²sr cm⁻¹) occurs with RFM higher than FM2d and it is suspected that a H₂O continuum difference in these regions may be the factor causing this difference.

In order to investigate the impact of scattering on the cloud cases investigated here, the simulations of all microwindows are repeated using FM2d with a cloud setup similar to that used in the RFM simulations, for consistency within the experiments. The primary focus of this test is to determine whether the simulations that include multiple scattering reproduce the real MIPAS spectra and the corresponding CI-A values. This can help to evaluate whether scattering influences are in fact relevant in the spectral region and clouds assumed here.

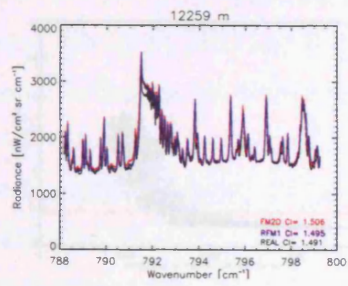
Activation of the scattering parameters in the FM2D atmosphere driver table allows scattering to be included in the radiative transfer equation for each tangent height calculation. The R_E and IWC combination used here are based on some "realistic" cloud scenarios used in Kerridge et al. [2004a] in which FM2D and other multiple scattering models were utilised for the purpose of simulating cloud radiances in the sub-millimetre and infrared spectral regions. First, a number of tests were performed to distinguish the range of radiance values in the cloud microwindows generated with different combinations of R_E and IWC. In each test, the radiance in the microwindow of interest was simulated using a certain R_E - IWC combination

and only modified by changing either the R_E and keeping IWC constant or changing IWC and keeping the R_E constant. The values of R_E tested covered a range of 5 to 98 microns and for IWC a range of 0.00171 g/kg to 1.71×10^{-5} g/kg and generally, it was found that the larger the particle size or the lower the IWC, the lower the radiances produced in the 12 micron region (in comparison to the real 12 km MIPAS cloud spectra used in section 4.4).

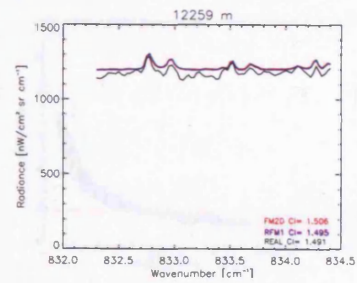
4.6.2.1 Cloud spectral simulations with FM2D

Figure 4.23 shows simulated FM2D spectra against the real MIPAS (CI-A = 1.49) and the RFM simulated spectra for the 12 km cloud used in this analysis. The cloud setup used in this case was for an R_E and IWC combination of 25 microns and 0.00016 g/kg respectively for the assumption that this is a “thin” cloud scene. The FM2D spectra shown are in good agreement with the real and RFM spectra particularly in terms of spectral line shapes and offsets. As the spectra show, the spectral lines in the real data are reproduced well as well as the cloud induced offsets in the real MIPAS data. The CI-A values calculated from MW1 and MW2 for both models and the real data are also in close agreement with each other. In order to test a range of CI-A values, the simulations for all microwindows were repeated using the same R_E values with a reduction in the IWC values. The IWC range used spanned from 0.00016 g/kg to 1.6×10^{-5} g/kg in order to produce a range of CI-A values representative of the real to clear sky conditions. The relationship between the FM2D CI-A and the FM2D spectra against the real MIPAS data and RFM spectra, for all microwindows are shown in Figure 4.24. The mean FM2D radiance in each microwindow corresponds to the yellow diamonds, the real data are the black diamonds and the green diamonds are indicative of the RFM radiances. Generally, there appears to be good agreement in all microwindows except for two H₂O microwindows which are known to have offset difference in the clear sky cases. The mean FM2D spectra follows the shape of the RFM curve well and bears a similar CI-A versus mean radiance relationship in the cloud microwindows. Similarly, the O₃ microwindows show relatively good agreement in mean radiance for the CI-A values tested with the FM2D. Again, the discrepancies in the H₂O_0002 and H₂O_0001 are visible with the RFM mean radiances consistently higher than the FM2D.

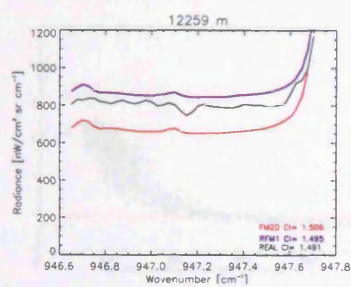
The exercise was repeated for the 18 km case and the Figures 4.25 and 4.26 show



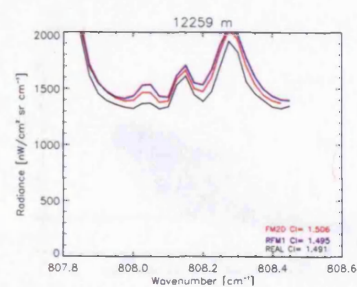
(a) MW1



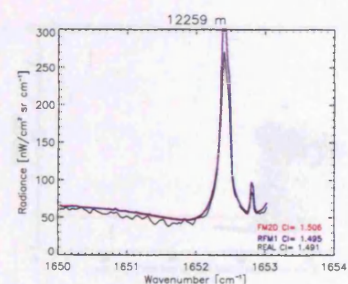
(b) MW2



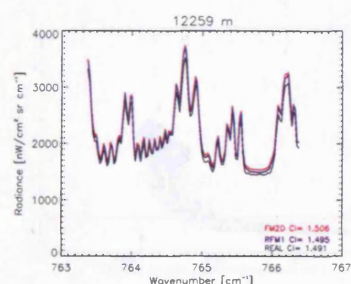
(c) H2O_0022



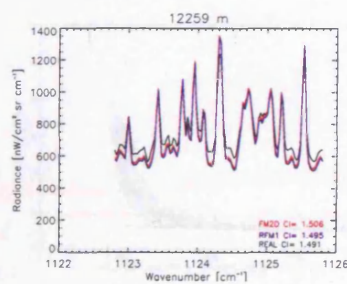
(d) H2O_0002



(e) H2O_0001

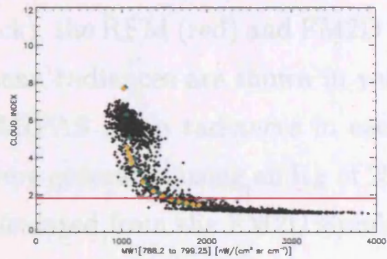


(f) O3_0021

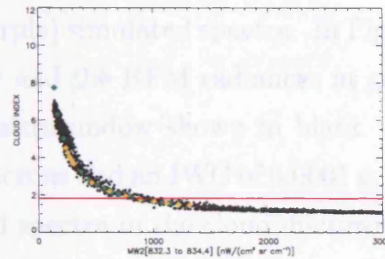


(g) O3_0001

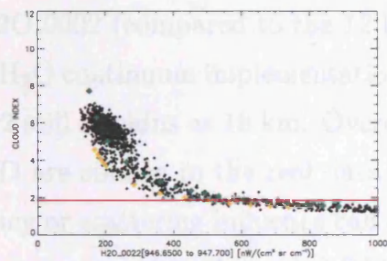
Figure 4.23: FM2D, RFM and real MIPAS spectra for the 12 km case



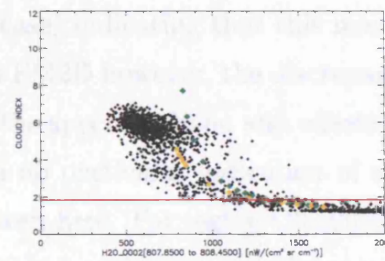
(a) CI-A vs. MW1



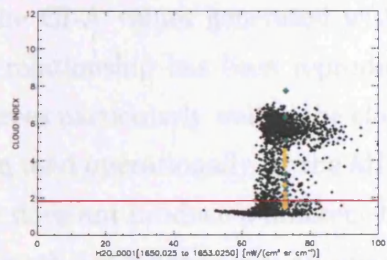
(b) CI-A vs. MW2



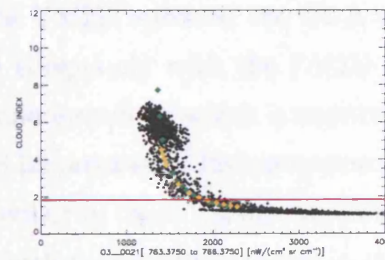
(c) CI-A vs. H2O_0022



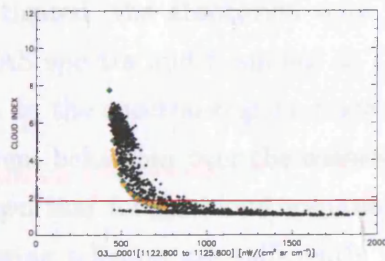
(d) CI-A vs. H2O_0002



(e) CI-A vs. H2O_0001



(f) CI-A vs. O3_0021



(g) CI-A vs. O3_0001

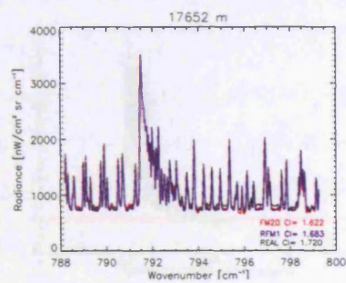
Figure 4.24: The CI-A vs mean radiance with the 12 km FM2D-generated cloud spectra plotted over the real and RFM spectra in each microwindow

the spectra and the CI-A versus mean radiance relationship are shown for real MIPAS data (black), the RFM (red) and FM2D (purple) simulated spectra. In Figure 4.26 the FM2D mean radiances are shown in yellow and the RFM radiances in green against the real MIPAS mean radiances in each microwindow shown in black. The FM2D spectra were generated using an R_E of 25 microns and an IWC of 0.0001 g/kg. The CI-A was calculated from the FM2D simulated spectra in the cloud microwindows using the methods explained earlier in this chapter. Generally, there is good agreement between the FM2D with the RFM and real 18 km MIPAS spectra used here (the same as the RFM spectra used earlier). There appears to be better agreement in region H2O_0002 (compared to the 12 km case) indicating that this may be an issue with the H₂O continuum implementation in FM2D however, the discrepancy in region H2O_0022 still remains at 18 km. Overall, the spectral shape and offsets produced in the FM2D are similar to the real data and no particular indication of a wavelength dependency or scattering influence can be seen here. For region O3_0001, the FM2D spectra are compared to the scaled RFM spectra and the results for this region show that the FM2D and scaled RFM are in good agreement, although both are still offset from the real MIPAS spectra.

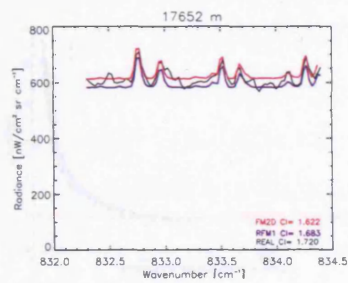
For the CI-A values generated with the FM2D spectra, the CI-A versus mean radiance relationship has been reproduced adequately with the FM2D model. The model agrees particularly well in the cloud microwindows which is important as this is the region used operationally by the MIPAS L2 processor. Incorporation of scattering processes does not produce a different behaviour in these regions nor does it indicate an wavelength dependency over all spectral regions simulated, shown in the remaining figures, for the cloud case investigated.

The results of the FM2D simulations have shown that for thin cloud cases, and for the CI-A values investigated, the absorption only model (RFM) is sufficiently reproducing the real MIPAS spectra and is similar to the spectral behaviour of the scattering model (FM2D). In the spectral regions investigated, the scattering model did not produce any different behaviour over the wavenumber ranges investigated.

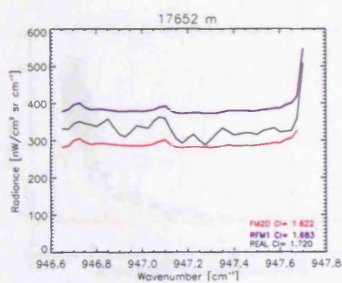
These results have shown that for the cloud scenarios investigated, the zero scattering and multiple scattering schemes are sufficiently able to reproduce real cloud spectra, for thin cloud scenarios with CI-A values ranging from 1.49 to clear sky



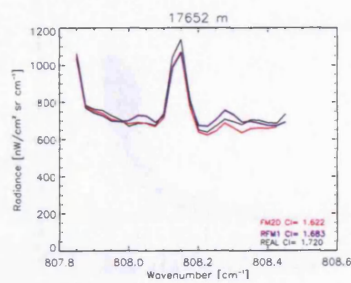
(a) MW1



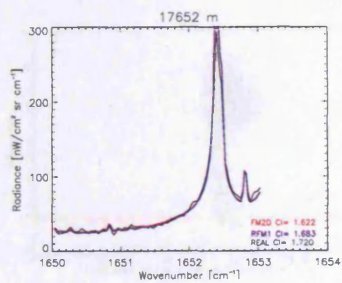
(b) MW2



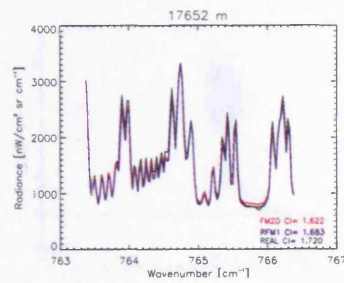
(c) H2O_002



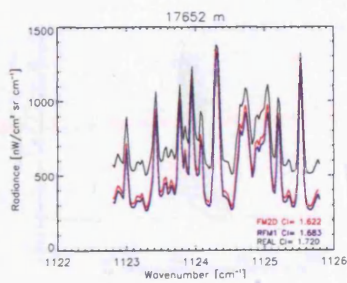
(d) H2O_0002



(e) H2O_0001

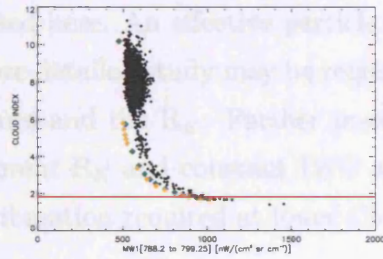


(f) O3_0021

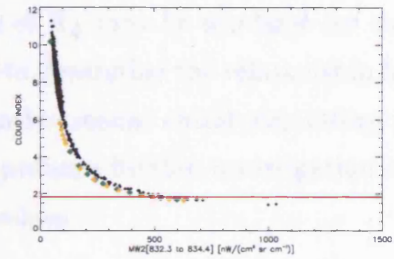


(g) O3_0001

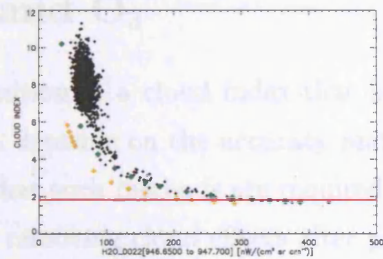
Figure 4.25: FM2D, RFM and real MIPAS spectra for the 18 km case



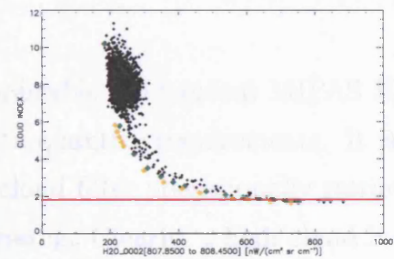
(a) CI-A vs. MW1



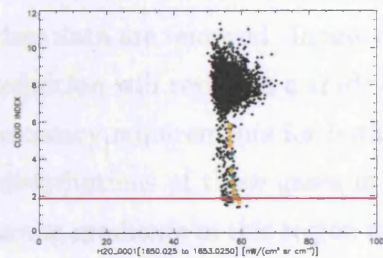
(b) CI-A vs. MW2



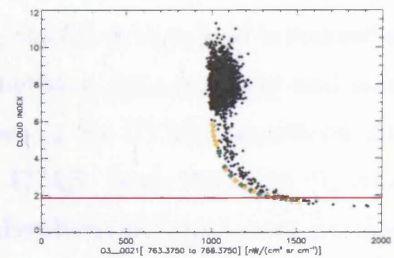
(c) CI-A vs. H2O_0022



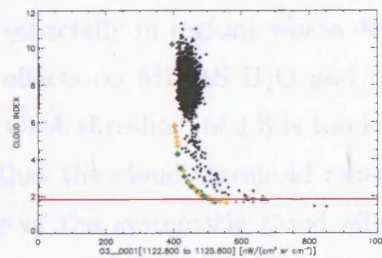
(d) CI-A vs. H2O_0002



(e) CI-A vs. H2O_0001



(f) CI-A vs. O3_0021



(g) CI-A vs. O3_0001

Figure 4.26: The CI-A vs mean radiance with the 18 km FM2D-generated cloud spectra plotted over the real and RFM spectra in each microwindow at 18 km

values. However, this does depend on the cloud situation assumed for spectral simulations used here. An effective particle size of R_E may be too large for these regions and a more detailed study may be required to determine the relationship between the CI-A values and the R_E . Further investigation would entail simulating the spectra with different R_E and constant IWC and perhaps further investigation of the R_E - IWC combination required at lower CI-A values.

4.7 Definition of a cloud index for tropical H₂O and O₃

The definition of a cloud index that is applicable for tropical MIPAS H₂O and O₃ retrievals depends on the accuracy and data quantity requirements. It is important to note that such methods are required to cloud filter operationally retrieved data as a way of removing cloud effects after processing. Clearly, a high cloud index threshold such as CI-A > 6 will screen the data efficiently although the quantity of data available for averaging will be compromised. For larger data-set requirements, such as for validation or seasonal analysis, a more relaxed CI-A threshold may be suitable meaning less data are removed. In any case, the CI-A threshold is somewhat arbitrary and its definition will result in a trade-off between data quantity and accuracy.

The accuracy requirements for both gases in the UTLS depends on the variations and the distributions of these gases in the UTLS. Both H₂O and O₃ concentrations display strong gradients in this region and the observed concentrations change rapidly over the few kilometres distance from the upper troposphere to the lower stratosphere. At 12 km, O₃ concentrations may be less than 0.5 ppmv and at 18 km, typical concentrations may be in the range of 1 - 1.5 ppmv. At 18 km, H₂O concentrations may vary by 2 or 3 ppmv especially in regions where dehydration is observed.

The analysis of cloud effects on MIPAS H₂O and O₃ performed in this chapter have demonstrated that a CI-A threshold of 1.8 is too low to remove cloud corrupted H₂O data at 12 km and that the cloud threshold must be raised. Using the cloud deviations as an indicator of the systematic cloud effect combined with the effect of cloud on the random error, the CI-A threshold can be deduced for both gases for the two cloud altitudes investigated. For H₂O and O₃ at 18 km, and O₃ at 12 km, no distinct systematic cloud effect can be deduced although the effect of cloud

presence on the random error could be used as a guide as what an alternative and more stringent cloud index be.

The analysis at 12 km showed that MIPAS H₂O at 12 km suffers a distinctive systematic effect that increases the estimated clear sky systematic error from 13.5 % to almost 40 % for a cloud of CI-A = 1.8. To reduce the impact of cloud at H₂O at 12 km, several factors can be considered as a guide to selecting a more suitable CI-A such as:

1. One approach would be to not allow the systematic error to exceed the clear sky estimated systematic error in which case a CI-A ≥ 4.0 would be a suitable threshold. This is consistent with a simultaneous study carried out by Glatthor et al. [2006] that found a CI-A threshold (≥ 4.0) is required to remove cloud corruption from MIPAS retrievals of O₃ by the IMK processor.
2. Alternatively, allowing a *minimum* 20 % systematic cloud error (indicated by the deviation of the 12 km H₂O from the expected clear sky concentration) would correspond to a CI-A of 2.2 that results in an increase in the estimated clear sky systematic error of almost 10 %.
3. Another approach would be to compare the cloud affected MIPAS systematic and random errors to the systematic and random errors of pre-existing limb sounders such as HALOE and MLS that have measured upper tropospheric H₂O (and O₃) since the MIPAS instrument has been in operation. The *allowed* error due to cloud in accuracy and precision estimates of MIPAS should ideally be similar or better than those achieved by these instruments.

4.7.1 Cloud index thresholds for H₂O and O₃ at 12 and 18 km

The error on the H₂O at 12 km can be assumed to hold for all clouds that occur below the tropopause and combining this with the effect on the altitude above, the negative bias that is induced above the cloud altitude can also be taken into account. From the results of these investigations, it can be seen that a minimum 20 % systematic error due to cloud (below the tropopause) allows a 50 % negative deviation above the cloud altitude indicating, for example, that 15 km concentrations can be negatively biased

by at least 50 %. This is clearly critical for interpretation of H₂O concentrations in the TTL and such a bias can clearly be misinterpreted as a dehydration event in this region. For the real case investigated here, a CI-A threshold of 3.5 would increase the estimated MIPAS clear sky systematic error at 12 and 15 km by less than 5 % and 10 %, respectively. With respect to the deviations in H₂O at 18 km, a minimum CI-A value of 2.5 with removal of the cloud altitude only would be suitable and would allow a cloud error of less than 10 % to occur at these levels.

As a systematic cloud effect cannot be deduced for O₃ at 12 km the effect of cloud on the random retrieval error can be used as a guide. Considering that the retrievals of O₃ below the tropopause correspond to conditions of: a) cold temperatures and b) low concentrations (of the order 0.01 ppmv) and c) an estimated clear sky random error that is already quite large, a general cloud index threshold of 2.5 would remove possibly contaminated data points and allow the random errors to remain within 20 % of the expected clear sky errors. For 18 km the effect may be suggestive of a systematic effect, however the retrieval error also tends to increase and filtering under a CI-A value of 2.5 would potentially remove cloud affected data and allow the random error to remain within 10 % of the expected clear sky case.

4.8 Summary

An analysis of the impact of clouds on MIPAS retrievals of H₂O and O₃ was carried out using profiles retrieved by the ORM from simulated cloudy spectra. The cloud spectra were chosen to be representative of upper tropospheric and high altitude clouds that are usually observed in the tropics at altitudes near 12 and 18 km, respectively. From the analysis described above, the following conclusions can be made:

1. Based on the two situations examined here, and considering the effect of a 12 and 18 km cloud on MIPAS H₂O and O₃ retrievals, the improved CI-A thresholds and the cloud errors that these indices remove are found to be: a) for a systematic bias at 12 km and 15 km of less than 10 % and 20 % respectively, a CI-A = 3.5 is most suitable for H₂O, b) for H₂O at 18 km, a CI-A threshold of 2.5 allows the systematic bias to remain within 5 % of expected clear sky, c) for O₃ at 12 and 18 km, a CI-A threshold of 2.5 is most suitable and allows the

impact on the retrieval error due to cloud presence to remain within 20 % and 10 % at 12 and 18 km respectively.

2. The effect of a cloud on the retrieval errors is important for H₂O and O₃ at 12 and 18 km, and most likely therefore at all altitudes, as the random retrieval error always increases with increased cloud influence.
3. We are limited in how we can interpret these results because the actual random retrieval error on a single profile can be larger than the systematic bias of the cloud. Therefore the total estimated error on a single profile is likely to change, certainly above the cloud threshold.
4. The analysis is further complicated by the current *clear sky* retrievals near the tropopause which often have large error and can be negatively biased (for example O₃ at 15 km). Some caution must be used in interpreting the MIPAS H₂O and O₃ retrievals near the cold tropopause.
5. The cloud effects observed at 12 km for H₂O and O₃ may be representative for all instances in which cloud occurs below the tropopause. However, clearly only one situation has been studied here.
6. The random error increases in the presence of cloud and can potentially provide an indicator of cloud presence.
7. For some cases, we can determine the systematic effect of cloud, particularly for H₂O at 12 km where a definite systematic effect is observable compared to the random errors. Cloud effects are large enough to increase the estimated clear sky total error of 15 % to 40 % for a cloud with a CI-A of 1.8.
8. The results have shown that a cloud at one altitude often affects the retrieval at the altitude above even though this is nominally “clear-sky”. This aspect may be more important at the lower altitudes as a cloud at 12 km has considerably more influence on the 15 km retrieval than does the 18 km cloud on the 21 km retrieval. The atmospheric state at the altitude above the cloud in terms of temperature and mixing ratio clearly plays a role as already noted above.
9. From the analysis of scattering effects at 12 and 18 km, the FM2D model appeared to agree well with the real MIPAS and RFM spectra and no definitive

scattering impact (i.e increased offset or occurrence of absorption lines) on the spectra in the cloud and operational microwindows used for H₂O and O₃ retrievals could be deduced. The CI-A values and mean radiances produced in these cases were comparable to those observed in the MIPAS case.

10. An apparent wavelength dependency of cloud at 18 km was observed in the RFM and FM2D spectra. However, the origin of this offset still remains unclear.
11. Analysis of the CI-A and radiance relationship, in particular the radiances observed in the real data with clear sky CI-A values, that are higher than the clear sky radiances produced by the models, indicate that there always appears to be a particle contribution in the upper troposphere.

Chapter 5

Comparisons of tropical UTLS MIPAS L2 H₂O and O₃ with HALOE and *in situ* instruments

To assess the accuracy and quality of satellite retrieved products an inter-comparison must be performed by comparison of the satellite measurements (the validation instrument) to some co-located independent measurements (the reference instrument). Ideally, for pure validation, measurements from an ideal instrument (representing the true atmosphere with no measurement error) would be perfectly coincident with the instrument to be validated. In reality, this is not possible as no such instrument exists and therefore such experiments must be performed using pre-existing satellite or *in situ* instruments. Here, the emphasis is on validation of MIPAS H₂O and O₃ in the tropical UTLS, in the sense that MIPAS profiles are compared to independent sources to examine whether variability in the operationally retrieved concentrations are comparable those observed in other instruments. The “reference” instruments are those which can provide vertical profile information between approximately 215 mb and 50 mb.

Before comparisons of any satellite product can be performed a clear strategy for the validation is required as well as knowledge of the accuracy and precision of the reference instrument. In this chapter, an inter-comparison study of MIPAS UTLS H₂O and O₃ is performed by comparing co-located MIPAS measurements with H₂O and O₃ retrieved from the HALOE instrument and *in situ* measurements of H₂O

and O₃ from radiosonde and ozone sonde measurements, respectively. So far, no explicit validation of MIPAS H₂O and O₃ measurements in the tropical UTLS has been performed as most validation studies, even those during this thesis such as the study by Cortesi et al. [2007] concentrate primarily on stratospheric concentrations. A key focus will be the comparison of MIPAS H₂O and O₃ based on the operational and cloud-filtering strategy discussed in chapter four. The following sections describe the general inter-comparison methodology adopted in this study followed by a description of each inter-comparison experiment.

Inter-comparisons of MIPAS vertical profiles with an existing, well-established measurement source will firstly, produce a level of confidence for MIPAS showing that it is a characterised source of data for scientific analysis in the tropical UTLS, and secondly, reveal any instrumental or retrieval issues that should be taken into account when using MIPAS data. For the validation of an atmospheric remote-sensing instrument, single vertical profiles of target constituents are usually compared to those obtained by other instruments Ceccherini et al. [2003]. In order to quantify the same measurement by two different instruments, a coincidence criterion is required between the two instruments in terms of time and location. For example, if two remote sensing instruments measure ozone at a particular location, the measured profiles are expected to be identical. If the two instruments have different retrieval methods and are essentially two different types of instrument (i.e. one is a spectrometer and one is a radiometer), it is important that the random and systematic error sources are considered in each comparison. The correlative instrument itself will possess some degree of systematic and precision error and these should ideally be known before the quality and comparison of MIPAS systematic and precision errors can be assessed.

5.0.1 Previous inter-comparison of MIPAS L2 H₂O and O₃ profiles

Previous validation results for MIPAS Level 2 data products were obtained as part of the second workshop of Atmospheric Chemistry Validation of ENVISAT (ACVE-2) where nominal full resolution version 4.61 MIPAS data were compared to coincident satellite, balloon and aircraft measurements. Bracher et al. [2004] compared MIPAS H₂O and O₃ profiles to two occultation instruments (HALOE and SAGE II) for the

period July 2002 to December 2002. Using a co-location criteria of 250 km and same day profiles the authors found that MIPAS H₂O and O₃ generally agreed well between 0.5 and 50 mb. Both MIPAS H₂O and O₃ were found to agree to within 15 % of the correlative instruments with MIPAS displaying a positive bias for both gases in comparison to HALOE. For MIPAS and SAGE II, the comparisons showed that MIPAS possesses a positive bias for H₂O. For both instruments the bias became larger at pressures below 50 mb (in the lower stratosphere and beyond).

Kerridge et al. [2004b] compared MIPAS Offline version 4.61 O₃ data with the several limb sounding instruments including HALOE, SAGE II, ODIN and POAM satellite. At pressures below 50 mb, MIPAS O₃ compared well with all correlative instruments. The largest discrepancies were discovered to be in the tropics and polar latitudes at pressure levels above 50 mb (i.e. low altitudes) where MIPAS O₃ displayed an increasing positive bias (up to 25 %) at 100 mb. A positive bias in MIPAS O₃ was also observed in the comparisons with ODIN-SMR O₃ where the MIPAS positive bias was observed from 30 mb and pressures above. The authors postulated that an increasing bias at pressures above 100 mb is likely to be due to differences in co-location and cirrus presence in the tropics that affect retrievals in the UTL region.

MIPAS H₂O was also compared to *in situ* balloon and aircraft instruments by Oelhaf et al. [2004] and Pappalardo et al. [2004] who found that MIPAS H₂O often possessed a low bias in comparison to lidar and aircraft measurements particularly in the lower stratosphere. However, none of the comparisons were carried out in the tropics.

During the work on this thesis, further, more comprehensive studies have been performed for MIPAS O₃ data [Cortesi et al., 2007] and indeed some of the work performed here has contributed to this study. Some co-locations of MIPAS with lidar and ECMWF assimilated data was obtained at tropical latitudes and presented in this study. Generally it was found that the variability of MIPAS data increased below 20 km and that the largest differences between MIPAS and correlative instruments was observed near the tropical tropopause. These features were attributed to undetected cirrus clouds in MIPAS O₃ data although this was not proven. These factors are those being investigated in this thesis.

5.0.2 Intercomparison methodologies

The purpose of an inter-comparison study is ideally to demonstrate that the product to be validated agrees with correlative measurements to within their known limitations. For a meaningful comparison of retrieved quantities, a particular strategy must be adopted; the observing systems should both retrieve the same target quantity, x , that have the same units, thus measurements must be in mixing ratios or concentrations. The quantity to be validated and the reference measurement must be represented on the same vertical grid, i.e. kilometres (km) or pressure (mb). If the inter-comparison is performed with a quantity represented on a finer grid than the validation measurement retrieval grid, the averaging kernels of the validation instrument should be considered. It is therefore important to compare the theoretical capabilities of the observing system in the form of a) averaging kernels (this takes into account the altitude resolution and vertical range of the retrievals) and b) the retrieval noise covariance (characterises the accuracy and precision of the retrieval) [Rodgers and Conner, 2003].

In the case where the vertical resolution of the reference profile is significantly finer than that of the validation profile, the profiles cannot be directly compared and the reference profile must be smoothed to match the vertical resolution of the validation instrument. This is the approach that is adopted here in comparing the lower resolution MIPAS data to higher resolution ozone sonde and radiosonde profiles. Making the assumption that the reference profile, in this case, is considered to be a representation of the “true” atmospheric state, the profile can be smoothed so it corresponds to the true profile as *observed* by the validation instrument. This accounts for the different retrieval grids and vertical resolution of the two instruments and as a result, the degraded or smoothed profile can be directly compared with the validation profile. In order to make this comparison, the averaging kernel matrix (AKM) of the validation instrument is to be applied to the reference profile as the AKM describes how the observing system modifies the true state of the atmosphere. In the case when two profiles from two different satellite instruments, with different vertical resolutions are inter-compared, then the averaging kernels of both instrument must be applied to the opposite instrument. However, in practise, this case could be quite complicated to interpret.

Recall from chapter two that the averaging kernel matrix \mathbf{A} is described as:

$$\mathbf{A} \equiv \left. \frac{\partial \hat{\mathbf{x}}}{\partial \mathbf{x}} \right|_{\mathbf{x}_o} \quad (5.1)$$

where $\hat{\mathbf{x}}$ is the retrieved quantity and \mathbf{x}_o is some generic atmospheric state. In a realistic case where random and systematic errors are present in the measured signal and the instrument's forward model, the retrieved profile can be connected to the true atmospheric state by:

$$\hat{\mathbf{x}} - \hat{\mathbf{x}}_o = \mathbf{A}(\mathbf{x} - \mathbf{x}_o) + \mathbf{S}_x \quad (5.2)$$

Given that \mathbf{x}_o can be represented by a high resolution measurement, and \mathbf{x}_a is the *a priori* profile used to generate the averaging kernels of the low vertical resolution satellite, then the smoothed version of the high resolution profile is \mathbf{x}_s is given by:

$$\mathbf{x}_s = \mathbf{x}_a + \mathbf{A}(\mathbf{x}_o - \mathbf{x}_a) \quad (5.3)$$

Using this equation, \mathbf{x}_s describes how the high resolution or true atmosphere would be *perceived* by the low resolution satellite [Ceccherini, 2006].

Ceccherini et al. [2003] describe a sophisticated and complex method to assess two collocated measurements by analysing the functional space of both measurements. The authors found that a comparison of two profiles within an intersection space can be a useful comparison that does not involving degrading the measurements in any way. However, this method is difficult to visualise and interpret, in which case it is more convenient to compare the retrieved quantities and their associated errors from two instruments. Some parameters that can be used more conveniently for inter-comparison of satellite retrieved quantities are listed below.

5.0.2.1 *Accuracy, bias and precision determination*

For accuracy, bias and precision determination in pairs of co-incident profiles, von Clarmann [2006] outlines several methods that can be used. For *bias* determination, a statistical ensemble of matched profiles is usually required. The mean difference between the validation and reference datasets can be compared with the statistical uncertainty so that the bias of the validation dataset (in the comparisons performed here, MIPAS is the validation instrument) can be found.

For each profile, the bias in percentage terms, is determined by calculating the relative difference (RD) of the validation to the reference measurement, calculated by:

$$RD = \left(\frac{\hat{x}_{val} - \hat{x}_{ref}}{\hat{x}_{ref}} \right) * 100 \quad (5.4)$$

The results of the individual matched profiles can be collated into mean profiles for each instruments to indicate the overall behaviour of the validation instrument against the correlative measurements. In this case, the mean relative difference (MRD) and the root-mean-square (or standard deviation) of the matched profiles is calculated using Equations 5.5 and 5.6 respectively:

$$MRD = \frac{\langle \hat{x}_{val} - \hat{x}_{ref} \rangle}{\langle \hat{x}_{ref} \rangle} * 100 \quad (5.5)$$

$$\sigma = \sqrt{\frac{(\hat{x}_{val} - \hat{x}_{ref})^2}{\langle \hat{x}_{ref} \rangle}} * 100 \quad (5.6)$$

The MRD can be compared to the combined random and the combined systematic errors of the validation and reference instruments. The total error of each instrument can be found by root-sum-square of the systematic and random errors for each instrument (Equation 5.7). Similarly the combined errors of the validation and reference instrument can be found using Equation 5.8. By comparing the standard deviation of the MRD to the combined random error, the precision of the validation instrument can be evaluated. Similarly, comparing the MRD of all profiles to the combined systematic errors will indicate a bias that is not fully accounted for by the current estimated systematic errors.

$$\varepsilon_{Total} = \sqrt{(\varepsilon_{random})^2 + (\varepsilon_{systematic})^2} \quad (5.7)$$

$$\varepsilon_{Combined} = \sqrt{(\varepsilon_{validation})^2 + (\varepsilon_{reference})^2} \quad (5.8)$$

5.1 Inter-comparison strategy

The inter-comparison studies carried out in this analysis was conducted against measurements from three independent instruments. Firstly, both MIPAS L2 H₂O and O₃

profiles were compared to the solar occultation instrument, HALOE. Secondly, MIPAS H₂O profiles were compared to *in situ* H₂O profiles obtained from radiosondes in the tropics and similarly, MIPAS O₃ profiles were compared to O₃ profiles obtained from tropical *in situ* ozone sonde measurements. These instruments were chosen so that the accuracy of MIPAS H₂O and O₃ profiles could be assessed against a retrieved product from a long-running and established satellite dataset and with measurements from *in situ* instruments that are thought to be more accurate and possess smaller errors relative to satellite measurements. All inter-comparison experiments were carried out between 30°N and 30°S from July 2002 to March 2004. This provides a total of 20 months worth of full resolution nominal MIPAS data.

5.1.1 Coincidence criteria

As shown in the sections above, the validation of concentration profiles retrieved from satellite instruments require a time and location limit within which the data from the validation and reference measurements can be matched. Clearly the criteria for the profile matches depends on the species being validated as a highly variable trace gas species would require a stringent matching criteria whereas a gas that is relatively well mixed and does not vary significantly with location would be sufficiently validated with a more relaxed criterion.

In this analysis, a baseline coincidence criteria of matching the validation measurement to the reference measurement in time and space such as ± 300 km and ± 3 hours would have been preferable particularly for consistency with the criterion used for the general validation of MIPAS L2 products [Cortesi et al., 2007; Ridolfi et al., 2007]. However, as a statistically sufficient number of profiles and often no matches in the tropics were obtained using this criterion, the baseline criteria was allowed to increase to a maximum criterion of ± 600 km and ± 6 hours.

5.1.2 Analysis of results

MIPAS profiles retrieved by the offline 4.61 and 4.62 L2 processors are compared to profiles from three correlative instruments. The time, date, latitude and longitude information for MIPAS and each correlative data-set were extracted and matching profiles existed within each coincidence criteria were selected. For each MIPAS profile

and the correlative profiles, the VMR concentration profile and corresponding random retrieval error, the time and geolocation information, and quality flags (the quality indicator and the convergence flag) were obtained. The corresponding cloud index information for the MIPAS profiles was also extracted for each MIPAS profile, if available. All analysis are performed on those MIPAS profiles that satisfy the good quality flags and that have a concentration value at all or some tangent heights between 12 km and 40 km. In L2 MIPAS data, some VMR concentrations of 1×10^{-10} ppmv are observed within the profiles. These are clearly the result of a retrieval instability although explicit causes have not been identified so far. If such values occur in any of the selected MIPAS profiles they are removed from the profile and treated as bad data.

This analysis focusses on determining the bias between MIPAS and the correlative instruments. The vertical coordinate was chosen to be pressure as the tangent altitudes of MIPAS have been reported to contain a bias (see chapter three). Before calculations are performed on the data, all profiles must be represented on a common grid therefore, all MIPAS and correlative profiles are interpolated on to a mean MIPAS pressure grid. For each profile, the RD, MRD and root-mean-square of the MRD are calculated using Equations 5.4, 5.5 and 5.6. By comparing the MRD to the combined systematic error of the two instruments, any unexplained biases in MIPAS measurements can be identified and scattering of the standard deviation of the MRD compared to the combined random error, will allow MIPAS precision to be validated.

For each MIPAS profile used in these analyses, the corresponding L2 variance covariance matrix (VCM) is obtained simultaneously from the ESC L2 data that provides the random error of the MIPAS profile (by root-mean-square of the VCM). If the precision error for each reference profile is provided in the reference dataset, it is “root-sum-squared” with the MIPAS precision to provide the estimated *combined precision*. All components of the MIPAS systematic error, except the pT covariance, are taken from climatological estimates by the University of Oxford that were shown in chapter three. It has been found that the estimated pT component in the systematic error estimates exhibited random variability when averaged over several orbits over long time-scales and contributes to the standard deviation of the profiles rather than a systematic bias as stated in Cortesi et al. [2007]. For this reason, the pT error is root-sum-squared with the L2 random error and the systematic error is calculated as

the sum of all systematic contributors minus the MIPAS pT component.

5.1.2.1 Application of MIPAS averaging kernels

For the high resolution profiles used for comparison to MIPAS products, the profiles are convolved with the MIPAS tropical averaging kernels in accordance with Equation 5.3, where the ozone sonde profile is assumed to be a true representation of the real atmosphere.

Ceccherini [2004] states that there is negligible difference in the averaging kernels calculated for the global and seasonal scenarios therefore, only MIPAS averaging kernels that correspond to a mid-latitude 45° case in April are provided by the IFAC MIPAS retrieval team. However, to be conservative the tropical MIPAS averaging kernels, that were calculated by S. Ceccherini [pers. comm], are applied to the high resolution profiles as they are more representative for MIPAS tropical measurements. Equation 5.3 is applied to the high resolution sonde profile in order to obtain x_s , that is the new low resolution sonde profile, represented at the 17 pressure levels corresponding to MIPAS tangent measurements. The new sonde profile represents what the high resolution instrument would ‘see’ if it were to observe ozone using the same vertical resolution and retrieval characteristics that MIPAS uses.

5.1.2.2 Application of tropical cloud detection schemes for MIPAS H₂O profiles

The intercomparison analysis is performed on the operational MIPAS H₂O and O₃ profiles and is then repeated using a more stringent cloud filtering scheme by raising the cloud index threshold to several representative values selected in chapter four and a “clear sky” CI-A threshold of 6.0. This test is performed to: 1) examine whether a higher CI-A threshold for tropical cloud detection reduces the systematic bias observed in H₂O profiles and 2) eliminate the profiles that are expected to have high random retrieval error due to operationally undetected cloud. Several authors, including Kerridge et al. [2004b], and more recently Cortesi et al. [2007] have postulated that the reason for increased variability of tropical MIPAS data near the tropopause may be attributed to undetected cloud effects. Note that using “extra” cloud filtering will result in a loss of data points and therefore the mean profiles will be based on less data points at some altitudes. The CI-A values chosen for extra cloud filtering are

2.5, 3.5, 4.0 and 6.0. In the following sections, some examples of collocated profiles with operational cloud filtering will be presented. This is then followed by a comparison of the operational data to the data is cloud filtered with the new schemes. The impact of removing the data above the cloud, in relation to the cloud affects on the retrieved values above the cloudy tangent height is also examined. Where indicated, cloud filtering with removal of the cloud altitude and the altitudes below is termed ‘sbl’ whereas removal of the altitude above the cloud, the altitudes, the cloud altitude and all altitudes below is termed ‘sab’.

The effect of increased cloud filtering is examined following application to the statistically larger dataset. This is done so that the impact of removing cloudy data points can be examined from a large enough dataset.

5.2 Inter-comparison of MIPAS H₂O and O₃ with HALOE

Several solar occultation instruments have made global observations in the same time period as MIPAS full resolution measurements. One such instrument is the HALOE instrument that is a solar occultation infrared radiometer using the sun as a background source when measuring atmospheric absorption. Cloud cleared H₂O and O₃ version 19 HALOE data are readily available from NASA and can be downloaded from www.haloedata.larc.nasa.gov/home/. Solar occultation measurements such as those made by HALOE are expected to be more accurate than limb emission measurements because of the high signal to noise ratio provided by the solar radiation background. As shown in chapter one, HALOE measurements have been used by several authors for analysis of the tropical UTLS [Randel et al., 2001; Gettelman et al., 2004b] and can be thought of as a source of climatological H₂O and O₃ data. The HALOE instrument was switched off in 2005, therefore establishing an intercomparison between HALOE and MIPAS might be useful for continuing the 15 year record established by HALOE.

5.2.1 The Halogen Occultation Experiment

The HALOE instrument operated from September 1991 to November 2005 on-board the Upper Atmospheric Research Satellite (UARS). The UARS is in a circular orbit, inclined at a 57° angle at 585 km above the Earth's surface. A full latitudinal range of 80°N to 80°S is achieved in one year by a slow drifting orbit that covers narrow latitude bands of a few degrees with complete 360° longitude coverage (See Figure 5.1). The instrument uses broadband (for O_3 and H_2O) and gas filter radiometry to measure the absorption of solar radiation by the atmosphere during a sunrise and sunset event in infrared channels covering a range of $2.45\ \mu\text{m}$ to $10.04\ \mu\text{m}$ [Russell et al., 1993]. During each profile measurement, the solar disk is scanned with an 8 Hz sampling rate through an instantaneous field of view (IFOV) of 1.6 km with an effective vertical resolution of 2.5 km in which data are oversampled onto a 0.3 km vertical grid. A single profile measurement is obtained by scanning the solar disk from approximately 15 km to 60 - 130 km with H_2O and O_3 measurements obtained from the $6.6\ \mu\text{m}$ and $9.6\ \mu\text{m}$ channels, respectively. Additionally, aerosol is also measured in five channels that is used in the HALOE data processing for HALOE cloud detection. The HALOE retrieval algorithm first converts the solar measurements into altitude-sorted and geolocated transmission spectra and then performs a sequential retrieval of pressure and temperature, followed by NO , O_3 , H_2O and its remaining target gases (hydrogen chloride (HCl), hydrogen fluoride (HF), methane (CH_4) and nitrogen dioxide (NO_2)). The gas correlation measurements are modelled using a line-by-line forward model called LINEPAK and the broadband measurements are modelled using a BANDPAK routine [Russell et al., 1993]. The HALOE retrieval is performed using a modified onion peeling method that assumes no *a priori* profile. The retrieval code uses National Centre for Environmental Prediction (NCEP) auxiliary data and O_3 and gas spectroscopic information from the HITRAN 1991- 1992 database [Bruhl et al., 1996].

5.2.2 Sources of errors in HALOE data

HALOE O_3 and H_2O measurements have been extensively validated, as described by [Bruhl et al., 1996] and [Harries et al., 1996] respectively, for the results obtained with version 17 of the retrieval software. Although version 19 HALOE processing has

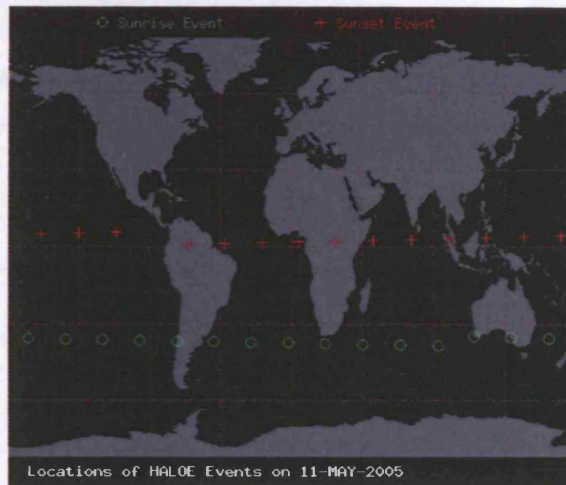


Figure 5.1: Example of HALOE sunset and sunrise events in a single UARS orbit. Source: www.haloedata.larc.nasa.gov/home/

included some changes since version 17 was released, mostly due to the addition of the cloud clearing scheme devised by [Hervig and McHugh, 1999], the estimated random and systematic errors are expected to be broadly similar for both versions of the data. The sources of error that can affect HALOE retrievals of O_3 and H_2O are discussed below. The cloud detection that has been implemented is based on characterisation of the extinction observed in four of the HALOE channels (over the $2.45 \mu\text{m}$ to $5.26 \mu\text{m}$ range), measured by gas radiometry, for the identification of cirrus clouds [Hervig and McHugh, 1999]. The aerosol extinctions that are higher than some threshold indicate cloud presence in the HALOE data.

Bruhl et al. [1996] describe the error estimation procedure and present O_3 random and systematic estimates at specific pressure levels. The errors are calculated by simulating O_3 signal profiles calculated by a forward model using realistic O_3 , H_2O , temperature and pressure and perturbing this signal profile to simulate the effects of particular error sources. Comparing these to the original unperturbed signal allows an estimate for the errors to be determined. The total error estimates for HALOE O_3 are shown in Table 5.1. For O_3 , the total (root-sum-square) error is largest (95 %) at 0.01 mb with the greatest contribution coming from instrument noise. Interference from H_2O and aerosol affect the O_3 channel adding to the random and systematic errors in HALOE O_3 profiles. The total error is found to be lowest near 0.4 to 1 mb and gradually increases at 100 mb (30 %) with the largest increase in the systematic error

component (due to deviations in the forward model and discrepancies/uncertainties in the registration altitude).

Error parameter	0.01 mb	0.04 mb	0.1 mb	0.4 mb	1 mb	4 mb	10 mb	40 mb	100 mb
Instrument noise	95	51	8	3	2	1	0	0	0
Pointing angle	0	0	1	1	2	4	5	7	11
H ₂ O random error	0	1	2	2	3	1	0	0	0
Aerosol	0	0	0	0	2	1	0	0	0
Forward model	1	2	4	4	5	5	7	9	15
Registration altitude	9	5	3	2	4	5	6	11	20
Aerosol	0	0	0	0	1	3	4	6	10
H ₂ O bias	0	0	1	1	2	2	3	5	9
Total	95	51	11	6	8	9	12	18	30

Table 5.1: Total error estimates for HALOE O₃ in percent. Source: Bruhl et al. [1996]

Harries et al. [1996] used a similar method for the estimation of HALOE H₂O error. The primary source of random errors are from detector noise and errors in the instrument pointing, in addition to tracker jitter and the measurement uncertainty caused by the presence of sunspots. The systematic error sources are mainly due to discrepancies in the forward model such as interfering gases and spectral line parameters, and other components such as pointing and response functions. In the troposphere, pointing uncertainty is the largest contributor to random error mostly in cloud or aerosol dominated regions. The total error estimates for H₂O is as high as 98 % at 0.01 mb with the highest contribution from the instrument and tracker noise (random components) and the lowest deviations are near 1 to 4 mb with total error budget as low as 14 %. H₂O retrieval uncertainties arise from aerosol and CH₄ interference which affect both random and systematic errors, however an additional systematic error source is due to O₂ continuum affecting the band intensity by 5 %. The H₂O error estimates for HALOE are shown in Table 5.2.

In general, significant systematic errors below 50 km are due to uncertainties in the retrieval algorithms forward model in particular, spectral line parameters and approximations, and the instruments altitude registration. Pointing errors increase

Error parameter	0.01 mb	0.04 mb	0.1 mb	0.4 mb	1 mb	4 mb	10 mb	40 mb	100 mb
Instrument noise	40	11	8	6	4	2	0	0	0
Tracker noise	89	23	18	14	8	5	5	13	13
CH ₄ random error	2	2	3	4	3	2	2	1	1
Aerosol	0	0	0	0	0	4	6	6	3
Forward model	1	2	4	4	5	5	7	8	10
Registration altitude	3	3	3	2	2	4	6	10	14
Aerosol	0	0	0	0	1	3	6	8	10
CH ₄	1	1	2	3	3	4	3	2	2
O ₂ continuum	0	0	0	0	1	2	4	7	10
H ₂ O line parameter	8	8	8	8	8	8	8	8	8
Total	98	27	22	19	14	14	17	24	27

Table 5.2: Total error estimates for HALOE H₂O in percent. Source: Harries et al. [1996]

rapidly in the lower stratosphere and below where cloud and aerosol interference start to dominate. At pressures above 100 mb, cloud corruption can cause large uncertainties in the HALOE H₂O and O₃ measurements. At 100 mb the fact that the instrument has difficulty in tracking the solar disk efficiently is also a large contributor to the increased uncertainty in this region. Overall, from the validation studies, HALOE version 17 H₂O and O₃ data were found to agree well within the errors associated with comparative sources. For O₃ in particular, the uncertainty of the HALOE profiles is expected to increase at lower altitudes due to the lack of signal at lower altitudes.

5.2.3 MIPAS H₂O and O₃ offline data comparisons with HALOE H₂O and O₃

Level 2 MIPAS vertical profiles of H₂O and O₃ retrieved by the version 4.61 and 4.62 offline processor are compared to HALOE Version 19 H₂O and O₃ vertical profiles. In this section, although the HALOE data in version 19 is represented on a 0.3

km vertical grid (due to over sampling), the actual vertical resolution of HALOE is between 2 and 3 km. As this vertical resolution is comparable to that of MIPAS, no MIPAS averaging kernels are applied to the HALOE profiles.

5.2.3.1 *Coincidence criteria*

All MIPAS and HALOE profiles compared in this analysis satisfy the coincidence criterion of distance and time differences between MIPAS and HALOE profile of less than 600 km and 6 hours. Ideally, the profile matching procedure should be carried out using more stringent criteria such as 300 km and 3 hour location and time difference. However, no matching profiles were obtained at tropical latitudes using this criteria hence the relaxation of the coincidence criterion. The total number of tropical matches obtained between MIPAS and HALOE for H₂O and O₃ in each criteria are presented in table 5.3.

Year	Month	No. of H ₂ O profiles	No of O ₃ profiles
2002	November	24	24
2003	February	66	70
2003	March	35	35
2003	April	11	11
2003	May	3	3
2003	June	23	23
2003	July	7	7
2003	August	87	63
2003	September	15	15
2003	October	17	17
2003	December	8	8
2004	January	22	26
2002-2004	TOTAL	328	302

Table 5.3: Number of matches found between July 2002 and March 2004 for the chosen criteria.

For an indication of the locations of the matched profiles, the latitude and longitudes of the matched profiles are shown in Figure 5.2 corresponding to criteria of 600 km and 6 hours. The red diamonds represent HALOE and blue diamonds represent MIPAS measurements. As the figure shows, within this criteria, the latitude and longitude positions of the matched profiles do not vary largely between each profile

match and a large representation of most tropical latitudes has been achieved.

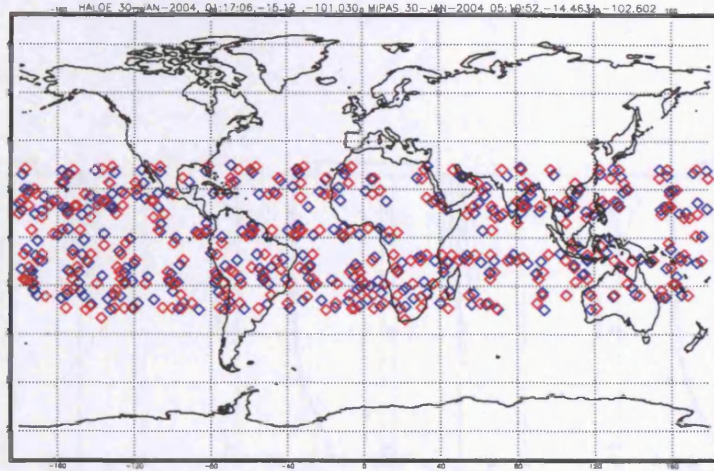


Figure 5.2: Locations of matched HALOE and MIPAS profiles

5.2.3.2 Results of H_2O inter-comparisons

Examples of collocated operationally filtered MIPAS (black) and HALOE (red) H_2O profiles are shown in Figures 5.3(a) to 5.3(f). The left hand side of each figure shows the mean profiles with the mean climatological profiles and the right hand side of each figure shows the deviation of the RD between -100% and 100% against the combined random and systematic errors. If the RD is off the scale it means that the RD between the two profiles is larger than 100%. The single MIPAS and HALOE profile matches agree relatively well around 40 mb and in the region around the TTL at pressures above 80 mb, the deviations between MIPAS and HALOE profiles tends to become larger. The combined precision and combined systematic errors are also shown to examine whether the differences between the two profiles are contained within the expected systematic and random errors of both instruments. MIPAS data often display random errors exceeding 50 % in the TTL region some of which could be related to cloud effects. In some of the of the profiles shown, the RD is well within the combined precision and systematic error estimates.

5.3.3.6. MIPAS profiles

Figure 5.3 shows examples of matched MIPAS and HALOE profiles. The MIPAS profiles are shown in the left column and the HALOE profiles in the right column. The profiles in the left column are the MIPAS profiles and the profiles in the right column are the HALOE profiles. The profiles in the left column are the MIPAS profiles and the profiles in the right column are the HALOE profiles. The profiles in the left column are the MIPAS profiles and the profiles in the right column are the HALOE profiles.

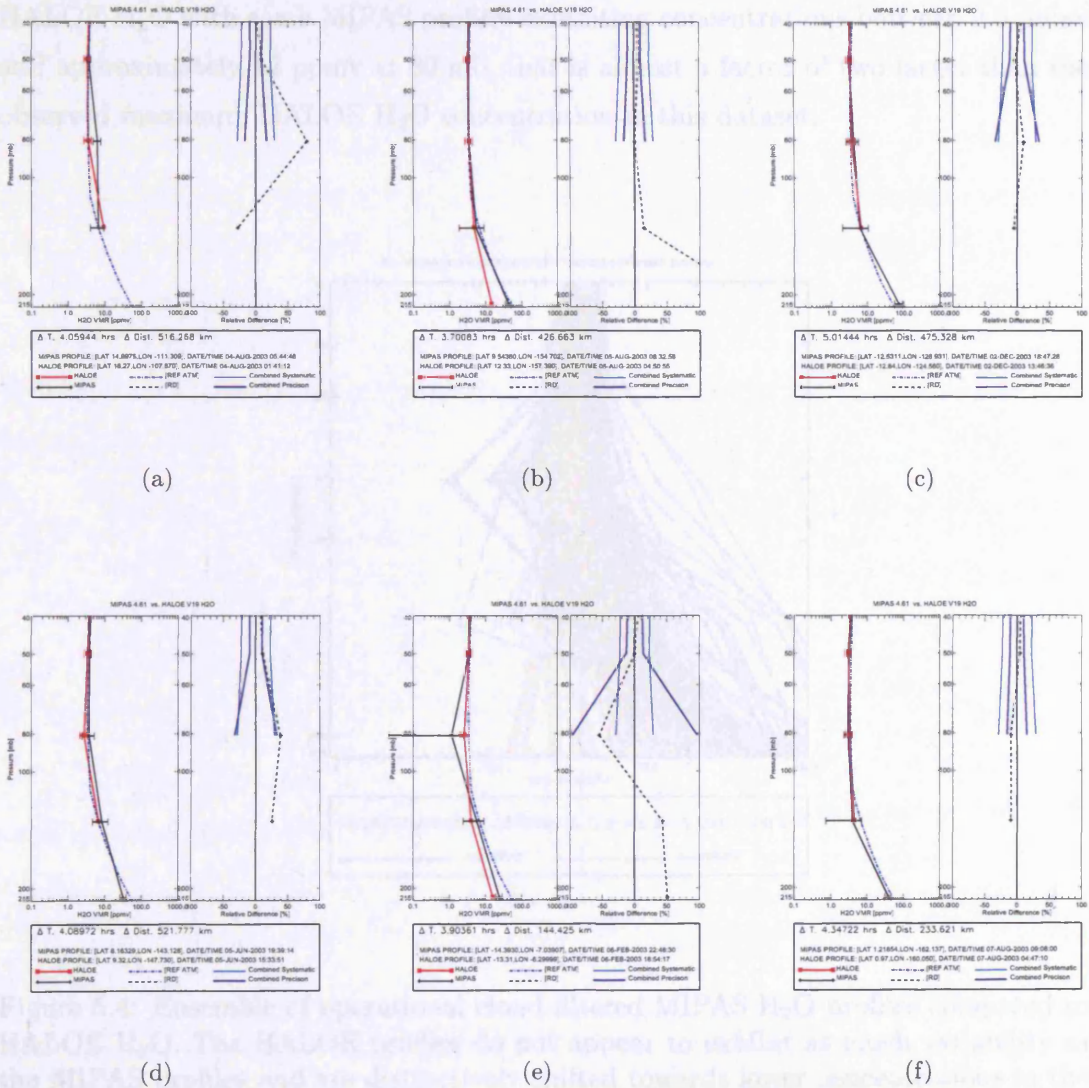


Figure 5.3: Examples of matched MIPAS and HALOE H₂O profiles. The profiles show good agreement at pressures close to 150 mb and above however there are some anomalous data points in some of the MIPAS profiles (Figure 5.3(e)) that could possibly be cloud related.

5.2.3.3 Mean profiles

Figure 5.4 displays an ensemble of all matched profiles and the mean MIPAS and HALOE profiles obtained in criteria 2. What is immediately evident from the ensemble profiles is that the MIPAS H₂O profiles appear to be much more variable than HALOE H₂O with some MIPAS profiles exhibiting concentrations between 0.5 ppmv and approximately 12 ppmv at 80 mb, that is almost a factor of two larger than the observed maximum HALOE H₂O concentration in this dataset.

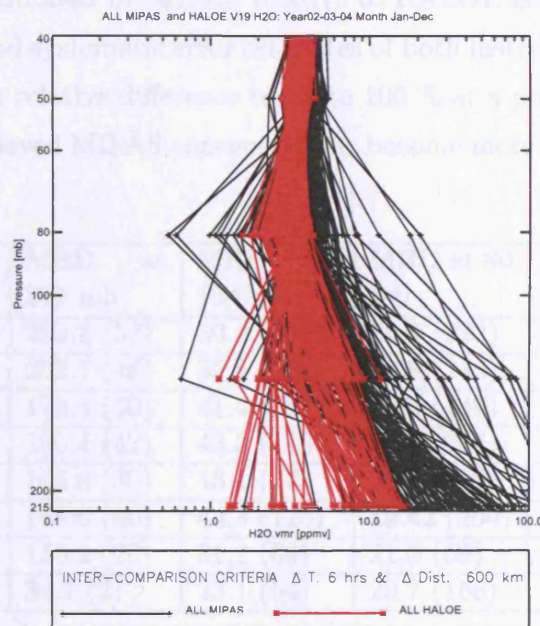


Figure 5.4: Ensemble of operational cloud filtered MIPAS H₂O profiles compared to HALOE H₂O. The HALOE profiles do not appear to exhibit as much variability as the MIPAS profiles and are distinctively shifted towards lower concentrations in the UTLS region.

In Figures 5.5(a) to 5.5(f), MIPAS versus HALOE H₂O are shown for the operational and tropical cloud filtering schemes. The details about each figure are given in the legend below each plot and the general order is that on the left-hand side of each figure, the mean equatorial climatology (dash-dot blue line) from the MIPAS standard atmosphere [Remedios et al., 2007] are plotted with the mean HALOE (red)

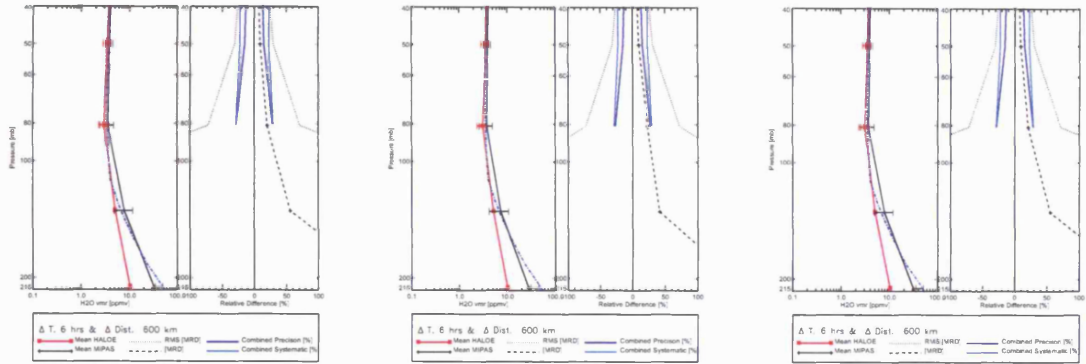
and MIPAS (black) profiles. On the right-hand-side, the MRD (between -100% and 100 %) and the standard deviation of the MRD are plotted against the combined random and systematic errors.

Comparison of the profiles show that the deviation between operational cloud filtered MIPAS and HALOE H₂O increases greatly below 50 mb with HALOE consistently lower than mean MIPAS profiles in this region and this difference continuously increasing with decreasing height. The *mean* climatological profile tends to be closer to the behaviour exhibited by the mean HALOE profiles rather than the MIPAS profiles. The MRD in comparison to the combined systematic and precision and shows that the behaviour exhibited by MIPAS relative to HALOE is consistent within the combined precision and systematic error estimates of both instruments. The standard deviation of the mean relative difference tends to 100 % at a pressure near 80 mb indicating that the retrieved MIPAS concentrations become more variable in the UTLS region.

CI-A	MRD at 211 mb	MRD at 134 mb	MRD at 80 mb	MRD at 49 mb
1.8	210.2 (52)	56.2 (134)	20.4 (223)	9.3 (288)
2.5 sbl	202.1 (48)	55.5 (128)	20.8 (214)	9.3 (285)
2.5 sab	173.4 (39)	41.4 (85)	22.6 (140)	9.7 (231)
3.5 sbl	160.4 (42)	43.3 (119)	20.6 (204)	9.4 (282)
3.5 sab	165.8 (30)	43.1 (77)	22.6 (132)	9.9 (218)
4.0 sbl	168.6 (40)	44.3 (113)	19.42 (200)	9.4 (281)
4.0 sab	155.2 (20)	31.2 (69)	21.3 (69)	9.8 (214)
6.0 sbl	34.7 (2)	23.1 (54)	20.7 (166)	9.5 (277)

Table 5.4: Summary of MIPAS and HALOE H₂O comparison with varying cloud filters. The numbers in brackets next to each MRD represents the number of points in each comparison.

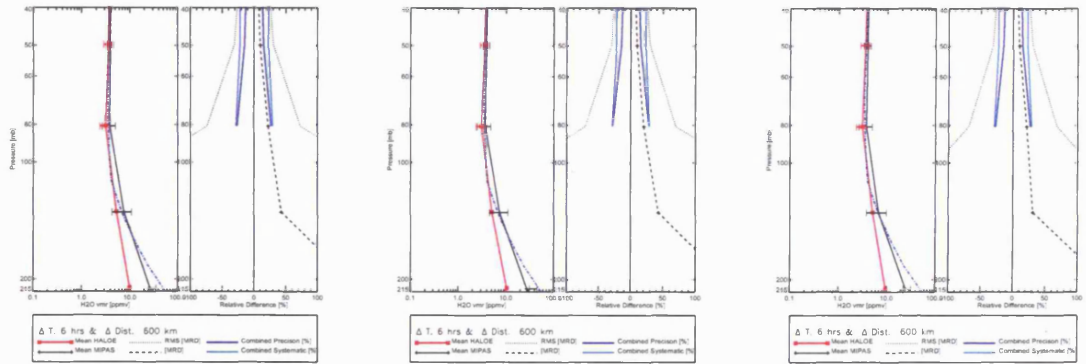
The results of each MIPAS and HALOE H₂O comparison carried out in this analysis are summarised in Table 5.4. The table shows the MRD for each cloud filtering case, at each tangent altitude between 215 and 50 mb. The number of points are highlighted in brackets with each MRD. For the varying cloud filtering schemes, the most obvious factor is that the MRD reduces quite significantly around 200 mb when using a cloud filtering scheme other than the operational filter. Certainly the MRD is smaller when using a CI-A threshold of 3.5. A threshold of 2.5 with removal of the altitude above the cloud makes a difference at approximately 134 mb and at



(a) CI-A ≤ 1.8

(b) CI-A ≤ 2.5 sab

(c) CI-A ≤ 2.5 sbl



(d) CI-A ≤ 3.5 sab

(e) CI-A ≤ 3.5 sbl

(f) CI-A ≤ 4

Figure 5.5: Mean MIPAS versus HALOE H₂O profiles with varying cloud filtering schemes. The blue dash-dot line in the left hand side of all figures is the equatorial climatological profile. In some cases, the MRD exceeds 100% (refer to Table 5.4 for values). The mean profiles in all cases agree to within 20 % and more above 80 mb and does not change with increased cloud filtering. The most significant effect of the cloud filtering is observed at lower pressures as is expected.

altitudes above there does not appear to be any change in the MRD between the two instruments. Close to 80 and 50 mb, MIPAS H₂O tends to remain within 20 % of HALOE measurements for all cloud filtering cases and within 10 % of HALOE measurements at 50 mb. These results suggest that the cloud filtering does not need to be as stringent at pressures below 80 mb but certainly, for H₂O, increasing the CI-A reduces the bias between the two instruments. The RD versus the longitude of all matched profiles are shown in Figure 5.6. Details about the figures are given in the figure caption and it can be noted here that larger RD values (the highest observed RD is more than 1000 %) are observed at lower tangent heights, as expected, and that no longitudinal dependence can be observed in this cases. Further discussion of these results, in addition to the results for MIPAS O₃ will follow in a later section.

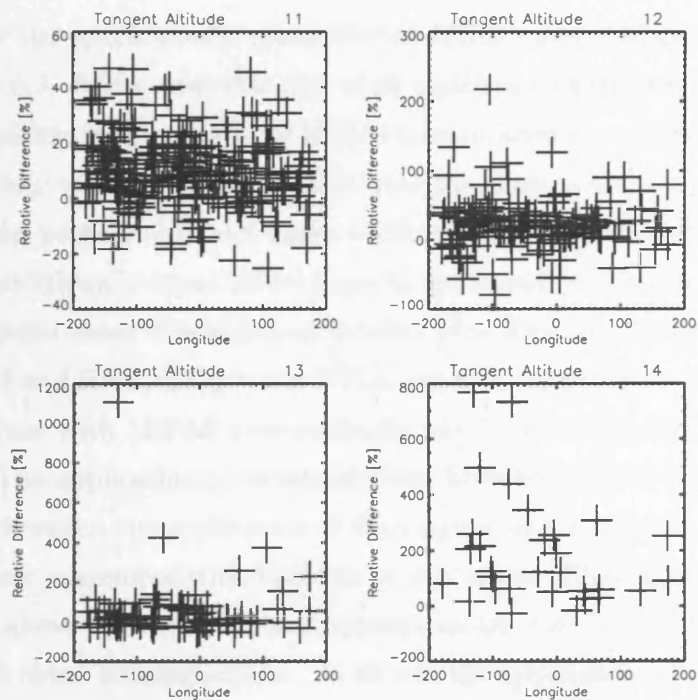


Figure 5.6: Longitudinal variation of RD between MIPAS and HALOE O₃ from tangent heights 11 (approximately 50 mb) to tangent height 14 (close to 215 mb). Note the largest differences between the two instruments occurs close to the tropopause (close to 120 mb - tangent height 13). Differences are less than 60 % at tangent height 11 (close to 50 mb) but increase at lower altitudes.

5.2.3.4 *Results of O₃ inter-comparisons*

Examples of single matched MIPAS and HALOE O₃ profiles are shown in Figures 5.7(a) to 5.7(f). The figures shown are similar to the H₂O figures with the HALOE, MIPAS and mean reference climatological profiles on the left hand side of the figure and the RD between -100% and 100% shown in each figure. If the RD is off the scale it means that the RD between the two profiles is larger than 100 %. It is clear that the profiles agree well at pressures lower than 50 mb and that more variability is observed at lower altitudes in the UTLS region. Quite often, the RD is outside of the combined precision and systematic errors.

5.2.3.5 *Mean profiles*

An ensemble of the operationally cloud filtered MIPAS and HALOE O₃ profiles are shown in figure 5.8. In the ensemble plot of all matched profiles used in this analysis, the HALOE profiles clearly tend to be shifted toward lower O₃ concentrations and do not appear to vary as much as the MIPAS concentrations at least at 80 and 146 mb.

For the mean profiles obtained under fulfilment of the chosen criteria, the operationally and additionally cloud filtered results are shown in Figures 5.9(a) to 5.9(f) with the equatorial mean climatological profile (blue dash-dot line). The difference between MIPAS and HALOE O₃ in the UTLS region is evident from the operationally cloud filtered case with MIPAS systematically larger than HALOE throughout the whole region. The application of increased cloud filtering does not reduce the bias a dramatically. However, the application of the tropical cloud filtering schemes appear to be allow closer agreement with HALOE at 216 mb for CI-A thresholds above 2.5 (with altitude above removed). There appears to be very little difference close to 135 mb for each cloud filtering scheme. At 83 mb, the application of a CI-A threshold of 2.5 appears to improve the agreement between MIPAS and HALOE but at higher altitudes, there is little impact from the cloud filtering schemes. This is expected as at such altitudes, cloud effects are expected to be negligible. The results of each MIPAS and HALOE O₃ for both criteria are summarised in Table 5.5.

The variation of RD across longitude for all matched profiles are shown in Figure 5.10. Details about the figures are given in the figure caption and here, it can be noted here that large RD values (as high as 10000 %) are observed at tangent heights 12,

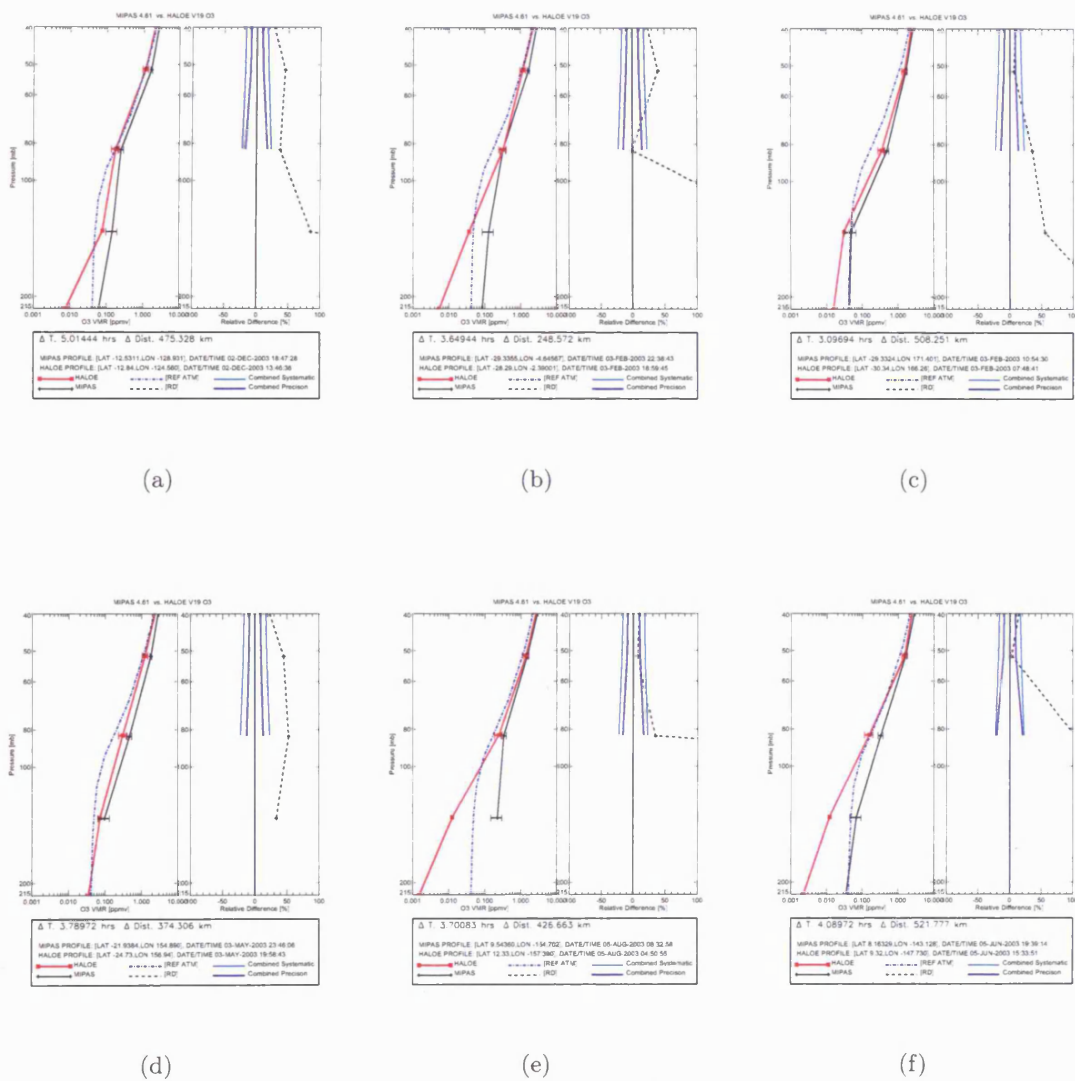


Figure 5.7: Examples of matched MIPAS and HALOE O₃ profiles. In nearly all profiles, MIPAS is consistently larger than HALOE that tends to small concentrations (<0.001 ppmv) in some cases.

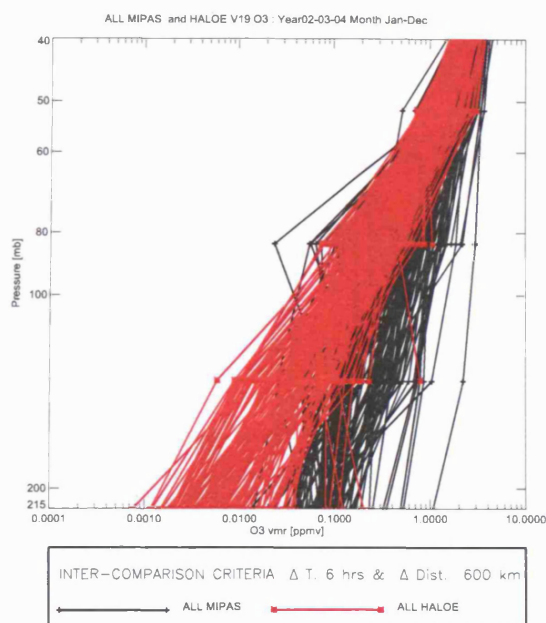
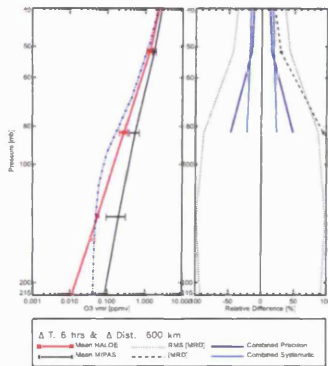


Figure 5.8: Ensemble of operationally filtered MIPAS and HALOE O₃ matched profiles. Similar to the case for H₂O the MIPAS profiles exhibit larger concentrations compared to the HALOE, consistently between 215 and 40 mb.

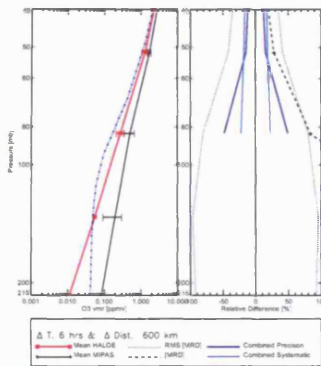
13 and 14, as expected, and that no obvious longitudinal dependence can be observed in this case, although the MIPAS data over the western longitudes that has larger RD values compared to the eastern longitudes may be perhaps be suggestive of some dependence at lower altitudes.

5.2.4 Discussion

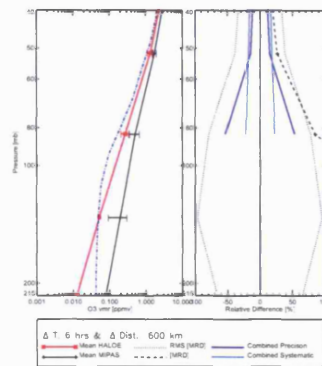
In general, operational MIPAS H₂O and O₃ are systematically larger than HALOE in the UTLS region. This is evident from all cases investigated. For H₂O, the MRD remains within the expected combined precision and systematic error estimates in the operational case above at and below 80 mb, however above 80 mb, the MRD in relation to the errors cannot be assessed as no HALOE error values are available above 100 mb. The impact of the increasing cloud filtering certainly appears to have an affect at CI-A values greater than 3.5 at lower altitudes.



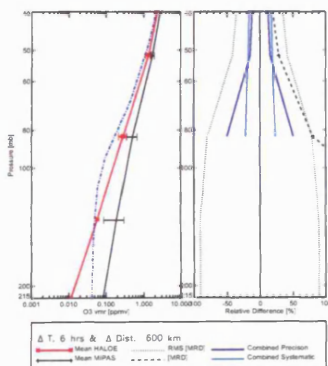
(a) CI-A ≤ 1.8



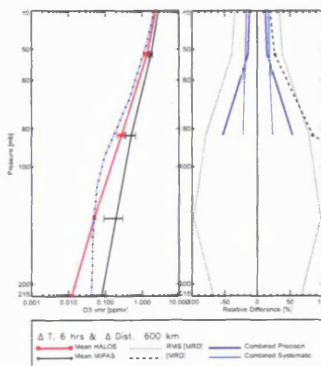
(b) CI-A ≤ 2.5 sbl



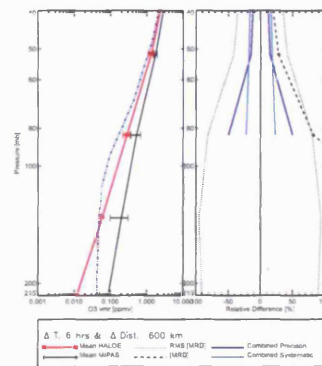
(c) CI-A ≤ 2.5 sab



(d) CI-A ≤ 3.5 sbl



(e) CI-A ≤ 3.5 sab



(f) CI-A ≤ 4.0

Figure 5.9: Mean MIPAS versus HALOE O_3 profiles with varying Dist cloud filtering schemes. In some cases, the MRD exceeds 100% (refer to Table 5.5 for values). In all cases, the MRD remains outside the combined errors even in the cases for increased cloud filtering, MIPAS is consistently larger than HALOE below 50 mb.

CI-A	MRD at 216 mb	MRD at 135 mb	MRD at 83 mb	MRD at 51
1.8	651.8 (72)	263.5 (122)	95.3 (191)	29.2 (269)
2.5 sbl	647.2 (69)	255.6 (117)	83.9 (178)	28.3 (261)
2.5 sab	501.2 (52)	267.7 (75)	85.4 (113)	26.9 (208)
3.5 sbl	634.9 (62)	223.6 (107)	80.6 (163)	28.4 (258)
3.5 sab	529.9 (37)	283.3 (67)	84.8 (109)	26.9 (198)
4.0 sbl	608.3 (57)	234.0 (101)	82.02 (157)	28.5 (256)
4.0 sab	502.6 (22)	271.5 (60)	81.2 (101)	26.7 (193)
6.0 sbl	1207 (1)	169.4 (42)	66.42 (116)	27.2 (245)

Table 5.5: Summary of MIPAS and HALOE O₃ comparison with varying cloud filters. The numbers in brackets next to each MRD represents the number of points in each comparison.

The fact that MIPAS is higher than HALOE is consistent with what may be expected from HALOE H₂O measurements as comparisons of HALOE H₂O with ATMOS and microwave instruments performed by Harries et al. [1996] showed that HALOE H₂O Version 17 tended to be lower than these correlative instruments. Similarly, comparisons of version 19 HALOE H₂O data with ACE-FTS (a solar occultation instrument) by McHugh et al. [2005] also showed that HALOE exhibits a consistently negative bias compared to ACE -FTS with HALOE H₂O relative difference increasing to 20 % below 20 km. The sources of error that dominate the HALOE H₂O measurements are the noise associated with the HALOE tracker, the registration altitude and uncertainties in the forward model. Although the MIPAS systematic and random errors are not shown here, the clear sky total error estimates at 100 mb are largest (approximately 47 %) reducing to 13 % close to 200 mb. For the MIPAS H₂O measurements, the sources of error that dominate in the tropical UTLS region are due to the assumptions of horizontal homogeneity and uncertainty in the spectral and radiometric calibration. Near 12 km, uncertainties in the spectral database also becomes a significant source of error in MIPAS H₂O retrievals. The additional tests carried out to examine the impact of removing potentially interfering thinner clouds reduces the bias in MIPAS H₂O from a CI-A threshold greater than 3.5 and through to a CI-A threshold of 6.0. However, care must be taken in interpretation of these results as an increase in CI-A reduces the available statistics. Certainly, these results appear to be consistent with the conclusions of chapter four in that MIPAS H₂O that correspond to low CI-A values (lower than 3.5 in this case) introduce a positive bias

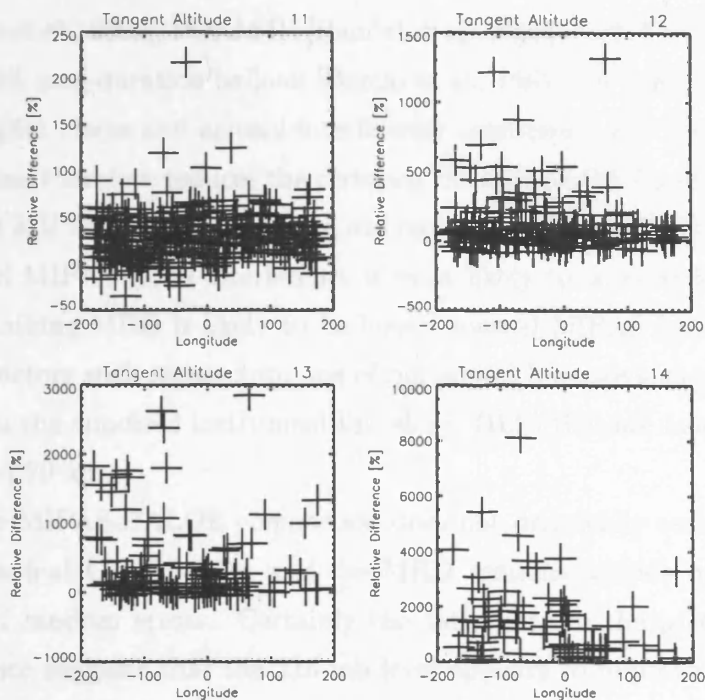


Figure 5.10: Longitudinal variation of RD between MIPAS and HALOE O₃. The largest differences occur at the lowest tangent height (approximately 200 mb) and decreases with increasing altitude

into MIPAS UTLS H₂O. However any evidence of a negative bias at altitudes above the cloud altitude is not evident in the HALOE intercomparison here.

The combined precision for MIPAS and HALOE O₃ is near 10 % below 50 mb and the MRD is consistently outside this range with a positive bias of 20 % with respect to HALOE. At 50 mb, the bias increases to 25 % and continues to increase at lower altitudes. As stated in the SPARC ozone report [Hofmann et al., 1998], the largest systematic HALOE errors arise at 16 km (around 100 mb) and below and are due to a) the HALOE pointing error that are due to uncertainties in the instruments registration altitudes and sun tracker and b) components of the HALOE forward model and the atmospheric state at the time and location of the retrieval (i.e. cloud and aerosol presence). It is assumed that a combination of these large error estimates extend to 150 mb and tend to 100 % at 300 mb. Several studies have compared updated HALOE ozone data (versions 18 and 19) with correlative satellite and *in situ* instruments that show that generally, HALOE tends to have a negative bias at all altitudes below the ozone peak particularly in comparison to SAGE II versions 5.93

and 6.0 [Morris et al., 2002], POAM III [Randel et al., 2003], ACE FTS [McHugh et al., 2005] and SAOZ long duration balloon [Borchi et al., 2005]. In regions where there is likely to be higher cirrus and aerosol interference dominance, the HALOE measured signal suffers and therefore reduces the certainty of the HALOE O₃ measurements. A combination of MIPAS systematic errors, discrepancies in the HALOE measurements and unremoved MIPAS cloud interference is most likely to account for the observed bias. The remaining MRD is likely to be biased toward MIPAS forward model and instrumental factors such as assumptions of horizontal homogenous atmosphere and uncertainties in the apodised instrument line shape (ILS) that are most significant 25 between 12 and 20 km.

For O₃, the MIPAS-HALOE comparison does not drastically reduce the positive bias in the tropical UTLS region and the MRD remains outside of the combined systematic and random errors. Certainly the variability in the precision decreases and the evidence suggests that the 216 mb level appears to improve the most when increasing the CI-A threshold. At a CI-A threshold of 6.0, the MIPAS and HALOE O₃ at 12 km is based on only one point, therefore cannot be fully representative of cloud cleared MIPAS data although it should be noted that removing points with CI-A thresholds of 2.5, 3.5 and 6.0 does tend to reduce the positive bias between the two.

5.3 Inter-comparison of MIPAS O₃ with SHADOZ O₃

Initiated by NASA in 1998, the SHADOZ program recognised the need for regular O₃ monitoring to overcome the lack of *in situ* measurements at tropical latitudes. Most measurements of the lower tropical atmosphere were reliant on short localised campaigns meaning ozone observations were occasional with large gaps in between. Such data acquisition would limit the input for climate models and are not ideal to study trace gas fields and transport processes on short timescales (i.e. days or weeks). Two particular objectives of the SHADOZ measurements are increased measurements to deduce O₃ trends over the Atlantic ocean and for the purpose of validating satellite measurements of O₃.

SHADOZ sites	Latitude [°]	Longitude [°]	Station Method	Station In- strument
Suva, Fiji	-18.13	178.4	2% KI	SPC
Pago Pago, Am. Samoa	-14.23	-170.6	2% KI	SPC
Papeete, Tahiti	-18	-149	2% KI	SPC
San Cristobel, Gala- pagos	-0.92	-89.6	2% KI	SPC
Paramaribo, Suriname	5.81	-55.2	1% KI	SPC
Natal, Brazil	-5.42	-35.38	1% KI	SPC/ENSCI
Ascension Island	-7.98	-14.42	1% KI	SPC/ENSCI
Cotonou, Benin	6.21	2.23	1% KI	SPC
Irene, South Africa	-25.25	28.22	1% KI	SPC
Nairobi, Kenya	-1.27	36.8	1% KI	ENSCI
Malindi, Kenya	-2.99	40.19	1% KI	SPC
Kuala Lumpur, Malaysia	2.73	101.7	1% KI	SPC
La Reunion	-21.06	55.48	0.5 % KI	SPC/ENSCI
Watakosek, Indonesia	-7.57	73.5	2% KI	ENSCI
Kaashidhoo, Maldives	5	73.5	2% KI	ENSCI

Table 5.6: SHADOZ measurement sites.



Figure 5.11: SHADOZ measurement sites. Source: www.croc.gsfc.nasa.gov/shadoz

5.3.0.1 Electrochemical concentration cell ozone sondes

All SHADOZ ozone sondes are flown with a standard radiosonde on a 1200 to 1500 g balloon at an operating temperature of 40°C and an operating pressure from sea level to approximately 1 mb (depending on where the balloon bursts). The Vaisala-tethered ozone sondes that are used by the SHADOZ program offer reliable and accurate ozone measurements with a high resolution and sampling rate [Thompson

et al., 2003]. A sampling rate of 1 second enables an in depth view of the TTL structure and the lower stratosphere. Although measurements are nominally made only once a week (daytime measurements) offering approximately four measurements per month at each site, the SHADOZ network offers an *in situ* reliable, continuous source of tropical ozone measurements. The principles of ECC ozone sondes were explained earlier in chapter one and the errors associated with the instruments will be discussed here.

5.3.1 ECC ozone sonde errors

The manufacturer, EN-SCI corporation specify an accuracy of $\pm 5\%$ and precision of $\pm 4\%$ at altitudes less than 10,000 ft or 3 km [Fitz, 1998]. Hofmann et al. [1998] report the results of the World Meteorological Organisation (WMO) Juelich Ozone Sonde Inter-comparison Experiment (JOSIE) that was conducted in February 1996. The study found that the best precision (5%) was achieved by all ECC type ozone sondes. All non-ECC type ozone sondes achieved a lower precision of only 10 - 15 % in the troposphere and stratosphere. Barnes and Bandy [1985] tested the accuracy and precision of the ECC sondes by constructing an experimental chamber specifically designed to simulate real-atmospheric conditions. From the response of the ozone sondes to such conditions, the authors concluded the following random and systematic estimates: For precision; 6-10% from surface to 200 mb, 5 to 6 % from 200 to 10 mb and >16 % from 10 to 6 mb, For accuracy - 8 to 14 % from 800 to 300 mb, 3 to 5 % from 300 to 50 mb, and >10 % from 50 to 6 mb. The authors also state that with the improvement of measurement techniques and instruments, these estimates are likely to improve by 2 to 3 % in the upper troposphere and lower stratosphere region. Laboratory tests were carried out more recently by Johnson et al. [2002] that found factors such as the concentration of sensing solution and the pump correction factors (PCF) that were found to vary considerably between ozone sonde measurements used in various studies. They tested ozone sondes operating with 0.5 %, 1 % and 2 % KI buffered solution with various PCF and found that often some sensing solution-PCF combinations that are standardly used in ozone sonde operations can lead to an overestimation of the ozone at 30 km by 10 - 15 % due to previously undetected side reactions in the sensing solutions.

In relation to SHADOZ, Thompson et al. [2003] compared more than 1100 SHADOZ

ozone sonde measurements for 1998 to 2000 with NASA's Total Ozone Mapping Spectrometer (TOMS) and investigated the accuracy and precision of the O₃ sensors. They estimate the SHADOZ sondes precision to be 5% and that overall the sonde total ozone measurements were within 5% of independent TOMS satellite measurements. They also state the various error sources that may cause the systematic errors such as flow rate uncertainties (1- 2% at the ground), response time of the solution and extrapolation of the profile to the top of the atmosphere (using O₃ climatologies). More recently Thompson et al. [2007] performed a detailed error analysis of the SHADOZ ozone sondes from 1998 to 2004 in laboratory chamber tests and found that certain variations in some of the ozone sonde measurements were due to differences in operation procedures in certain SHADOZ sites. They found that some artifacts in ozone sonde measurements were accounted for by variations in stations operating procedures (buffering of solutions). For example, a high O₃ bias (5-10 % higher than comparative measurements above 20 km) was detected in Nairobi station soundings that was attributed to the type of sonde and sensing solution used at this station. Measurement of sonde errors can be difficult to assess as each instrument used at each site is essentially a new instrument and different SHADOZ sites may use different measurement technique meaning that exact errors may differ slightly with each ozone sonde. At the present time, the estimated precision of ECC ozone sondes appears to vary between 5 and 7 % in the UTLS and between 3 and 5 % for accuracy. This study assumes a general sonde precision and accuracy estimated value of 5 % for precision and 5 % for accuracy from 0 to 30 km.

5.3.2 MIPAS O₃ comparisons with SHADOZ O₃

Level 2 MIPAS vertical profiles of O₃ retrieved by the version 4.61 and 4.62 offline processor are compared to SHADOZ vertical O₃ profiles. The SHADOZ profiles are compared to MIPAS profiles with and without the application of MIPAS averaging kernels. In the cases where MIPAS averaging kernels are not applied, the high resolution SHADOZ profiles are interpolated on to a mean pressure grid constructed from a mean of all MIPAS profiles.

5.3.2.1 *Coincidence criteria*

All MIPAS and SHADOZ profiles compared in this analysis satisfy the coincidence criterion of the distance and time differences between MIPAS and SHADOZ profile is less than 600 km and 6 hours.

Year	Month	Number of matched O ₃ profiles
2002	July	1
2002	August	3
2002	September	14
2002	October	4
2002	November	3
2003	February	6
2003	March	22
2003	April	13
2003	May	6
2003	June	2
2003	July	15
2003	August	12
2003	September	8
2003	October	6
2003	December	4
2004	January	11
2004	February	7
2004	March	20
2002-2004	TOTAL	157

Table 5.7: Number of matches found between July 2002 and March 2004 for the chosen criteria.

5.3.2.2 *Results of O₃ inter-comparisons*

Figures 5.13(a) to 5.13(f) show examples matched MIPAS and SHADOZ profiles without averaging kernel convolution. In some of the matched profiles, MIPAS and SHADOZ profiles appear to agree very well and within the combined precision error estimates and as shown by 5.13(c) and 5.13(f). In other cases, MIPAS does not capture the minimum O₃ values shown by the mean climatology and the SHADOZ profile. In some of the examples shown, agreement between MIPAS and SHADOZ profiles appears to better at pressure levels below 80 mb (i.e. at a higher altitude)

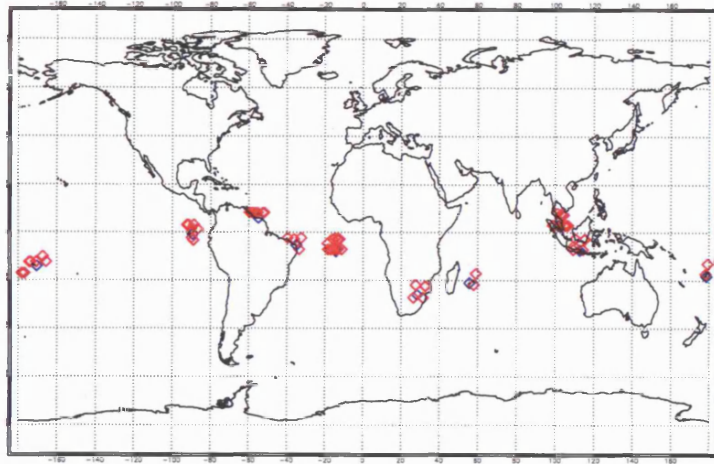


Figure 5.12: Locations of matched SHADOZ and MIPAS profiles

whereas in the region between 80 and 215 mb the MIPAS RD can exceed 100 % and agreement appears to be poor.

5.3.2.3 *Mean profiles*

The ensemble MIPAS and SHADOZ (with and without MIPAS averaging kernels) profiles are shown in Figures 5.14(a) and 5.14(b). The figures show that in comparison to the SHADOZ O_3 profiles, MIPAS O_3 appear to be more variable in the tropical UTLS region.

In Figures 5.15(a) to 5.15(f), the operationally and tropical cloud filtered results for the MIPAS - SHADOZ comparison are shown. Averaging kernels have been applied to all SHADOZ profiles in these cases. The mean MIPAS profiles display a distinct positive bias compared to the SHADOZ profiles that is most evident from 50 mb and at lower altitudes below that increases to be as large as 100% close to 100 mb. In all cases, the MIPAS profiles do not appear to capture the minimum O_3 behaviour observed in the mean SHADOZ and climatological profiles. From the increased cloud filtering, it can be seen that the difference between MIPAS and SHADOZ appears to be better at CI-A thresholds greater than 2.5 although the MRD remains outside the 100 % range (for values, see Table 5.8) but reduces when applying an 'sab' cloud filter. At pressures above 50 mb, the increased cloud filtering does not improve the MRD a great deal and MIPAS remains within 15 % of SHADOZ O_3 at this level. Using a CI-A threshold of 6 appears to reduce the variability of the MIPAS data however this

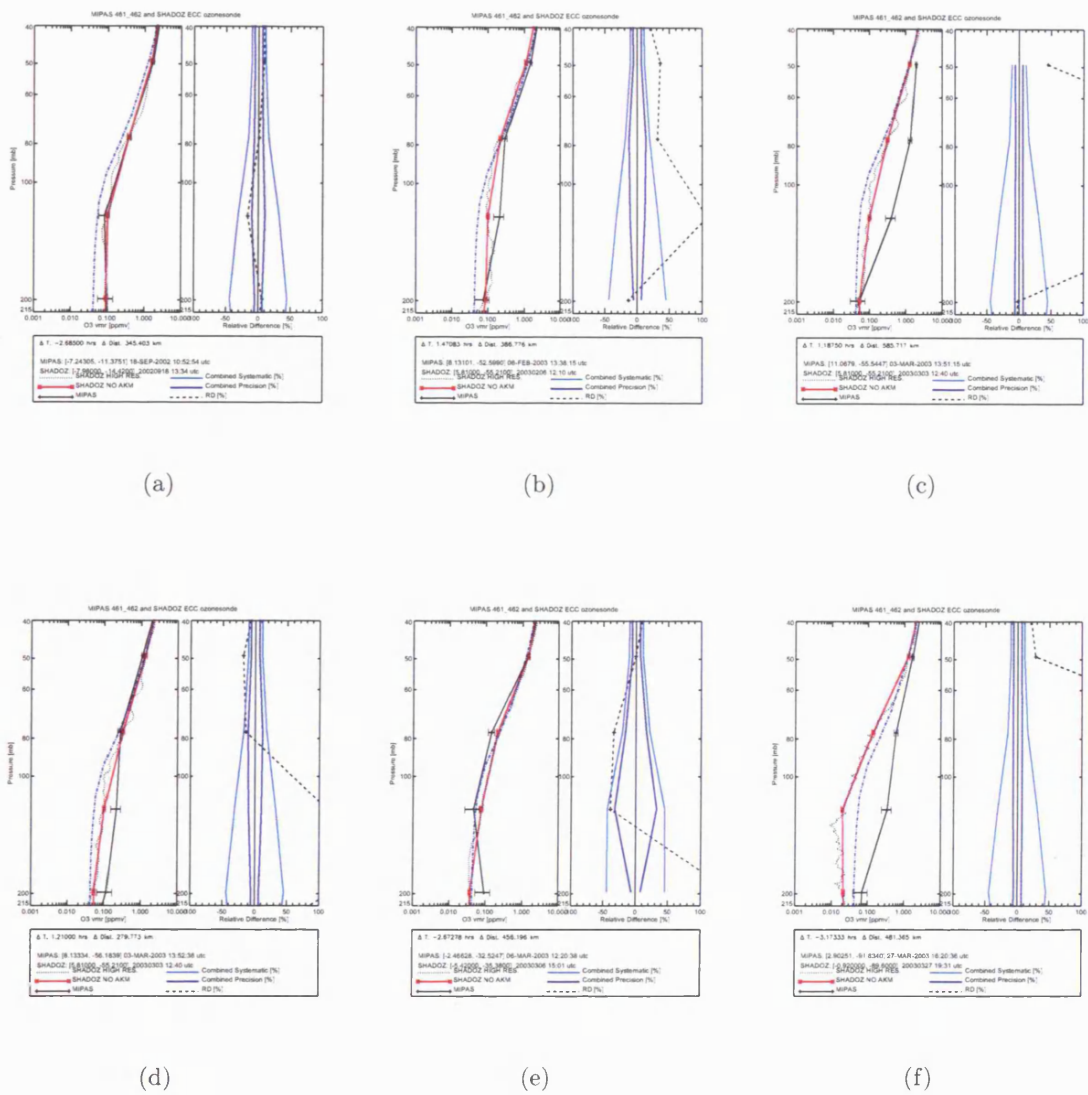
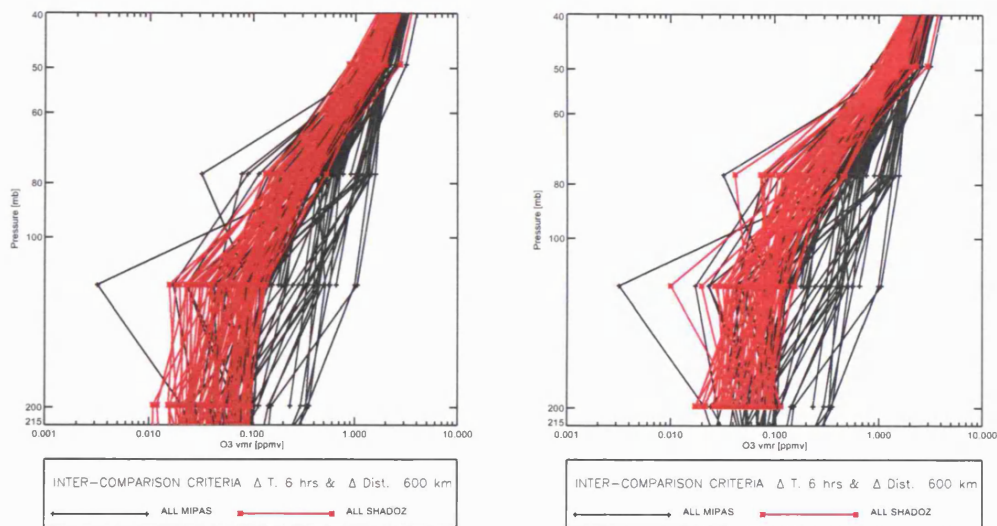


Figure 5.13: Examples of matched MIPAS and SHADOZ O₃ profiles



(a) All matched profiles

(b) All matched profiles with averaging kernels

Figure 5.14: Ensemble of operationally cloud filtered MIPAS O₃ and SHADOZ profiles with and without MIPAS averaging kernels

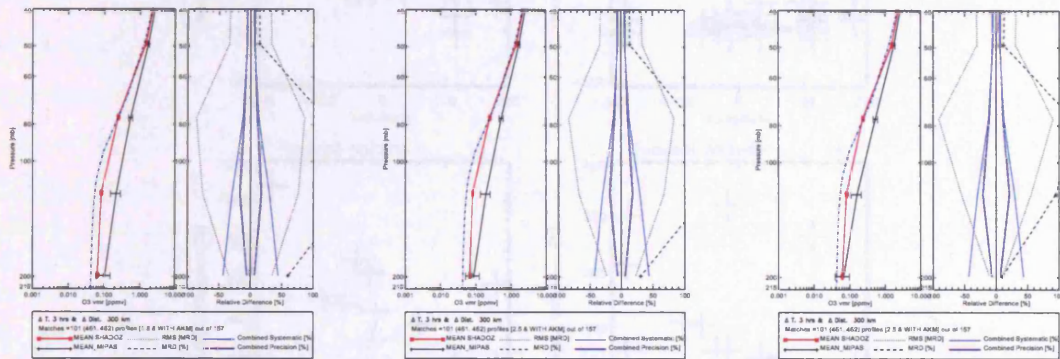
cannot be taken as a statistically significant result due to the lack of data.

The results of each MIPAS and SHADOZ O₃ with MIPAS averaging kernels for both criteria are summarised in Table 5.8.

The variation of RD across longitude for all matched profiles are shown in Figure 5.16. Details about the figures are given in the figure caption and here, it can be noted here that the RD values are largest in the region close to the tropopause (typically tangent heights 13 and 12) with RD as high as 2000%. There does appear to be some indication of a longitudinal bias with MIPAS tending to be lower than SHADOZ at longitudes east of the Greenwich meridian.

5.3.3 Discussion

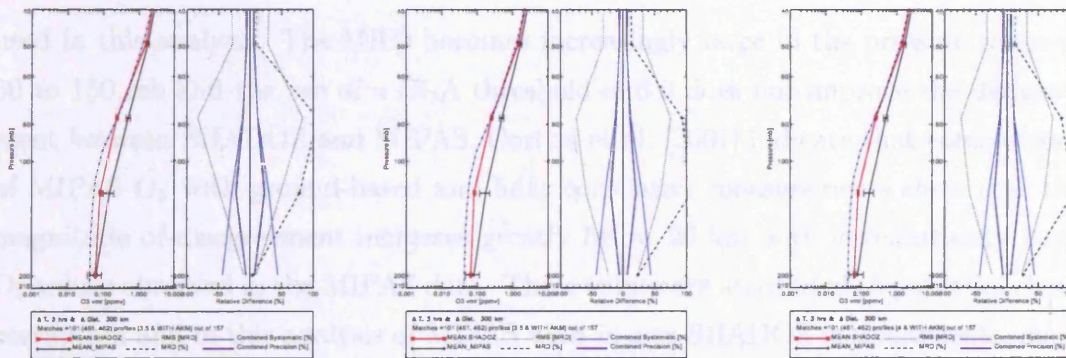
From the MIPAS-SHADOZ O₃ comparisons performed in this analysis it is found that MIPAS O₃ has a large positive bias in relation to the SHADOZ O₃ profiles



(a) CI-A ≤ 1.8

(b) CI-A ≤ 2.5 sbl

(c) CI-A ≤ 2.5 sab



(d) CI-A ≤ 3.5 sab

(e) CI-A ≤ 3.5 sbl

(f) CI-A ≤ 4

Figure 5.15: Mean MIPAS versus. SHADOZ O₃ profiles with varying cloud filtering schemes and shows that MIPAS is consistently higher than the mean SHADOZ O₃ profiles. The impact of the tropical cloud filtering appears to make the largest improvement close to 215 mb but does not improve the large differences at 150 and 80 mb between SHADOZ and MIPAS.

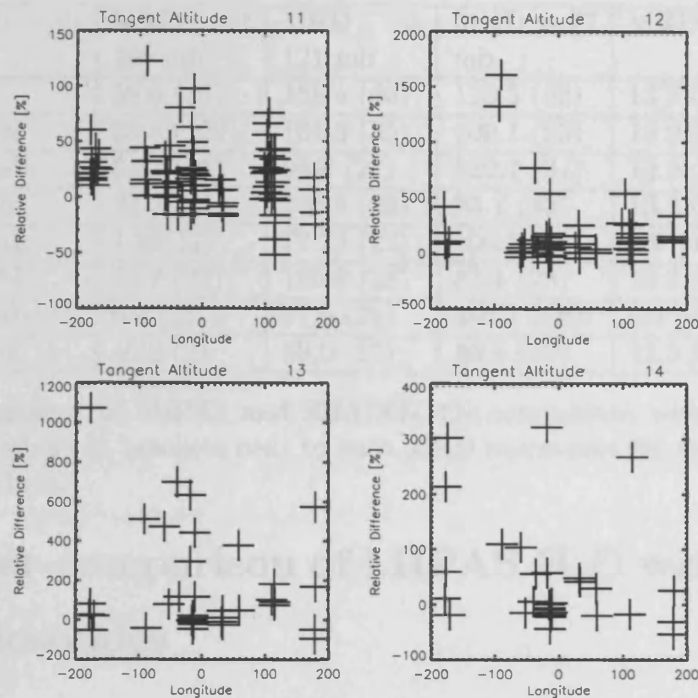


Figure 5.16: Longitudinal variation of RD between MIPAS and SHADOZ

used in this analysis. The MRD becomes increasingly large in the pressure range of 50 to 150 mb and the use of a CI-A threshold of 6.0 does not improve the disagreement between SHADOZ and MIPAS. Cortesi et al. [2007] indicate that comparisons of MIPAS O_3 with ground-based and lidar correlative measurements show that the magnitude of disagreement increases greatly below 20 km with unrealistically large O_3 values observed in the MIPAS data. These values are attributed to potential cloud corruption and in this analysis of MIPAS with *in situ* SHADOZ measurements, more stringent cloud filtering appears to improve the agreement at 198 mb, particularly in the 2.5 sab case. However, there is a marginal change to the agreement at pressures below 77 mb with increased cloud filtering. Also highlighted in the Cortesi et al. [2007] study is that the clear sky MIPAS random error estimates for the UTLS region may be underestimated and this would imply that the precision of the O_3 retrievals in these regions is in fact more uncertain than previously envisaged.

CI-A	MRD at 198 mb	MRD at 121 mb	MRD at 77 mb	MRD at 49
1.8	59.6 (34)	158.4 (40)	119.5 (62)	13.9 (87)
2.5 sbl	30.53 (29)	134.5 (35)	109.1 (53)	13.9 (87)
2.5 sab	9.33 (14)	94.8 (27)	122.7 (34)	12.0 (54)
3.5 sbl	23.2(22)	106.9 (28)	93.1 (46)	13.2 (85)
3.5 sab	4.33(12)	77.73 (22)	106.5 (29)	9.9 (49)
4.0 sbl	25.7 (21)	106.9 (28)	87.4 (28)	13.2 (85)
4.0 sab	9.9 (7)	77.5 (21)	107.1 (28)	9.4 (47)
6.0 sbl	49.2 (3)	69.0 (17)	80.8 (40)	12.5 (83)

Table 5.8: Summary of MIPAS and SHADOZ O₃ comparison with varying cloud filters. The numbers in brackets next to each MRD represents the number of points in each comparison.

5.4 Inter-comparison of MIPAS H₂O with Vaisala radiosondes

Vaisala radiosondes are regularly launched from the Rosenstiel Laboratory located on the “Explorer of the Seas” Royal Caribbean cruise ship. The ship cruises the western and eastern Caribbean sea covering a latitude and longitude range of approximately 18 °N to 30 °N and 60 °W to 80 °W. The radiosonde data archives from the Rosenstiel laboratory date from 2002 to 2005 and the number of sondes launched per year varies between 135 and 249 sondes with at least one to three sondes launched per day. The Explorer radiosonde data-set consists of each radiosonde reading, its latitude and longitude, time, date and the radiosonde serial number which is particularly important for Vaisala radiosondes measurements as it can help to distinguish the kind of sonde that is being used and allow a quantification of the possible biases that the particular sondes are known to have.

The Rosenstiel laboratories radiosonde data archive was found to be well documented as each radiosonde launch had a corresponding radiosonde type and serial number. This is important information because as explained in chapter two, atmospheric conditions, such as incident solar radiation or extremely cold temperatures can introduce biases into the radiosonde data that must be taken into account. Many of these biases depend on the radiosonde type and age. The type of Vaisala radiosondes and their age can only be identified from the serial number that contains information about the manufacture date in particular information about the day of the week and

the year is given [Miloshevich et al., 2004]. The general rule is that RS90/92 sonde serial numbers begin with a letter that correspond to particular years, for example a “V” corresponds to the year 2000. RS80 sonde serial numbers begin with a digit that correspond to the last digit of that year for instance, “9” would correspond to the year 1999. The remaining part of the serial numbers correspond to the day of the week, and month of the manufacturing data and the difference between the launch and manufacturing date corresponds to the age of the radiosonde. Other datasets that were considered for this analysis were the WMO radiosonde network that have global radiosonde measurements and therefore are more representative of the tropical latitudes. However, various kinds of radiosondes are used at each station that introduced an extra source of variability in the data and for the stations where Vaisala radiosondes are used, the radiosonde serial numbers are not documented meaning that the age of sonde cannot be deduced.

5.4.1 Sources of errors and corrections for Vaisala radiosondes

All Vaisala radiosondes are subjected to measurement uncertainty. The overall uncertainty, that includes measurement repeatability, of the humidity sensors used in Vaisala radiosondes is not expected to exceed 5% [Antikainen et al., 2002]. Often Vaisala radiosondes can exhibit substantial and unrealistically dry values in atmosphere in the atmospheric measurements. The source of this dry bias in the data was investigated further in studies such as those by Wang et al. [2002]; Miloshevich et al. [2001]; Kley et al. [2000] and several significant contributors towards this radiosonde dry bias were found to exist. Miloshevich et al. [2006] recognised the growing interest in upper tropospheric H₂O measurements particularly for satellite H₂O retrieval validation and climate-related research as well as the need for an accuracy assessment.

Wang et al. [2002] investigated the performance of RS80-A and RS80-H radiosondes in several laboratory tests to uncover the sources of errors that cause the dry bias in Vaisala radiosondes. The authors reported several sources of bias and developed correction models that could be applied to each sonde individually to obtain the ambient or true relative humidity measurement. The two most significant contributors towards the dry bias are the error due to contamination and a temperature

dependent error. A chemical contamination error was found to occur in Vaisala radiosondes packaged in Mylar foil bags where outgassing of the bag material resulted in some binding sites being occupied by non-water molecules leaving less binding sites for water molecules and thereby resulting in a dry bias. The average contamination in RS80-A and RS80-H sondes was investigated as a function of sonde age, relative humidity (RH) and temperature and increased with sonde age and was found to be smaller for RS80-A than RS80-H. Radiosondes that were produced after May 2000 are not affected by any contamination [Miloshevich et al., 2006].

The temperature dependent (TD) error is due to inaccuracies in the calibration model where the sensor response to the changing temperature particularly at cold temperatures. The temperature dependent correction can be thought of as a more accurate calibration model that is required only to improve the temperature dependent calibration model that was originally applied to the RS80-A and RS80-H sondes. The TD correction is not required for RS90 and RS92. For Vaisala RS80-H the TD correction is given by Wang et al. [2002] and the basic principle is to remove the old incorrect calibration model and apply a more accurate model. The correction factor that is dependent on temperature was found to be around 1.1 at a temperature of -30°C and 2.5 at temperatures of -70°C .

Another source of significant error that was found to affect all Vaisala radiosondes was a timelag (TL) error that occurs due to a non-zero time response of the humidity sensor to changes in the ambient humidity fields that affect the sensor's ability to maintain equilibrium with the environment [Miloshevich et al., 2004]. In order to correct this error, TL correction was developed by Miloshevich et al. [2004] to correct the error due to sensor's non-zero response time as a function of RH, temperature and time. The time constant (τ_s) describes the time response of the sensor, or the time taken for the sensor to respond to 63 % of an instantaneous change in the ambient RH. The TL correction essentially calculates what the true RH should be using the measured RH and temperature with laboratory measured time constants. The TL correction is more like a procedure than a simple correction equation that constitutes four steps: 1) A "skeleton" profile of the measured RH and the temperature profile is made so that a single RH value represents each constant RH period, 2) The skeleton profile is smoothed within some allowed smoothing tolerance to ensure that it retains the shape of the original RH curve, 3) The TL correction is applied to the smoothed

skeleton profile and finally 4) The smoothing and TL correction are performed a number of times and simultaneously regenerating the original RH and temperature profiles by adding points to the profiles after each TL correction step.

The TL error is not a bias as such, but simply recovers structures from the atmospheres that have been smoothed by the TL. By testing the impact of the TL correction on several radiosonde datasets, Miloshevich et al. [2004] found that the TL correction tends to change the humidity profile by making it wetter in the upper troposphere and drier in the lower stratosphere. The RH values near the troposphere were found to increase by as much as 10 % RH after the correction.

The SPARC water vapour assessment [Kley et al., 2000] reported that for *in situ* H₂O measurements, Humicap sondes performed better than carbon hygrometers that were found to have larger errors in the UT. Applications of the key corrections were reported to reduce the bias in the Vaisala measurements and therefore potentially make them suitable for climate analysis. Recently, Miloshevich et al. [2006] performed an extensive evaluation of the performance of six well known radiosondes including Vaisala RS80-H, RS90, and the RS92 against a reference instrument of known accuracy called the Cryogenic Frostpoint Hygrometer (CHF). They found that application of the TL correction reduced the variability observed in the Vaisala radiosonde upper tropospheric measurements. Miloshevich et al. [2006] deduced that Vaisala RS90 and RS92 radiosondes could be suitable validation of upper tropospheric H₂O measurements from the AIRS instrument on board the AQUA satellite.

5.4.1.1 *Coincidence criteria*

The coincidence criterion used for the SHADOZ comparisons were applied to the MIPAS and VAISALA data. Ideally an extremely stringent coincidence criteria should be used such as 100 km and 1 hour difference between the MIPAS and Vaisala launches as relative humidity can vary greatly in the upper troposphere. Unfortunately, no matches were obtained using this criteria and therefore the baseline criterion had to be increased. The number of profiles obtained in the larger criterion and the locations of the matched profiles are shown in Table 5.9 and Figure 5.17.

Year	Month	Number of matched H ₂ O profiles
2002	July	7
2002	August	1
2002	September	5
2002	October	1
2002	November	3
2003	February	12
2003	March	9
2003	April	2
2003	May	9
2003	June	3
2003	July	8
2003	August	8
2003	September	7
2003	October	8
2003	November	9
2003	December	9
2004	January	4
2002-2004	TOTAL	98

Table 5.9: Number of matches found between July 2002 and March 2004 for the chosen criteria.

5.4.1.2 *Application of Vaisala corrections*

In this analysis, H₂O measurements obtained from RS80-H and RS90 radiosondes were compared to coincident MIPAS H₂O profiles. The radiosonde profiles were compared with and without corrections and where applicable, appropriate corrections were applied to the radiosonde measurements. As the radiosonde measurements are in given in terms of RH, they must be converted to a form that is suitable for comparison to MIPAS H₂O profiles. The RH is calculated as the ratio of the vapour pressure, e , to the saturation vapour pressure e_s for which many different formulas for the calculation e_s exist [Vomel, 2005]. Vaisala radiosondes use the Wexler definition for the formulation of H₂O vapour pressure and to keep consistency in the calculations used here, the Wexler formula is also used for the calculation of H₂O volume mixing ratio. The RH measurements are first converted to the H₂O mass mixing ratio in g/kg using Equation 5.9:

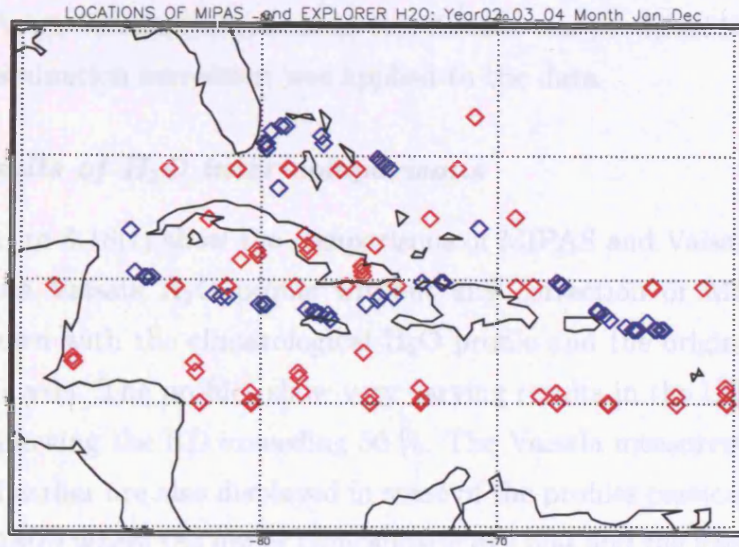


Figure 5.17: Locations of matched Explorer and MIPAS profiles

$$X_v = \frac{e_s * e}{P - e} \quad (5.9)$$

where e is calculated by:

$$e = \frac{RH}{100} * e_s \quad (5.10)$$

Given that the molecular mass of water and dry air are M_{H_2O} and M_{Dry} , respectively, the H_2O volume mixing ratio can be calculated from Equation 5.11:

$$vmr = \frac{M_{Dry}}{M_{H_2O}} * X_v \quad (5.11)$$

The Vaisala radiosondes that were used in this analysis had the appropriate tropical MIPAS H_2O averaging kernels applied to them similar to the method described in the MIPAS - SHADOZ section. In terms of Vaisala corrections, as the TD and TL corrections were found to have the most substantial effect, an attempt to correct the Vaisala radiosondes using the appropriate correction was also made in this analysis. As the corrections require information on the temperature, measurement time and RH, the corresponding information was extracted with the sonde measurement. In order to apply the right correction, the serial number of each sonde is used to identify the type and age of the radiosondes using the methodology explained in Miloshevich

et al. [2004]. As no Vaisala radiosonde in this dataset was produced before 25th June 2001, no contamination correction was applied to the data.

5.4.1.3 Results of H₂O inter-comparisons

Figures 5.18(a) to 5.18(f) show the comparisons of MIPAS and Vaisala H₂O. In each comparison, the Vaisala H₂O profile without any correction or MIPAS averaging kernels are shown with the climatological H₂O profile and the original sonde profile used in the analysis. The profiles show very varying results in the UTLS region with some profiles showing the RD exceeding 50 %. The Vaisala measurement biases that were discussed earlier are also displayed in some of the profiles particularly in Figures 5.18(b) and 5.18(c) where the upper tropospheric dry bias and the lower stratospheric moist bias is clearly visible in the sonde profiles.

5.4.1.4 Mean profiles

An ensemble of all MIPAS and Vaisala RS90 and RS80-H profiles obtained in criteria 2 are shown in Figures 5.19. The Vaisala ensemble appears to be in good agreement with MIPAS H₂O in the pressure range of 215 mb to 80 mb. Above 80 mb, there is a distinctive positive bias present in the Vaisala profiles in the tropical lower stratosphere. This clear overestimation in the lower stratosphere suggests that the Vaisala radiosonde profiles are not suitable for sounding of the lower stratosphere region likely to be due to the larger uncertainty (larger than 100 %) at low humidity values Miloshevich [Pers. Comm.].

The mean MIPAS and corrected (with MIPAS averaging kernels) Vaisala H₂O profiles for the operationally and cloud filtered measurements are shown in Figures 5.20(a) to 5.20(f) and summarised in Table 5.10.

From the results of the tropical cloud filtering of MIPAS data against Vaisala, it can be seen that there is marginal improvement close to 213 mb with increased CI-A (i.e. using 2.5 sbl/sab) however, agreement is poor close to 131 mb and the most likely cause for this is the inadequate performance of radiosondes to measure accurately at low temperatures and the possible tendency of MIPAS H₂O to be high near this region (from the results of the MIPAS -HALOE H₂O comparison). At 82 mb, the agreement between MIPAS and Vaisala appears to be within 10 % for most cases however, the differences tend to increase in the 'sab' case similar to the large

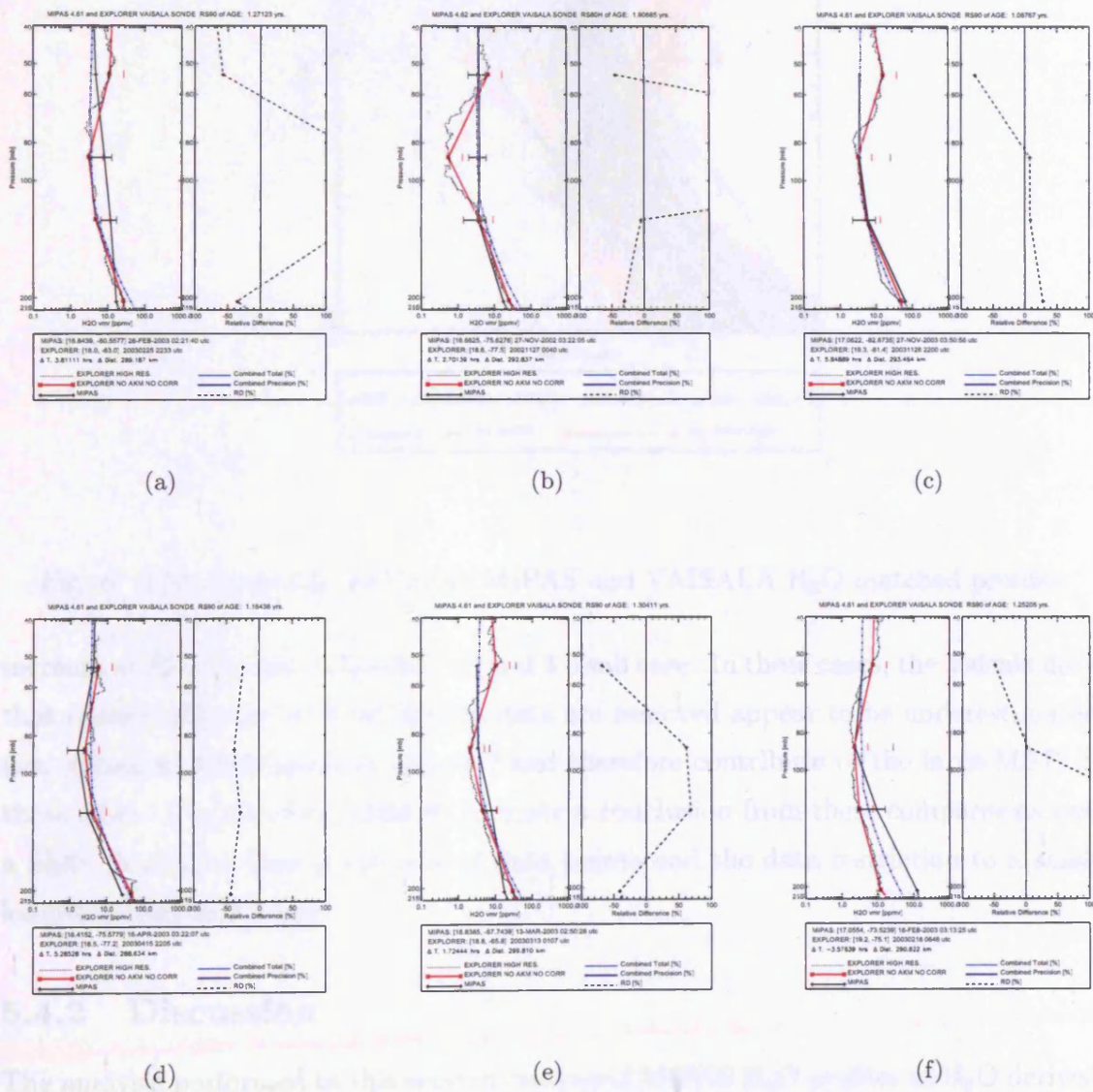


Figure 5.18: Examples of matched MIPAS and Vaisala H₂O profiles

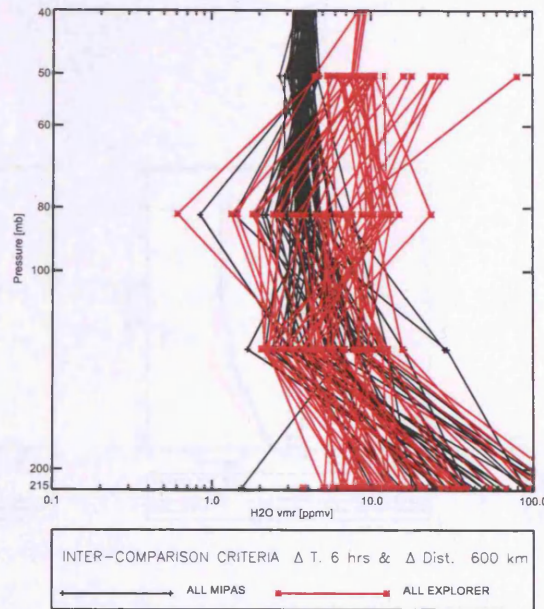
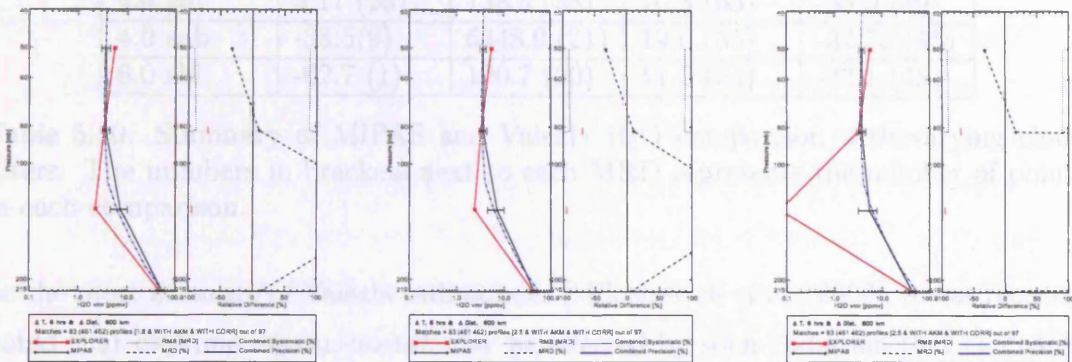


Figure 5.19: Ensemble and mean MIPAS and VAISALA H₂O matched profiles

increase at 131 mb seen in the 2.5 sab and 3.5 sab case. In these cases, the Vaisala data that remain after extra cloud filtered data are removed appear to be underestimated (i.e. values of 0.086 ppmv at 131 mb) and therefore contribute to the large MRD in these cases. It is however, difficult to make a conclusion from these comparisons and a likely limitation here is the lack of data points and the data restriction to a small longitude/latitude range.

5.4.2 Discussion

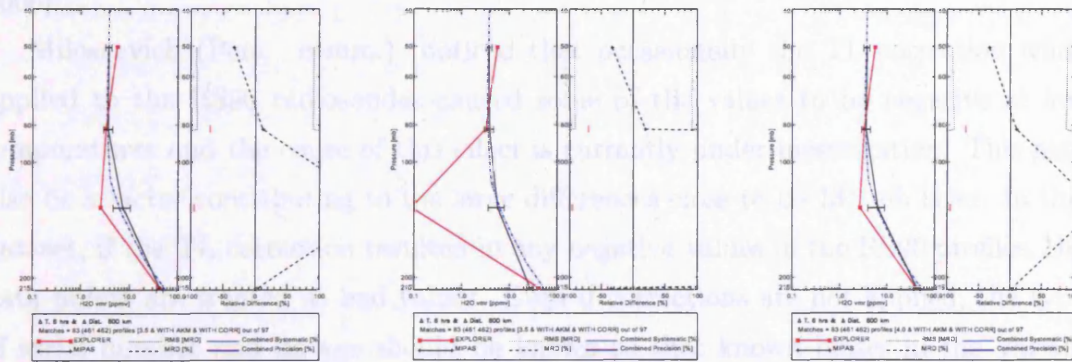
The analysis performed in this section compared MIPAS H₂O profiles to H₂O derived from Vaisala RS80-H and RS90 sondes. As the ensemble figures have shown, the MIPAS and Vaisala appear to exhibit similar variability in H₂O concentrations in the upper tropospheric region. However, the Vaisala radiosondes are clearly biased positively in the lower stratosphere that emphasises the inability of radiosondes to measure accurately in lower stratosphere. Although RS90 radiosondes were found to



(a) CI-A ≤ 1.8

(b) CI-A ≤ 2.5 sbl

(c) CI-A ≤ 2.5 sab



(d) CI-A ≤ 3.5 sbl

(e) CI-A ≤ 3.5 sab

(f) CI-A ≤ 4 sbl

Figure 5.20: Mean MIPAS versus Vaisala H₂O profiles with varying cloud filtering schemes

CI-A	MRD at 213 mb	MRD at 131 mb	MRD at 82 mb	MRD at 50 mb
1.8	15.2 (33)	223.5 (44)	9.7 (69)	-32.7 (50)
2.5 sbl	7.21 (28)	200.2 (42)	10.3 (67)	-32.7 (50)
2.5 sab	1.9(22)	7216.9 (26)	17.2 (37)	-32.5 (47)
3.5 sbl	3.17 (25)	191.34 (40)	11.8 (65)	-33.0 (49)
3.5 sab	-34.4(12)	6348.4 (21)	19.33 (35)	-32.7 (45)
4.0 sbl	3.17 (25)	138.5 (38)	10.3 (63)	-33.0 (49)
4.0 sab	-38.5(9)	6348.9 (21)	19.0 (35)	-32.76 (45)
6.0 sbl	-62.7 (1)	190.7 (20)	11.5 (54)	-33.1 (48)

Table 5.10: Summary of MIPAS and Vaisala H₂O comparison with varying cloud filters. The numbers in brackets next to each MRD represents the number of points in each comparison.

be the most accurate of Vaisala radiosondes [Miloshevich et al., 2006], it was recently noted that daytime measurements may be affected by solar radiation that can cause a dry bias in the measurements particularly in the upper troposphere. Methods of correcting this bias are currently under development. In this comparison the results have not been screened for day and night measurements and further work would be to distinguish between the two and correct for RS90 daytime dry bias [Vomel et al., 2006].

Miloshevich (Pers. comm.) noticed that occasionally the TL correction when applied to the RS90 radiosondes caused some of the values to be negative at low temperatures and the cause of this effect is currently under investigation. This may also be a factor contributing to the large differences close to be 131 mb layer. In this dataset, if the TL correction resulted in any negative values in the RS90 profiles, the data points are treated as bad values. Even if corrections are not applied, the type of serial number and its age should be known so that known biases in the Vaisala measurements can be identified. Clearly it is difficult to totally assess radiosonde accuracy as they can be affected by many atmospheric conditions. However, these results have provided an interesting intercomparison and that reveals many of the difficulties in sounding the UTLS with *in situ* instruments and highlights some of the merits of using remote sensing instruments to observe this region. The issue of cold temperatures near the tropical tropopause can be an issue for both *in situ* and remote sensing instruments.

5.5 Summary

Following an intercomparison of MIPAS H₂O and O₃ with correlative satellite and *in situ* measurements, some conclusions can be made about the quality of MIPAS in the tropical UTLS:

5.5.0.1 H₂O

1. Comparisons to Vaisala radiosondes at 200 mb and 80 mb reveal very good results (<10 %) difference. However, at 100 mb, the comparisons are highly variable most likely because of the TL corrections. At 50 mb, it is difficult to assess the quality because of the larger uncertainty surrounding the radiosonde measurements at low H₂O concentrations. Although radiosondes are considered to be accurate to be used as real atmospheric representation, they can also suffer from biases which even with corrections, cannot be resolved. Radiosondes are a potentially excellent source of upper tropospheric H₂O and the intercomparisons have presented some interesting results. However, there are still some issues with some of the corrections applied here with ongoing attempts to improve them.s
2. The results for the Vaisala radiosondes are limited by the fact that closer coincidences, particularly with the Vaisala radiosondes were not attainable. In addition, comparisons were only performed at one region.
3. Overall the intercomparisons with radiosondes were good but did not confirm the absolute quality of MIPAS data at pressures above 100 mb.
4. The intercomparisons of MIPAS H₂O with HALOE showed that operationally cloud-filtered H₂O between 12 km and 18 km exhibit a positive bias that is potentially due to undetected clouds. Using cloud thresholds to remove undetected clouds and biases from MIPAS H₂O data reduced the bias between MIPAS and both HALOE and Vaisala H₂O measurements.
5. With sufficient cloud screening using a CI-A threshold of 3.5, the positive bias at 12 km can be reduced (although still remains large) compared to HALOE that is within approximately 40 % at 15 km. However, the possibility that the HALOE H₂O used in this analysis may possess a dry bias cannot be ruled out.

6. The best results from the MIPAS-HALOE comparison were obtained with a CIA of 3.5 (similar for sab and sbl). From the more global comparisons performed on HALOE data ([Harries et al., 1996; Montoux et al., 2007]), it is clear that HALOE has a dry bias in comparison to MIPAS data. This has been identified by other authors and the results obtained here are in line with this.

Comparisons at higher altitudes show that even with extra cloud filtering, MIPAS H₂O performs to within 20 % (at approximately 80 mb) and within 10 % close to 50 mb.

7. Although using a greater cloud index reduces the bias, the cost of doing so also reduces the quantity of tropical UTLS H₂O data. However, the coverage will still be better than that achieved by *in situ* instruments.
8. From the examinations of cloud effects on single H₂O retrieved profile in chapter four, measurements near the tropopause may be dry biased when there is a cloud at a lower tangent height. However, in these comparisons, no evidence for such an effect, in comparison to the data being compared to, could be found.

5.5.0.2 O₃

1. For tropical MIPAS O₃ the bias between MIPAS and correlative instruments was found to be consistently large in the upper tropospheric region with large variability from 50 - 250 mb. At pressures above 50 mb in the lower stratosphere MIPAS O₃ measurements possess a positive bias and although the bias is outside of the combined errors, it is closer than the agreement achieved below the tropopause and beyond.
2. SHADOZ O₃ agrees very well with MIPAS data at 200 mb (with 2.5 sab) and 50 mb to approximately 10 %. The 50 mb results are not particularly affected by the cloud clearing. At intermediate levels, MIPAS appears to be approximately a factor of 2 higher than SHADOZ for reasons that are not understood.
3. From the MIPAS O₃ comparisons to HALOE, the results showed extremely large relative differences; however, as O₃ concentrations are expected to be small at such altitudes, the calculated relative differences will appear large. Similarly,

for the H₂O case, the MIPAS O₃ agreement with HALOE does not alter at pressures close to 50 mb.

4. The comparisons to HALOE do not shed any light on these factors. As for the HALOE H₂O comparison, HALOE data have a large low bias compared to MIPAS results. Cloud filtering options make only a small difference. At 50 mb, agreement with HALOE is within 30 %.

In terms of MIPAS errors and uncertainty, the dominating contributing factors to the increased variability in MIPAS H₂O and O₃ below the lower stratosphere can be deduced from the Oxford analysis as the line of sight gradients in MIPAS data.

Clearly, much further work is required to deduce a reliable validation system for the tropical UTLS.

Chapter 6

Tropical UTLS averages of MIPAS H₂O and O₃

In chapter four, the detrimental effect of clouds on MIPAS H₂O and O₃ retrievals was demonstrated by simulating cloud effects in the wavelength range used for H₂O and O₃ retrievals and examining the resulting systematic biases and changes in retrieval uncertainty. The main findings were that:

1. An increase in retrieval uncertainty and a decrease in precision was demonstrated by an increase in the random retrieval error of the H₂O and O₃ profiles.
2. There is a direct systematic effect on the retrieved H₂O concentrations at the cloud altitude that is anti-correlated with the retrieval level above.
3. The presence of cloud tends to exaggerate the pre-existing random error associated with MIPAS O₃ retrievals near the cold tropopause region.

The inter-comparisons carried out in chapter five showed that the operationally cloud filtered H₂O and O₃ in the tropical UTLS region can contain significantly large errors particularly near the cold tropopause. The variability of the data near the UTLS region, caused by suspected cloud was shown to be reduced when using a higher threshold. Therefore, additional cloud filtering is a necessary step to improve the accuracy of MIPAS H₂O and O₃ measurements for this region. The impact of the increased filtering is an important step for both of these gases in the tropics for a number of reasons. For example, the simulation of cloud effects performed in chapter

four showed that at low CI-A values (thicker clouds), O_3 concentrations near the tropopause could in fact be larger than those expected in the clear sky values. Such a retrieved value could be misinterpreted as an enhanced O_3 concentration in the UTLS although the error assigned to the retrieval would also have increased. Similarly, low CI-A values were shown to result in a high bias in H_2O values at the cloud altitude and simultaneously produce lower values above the cloud. This is a particularly important detail as dehydration of air masses occurs at the tropical tropopause, as shown by Gettelman et al. [2002c], Read et al. [2004]; Jensen and Pfister [2004] and such a bias in MIPAS data can significantly impact the interpretation and furthermore, the potential value of the data in this sparsely monitored region.

In this chapter, the seasonality of H_2O and O_3 in the tropical UTLS region is investigated using the proposed improved cloud indices found suitable for tropical MIPAS retrievals of H_2O and O_3 . A particular focus of this study is to demonstrate that MIPAS observes expected features and to show that MIPAS data could be suitable for further studies of some important phenomenon in the UTLS.

In the following sections, having described the methodologies for seasonal averages and shown seasonal cloud behaviour, the performance of the operational cloud detection will be evaluated against the tropical cloud flagging schemes proposed in chapter four. The impact of varying averaging methods in longitude is examined and the implications are drawn for the interpretation of the of the MIPAS data. The seasonal distribution of H_2O and O_3 in the tropical UTLS as measured by the MIPAS instrument will be presented on layers representative of the tropical UTLS. As the MIPAS instrument's ability to resolve layers in the TTL is limited by a 3 km, relatively coarse FOV (in comparison to the soundings achieved by *in situ* measurements), only particular layers within the UTLS region can be analysed. Pressure levels are a suitable vertical coordinate to show the concentrations throughout the UTLS and emphasis will be given to layers representative of the upper troposphere (215 mb), the tropopause (100 mb) and the lower stratosphere (68 mb). Finally, two case studies of H_2O and O_3 will be examined focussing on an O_3 maximum in the South Atlantic and elevated H_2O in the summer monsoon season.

6.0.0.3 Methodologies for seasonal averages

The data used in this section are the OL (offline) versions 4.61 and 4.62 MIPAS L2 data from July 2002 to March 2004 and the corresponding cloud index information, calculated at Leicester University from L1B spectra. For each month of data used in each season for this analysis period, monthly cache files were generated by extracting all MIPAS data from each orbit file of each month and merged to produce seasonal datasets. In one day, there are 14 MIPAS orbit files that contain around 75 profiles. In each MIPAS orbit file, information about all retrieved MIPAS L2 profiles (including temperature and pressure), MIPAS time identification (TID), longitude, latitude information for each profile, the quality and convergence flags and the covariance variance matrix (the random retrieval error) are included. Each cache file generated at Leicester University contains this information as well as the complementary CI-A values for all MIPAS bands, the CI-A TID and CI-A geophysical data for all the days in one season. From each dataset, non-convergent data are removed and the only data retained are those for which both good trace gas retrievals and valid cloud information are available.

To calculate seasonal averages, results for each gas are analysed separately. This is done because the number of valid profiles is different for each gas and therefore the matching of gas profiles and CI-A profiles is different. Differences are small, however, as implied by Raspollini et al. [2006] who found that for the H₂O and O₃ profiles processed by the OL processor at that time, at least 93% of H₂O and O₃ profiles successfully reached convergence and similar numbers of converged profiles were found in this analysis. Since MIPAS tangent altitudes drift in both altitude and pressure it is necessary to interpolate each point in the profile, at a certain tangent height, to a specified reference level. In this case, the levels used for vertical interpolation of the data are those first proposed for the UARS project of level 3 gridded levels and are shown in Table 6.1; UARS instruments were of comparable vertical resolution to MIPAS. For each MIPAS data and random error profile, logarithmic interpolation is performed within the vertical range that contains only valid good data points. Representing data on the UARS pressure surface is a useful measure of comparison to previous measurements of H₂O and O₃ from instruments onboard the UARS satellite including HALOE and MLS as well as comparisons to TTL trajectory studies (although not particularly utilised here).

UARS level	Pressure [mb]
2	464.14
3	316.23
4	215.44
5	146.78
6	100.00
7	68.3
8	46.42

Table 6.1: UARS Pressure levels for the UTLS region.

The MIPAS data shown in this chapter will be presented in several ways: for seasonal maps of H₂O and O₃ (and temperature), the data are initially gridded into 5° latitude and 5° longitude bins over a range of 180°E to 180°W and a latitude range 50°N to 50°S. This latitudinal limit is chosen to highlight the gradient between the tropical and mid-latitude regions for H₂O and O₃. Grids of 10° and 15° longitudinal averaging are also used.

The seasonally averaged vmr concentrations are presented together with the random error on the mean value of the grid box. This error on the mean is calculated by taking the mean of the level 2 retrieval errors, assumed to be random, of the points in each box, and reducing the error by the square root of the number of points. Hereafter this error is referred to as the grid box error. The data are also presented in terms of longitude and latitude cross sections that involves averaging the data within 5° latitude or longitude bins and over the vertical scale used for analysis. Analysis is mainly performed on selected pressure levels from the UARS pressure grid:

1. The 215 mb layer is used as a representation of the upper troposphere roughly equating to the 12 km MIPAS tangent height.
2. The tropopause region, corresponding to approximately 16 km is represented on a 100 mb layer as a proxy to the tropical tropopause.
3. Finally, using the TTL definitions from chapter one, an altitude greater than 70 mb (close to 19 km) should be representative of the upper limit of the TTL/lower stratospheric region. In this case, the data are represented on a 68 mb layer.

All seasonal averages are calculated as: 1) DJF = December 2002, January 2003, February 2003, 2) MAM = March 2003, April 2003, May 2003, 3) JJA = June 2003,

July 2003, August 2003 and 4) SON = September 2003, October 2003, November 2003. For each season, the cloud top pressures are also calculated and when used synergistically with both H₂O and O₃ can provide a useful indication as to whether particular features may be associated with potential convective activity and also aid in diagnosis as to whether features may or may not be influenced by clouds. For an indication of where the coldest temperatures occur in relation to enhanced or reduced H₂O and O₃ concentrations, the mean tropical UTLS temperatures are also shown.

Throughout this chapter, references will be made to particular regions in the tropics, and the locations of these are given in Table 6.2. These are the approximate co-ordinates for the primary regions of interest.

Region	Co-ordinates latitude/longitude [°]
West and East Pacific	20 N to 20 S/120 E to 120 W
Central America/Brazil	10 N to 20 S/40 W to 80 W
Equatorial Africa	20 N to 20 S/0 to 40 E
South Atlantic Basin	0 to 30 S/40 W to 10 E
South Asia	30 N to 10 N/ 50 E to 120 E
Micronesia	10 N to 20 S /100 E to 160 E

Table 6.2: Approximate co-ordinates of tropical regions featured in this chapter

6.0.0.4 Cloud top pressure, occurrence frequency, and “tropopause” temperatures

Cloud information is not only useful because it indicates where data quality might be affected. Cloud information such as the CI-A also gives an indication of the amount of cloud or aerosol particles relative to the trace gas signatures in a specific part of the atmosphere. For instance, H₂O measurements made in a completely clear sky scenario will equate to a different mixing ratio compared to one that is obtained in the presence of ice particles from cirrus clouds. This does not mean that a higher cloud index will reduce or change the retrieved value but can instead provide some indication of the particle amount in that particular instantaneous measurement. As mentioned earlier in this thesis, in order to obtain only “clear sky” concentrations of H₂O, using a cloud filter of greater than 6 would be favourable and screen any H₂O mixing ratios that are dependent on thin cloud presence. However, a significant caveat to this is that for completely “clear sky” MIPAS measurements, the number

of data points will reduce in accordance with the changing CI-A values as shown by the CI-A statistics presented in chapter four. To determine the suitability of CI-A filtering it is useful to take into account how often MIPAS encounters a “clear sky” tropical atmosphere. The reality is that the tropical upper troposphere is not cloud-free as demonstrated by Wang et al. [1994] and Spang et al. [2002] who observed high cloud occurrence frequencies, often as high as 70%, in some tropical regions. Using the CI-A information in synergy with tropical MIPAS H₂O and O₃ measurements can act as a useful tool for the interpretation of the observed concentrations, depending on the cloud filter used.

The mean cloud top pressures (CTP) for the tropics are estimated directly from the cloud index files by converting the cloud altitudes to cloud pressure by simple integration of the hydrostatic equation (Equation 6.1): where z is the cloud altitude, P is the apparent cloud top pressure, P_o is the surface pressure taken as 1000 mb and H is the scale height (that is the height interval by which atmospheric pressure falls exponentially), taken as 7 km. The error at the altitude of interest is expected to be a maximum of 10 mb and are sufficiently accurate for the cloud top indication used here.

$$P = P_o \exp\left\{\frac{-z}{H}\right\} \quad (6.1)$$

It should be noted that the cloud top pressure maps give an indication of the “apparent” cloud top pressure and are calculated by taking into account the tangent height above which the cloud index increases to a “clear sky” value using a cloud definition of 1.8.

The cloud altitudes correspond to the MIPAS engineering altitudes and are known to have an associated bias of up to 900 m [Raspollini et al., 2006]. Nevertheless, the CTP estimates can provide an indication of the geographical “cloudiest” regions along the tropics and also regions where high/low clouds are persistent.

Seasonal mean cloud top pressures are shown in Figure 6.1 calculated for each season. Some distinctive features can be observed throughout the year and some of them are highlighted here. In the DJF and MAM seasons, higher cloud tops appear to be located over the East and West Pacific Oceans, South America and Equatorial Africa with cloud top pressures in the region of the tropopause (close to 100 mb) indicating the cloud presence, particularly in these regions, can potentially reach

higher than the tropopause. In JJA and MAM, the behaviour changes considerably as the apparent CTPs are no longer constrained to the 20°N and 20°S band as in DJF and MAM. In JJA, higher clouds tend to migrate northwards in compliance with the ITCZ behaviour for this time of the year and are centralised over Mexico and India particularly. The movement of the ITCZ from the south of Equatorial Africa to the north of the equator is also visible in the highest clouds. In SON, there appears to be more spreading and the highest cloud tops are no longer over the South Asian Monsoon region but have evolved south-east towards Indonesia and North Australia. The tropical distributions observed here are in good agreement with the distribution of cloud top heights estimated by Liu and Zipser [2005] who demonstrated that these regions are associated with convective activity.

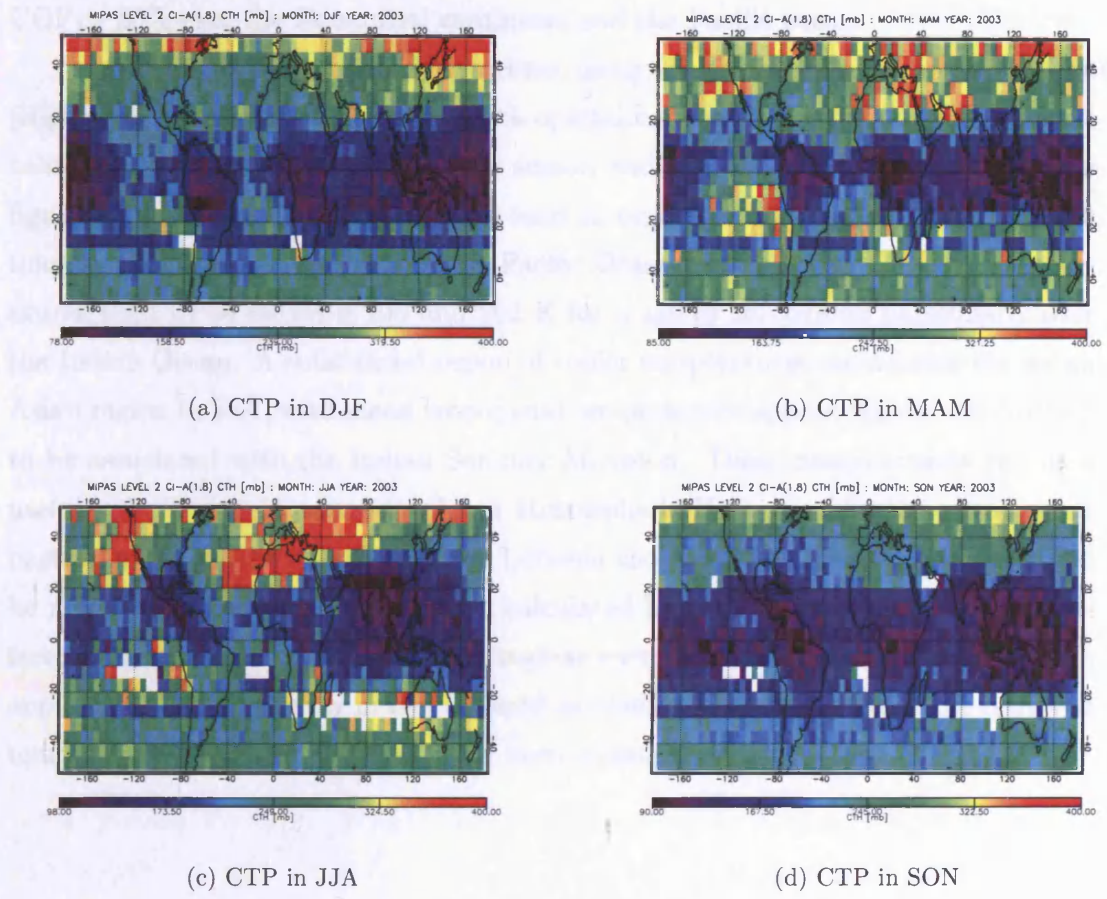


Figure 6.1: Seasonal cloud top pressures calculated using operational CI-A threshold 1.8. Note that the strip of data near to 22° south is an artificial artifact in the original MIPAS LIB data files.

Cloud occurrence frequencies (COF) are also a useful diagnostic parameter. Greenhough et al. [2005] calculated cloud occurrence frequencies as the number of cloudy spectra divided by the total number of points in a grid box of 5° and 5° between the altitudes of 12 km and 30 km, expressed as a percentage. The cloud in these cases are defined using a CI-A threshold of 2.2 (for the inclusion of potentially thinner clouds) and are shown in Figure 6.2. The figures show a similar pattern to the cloud top heights as would be expected with the largest frequencies occurring close to the regions of the highest clouds. In DJF and MAM, larger cloud occurrence is over the Pacific, Central America, Africa and extending over the Indian and West Pacific regions with $\text{COF} > 80\%$ in some regions. In JJA, the cloud occurrence over the Pacific is reduced and pattern migrates northwards consistent with the movement of the ITCZ. In SON, a similar behaviour to that observed in MAM can be seen with $\text{COF} > 80\%$ over the Equatorial continents and the Pacific ocean.

Tropical tropopause mean temperatures, using the 100 mb definition of the tropopause [Highwood and Hoskins, 1998] and with operational cloud filtering of $\text{CI-A} \leq 1.8$ are calculated from MIPAS data for each season and are shown in Figure 6.3. As the figures show the coldest temperatures tend to occur in DJF through to MAM with temperatures close to 190 K over the Pacific Ocean and Indonesia. In JJA, temperatures tend to be between 198 and 202 K for much of the tropics particularly over the Indian Ocean. A substantial region of cooler temperatures occurs over the South Asian region in JJA, with mean tropopause temperatures approximately 195 K likely to be associated with the Indian Summer Monsoon. These measurements can be a useful indicator as to where the lower stratospheric H_2O concentrations may occur particularly from the distinct relation between the two [Mote et al., 1996]. It should be noted that the mean temperatures calculated here are based on operationally filtered data and that some of the colder regions are distinctively close to regions of high apparent CTP. There may in fact be residual cloud effects remaining in the retrieved temperatures although these have not been investigated in this thesis.

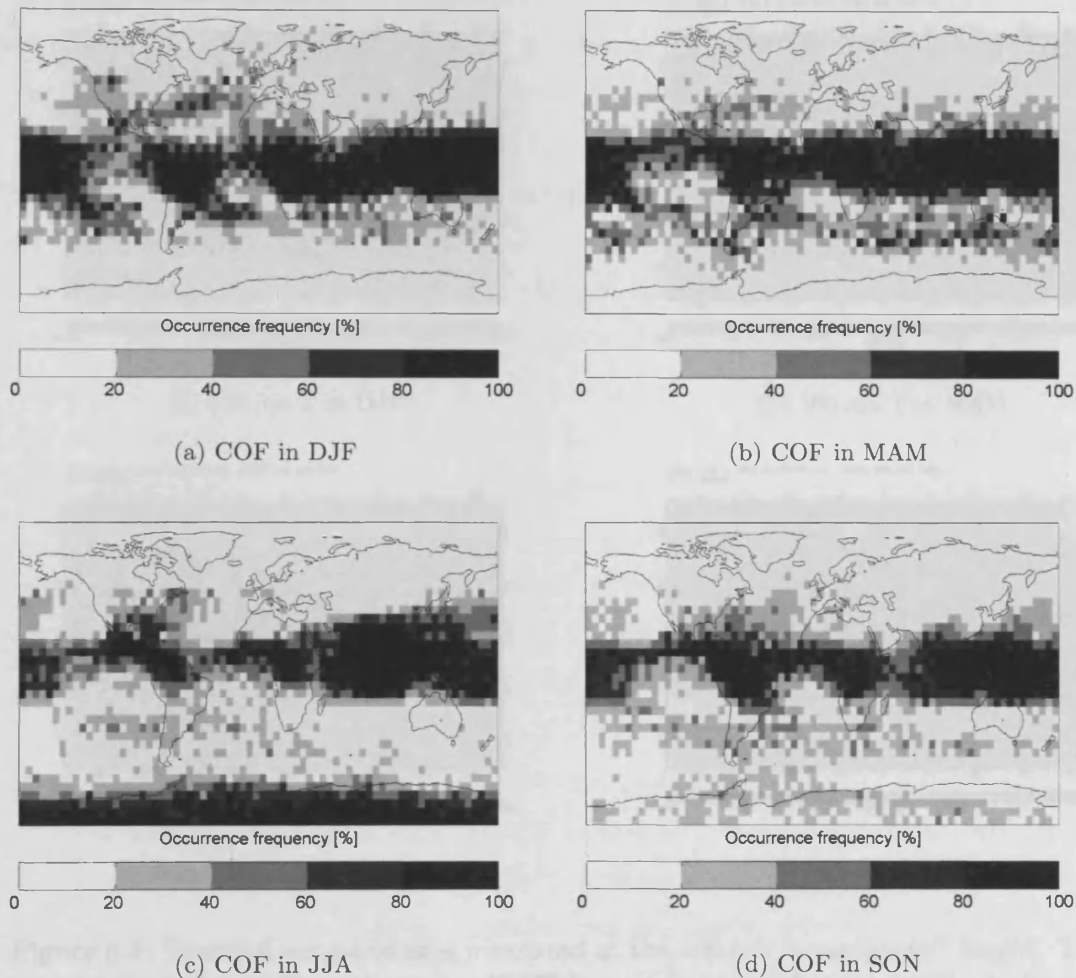
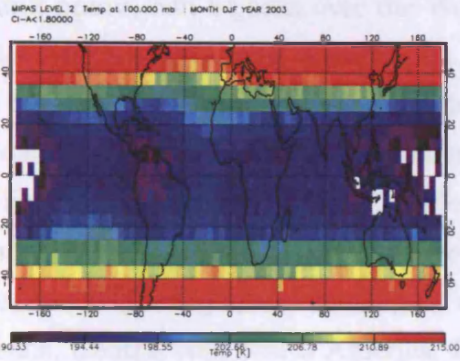


Figure 6.2: Seasonal cloud occurrence frequencies calculated using operational CI-A threshold 1.8. See text for description of calculations. Highest COFs occur at the tropics with COFs exceeding $> 80\%$ over regions such as the Pacific, Equatorial Africa and Brazil throughout the year.

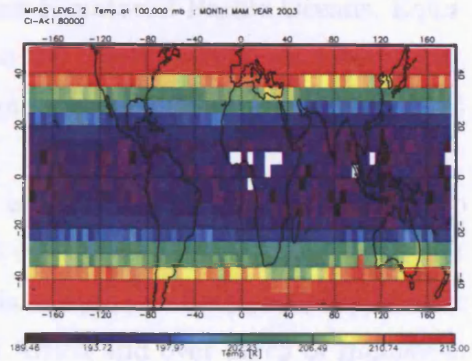
6.1 Operational and improved cloud cleared MIPAS averages

In this section, averages are derived from operational MIPAS data and compared with results using the additional cloud-filtering suggested in this thesis. Results are shown for DJF which is representative of the average behaviour of the tropics.

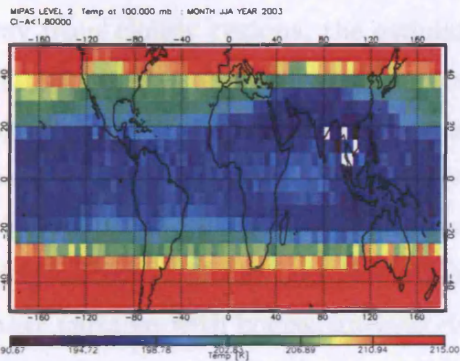
In Figure 6.4 the concentrations and the estimated grid box error on the seasonally averaged MIPAS H_2O data at 68 mb and 215 mb, for DJF are shown. The white



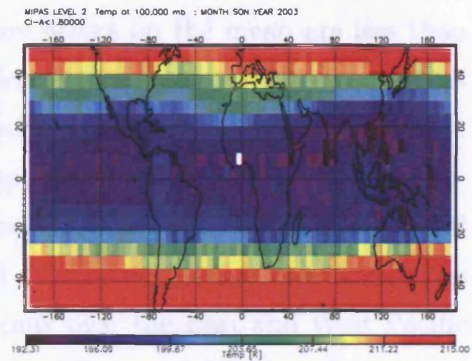
(a) 100 mb T in DJF



(b) 100 mb T in MAM



(c) 100 mb T in JJA



(d) 100 mb T in SON

Figure 6.3: Seasonal temperatures measured at the 100 mb “tropopause” height. The migration of the northward moving ITCZ is a pronounced feature, particularly over South Asia. Also notice the cold tropopause temperatures (≤ 190 K) over the east and west tropical Pacific ocean.

regions in the figures are due to missing or removed data-points from operational cloud screening. At 68 mb, in the region of lower stratosphere, data are not removed using the operational CI-A value indicating that no cloud (using the $CI-A < 1.8$) reaches these altitudes. Some features that are evident in DJF are regions of apparent localised low mixing ratios, that on the one hand could indicate dehydrated air parcels that have travelled through the tropical tropopause region and on the other hand, these dry values could arise from the effect of clouds at altitudes below 18 km that introduce a dry bias into the H_2O profiles above the cloud.

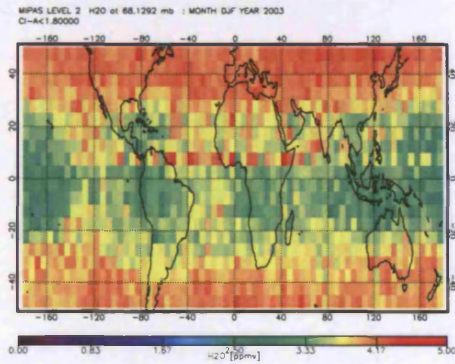
Particular regions where concentrations tend to be lower than 3 ppmv (but greater

than 2 ppmv) can be seen over the West and East Equatorial Pacific Oceans, Equatorial Africa and Central America. In relation to the corresponding retrieval errors, the mean retrieval error (mean precision over square root of the number of profiles) tends to remain below 10% for most grid boxes.

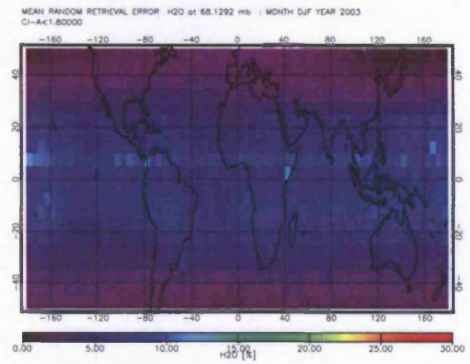
For H₂O at 215 mb, the most evident feature is that the concentrations appear to be much more variable than those observed at 68 mb. Another point to notice is that there are white regions of missing or removed data over the East and West Pacific Oceans, Central and South America, Equatorial Africa and over much of Indonesia. These regions correspond to missing data because of operational cloud filtering and are consistent with the regions of highest cloud top pressures as seen in Figures 6.1. Away from cloudy regions, the estimated grid box errors on the mean are less than 10%. However, some regions show variability from grid box to grid box which is larger than indicated. This would be consistent with the expectations of large errors, depending on the cloud altitude as shown in chapter four.

Figure 6.5 shows the operationally cloud filtered O₃ concentrations and estimated grid box error at 68 mb and 215 mb for DJF. At 68 mb the observed concentrations appear variable with concentrations close to 1 ppmv over the East and West Pacific Oceans, Central and South America, Micronesia and Equatorial Africa. In contrast to these, a distinctive band of lower O₃ concentrations is apparent over the Pacific Ocean, close to the coast of South America, the Equatorial Atlantic and Indian Ocean as well as a distinctive band of low O₃ (concentrations between 0.38 and 0.7 ppmv) in the 20°N - 0°N band extending over Central America, Africa and India. The corresponding random retrieval errors in both cases remain below 10% over much of the tropical latitudes although some scattered high random retrieval error regions, particularly in the DJF are visible over some parts of the tropics.

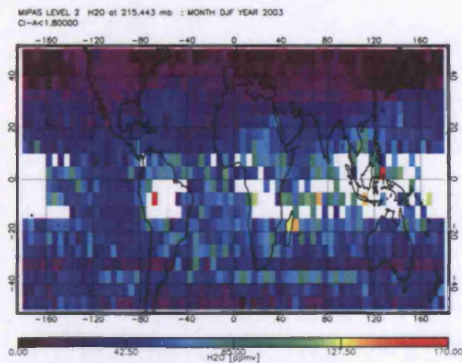
At 215 mb, O₃, similar to H₂O, exhibits much variability even in the averaged concentrations with particularly striking contrasting O₃ concentrations over the Pacific, Atlantic and Indian Oceans in both DJF. This could correspond to the prominent zonal wave-one O₃ pattern [Wang et al., 2006], that relates to enhanced O₃ features over the southern Atlantic. This apparently shows concentrations greater than 0.08 ppmv. Lower concentrations appear over the east and west Pacific Ocean ranging between 0.04 and 0.06 ppmv, possibly suggesting uplift of low O₃ air over these regions. However, these distinctive low O₃ mixing ratios appear to possess higher estimated



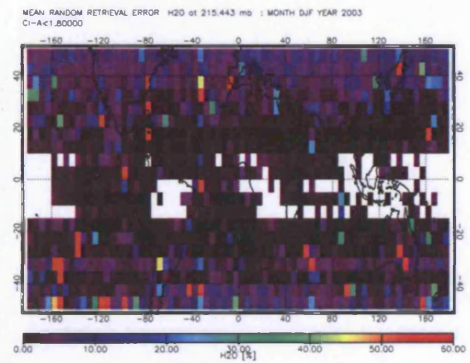
(a) 68 mb concentrations



(b) 68 mb estimated grid box errors



(c) 215 mb concentrations



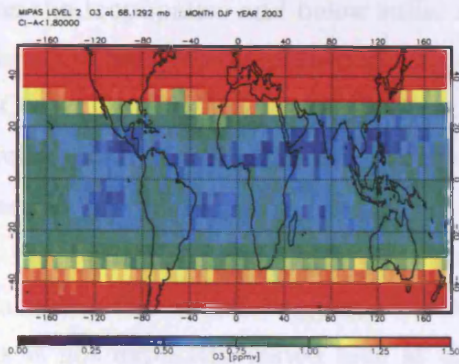
(d) 215 mb estimated grid box errors

Figure 6.4: L2 H₂O concentrations and estimated grid box error at 68 mb and 215 mb with operational detection CI-A ≤ 1.8 for DJF. All data are averaged on 5° by 5° grid boxes. Upper limits on the colour bar indicate where the data or grid box error exceeds these limits.

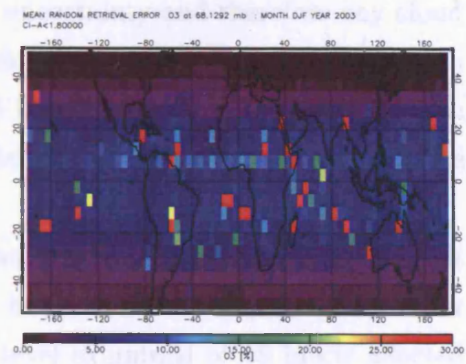
grid box errors between 50 % and 100 % meaning that a dominating factor is the decreased precision at these low O₃ values. High grid box to grid box variability is observed in these regions. Again, the regions of missing data are consistent with what is expected due to cloud interference in these regions.

6.1.1 Tropical cloud filtering schemes for H₂O and O₃

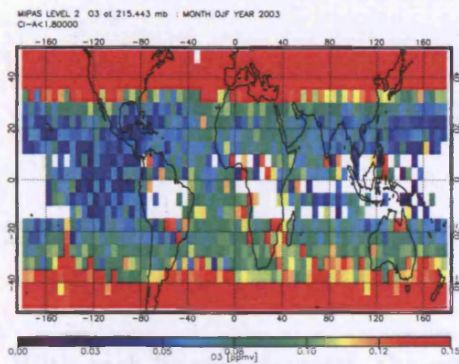
Here, additional cloud filtering schemes are applied to tropical UTLS MIPAS H₂O and O₃. The schemes are demonstrated on the DJF season only and are based largely on the cloud effects discovered in chapter four and the validation in chapter five. To



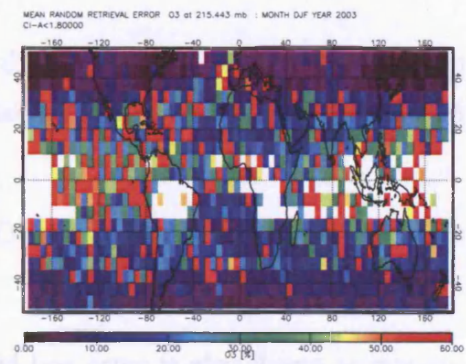
(a) 68 mb concentrations



(b) 68 mb estimated grid box errors



(c) 215 mb concentrations



(d) 215 mb estimated grid box errors

Figure 6.5: L2 O₃ concentrations and estimated grid box errors at 68 mb and 215 mb with operational detection CI-A ≤ 1.8 for DJF. All data are averaged on 5° by 5° grid boxes. Upper limits on the colour bar indicate where the data or grid box error exceeds these limits. White regions indicate missing data.

reiterate the impact for H₂O, it was found that at the cloud altitude, H₂O concentrations can be expected to possess a positive systematic bias with a simultaneous negative bias above the cloud altitude (which was more than 70% for the CI-A = 1.49 case analysed). Using an improved cloud index threshold of 3.5 was found to reduce such biases, to values close to 5% and -10%, above and below the cloud altitudes, respectively. For O₃, although no systematic effect could be determined, the estimated random error would be expected to reduce by almost 50 % if a CI-A threshold of 2.5 and that this would also marginally decrease the estimated random error above the cloud. Although the cloud systematic error is unknown, it is likely to be considerably reduced in accordance with reducing random error. However, MIPAS O₃ retrievals

near the tropopause and below suffer from large uncertainty and therefore any cloud effects are likely to be masked in comparison to this pre-existing uncertainty for both H₂O and O₃. The figures quoted here should not be taken as “exact” biases for each profile but rather denote the magnitude and direction of the cloud biases that are possible.

For both H₂O and O₃, two schemes are tested here. In previous chapters, it was noted that cloud flagging thresholds could be relaxed above 18 km. However this is not explicitly tested here as the highest level examined of 68 mb is affected considerably by data from tangent heights near 18 km and therefore subject to strict cloud clearing. The two schemes proposed are:

1. Scheme A that removes the MIPAS data at the cloud altitude and at the altitude above the cloud for MIPAS H₂O and O₃ using the respective thresholds of 3.5 and 2.5.
2. Scheme B that requires removal of the H₂O and O₃ data at the cloud altitude only with the respective CI-A thresholds.

With each filtered data-set, the estimated grid box error is also shown to demonstrate the effect of each filtering scheme on the overall quality of the remaining data. It is important to note that this additional filtering is a way of maximising the potential quality of the data after it has been retrieved in a region where clouds are a persistent, semi-permanent feature. Of course, this will lead to a significant reduction in the number of data points as demonstrated in the inter-comparisons performed earlier. This will also impact the estimated grid box error for the calculated seasonal means that is largely dependent on, and improved by a large number of data points.

6.1.2 Impact of cloud filtering improvements on tropical UTLS H₂O and O₃

6.1.2.1 Scheme A and B for H₂O

Beginning with H₂O, the data for DJF at 68 mb and 215 mb cloud filtered under scheme A are shown in Figures 6.6. At 215 mb, the most significant effect of using a more stringent cloud filtering is the large loss of data particularly over the continental

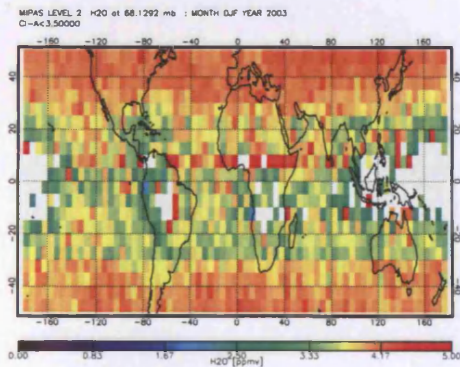
regions and the Equatorial Pacific Ocean coincident of course with prominent cloud coverage. Many of the regions with high concentrations of H₂O have been removed and from cloud tests performed in chapter four, this indicates that removed data values were likely to have an associated systematic bias larger than 20 %.

At 68 mb, data in regions such as the Pacific ocean and over the Equatorial continents, where the lowest H₂O concentrations were observed, have been removed and near the regions where clouds are at lower altitudes. For example, off the west coast of South America, the concentrations remain unchanged between the operational and scheme A cloud clearing cases. In comparison to the estimated grid box error, the concentrations observed over Equatorial South Pacific and Atlantic Oceans are close to 3.5 - 4.0 ppmv and the corresponding random retrieval errors are less than 7.5 %. Over the Indian Ocean, concentrations vary between 3 and 4 ppmv and the corresponding random errors lie between 10 % and 20 %. With reference to the apparent CTP for this season, it can be seen that there appears to be some higher clouds present in this region (compared to the Pacific and Atlantic Oceans). Comparing these 68 mb H₂O concentrations to the 68 mb concentrations using scheme B as shown in Figure 6.7(a), it can be seen that much of the drier concentrations over the Equatorial Pacific and continents are removed and using the evidence from the cloud tests in conjunction with the apparent positions of the cloud tops, it is likely that the retrieved concentrations at this altitude are dry biased in the operational data and scheme B and remain due to underlying cloud. This demonstrates the importance of removing the altitude above the cloudy tangent height.

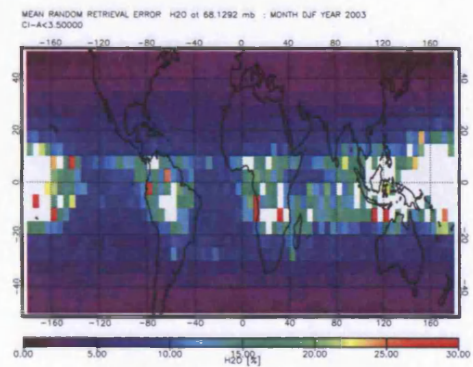
What can be seen is a clear difference between scheme A and the MIPAS operational/scheme B results in the dry regions. There remains a possibility that the differences are real but it is also clear that the retrieval error is an equally possible source. Therefore a conservative approach is adopted which is to remove the altitude above the cloud. We adopt scheme A in the following work.

6.1.2.2 Scheme A and B for O₃

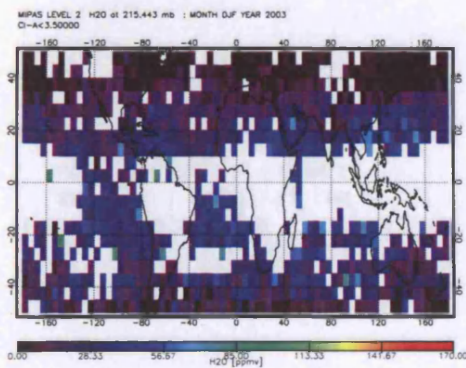
The additional cloud filtering schemes selected for MIPAS O₃ are presented in Figures 6.8 and 6.9 for the pressure levels at 68 and 215 mb. At 215 mb, large-scale features of O₃ concentrations between 0.3 and 0.5 ppmv can be observed over the north-west Equatorial Pacific ocean in the data filtered with scheme A, and seemed to be quite a



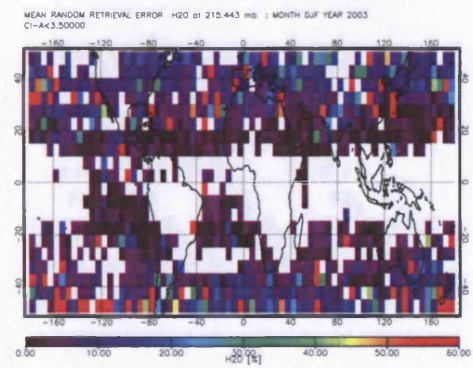
(a) 68 mb concentrations



(b) 68 mb estimated grid box errors



(c) 215 mb concentrations

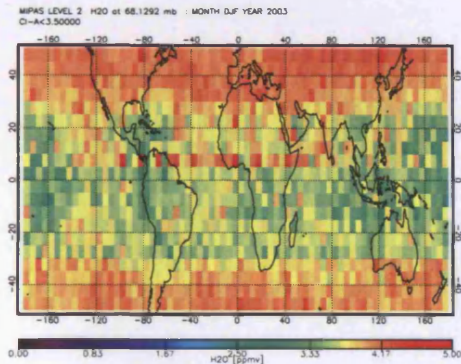


(d) 215 mb estimated grid box errors

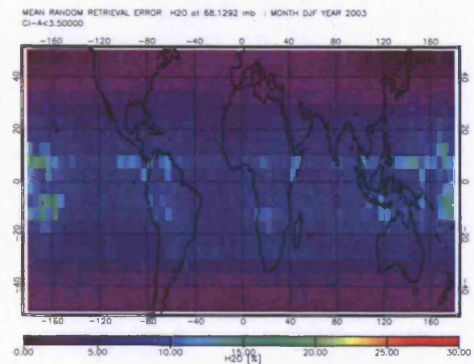
Figure 6.6: H₂O averaged concentrations and estimated grid box error filtered with scheme A. All data are averaged on 5° by 5° grid boxes. Upper limits on the colour bar indicate where the data or grid box error exceeds these limits.

robust feature that is prevalent in the operationally cleared data also. Similarly the band of O₃ with concentrations between 0.8 and 1.0 ppmv over the southern Atlantic remains even after filtering with a cloud index threshold of 2.5 in both schemes A and B. However, the features of low O₃ concentrations over the Pacific ocean correspond to errors greater than 60 % in some cases indicating that the uncertainty of MIPAS O₃ retrievals in this region remains despite the removal of cloud effects.

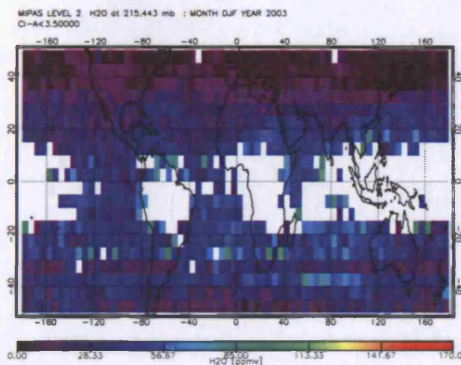
At 68 mb, the impact of using the cloud filtering scheme A on the retrieved concentrations seems more apparent than that observed at 215 mb. Over the Equatorial Pacific, Brazil, Africa and the Indonesian regions, O₃ concentrations close to 1 ppmv can be observed in the operationally filtered data (Figure 6.5(a)). Application of



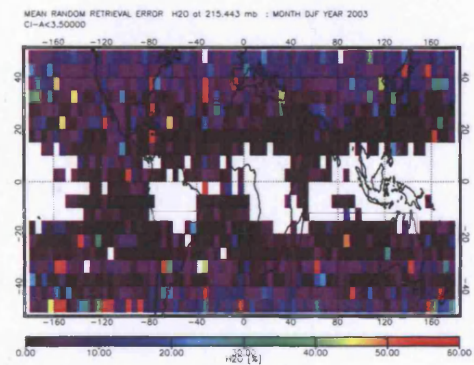
(a) 68 mb concentrations



(b) 68 mb estimated grid box errors



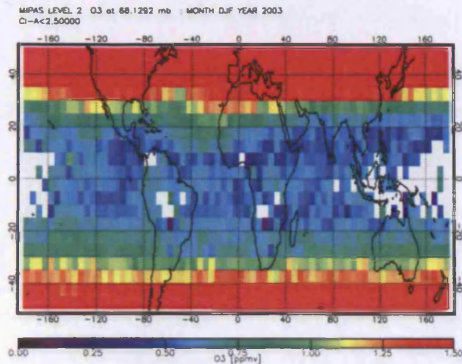
(c) 215 mb concentrations



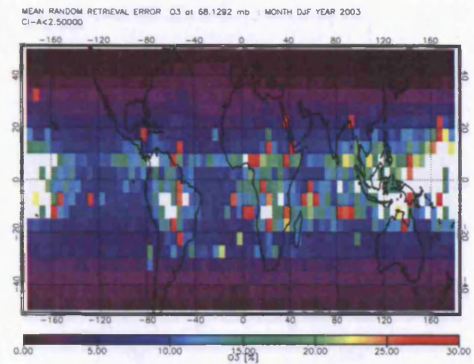
(d) 215 mb estimated grid box errors

Figure 6.7: H₂O averaged concentrations and estimated grid box error filtered with scheme B. All data are averaged on 5° by 5° grid boxes. Upper limits on the colour bar indicate where the data or grid box error exceeds these limits.

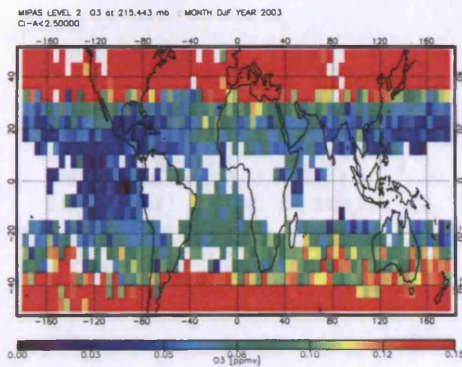
a CI-A threshold of 2.5 in scheme B appears to shift these concentrations towards values closer to 0.75 ppmv. Under scheme A, many of these data are removed and the remaining data points tend to lower concentrations closer to 0.5 to 0.6 ppmv. Although no indication of any systematic effect on O₃ concentrations was deduced from the cloud tests, it can be expected that a CI-A threshold of 2.5, at best, would result in a removal of any O₃ profile with greater than 20 % cloud induced uncertainty. For O₃ in the UTLS region, even if the suspected anomalous cloud affected profiles are removed from the analysis, the fact that the associated noise in this region can be large combined with the reduction in data quantity using scheme A or B will unavoidably increase the estimated grid box error in this region.



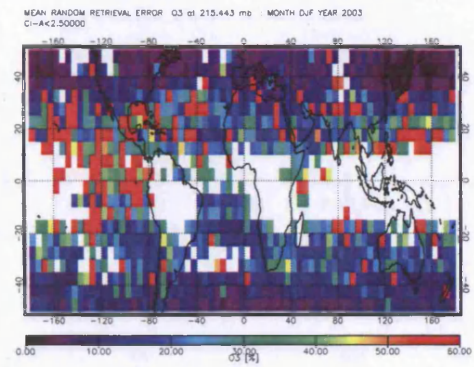
(a) 68 mb concentrations



(b) 68 mb estimated grid box errors



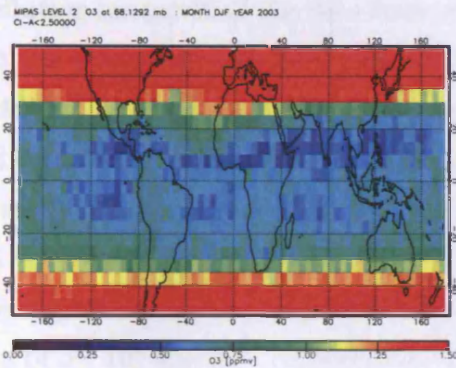
(c) 215 mb concentrations



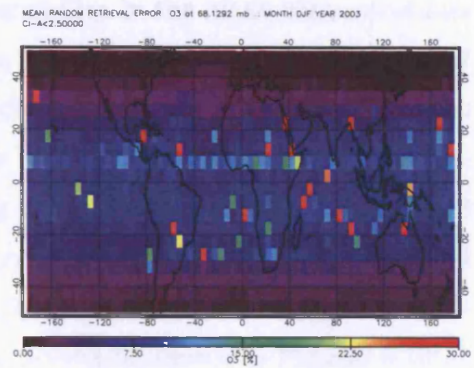
(d) 215 mb estimated grid box errors

Figure 6.8: O₃ averaged concentrations and estimated grid box error filtered with scheme A. All data are averaged on 5° by 5° grid boxes. Upper limits on the colour bar indicate where the data or grid box error exceeds these limits.

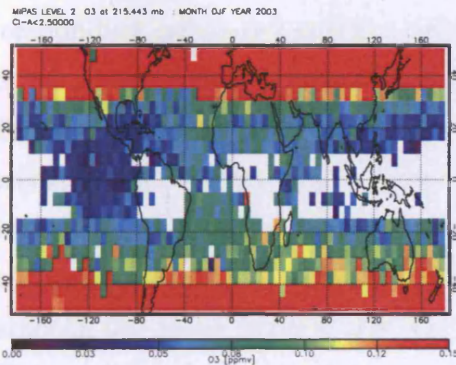
The impact of the proposed schemes on H₂O and O₃ retrieved concentrations and estimated grid box errors unfortunately presents a conflicting situation. On the one hand, using knowledge of the CI-A effect on H₂O and O₃ retrievals near this region in conjunction with apparent cloud position allows suspected cloud affected data to be removed but at the cost of losing data in this region. Between 30°N - 30°S, approximately 40 % more data points are lost at 215 mb as a consequence of using scheme A compared to the operationally filtered data for H₂O. Similarly, for O₃, approximately 30 % more data points are lost as a result of scheme A cloud filtering. With less data samples in the UTLS region, the uncertainty in this region grows and this can be a crucial factor particularly for O₃ where the random noise can



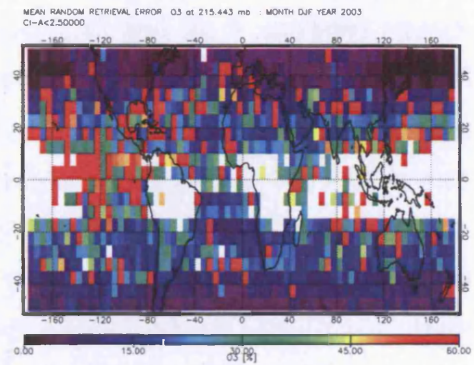
(a) 68 mb concentrations



(b) 68 mb estimated grid box errors



(c) 215 mb concentrations



(d) 215 mb estimated grid box errors

Figure 6.9: O₃ averaged concentrations and estimated grid box error filtered with scheme B. All data are averaged on 5° by 5° grid boxes. Upper limits on the colour bar indicate where the data or grid box error exceeds these limits.

quite often be significantly large. The choice of CI-A threshold depends entirely on user requirements, for example, in the case where better data coverage is required in the region above the TTL/lower stratosphere region, then scheme B would be more suitable with the caveat that the H₂O concentrations may be dry-biased by more than 20 % above cloud. In the work that follows the stringent thresholds of 3.5 and altitude above for H₂O and 2.5 and the altitude above for O₃ are adopted.

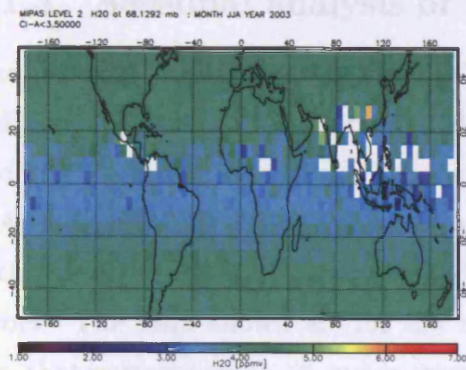
6.1.3 Longitudinal resolution effects

The MIPAS data maps that have been presented previously in this chapter have been averaged on to a 5° by 5° latitude versus longitude grid. This gridding provides a high

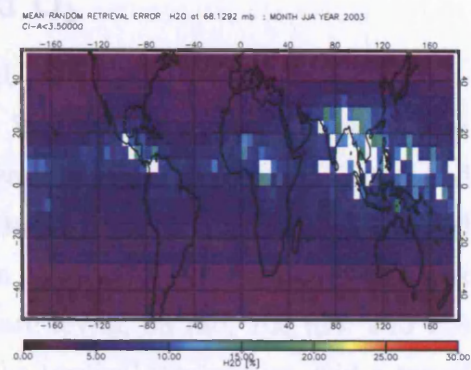
resolution snapshot of the data from which the variability in the mean concentrations and the errors can clearly be observed. Here, the effect of changing the longitudinal gridding is investigated with particular focus on the modulation in trace gas features and whether changing the averaging can change the interpretation of observed features and their corresponding estimated grid box error. In Figure 6.10, JJA MIPAS H₂O averaged concentrations and mean random retrieval errors at 68 mb with cloud filtering scheme A, are displayed using a latitude gridding of 5° and a longitude gridding of 5°, 10° and 15°, respectively. The 5° by 5° averaging shown in Figures 6.10(a) and 6.10(b) demonstrate the most variability in the mean concentrations particularly around the South Asian region with concentrations ranging from 4.5 to 6 ppmv. The corresponding estimated grid box error vary between 15 and 20 % amongst regions of missing data points. Increasing the longitude gridding to 10° (Figures 6.10(c) and 6.10(d)) removes some of the higher observed concentrations and emphasises drier concentrations over the North American and South Asian regions both with higher estimated grid box errors than the surrounding fields. Increasing the longitude averaging even further to 5°, 10° averaging as shown by Figures 6.10(e) and 6.10(f) tends to smooth out these dry features and their estimated grid box errors no larger than 10 % in contrast to some of the errors observed in the 10° longitude averaging case.

In some ways, the degree of averaging assigned to the data depends on the data requirement and all have different advantages. For example, the 5° by 5° averaging provides a diagnostic view of the data and certainly gives more information about the variability in the averaged concentrations and estimated grid box error. Regions where large variability may be due to cloud presence may in fact be hidden by the larger longitudinal averaging and therefore mask potential cloud effects (whether retrieval errors are real) in the data. However, for analysis of broad-scale structures, such as any contrasting features over landmass and oceans, a slightly less stringent spatial averaging like 5° by 10° may be more suitable. Using a larger averaging could potentially conceal “no data” regions although yield smoother large scale structures.

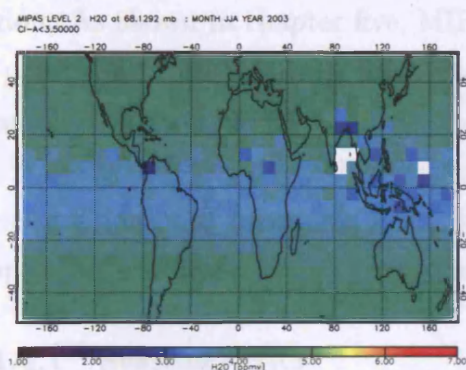
The MIPAS data maps shown in the remaining parts of this chapter will be represented on a 5° by 10° so that some of the variability is distinguishable as well as the locations of broader features.



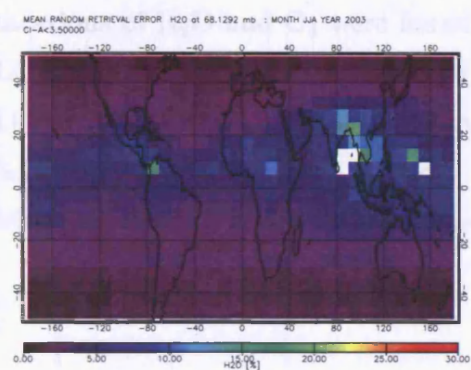
(a) 68 mb H₂O VMR with 5° averaging



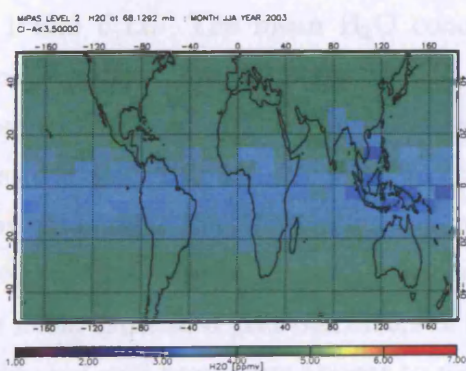
(b) 68 mb H₂O grid box errors with 5° averaging



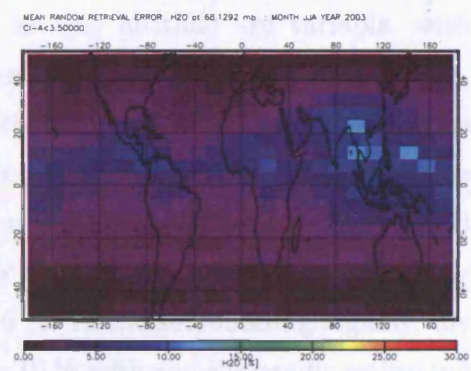
(c) 68 mb H₂O VMR with 10° averaging



(d) 68 mb H₂O grid box errors with 10° averaging



(e) 68 mb H₂O VMR with 15° averaging



(f) 68 mb H₂O random error with 15° averaging

Figure 6.10: JJA H₂O with varying longitude averaging. Note the effect of using larger longitudinal grid box size results in removal of "missing" data regions and less variability in the averaged concentrations and estimated grid box errors.

6.1.4 Seasonal analysis of H₂O and O₃

The seasonal behaviour of H₂O and O₃ captured by the MIPAS L2 data with tropical cloud filtering are now presented using the improved cloud filtering scheme A and the 5° by 10° averaging. The average concentrations for two seasons, DJF and JJA, with cloud filtering scheme A (removal of the tangent altitude above the cloud with the consecutive CI-A thresholds) are shown along with the estimated grid box errors. The data shown are for the three pressure levels, 68 mb, 100 mb, and 215 mb, that correspond to an upper tropospheric, the tropical tropopause, and a top of the TTL/lower stratospheric layer. A particular focus of this section is to evaluate the distributions of both gases that the MIPAS instrument observed in 2003 in this region. As shown in chapter five, MIPAS concentrations of H₂O and O₃ were found to possess a positive bias in comparison to HALOE and *in situ* measurements (for example, less than 15 % for MIPAS O₃ compared to SHADOZ at 50 mb and less than 10 % at 80 mb for MIPAS H₂O compared to Vaisala radiosondes). Here the mean concentrations will be quoted although the positive bias for both gases around the tropical tropopause must be kept in mind.

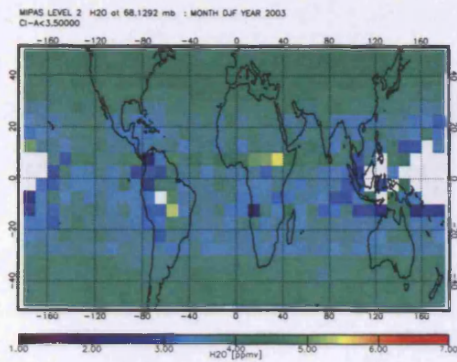
6.1.4.1 Seasonal H₂O

Beginning with H₂O, the mean concentrations and the corresponding estimated grid box errors, as measured by the MIPAS in DJF and JJA 2003 are shown in Figures 6.11 and 6.12. The mean H₂O concentrations at this altitude are variable, with concentrations from 20 ppmv to >60 ppmv observable over the east Pacific Ocean, close to the west coast of South America, over the Atlantic ocean and close to the west coast of Africa. In relation to the cloud occurrence frequencies, it can be seen that these region are particularly cloud-free (occurrence frequencies less than 20 %) meaning that these mean concentrations are likely to be valid as also demonstrated by the mean estimated grid box errors of less than 10 %. In the surrounding regions, the estimated grid box errors appear to remain below 10 % with some sporadic estimated grid box errors greater than 60 %. At 100 mb, the observed concentrations appear to have reduced dramatically, varying between 3 and 5 ppmv over most of the tropics and for most of these grid boxes, the corresponding estimated grid box errors remains close to 10 % or less. What is noticeable is that for regions where concentrations are

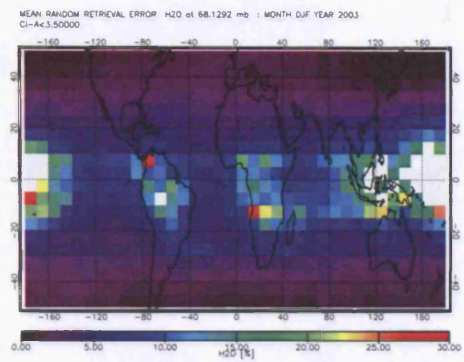
lower than or close to 3 ppmv, the estimated grid box errors tend to rise to as high as 60 % in some cases. Although any cloud based error has been removed using the verification of cloud effects from chapter four, the removal of data points in this region inadvertently results in an increase in the estimated grid box errors. Ascending higher in altitude to 68 mb, the mean concentrations for most of the tropics at this altitude are close to 3.5 ppmv with an associated estimated grid box errors of almost 5 %, rather similar to those observed by MLS [Clark et al., 2003]. The dehydrated features appear to be more widespread than those observed earlier by Clark et al. [2003] in regional patterns, such as close to the Equatorial Pacific, South America and African continents as well as over Micronesia. However, the concentrations tend to be closer to 2.5 ppmv (with associated estimated grid box errors close to 20 %) but appear to follow a similar pattern to that observed by MLS. It should be noted that in some of these regions, there are no more than 9 data points and combined with the fact that the estimated clear sky random error (refer to the Oxford University estimates shown in Chapter three, section 3.7) is larger here (approximately 25 %), this provides the reason for the increase in errors.

In JJA, the average concentrations nearer to the continents, particularly near Africa, Brazil and the East Equatorial Pacific ocean, vary between 60 and 80 ppmv with estimated grid box error less than 10 %. No data are available over the North American and South Asian regions consistent with the patterns of highest cloud occurrence and cloud tops. At 100 mb, the average concentrations over much of the tropics are >5 ppmv and wetter than those observed in DJF with the estimated grid box error less than 10 %. Lower concentrations close to 3.5 ppmv are prevalent in a distinctive band extending from Indonesia, over the Indian Ocean and part of the North Equatorial African region. However, these lower concentrations in the tropopause region correspond to greater estimated grid box error that in these cases are less than 20 %. Similar features of drier mixing ratios can be observed close to India at 68 mb, and most of the tropical regions are close to 3 ppmv over much of the tropics, with corresponding estimated grid box error of less than 5 %. At this time of the year, H₂O concentrations are influenced by a combination of the strong convective activity and association with the anti-cyclonic systems of the monsoon [Barry and Chorley, 1998].

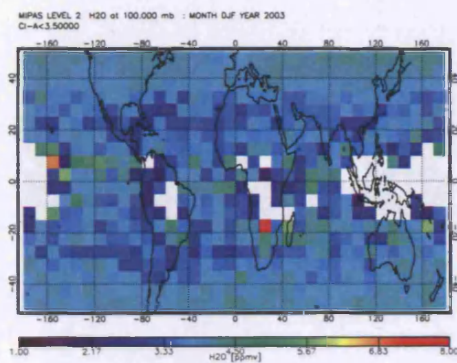
The seasonal distribution of tropical UTLS H₂O have shown distinctive behaviour



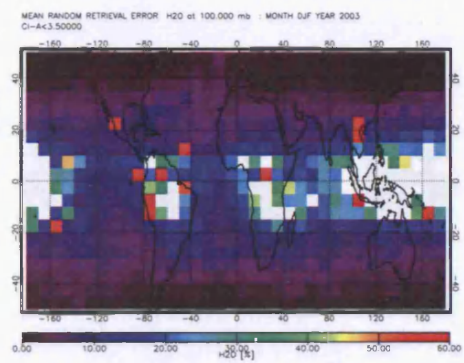
(a) 68 mb concentrations



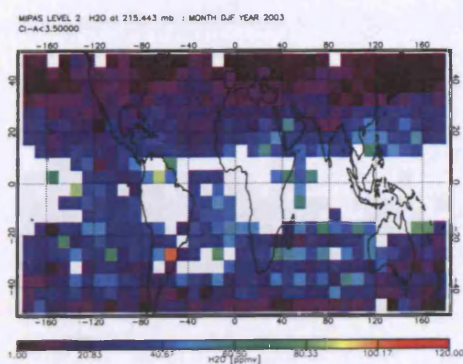
(b) 68 mb estimated grid box errors



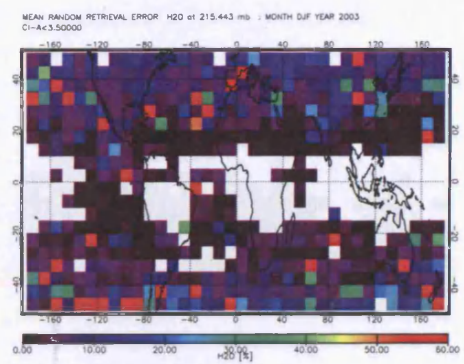
(c) 100 mb concentrations



(d) 100 mb estimated grid box errors

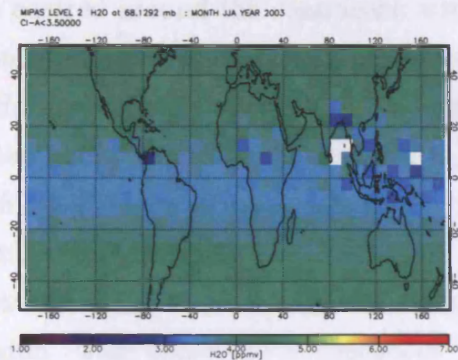


(e) 215 mb concentrations

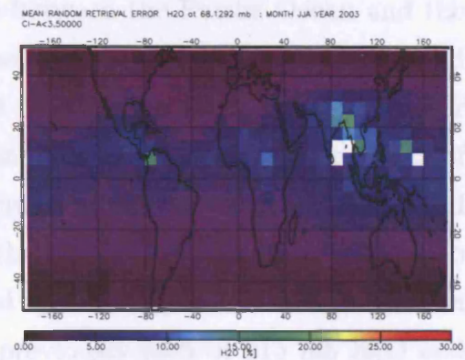


(f) 215 mb estimated grid box errors

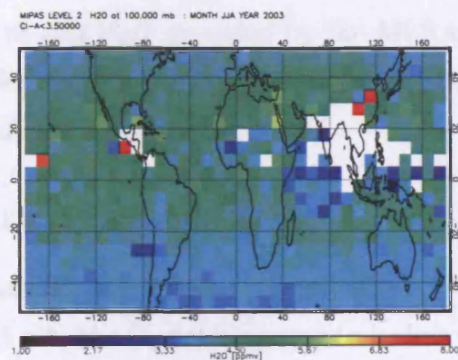
Figure 6.11: MIPAS H₂O for DJF at 68 mb, 100 mb and 215 mb cloud filtered with CI-A threshold of 3.5 under scheme A. White regions in the data indicate missing data.



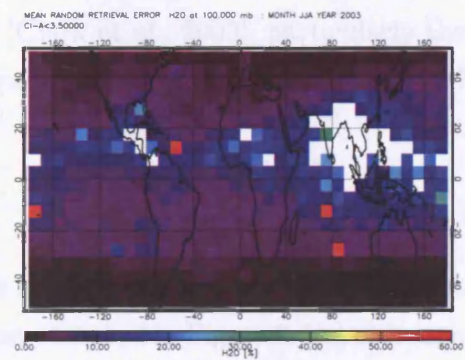
(a) 68 mb concentrations



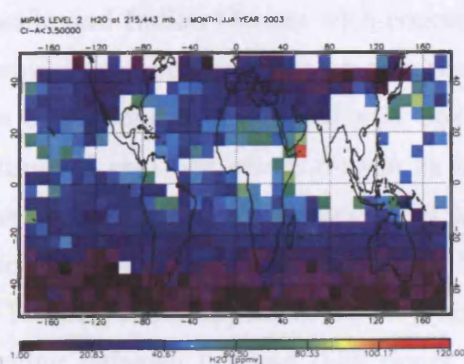
(b) 68 mb estimated grid box errors



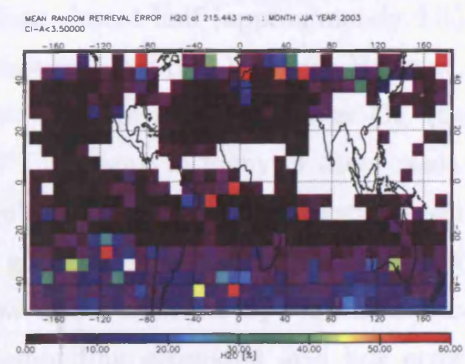
(c) 100 mb concentrations



(d) 100 mb estimated grid box errors



(e) 215 mb concentrations



(f) 215 mb estimated grid box errors

Figure 6.12: MIPAS H₂O for JJA at 68 mb, 100 mb and 215 mb cloud filtered with CIA threshold of 3.5 under scheme A. White regions in the data indicate missing data.

over certain regions in the tropics. In DJF, higher H₂O concentrations appear to be centred around the continents, with a region between the Pacific Ocean and the South America where lower concentrations (between 20 and 40 ppmv) and no cloud influence can be observed. Although the H₂O distribution is likely to vary over interannual timescales, the general H₂O field is similar to previous measurements of 215 mb H₂O concentrations from the MLS instrument Stone et al. [2000] who found similar concentrations in this region. In JJA, the higher concentrations appear to span all of the tropical longitudes but are shifted upwards over the Northern Indian region. This behaviour is consistent with that previously seen in 215 mb H₂O and upper tropospheric humidity distributions [Chen et al., 1999; Stone et al., 2000]. The distribution of H₂O at 68 mb is similar to that observed in previous measurements of 68 mb H₂O provided by the MLS instrument [Clark et al., 2003], particularly the drier regions off the west coast of South America and over much of the Pacific and Indonesian region.

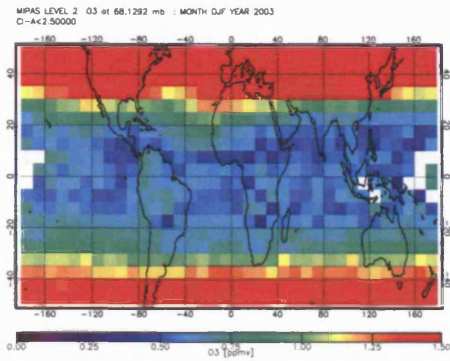
6.1.4.2 Seasonal O₃

Seasonal MIPAS O₃ concentrations are presented in Figures 6.13 and 6.14. In DJF at 215 mb, the O₃ fields appear to be less variable than observed in Figure 6.5(c) although this is probably also an effect of increased longitudinal averaging. The observed O₃ show a striking disparity over the South Atlantic Ocean in comparison to the Pacific and Indian Oceans with concentrations here almost half (approximately 0.05 ppmv) in comparison to those over the South Atlantic (close to 0.1 ppmv). However, the corresponding estimated grid box error shows that in regions of lower O₃, the estimated grid box errors remain as large as 60 % or more in many of these cases. The South Atlantic O₃ enhancement and some enhanced features over the south-east Pacific, however, yield estimated grid box errors generally less than 15 %. Ascending to 100 mb, there appear to be deep regions of low values with the O₃ concentrations varying between 0.1 and 0.25 ppmv with corresponding estimated grid box error close to 60 % or more for some of these regions. Over the south-east of the Pacific Ocean close to the west coast of South America, and the Equatorial Atlantic Ocean, estimated grid box errors are less than 20 %. At 68 mb, the O₃ concentrations vary between 0.5 and 1 ppmv with the latter appearing close to regions where clouds have a higher occurrence frequency. For a large extent of the tropics, the estimated grid

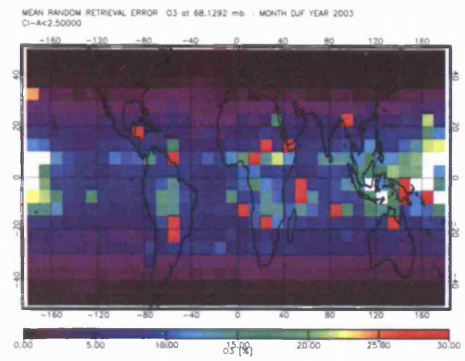
box error are less than 12 %. The behaviour shows much variability here with O₃ concentrations apparently elevated over South America however, with grid box errors close to 20 %.

In JJA, the enhanced O₃ feature observed in DJF is still a prominent feature in the South Atlantic region with random retrieval errors less than 10 % at 215 mb. Similarly, the lower concentrations observed over the Pacific and Indian Oceans remain but with some regions yielding lower random retrieval errors of less than 10%. At 100 mb, MIPAS O₃ concentrations appear to have increased in comparison to DJF towards the northern hemisphere. There is also a display of a distinct bands of low O₃ concentrations between 0.15 and 0.25 ppmv spanning across all tropical longitudes with estimated grid box errors between 20% and 60%. A distinct O₃ enhancement can be observed from the west coast of Africa, over northern Equatorial Africa and extending over the Indian Ocean with concentrations between 0.3 and 0.4 ppmv, corresponding to estimated grid box errors less than 20 %. Another distinguishable feature that has appeared in JJA is a region of reduced concentrations over Saudi Arabia, Northern India and North west China between 25°N and 35°N. The corresponding grid box errors are close to 30 % increasing to 60 % or greater. At 68 mb, the concentrations appear to be uniform and not as low as those observed in DJF. Recently, Folkins et al. [2006] examined the seasonal cycle of O₃ in SHADOZ data between 20°N and 20°S and similarly found a cycle where O₃ at 17 km were higher in JJA compared to those in DJF. Also visible in MIPAS data is a feature of potential mixing with mid-latitude O₃ appears over the South Asian subcontinent with more elevated estimated grid box errors close to 15 %.

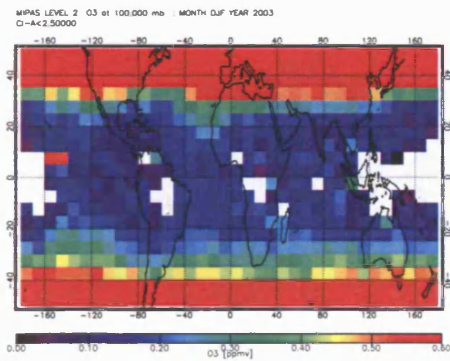
The continual O₃ enhancement observed in the upper troposphere in both seasons is consistent in terms of distribution with the zonal wave one maximum that has been reported by Thompson et al. [2003], Edwards et al. [2003] and Wang et al. [2006]. Similarly, the low upper tropospheric O₃ concentrations observed over the Pacific and Indian Oceans in both seasons are consistent with the low O₃ concentrations by observed in ozone sonde measurements over the Pacific by Oltmans et al. [2001] in other seasons.



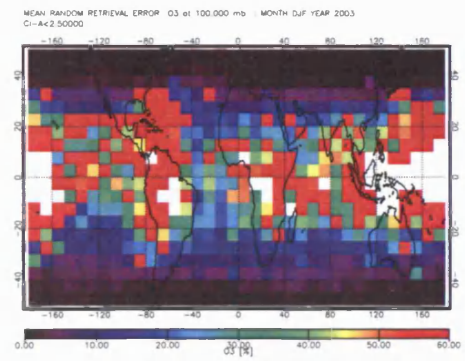
(a) 68 mb concentrations



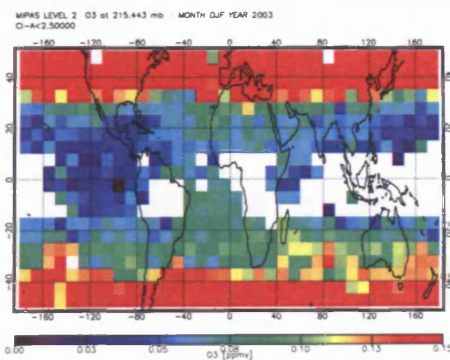
(b) 68 mb estimated grid box errors



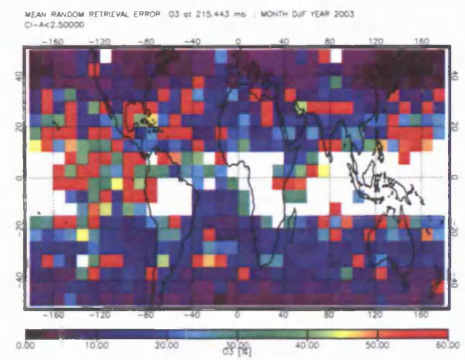
(c) 100 mb concentrations



(d) 100 mb estimated grid box errors

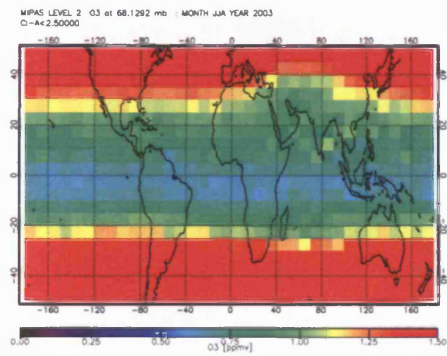


(e) 215 mb concentrations

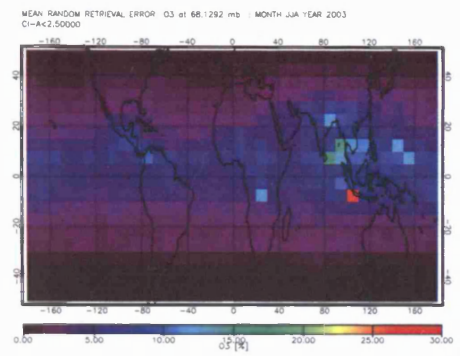


(f) 215 mb estimated grid box errors

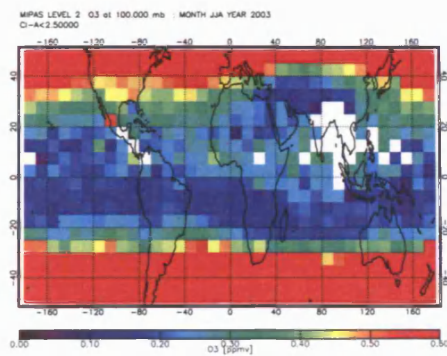
Figure 6.13: MIPAS O₃ for DJF at 68 mb, 100 mb and 215 mb cloud filtered with CI-A threshold of 2.5 under scheme A. White regions in the data indicate missing data.



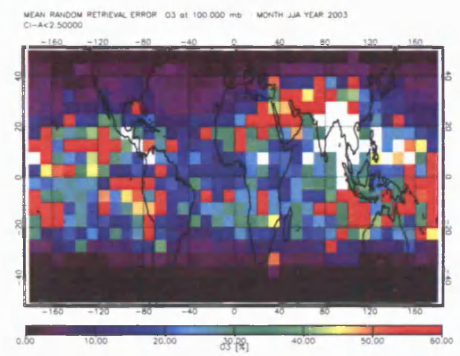
(a) 68 mb concentrations



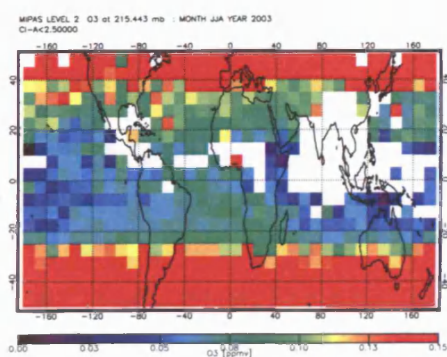
(b) 68 mb estimated grid box errors



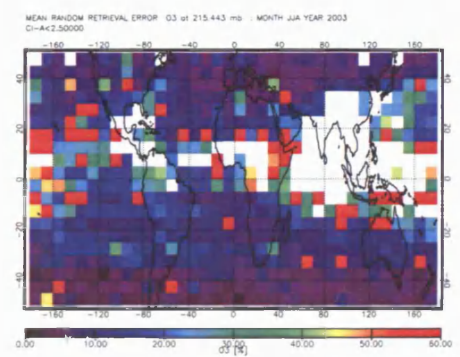
(c) 100 mb concentrations



(d) 100 mb estimated grid box errors



(e) 215 mb concentrations



(f) 215 mb estimated grid box errors

Figure 6.14: MIPAS O₃ for JJA at 68 mb, 100 mb and 215 mb cloud filtered with CI-A threshold of 2.5 under scheme A. White regions in the data indicate missing data.

6.1.5 Regional analysis of MIPAS H₂O and O₃

The examination of MIPAS H₂O and O₃ under the improved cloud filtering schemes have shown that in particular regions of the UTLS, despite the large retrieval uncertainty in MIPAS H₂O and O₃ in some regions, particularly near the cold tropopause, some robust features of enhanced or reduced concentrations can still be identified. Unfortunately, the enhanced cloud filtering also means that the number of fitted grid boxes reduce and the estimated grid box error also increases in accordance with the decreasing numbers in each box. Using this scheme also means that in some regions, no data coverage is possible over many tropical regions due to a large number of contaminated scans being removed. Regions of potential interest that may be analysed using operational MIPAS tropical UTLS with additional cloud filtered data are:

1. The Western Pacific and Micronesian region for an indication of dehydrated air as shown by reduced H₂O concentrations in the tropical lower stratosphere and tropopause [Holton and Gettleman, 2001].
2. Equatorial Africa, Central and South America for possible biomass burning induced O₃ enhancements in the upper troposphere [Diab et al., 2003].
3. Zonal wave-one activity over the South Atlantic basin to indicate regions of O₃ enhancement [Thompson et al., 2003].
4. North American and South Asian monsoon regions for analysis of H₂O and O₃ fields in the tropopause region [Gettelman et al., 2004b].

In the following sections, the seasonal evolution of H₂O and O₃ fields in selected seasons and tropical regions in the UTLS layer are presented.

6.1.6 Investigating the South Atlantic O₃ enhancement

The origin of the South Atlantic O₃ maximum is a well documented and a fine example of the merging of photochemical and dynamical processes [Valks et al., 2003; Edwards et al., 2003; Thompson et al., 2004]. In both continents surrounding the South Atlantic ocean, biomass burning occurs throughout the year and is a major source of O₃ precursors such as CO, NO_x and VOCs [Sinha et al., 2004; Sauvage et al., 2007]. The motion of reactive pollutants into the upper troposphere through

deep convective clouds can lead to a 3-4 times increase in O_3 concentrations and both South America and Africa are primary contributors to the south Atlantic O_3 maximum [Thompson et al., 1997]. Some of the O_3 pollution in this region also travels eastwards towards the Indian Ocean although much of the lower O_3 concentrations as observed in the Eastern part of the Indian Ocean. The large abundance of precursors close to the South Atlantic are thought to be recirculated in the anti-cyclonic flow that directs air towards the west coast of Africa prompting an O_3 buildup. Some of the O_3 is formed due to South American biomass burning that is also directed to this region of subsidence. Edwards et al. [2003] reported that O_3 precursors that are emitted in northern hemisphere African burning during the dry season are actually advected southwest towards and over the ITCZ and into the region of the South Atlantic. This effect is often called the South Atlantic “ozone paradox”.

The O_3 maxima is not attributed to African biomass burning alone: Martin et al. [2000] attributed 20 % of the tropospheric O_3 observed in a fourteen year record of tropical tropospheric O_3 columns over the South Atlantic to lightning induced NO_x formation. It is possible that some of this signal could contribute to the upper tropospheric O_3 signature in this region. Recently, Chatfield et al. [2004] and Chatfield et al. [2007] found that some of this Atlantic upper tropospheric O_3 could also be attributed to convective lofting of O_3 precursors from the Indian subcontinent. Alternative suggestions were made earlier by Suhre et al. [1997] who observed O_3 -rich air of stratospheric origin in upper tropospheric air measurements obtained from MOZAIC aircraft flying near 12 km. Some of the O_3 rich signal was observed near regions of cumulus anvil clouds and the downward transport of stratospheric O_3 was attributed to either: 1) downward transport of O_3 -rich air in falling ice particles, following the overshooting anvil reaching the lower stratosphere or 2) quasi-isentropic transport of O_3 -rich air entering convective regions near the aircraft.

In contrast to the signatures observed over the south Atlantic, O_3 -poor air has been documented over the Pacific Oceans [Thompson et al., 2004] and are related to the uplift of clean O_3 -free air associated with deep convection in these regions. O_3 concentrations are generally lower over the Pacific upper troposphere [Oltmans et al., 2001] with reduced or near zero concentrations attributed to deep convection and horizontal transport and O_3 destruction from photochemical reactions involving hydrogen radicals [Solomon et al., 2005].

Here, the south Atlantic feature observable in MIPAS O₃ in DJF and JJA is investigated further. In Figure 6.15 upper tropospheric O₃ in the region between 120°W and 60°E, 20°N and 40°S, covering the North Pacific, South Atlantic, South America and Equatorial African regions are shown for each season. The figures show that the south Atlantic O₃ enhancement exists throughout the year with concentrations increasing in the SON season. The concentrations in this region tend to be at least 40 % higher than those observed in the North Pacific Ocean. Similarly, the O₃ concentrations tend to be higher over Southern Africa, around 0.11 ppmv, extending over the continent, towards the Indian Ocean and Madagascar. The concentrations also tend to become enhanced over the South American region.

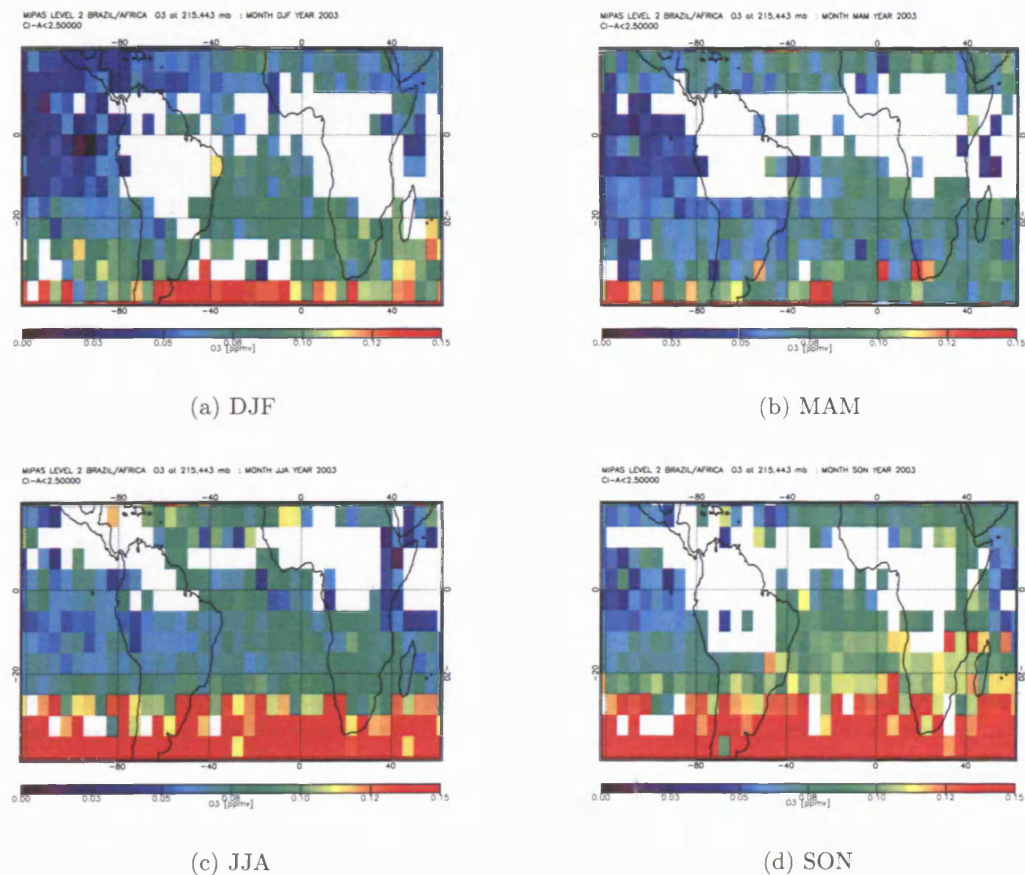


Figure 6.15: Brazil and Africa O₃ concentrations shown with the zonal wave-one regions of the South Atlantic and Pacific oceans

In Figure 6.16, a longitude versus pressure cross section from the Equator to 20°

South is shown for each season. All seasons show a region of enhancement, of O_3 concentrations greater than 0.08 ppmv, between $40^\circ W$ and close to $60^\circ E$. A similar O_3 enhancement over the same region was observed in a seventeen year SAGE II O_3 climatology [Wang et al., 2006] and in a four year ozonesonde climatology of SHADOZ ozonesonde data [Thompson et al., 2003], although in these studies, the O_3 concentrations were closer to 0.045 ppmv. This behaviour of MIPAS showing concentrations higher than those observed by other instruments is consistent with the results of the tropical MIPAS O_3 validation (against SHADOZ) performed earlier in this thesis.

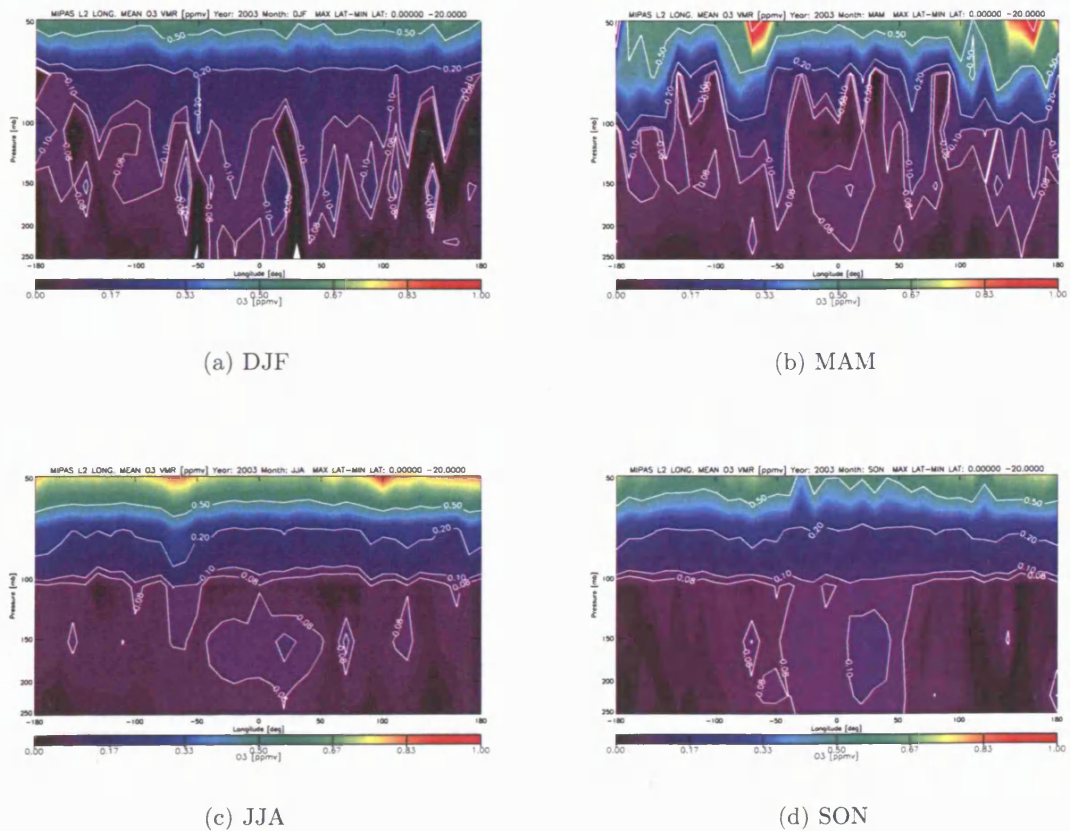


Figure 6.16: Longitude-Altitude cross section of O_3 from Equator to 20° South. Note the region of enhanced O_3 close to the Greenwich meridian from 215 to approximately 150 mb in DJF, MAM and JJA.

The vertical extent of the MIPAS O_3 maximum, in comparison to the Pacific

region can be seen further by analysing the southern hemisphere longitude mean O_3 concentrations on selected pressure layers in the tropical UTLS. Figures 6.17 to 6.20 show the mean O_3 concentration along the longitude coordinate at 215 mb, 147 mb, 100 mb and 68 mb for each season. In each sub-figure, the black line corresponds to the mean of the retrieved concentrations, and the blue line corresponds to the estimated grid box errors in the chosen latitude band of 17.5°S , so that the variability close to the O_3 maximum can be captured. Each sub-figure is labelled with the pressure level that it corresponds to. The top left hand plots of each figure shows the mean concentration, over all longitudes at the 215 mb layer. In all 215 mb plots, maximum concentrations occur slightly east of the Greenwich meridian and tend to become smaller on either side towards 180°E and 180°W . The corresponding errors give some indication of the estimated standard deviation one can expect from these features, with the removal of suspected clouds. It appears that for lower mean concentrations, higher estimated grid box errors tend to occur although this is not always true (for instance MAM and JJA at 215 mb). Some of this behaviour extends into the 147 mb layer with a slight increase in concentrations. Despite regions of large estimated grid box errors, some definitive structure is evident at particular altitudes. Some indication of a wave-one like structure is evident in most of the 215 and 147 mb layers. The longitudinal variation of O_3 at 100 mb appears to be much more variable with concentrations varying from 0.05 ppmv to as high as 0.3 ppmv, with estimated grid box errors often comparable to the actual retrieved concentrations. The difficulty in retrieving O_3 near the tropopause was demonstrated in chapter four and is evident here in the random retrieval errors. At 68 mb (bottom right hand plot in Figures 6.17 to 6.20), concentrations remain between 0.6 and 0.8 ppmv with some variability over the longitudinal range in DJF. In the JJA season, concentrations tend to become slightly lower towards the east of the African continent near the top of the TTL/lower stratospheric region. In SON, the wave-one like feature is evident at 215 and 147 mb, however, such behaviour does not appear at 100 and 68 mb (similar to throughout the rest of the year). This would suggest that the source of enhancement might not be the stratosphere but rather enhanced production in the troposphere.

In order to examine whether South American and African biomass burning may be contributing to the enhanced MIPAS O_3 feature over the South Atlantic, seasonal

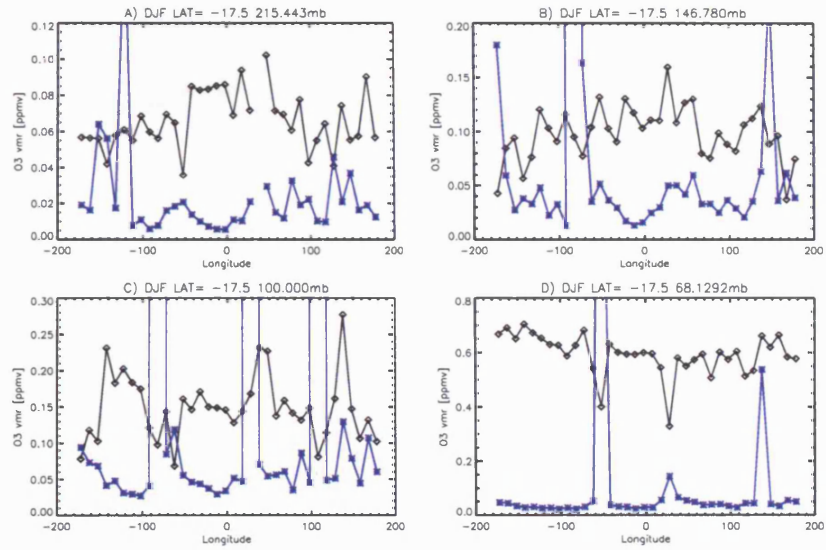


Figure 6.17: Vertical structure of SH O₃ in DJF

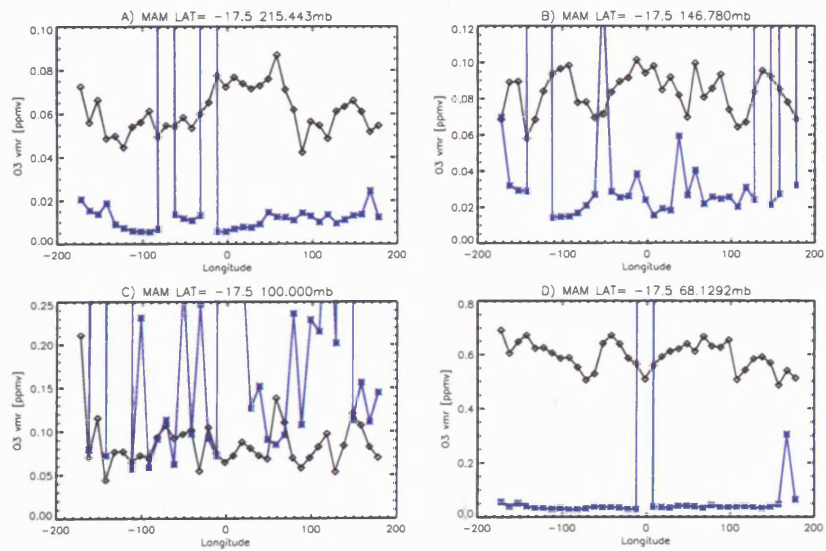


Figure 6.18: Vertical structure of SH O₃ in MAM

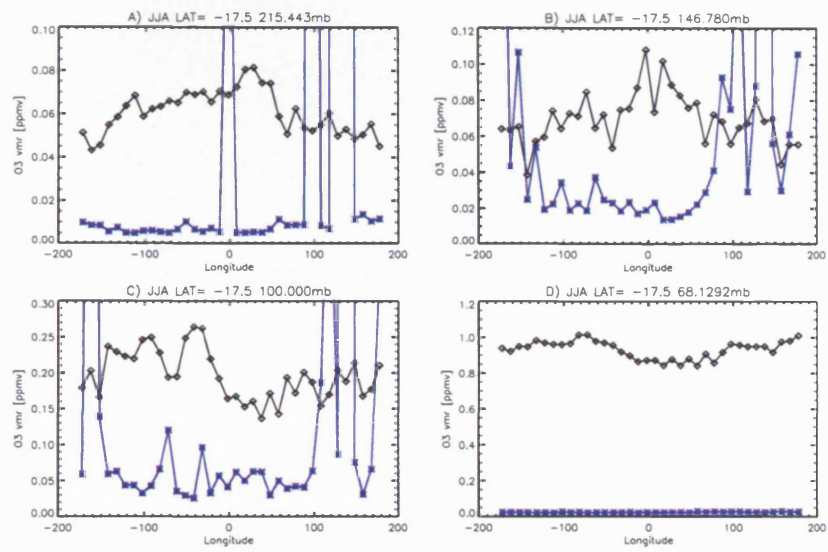


Figure 6.19: Vertical structure of SH O₃ in JJA

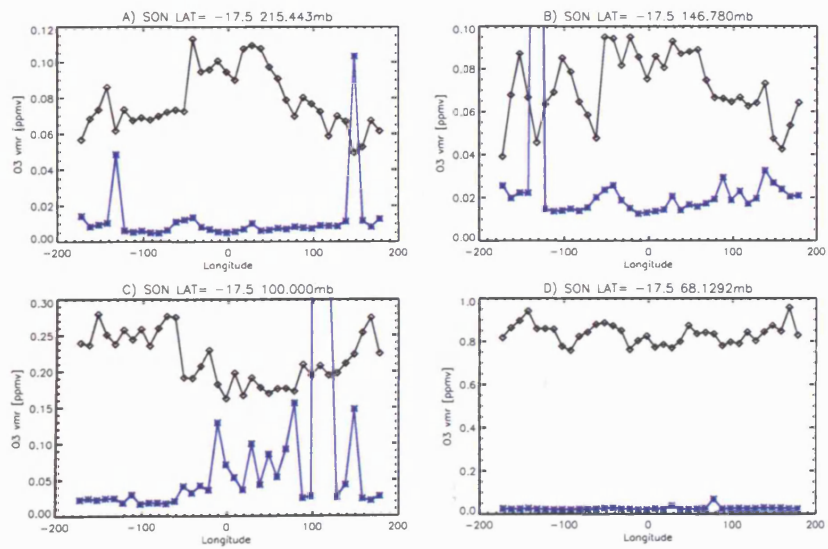
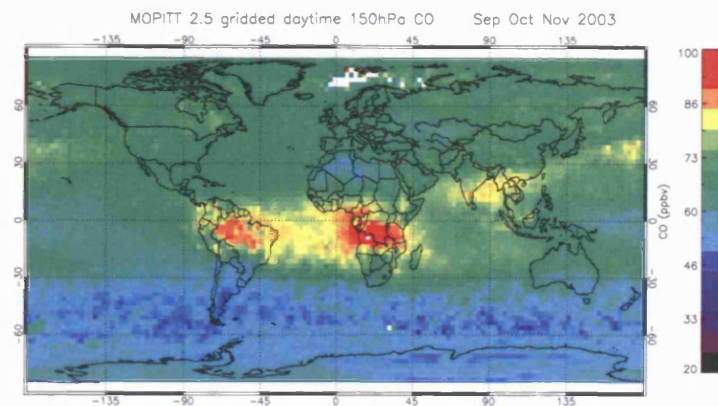
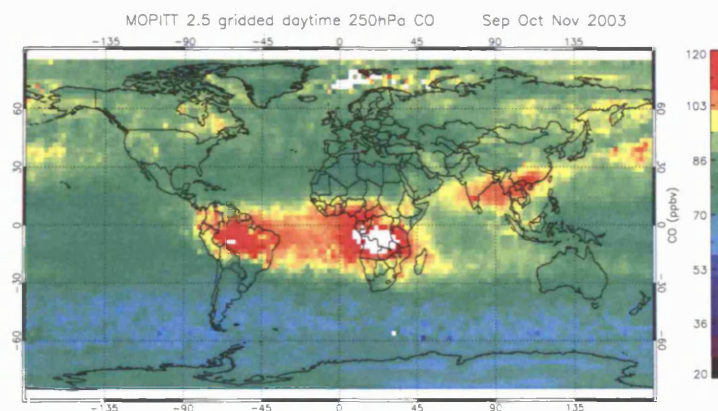


Figure 6.20: Vertical structure of SH O₃ in SON



(a) MOPITT CO at 150 mb



(b) MOPITT CO at 250 mb

Figure 6.21: Global maps of MOPITT CO at 150 and 250 mb for SON 2003. Note the CO enhancements visible over west coast of Africa. Courtesy of V. Kanawade, University of Leicester

maps of tropospheric CO measured by the Measurements of Pollution in the Troposphere (MOPITT) instrument are analysed. In Figure 6.21, the data for SON 2003 at 150 mb and 250 mb daytime measurements are shown. Enhanced CO features of concentrations greater than 100 ppbv are seen over South America and South Africa spanning directly across the South Atlantic Ocean at 250 mb with evidence of this feature still observable at 150 mb. Some higher CO concentrations (>90 ppbv) can be seen extending eastwards toward the Indian Ocean. A comparison of these high MOPITT CO signatures appear to be coincident with the enhanced MIPAS O₃ features observed in the same season (Figure 6.15(d)) suggestive of the fact that the MIPAS

O₃ may be related to the same processes during elevated CO over the Atlantic.

Overall, the patterns observed in the MIPAS O₃ profiles are in agreement with the general consensus that broad O₃ enhancements occur over the South Atlantic with reduced O₃ concentrations over the east and west Pacific Oceans [Takashima and Shiotani, 2007]. The advantage of using MIPAS limb observations is that certain features such as the vertical evolution of the O₃ maxima can be observed at each tangent height. The feature appears to have remained persistent throughout the year despite the larger errors associated with the measurements and the difficulty in sounding this region. From the longitude versus altitude cross sections, the lack of O₃ enhancements observed at 100 mb suggests that such features may be of tropospheric origin and therefore potentially related to the biomass burning rather than of stratospheric. Recently, von Clarmann et al. [2007] observed similar enhancements of O₃ and C₂H₆ from MIPAS data retrieved from the IMK operational processor and found these to be associated with a southern hemisphere biomass burning plume and not from a stratospheric source. The behaviour observed in the longitudinal cross sections (Figure 6.16) may suggest a similar reason for the enhancements observed.

6.1.7 Evidence of monsoon signatures in MIPAS H₂O

In boreal summer, a deep, upper-level anti-cyclonic system develops associated with an elevated Plateau (>4 km) in Tibet to the north of India and covering a range of 70-105 °E and 25 - 40 °N [Barry and Chorley, 1998]. This large scale topographical feature induces the summer monsoon season over Northern India. Similar monsoons are observed over Africa and North America due to continental sea breeze circulations. The North American and Indian Monsoons, with the Indian monsoon a more prominent and isolated event, is a direct example of stratospheric-tropospheric air exchange with rapid meridional transport of tropospheric air directly into the lower stratosphere bypassing the cold point tropopause completely, up to a maximum height of 30 mb [Dunkerton, 1995].

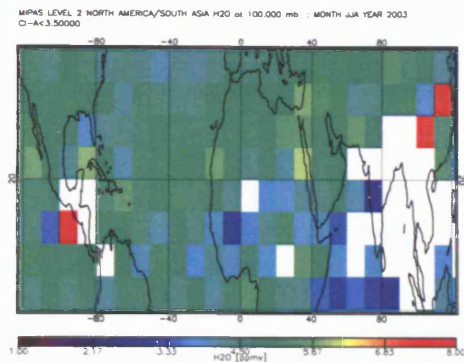
Several satellite observational studies have focused on the South Asian and North American monsoons and discovered enhanced H₂O concentrations due to the intense convective uplifting of moist air into the lower stratosphere. Randel et al. [2001] used nine years HALOE H₂O and SAGE O₃ data to show that H₂O concentrations are similarly enhanced to greater than 4.6 ppmv in the lower stratosphere (390 K,

approximately 83 mb) with simultaneous low O₃ (less than 0.15 ppmv) regions indicating a strong coupling to the troposphere. These results were mirrored by the analysis of Gettelman et al. [2004b] who showed 100 mb HALOE concentrations of H₂O close to 5.25 ppmv over the summer monsoon and 4.6 ppmv over the North American monsoon region in July. Coincident O₃ measurements from SAGE showed that O₃ concentrations were of less than 0.2 ppmv over South Asia and close to 2 ppmv over North America. Their results compared well to MOZART model simulation of these fields, although HALOE was slightly drier than the model, and attributed the summer monsoon to be responsible for at least 75 % of the net upward moisture flux into the tropopause region. At the chosen levels observed here, the effect of the anti-cyclonic monsoon activity appears to have been captured suitably by the MIPAS measurements.

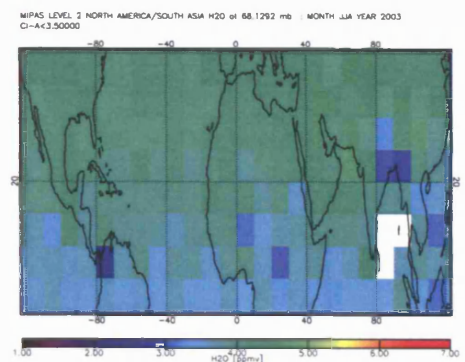
To determine whether monsoon effects can be observed in MIPAS operational H₂O measurements in the tropical UTLS, MIPAS H₂O in particular seasons and regions are analysed.

Figure 6.22 shows latitude-longitude cross section of MIPAS H₂O measurements over 0° to 40°N and 120°W to 120°E. Also shown are the corresponding O₃ measurements for the same season and location. At 100 mb, regions close to North America and South Asia/China show enhanced H₂O concentrations amidst regions of missing data due to the cloud filtering. Higher up at 68 mb, concentrations remain close to 5 ppmv over China, Northern India with similar concentrations over Mexico. The O₃ fields over the same region at 100 mb show distinctive reduced O₃ concentrations, close to 0.15 ppmv, over much of Northern India. Higher at 68 mb, the same region appear to show mixed concentrations and particularly interesting about this feature is that no distinction between the mid-latitude subtropical jet region and the tropics can be made.

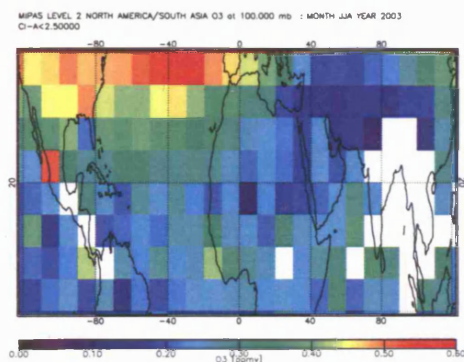
The longitude mean cross sections, and vertical extent of these features, with their corresponding errors, for H₂O and O₃, are evaluated in Figures 6.23 and 6.24. Although it is quite difficult to distinguish obvious features in some of the regions, particularly those close to the Monsoon region, because of cloud filtering, the general enhancements or reductions can potentially be deduced from the data available in these regions. Unfortunately, the mean longitudinal concentrations of H₂O at 215 mb are removed around 100°E over the Indian sub continent and 100°W over



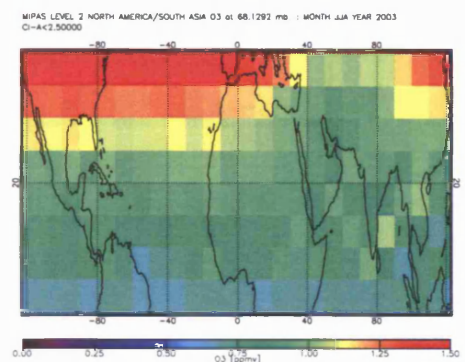
(a) H₂O at 100 mb



(b) H₂O at 68 mb



(c) O₃ at 100 mb



(d) O₃ at 68 mb

Figure 6.22: H₂O and O₃ at 68 mb and 100 mb in JJA over the North American and Summer Monsoon regions. The figures show potentially elevated H₂O regions close to the Asian Monsoon region with a corresponding reduction in O₃ concentrations at 100 mb.

the North American Monsoon region where elevated H₂O concentrations would be expected. Certainly at higher altitudes, at 100 mb, there appears to be some evidence of increased H₂O concentrations over North America and Asian monsoon regions with concentrations greater than 5 ppmv with corresponding random retrieval errors low in these regions.

Recently, Milz et al. [2005] observed enhancements of H₂O over the Arabian Peninsula in JJA at 18 km and attributed such enhancements (VMR > 5.5 ppmv) to the Summer Monsoon in the IMK retrieved H₂O product that is flagged using a CI-A threshold of 4.0. The feature observed here, in the operational data with more stringent cloud filtering does not appear to be as enhanced as that observed by Milz et al.

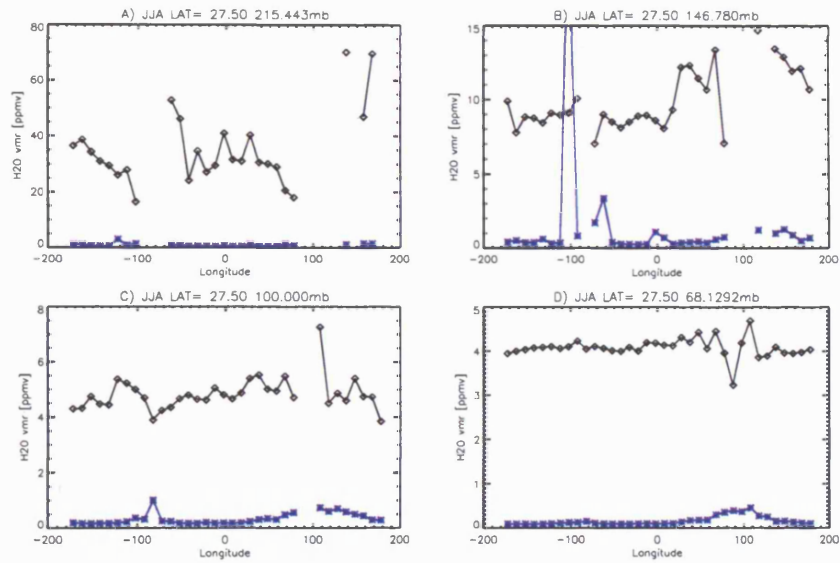


Figure 6.23: Vertical structure of NH H₂O in JJA

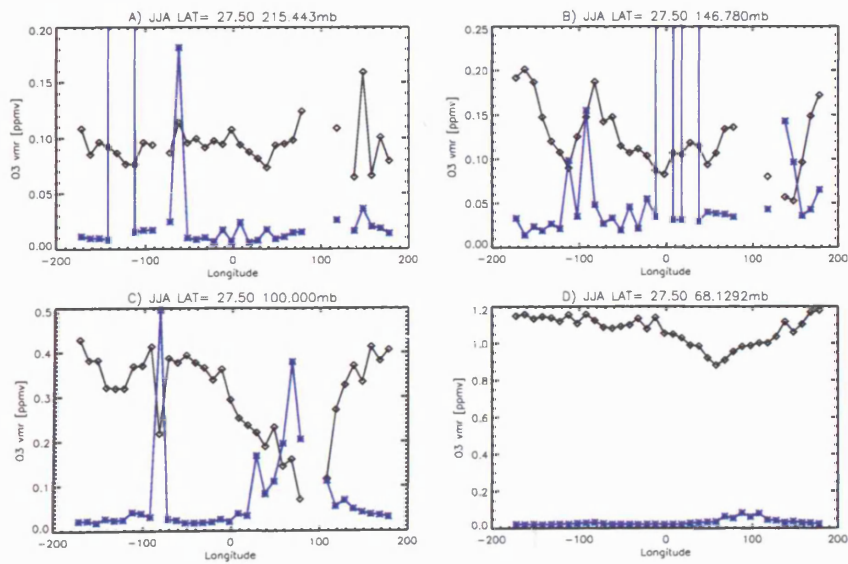


Figure 6.24: Vertical structure of NH O₃ in JJA

[2005] (here it is closer to 5 ppmv) and this difference is potentially due to the different cloud filtering schemes applied between the two datasets.

6.1.8 Summary

The results presented here evaluated the performance, in terms of estimated grid box errors and average retrieved concentrations, of the operational cloud filtered MIPAS data against the cloud filtering schemes presented in chapters four and five. The methods used were formulated to manipulate the operationally retrieved MIPAS data in a region where H₂O and O₃ retrievals are inevitably affected by high cloud presence as well as large retrieval errors. Based on the evidence of cloud effects as well as the performance of MIPAS H₂O and O₃ from previous chapters, more stringent cloud filtering schemes were applied to H₂O and O₃. The two major caveats related to this are: a) often a significant amount of data (sometimes up to 40 % more data compared to operational data) are removed from the operational dataset meaning that regions where dynamically or chemically induced features may be observable were in fact inaccessible and b) the estimated grid box error becomes “worse” with the removal of data points from the analysis.

Conversely, the application of more stringent cloud filtering results in the removal of potentially cloud biased data points and impacts the calculated average concentrations observed in the seasonal distributions shown in Figures 6.11 to 6.14. Calculations of apparent cloud top pressures and cloud occurrence frequencies have shown that clouds are present continuously, often with occurrence frequencies greater than 80 % in the tropical UTLS. Nonetheless, it is possible to use the operational data for analysis of the tropical UTLS region however, knowledge of the cloud index and cloud distributions are important tools that must be used in conjunction with the data.

To summarise, MIPAS L2 data used to examine H₂O and O₃ fields in the tropical UTLS were used to show:

1. Regional variability in H₂O and O₃ concentrations were observed at 215 mb, 100 mb and 68 mb in the operationally cloud filtered data and the corresponding estimated grid box errors often showed similar variations at each altitude.
2. The effects of the two proposed cloud filtering schemes were compared to the

operationally filtered MIPAS H₂O and O₃ data. These schemes involved removing the altitude above the cloud altitude and conversely, only removing the cloud affected altitude.

3. From these two schemes, it was seen that at 68 mb, apparent dehydrated H₂O regions were removed following a more stringent cloud filtering and for O₃, regions of apparent enhancements such as over the Central America were removed.
4. For H₂O, using a more stringent cloud filtering maintains estimated grid box errors of less than 10 % at 215 mb and estimated grid box errors less than approximately 7 % at 68 mb.
5. For O₃, using a stringent cloud filtering scheme maintains the majority of the estimated grid box errors at 215 mb to a level less than 30 % and at 68 mb, the estimated grid box errors tend to be less than 20 %. However, some O₃ measurements suffer from large estimated grid box errors (often larger than 60 %), particularly around colder temperatures.
6. The consequence of using a more stringent cloud filtering is a reduction in the number of data points meaning that the precision also decreases relative to this reduction in the number of samples. This can make it difficult assess the impact of the more suitable cloud filtering on the random retrieval errors.
7. MIPAS H₂O and O₃ concentrations through the UTLS are observed for DJF and JJA in 2003 at the 215 mb, 100 mb and 68 mb layer. For H₂O in DJF, much of the data are removed over the Pacific cold trap region, the south American and African continents and much of Micronesia at 215 mb due to increased cloud filtering.
8. Following the application of more stringent cloud filtering schemes, some features in seasonal MIPAS H₂O and O₃ were observable such as apparent regional dehydration in DJF at 68 mb over the west Pacific, Africa Brazil. Widespread drier concentrations at 100 mb in DJF compared to more variable, wetter concentrations in JJA.
9. For O₃, regions of low values can be observed throughout the tropics with evidence of enhancements over Brazil at 100 mb and 68 mb in DJF. In JJA,

higher concentrations of O₃ can be observed north of equator, possibly related to the ITCZ movement with some apparent low concentrations over the Summer Monsoon region. A similar band of low O₃ region can be observed at 68 mb.

10. Two regions where apparent features of enhancements can be seen are the zonal wave-one O₃ maxima and the South Asian Monsoon region. Both regions were analysed here and it was found that the O₃ maxima persists throughout the year and appears to be significantly stronger in the SON season. MOPITT CO maps for the same season verify that pronounced biomass burning in the exact same region and time can be observed. Longitude vs. altitude cross sections suggest that the source of this feature is likely to be tropospheric.

Features of enhanced H₂O were examined for the Summer Monsoon period and in relation to features observed in the IMK MIPAS H₂O retrievals [Milz et al., 2005], high H₂O was observed but not to the same magnitude of that observed in the IMK case. O₃ fields over the same region showed low O₃ concentrations suggesting that uplift of low O₃ could be the reason for such values.

11. Using these methods are the only way to manage the operational pre-processed data to obtain “accurate” near-clear sky estimates of two species that are heavily affected by chemistry and dynamics in this complex region.
12. With knowledge of how the retrievals are affected, we can make recommendations on how to improve the data.

Chapter 7

Conclusions and future work

7.1 Summary of conclusions

In this thesis, the aim was to examine H₂O and O₃ distributions measured by the MIPAS instrument from the ENVISAT platform in the tropical UTLS, a region where both H₂O and O₃ concentration profiles have sharp vertical gradients, and where a variety of clouds exist, often persistently and reaching high altitudes. In particular, the aim of this project was to examine whether tropical UTLS distributions of these gases, in both “clear sky” and thin cloud conditions, could be inferred from profiles retrieved from the infrared measurements made by the MIPAS instrument.

The work undertaken in this thesis was based on the offline (i.e reprocessed) operationally retrieved MIPAS versions 4.61 and 4.62 data. No additional data were retrieved in this analysis and all results focussed on analysis of the operational offline dataset. As necessary, before the data can be used for scientific interpretation, a major part of this thesis has been concerned with an assessment of the factors that could affect the quality of the data and how the impact of these factors lessened post-processing. The analysis performed followed three distinctive routes that will be discussed in turn below with a short summary of the main findings and their scientific application to MIPAS data.

In chapter four, following an evaluation of cloud statistics for the tropical UTLS region and the cloud removal technique used operationally by the L2 processor, the impact of clouds on the retrieved products from the L2 processor was investigated. The focus of this part of the study was to examine how clouds, given a definition of

cloud index values from MIPAS band A (CI-A), propagate into the retrieved products due to their contributions to the measured radiances. This is the most comprehensive study so far that has examined such an effect for the operational MIPAS processor.

The examination of the impact of cloud on MIPAS L2 retrievals of H₂O and O₃ using model simulations of representative cases for MIPAS retrievals has revealed a number of results; as postulated, the current cloud detection thresholds do not sufficiently allow the effects of thin clouds to be removed from the operational MIPAS product and:

1. For H₂O, it was found that concentrations tended to be enhanced in the presence of cloud and were simultaneously negatively biased above the cloud. These deviations in the profiles from expected climatology appeared to enhance the instabilities already present in the retrievals.
2. For O₃ the results obtained showed that the retrieved concentrations in these regions are dominated by a combined effect of atmospheric conditions (i.e colder temperatures in this region), low concentrations and increased random error and that the primary effect of cloud tended to make the random retrieval error larger. Systematic cloud effects will be present but are masked by the random error on the profile.
3. In terms of improved cloud filtering, a suitable CI-A threshold suggested to remove these effects was 3.5 for H₂O with removal of the cloud-affected sweeps at CI-A <3.5 and the altitude above. This allowed the systematic bias on the H₂O of more than 5 % at the cloud altitude and more than 10 % above the cloud altitude to be removed. At 18 km, a CI-A of 2.5 or larger, would allow profiles with a cloud induced systematic bias larger than 10 % to be removed. For more stringent clearing, a CI-A of 3.5, that allows almost no deviation, would be suitable.
4. A CI-A value of 2.5 or larger from the cloud tests suggested that for O₃, the random error would remain approximately within 20 % at 12 km (and 10 % at 18 km) of expected clear sky error. In all cases, the estimated systematic biases and the random retrieval errors were found to improve using this threshold in comparison to the cloud effects observed at values close to or equal to the operational cloud filter of 1.8.

The cases presented in this section were representative cases for the operational MIPAS data set for the tropics and the results from this analysis were then applied to an intercomparison study of MIPAS H₂O and O₃ with correlative solar occultation and *in situ* instruments in chapter five. Both the operationally and extra cloud filtered MIPAS H₂O and O₃ profiles were compared to profiles from the HALOE version 19 dataset, to ECC ozone sondes from the SHADOZ network and Vaisala radiosondes launched on the Explorer of the Seas. A comparison of the performance of the operational and cloud filtered data showed that in all intercomparisons, for both H₂O and O₃, the impact of using an increased cloud filter improved the bias between MIPAS and correlative instruments, which was almost always observed to be positive in relation to the comparison data.

For Vaisala radiosondes, the comparisons were good close to 200 mb and 80 mb with differences often less than 10%. However, it was difficult to assess the quality from these comparisons at the tropopause and the lowermost stratosphere, for two main reasons: a) the radiosondes performed inadequately in the lower stratosphere where humidity is low and often the associated error increases and b) the applied corrections are affected by the cold temperatures near the tropopause in which case they often resulted in unrealistically low concentrations and c) the statistical representation of the Vaisala radiosondes was often poor in some cases. The Vaisala and MIPAS comparisons however highlighted some of the difficulties encountered by both limb sounders such as MIPAS and *in situ* instruments in observing the tropical tropopause region.

Generally, for MIPAS H₂O, comparisons to HALOE showed a better agreement close to 215 mb when using a cloud index 3.5 (and altitude above) for cloud filtering. When compared to the corrected Vaisala radiosondes, using a CI-A threshold larger than the operational also improved the agreement between the two. At altitudes higher than 80 mb, generally the varying schemes used (with and without removal of the altitude above) did not change the agreement drastically between MIPAS and HALOE and the differences remained within 20 % at 80 mb and 10 % at 50 mb.

For O₃, the primary data set were the SHADOZ profiles. The results showed that the more stringent cloud filtering schemes certainly improved the agreement between MIPAS and SHADOZ close to 215 mb (within 10 %), with some marginal improvements (within 13 %) observed at 50 mb. However, in the MIPAS O₃ SHADOZ

comparisons and in all comparisons in general (including MIPAS H₂O) with correlative instruments, agreement was worse, and remained unchanged with increased cloud filtering near 150 mb suggesting that, MIPAS as well as both HALOE and the *in situ* instruments, perform poorly here (high random errors; uncertain bias). The colder temperatures and sharp gradients of both gases may well be the dominating factors controlling the errors in the retrieved concentrations observed here.

For MIPAS O₃, the comparisons to HALOE O₃ showed that MIPAS was consistently higher than HALOE and that under the cloud filtering schemes, the data were in closer agreement to HALOE at 215 mb with not much difference observed at 150 mb. Above these pressure levels, using the improved cloud filtering changed the agreement marginally and the differences between the two instruments remained within 80 % close to 80 mb and within 30 % at 50 mb.

Overall, the intercomparisons with *in situ* instruments highlighted that in some regions, for example close to 215 mb, MIPAS H₂O and O₃ compared well, however, at pressure levels close to the tropopause, the agreement was poor, throughout all comparisons, and for both species, highlighting the difficulty faced by the MIPAS instrument in sounding close to the tropopause. From the HALOE measurements, a low bias in the version 19 H₂O and O₃ data was found at the tropical UTLS levels similar to those observed by previous authors [Harries et al., 1996; Borchi et al., 2005].

A primary conclusion from this chapter is that both MIPAS H₂O and O₃ are generally high biased in the tropics, however, with application of the improved cloud filters, these biases can be reduced.

In chapter six, the improved tropical cloud detection schemes, based on the evidence of detrimental cloud effects on the retrieved profiles of both species discovered in chapter four, were applied to the operational MIPAS data for the purpose of manipulating and removing cloud effects from the given operational L2 data. As MIPAS H₂O and O₃ concentrations are variable in the tropical UTLS, and this variability has been attributed to cloud presence, the application of improved cloud filters was an important step in removing cloud-induced biases and variability. Using the conservative 3.5 sab and 2.5 sab modes for H₂O and O₃, respectively, where the ‘sab’ data scheme removed data points with CI-A less than threshold and removal of the altitude above, it was found that averaged H₂O and O₃ concentrations were modified in accordance with the expected cloud effects. For example, close to 68 mb, low H₂O

concentrations, that could be construed to be apparent dehydration, were removed following the improved filtering. The estimated grid box, with apparent cloud top pressures and cloud occurrence frequencies act as useful tools to "track" possible cloud effects. Increasing the cloud filter however, results in a reduction in the number of data points meaning that the precision decreases relative to this reduction. Given that the estimated clear sky precision in this region is often high (from Oxford University estimates, H₂O at 15 km has a random error of 25 % and O₃ a random error of 57 %), it can be difficult to assess the impact of the more suitable cloud filtering on the estimated grid box errors.

Despite the variability of the MIPAS data in this region, particularly for O₃, and the removal of MIPAS data over the tropics following cloud filtering, regional variations in both species can be observed, where data are available. Such features were: a) a pronounced O₃ enhancement over the South Atlantic, with simultaneous low O₃ concentrations observed over the Pacific ocean, suggestive of zonal wave-one behaviour observed by the MIPAS instrument, and b) regions of enhanced and reduced H₂O concentrations throughout the tropics, particularly close to the northern hemisphere Summer Monsoon region.

From the analysis, no indication of a "chemopause" or "hygropause" could be determined from MIPAS data, most probably due to the 3 km vertical resolution of MIPAS that is unable to resolve layers in the UTLS/TTL, and also due to the high random errors for O₃.

7.2 Recommendations for future work

In relation to the work performed in this thesis, several recommendations for improvements and further work can be made here, that are summarised below:

An extension of the analysis of cloud propagation into MIPAS retrievals would include the examination of cloud effects at 15 km, allowing a more conclusive idea of how clouds at the tropopause can affect MIPAS H₂O and O₃ retrievals. An important addition to this work would be to perform a more extensive study, using the same principles, that includes investigation of cloud effects on other L2 species, and other geographical regions such as at the poles, where high altitude PSCs can potentially affect retrieved quantities. Here, single case studies were performed and although they

can be taken as representative of the L2 processor response to clouds, a larger scale study would allow better representation of the cloud effects on the MIPAS dataset.

Based on the cloud analysis performed, it is recommended that MIPAS data users screen tropical UTLS region data with the proposed cloud filters, however, ultimately the choice of CI-A relates to three factors that are: a) the data coverage requirements, meaning that for a better coverage, a lower CI-A would be more suitable and, b) the requirement for better representation of clear sky MIPAS measurements in which case a higher CI-A threshold for clearing is needed, and c) the systematic errors that can be tolerated for the application. It is also imperative that users of the operational data consider the effect of cloud error propagation into the altitudes above the cloud particularly, as clouds have been found to emphasise the already-present instabilities in the retrievals.

In terms of the MIPAS L2 retrieval, the cloud effects shown in chapter four have demonstrated that position of the cloud in relation to the tropopause is important. Therefore, perhaps differential cloud clearing for these species, above and below the cold tropopause, may be better representative of the cloud effects that have been shown to occur in MIPAS retrievals. Most importantly, the cloud effect analysis have demonstrated that the current CI-A threshold is too low to fully remove cloud contamination and that the threshold should be increased.

Other retrieval effects that should be taken in account, that may in fact have a worse or comparable effect to clouds is the treatment of the remaining profile after the cloud altitude has been removed from the profile. This effect is analysed using the 12 km cloudy and clear sky spectra used in chapter four.

Figure 7.2 shows the 12 km test case where a cloud was imposed at 12 km in the H₂O and O₃ profiles. In these tests, the retrievals are started with a lower altitude of 15 km and results compared to the clear sky retrieval. The H₂O profile shows that the removal of the cloud scan can also produce a bias in retrieved profiles when lower altitude spectra are not included in the retrieval.

These tests were necessary to examine and quantify how the operational data in the difficult to observe tropical UTLS region could be improved. The tests have also highlighted potential issues with the L2 retrieval code, namely the stability of the retrieval, that becomes highly compromised when a cloud is present in the FOV.

An important factor about the MIPAS L2 retrievals that has been highlighted by

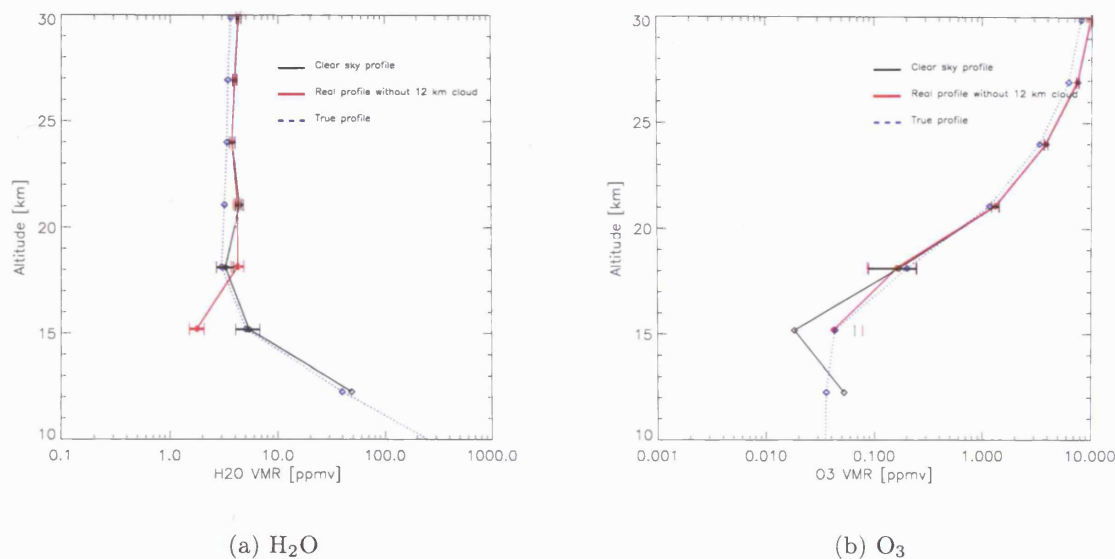


Figure 7.1: H₂O and O₃ retrieved by the ORM with and without a cloud at 12 km

this study is the difficulty that the MIPAS retrieval encounters when retrieving these gases near the region of the cold tropopause. This was highlighted in the clear sky O₃ retrievals that suggested that the clear sky retrievals could in fact be lower than the cloud cases close to the tropopause region.

The selected cloud indices can only remove the expected biases and loss in certainty on H₂O and O₃ concentrations. However, for MIPAS measurements around the UTLS, and for all limb sounding instruments, the limited accuracy and precision will always be a constraint on achieving accurate observations of trace gases in the tropical UTLS.

In terms of the intercomparisons of tropical UTLS data performed in chapter five, an important addition to these tests would be to perform a more extensive validation study, based solely on the tropical UTLS, incorporating other satellite instruments such as SAGE II, ACE-FTS and ODIN-SMR. A further useful comparison could be to the EOS-MLS instrument on the AURA satellite as clouds appear to be relatively transparent in the microwave region. However, this would have to be conducted with the reduced resolution data as the MIPAS nominal mode data and EOS-MLS data do not overlap temporally. Also the variation of concentrations in the true atmosphere in clear and cloudy conditions would be taken into account.

Ideally, validation of MIPAS data in the tropical UTLS should be performed with

large data sets of closely matched profiles particularly for H₂O that varies greatly in the atmosphere and can be difficult to validate. Validation programs should be carried out with a synergistic approach incorporating both *in situ* and satellite measurements particularly as *in situ* instruments can resolve the fine scale structure with lower measurement errors and satellites can provide greater coverage remotely.

Certainly, for general improvement of MIPAS retrievals, and for application toward future infrared limb sounding missions, long term validation of H₂O and O₃ data in the tropical UTLS region is a valuable exercise that should be carried out in both clear sky and cloudy conditions.

In situ instruments such as radiosondes and ECC ozone sondes are an important source of tropical UTLS data and have been used in many studies of this region [Gettelman et al., 2004b; Takashima and Shiotani, 2007]. The SHADOZ network is excellent source of *in situ* data however, it could benefit from more regular measurements and certainly more measurement sites in the tropics. Although most meteorological stations make regular radiosonde launches, it is imperative that data providers document factors such as radiosonde type and serial number because these can have an important impact on the interpretation of the data. Radiosondes still require considerable improvement near the cold tropopause.

From the seasonal analysis performed in chapter six, there are many limitations using the current operational data and the proposed schemes. The most significant of which is the loss of data following increased cloud filtering. However, the cloud filtering does provide some degree of confidence for the retrievals in these regions and where data coverage permits, the relationship between H₂O and O₃ can be analysed, particularly for the summer monsoon region, where correlations on theta levels could be indicative of stratosphere- troposphere exchange. Similarly, regions of dehydration that are expected over Indonesia and the Pacific, could be used in conjunction with 3D trajectory models to trace the origin of the air and the timescales that transport processes in the UTLS region take. Trajectory analysis would also verify that the suggestion of a tropospheric source for the observed O₃ enhancement in SON could be due to the African biomass burning observed in the same season.

Retrievals of cloud properties directly from the MIPAS data to indicate types of clouds in particular regions, used in conjunction with MIPAS H₂O fields could help distinguish whether particular dehydration events are due to transport processes or

cirrus interactions.

Infrared measurements provided by the MIPAS can potentially, with the correct manipulation be indicative of near “clear sky” (and thin cirrus) estimates, for H₂O for example and better quantify the radiative effects and the gradient of H₂O in the UTLS.

Overall, observing the tropical UTLS region using the MIPAS instrument is a complex task because of many factors that affect the quality of the retrievals in this region. Improvements to the MIPAS retrieval and the new MIPAS “RR” mode will improve the sampling and the stability of the retrievals in this region, however, the random error associated with these data may still remain to be large.

Bibliography

- Andreae, M. [1990], 'Biomass burning in the Tropics: Impact on Environmental Quality and Global Climate', *Population and Development Review* **16**, 268–291.
- Andreae, M.O., A. P., Fisher, H., Freitas, S., Gregoire, J.-M., Hansel, A., Hoor, P., Kormann, R., Krejci, R., Lange, L., Lelieveld, J., Lindinger, W., Longo, K., Peters, W., de Reus, M., Schreeren, B., Silva Dias, M., Strom, J., Velthoven, P. v. and Williams, J. [2001], 'Transport of biomass burning smoke to the upper troposphere by deep convection in the equatorial region', *Geophysical Research Letters* **28**, 951–954.
- Antikainen, V., Paukkunen, A. and Jauhianen [2002], Measurement Accuracy and Repeatability of Vaisala RS90 Radiosonde, Technical report, Vaisala.
- Banwell, C. [1972], *Fundamentals of Molecular Spectroscopy, Third Edition*, McGraw-Hill (UK).
- Barnes, R. and Bandy, A. R. [1985], 'Electrochemical Concentration Cell Ozone Sonde Accuracy and Precision', *Journal of Geophysical Research* **90**, 7881–7887.
- Barry, R. and Chorley, R. [1998], *Atmosphere, Weather and Climate, Seventh Edition*, Routledge.
- Bonazzola, M. and Haynes, P. [2004], 'A trajectory-based study of the tropical tropopause region', *Journal of Geophysical Research* **109**(D20), doi: 10.1029/2003JD004356.
- Borchi, F., Pommereau, J.-P., Garnier, A. and Pinharanda, M. [2005], 'Evaluation of SHADOZ sondes, HALOE and SAGE II ozone profiles at the tropics from SAOZ UV-Vis remote measurements onboard long duration balloons.', *Atmospheric Chemistry and Physics* **5**, 1381–1397.

- Bracher, A., Bramstedt, K., Sinnhuber, M., Weber, M. and Burrows, J. [2004], Validation of MIPAS O₃, NO₂, H₂O and CH₄ profiles (V4.61) with collocated with measurements of HALOE and SAGE II, *in* ‘Proceedings of the Second Workshop on the Atmospheric Chemistry Validation of ENVISAT (ACVE-2), 3-7 May, ESA Esrin, Frascati, Italy’.
- Brenninkmeijer, C. A. M., F, S., Koepfel, D., Scharffe, D., Pucek, M., Leliveld, J., Crutzen, P., Zahn, A., Sprung, D., Fisher, H., Herman, M., Reichelt, M., Heintzenberg, J., Schlager, H., Ziereis, H., Schumann, U., Dix, B., Platt, U., Ebinghaus, R., Martinsson, B., Ciais, P., Flippi, D., Leuenberger, M., Oram, D., Penkett, S., van Velthoven, P. and Waibel, A. [2005], ‘Analysing Atmospheric Trace Gases and Aerosols Using Passenger Aircraft’, *EOS* **86**, 82–83.
- Brewer, A. [1949], ‘Evidence for a world circulation provided by the measurements of Helium and Water Vapour distribution in the stratosphere’, *The Quarterly Journal of the Royal Meteorological Society* **71**, 351–363.
- Bruhl, C., Drayson, S., Russell III, J., Crutzen, P., McInerney, J., Purcell, P., Claude, H., Gernadt, H., McGee, T., McDermid, I. and Gunson, M. [1996], ‘Halogen Occultation Experiment ozone channel validation’, *Journal of Geophysical Research* **101**, 10,217–10,240.
- Campbell, J. B. [1996], *Introduction to Remote Sensing, Second Edition*, Taylor & Francis Ltd.
- Carlotti, M. [1988], ‘Global-fit approach to the analysis of limb-scanning atmospheric measurements’, *Applied Optics* **27**(15), 3250–3254.
- Carlotti, M., Hopfner, M., Raspollini, P. and Ridolfi, M. [2001], High level algorithm definition and physical and mathematical optimisations, (MIPAS Level 2 Algorithm Theoretical Baseline Document) Issue 3, Technical report, IROE-CNR.
- Ceccherini, S. [2004], Averaging Kernels for MIPAS off-line Level 2 retrievals, Issue 1, Technical report, IFAC-CNR, Contract No: 17580/03/I-OL.
- Ceccherini, S. [2006], Test of the range of validity of the first order expansion of the retrieved profile as a function of the true profile and some considerations on the

mipas averaging kernels, Technical report, IFAC-CNR, Contract No: 17580/03/I-OL.

Ceccherini, S., Carli, B., Pascale, E., Prosperi, M., Raspollini, P. and Dinelli, B. [2003], 'Comparison of measurements made with two different instruments of the same atmospheric vertical profile', *Applied Optics* **42**, 6465– 6473.

Chatfield, R., Guan, H., Thompson, A. and Smit, H. [2007], 'Mechanisms for the intraseasonal variability of tropospheric ozone over the Indian Ocean during the winter monsoon', *Journal of Geophysical Research* **112**, doi: 10.1029/206JD007347.

Chatfield, R., Guan, H., Thompson, A. and Witte, J. [2004], 'Convective lofting links Indian Ocean air pollution to paradoxical South Atlantic ozone maxima', *Geophysical Research Letters* **31**, doi: 10.1029/2003GL018866.

Chen, M., Rood, R. and Read, W. [1999], 'Seasonal variations of upper tropospheric water vapour and high clouds observed from satellites', *Journal of Geophysical Research* **104**, 6193– 6197.

Clark, H., Harwood, R., Billingham, A. and Pumphrey, H. [2003], 'Cirrus and water vapour in the tropical tropopause layer observed by the Upper Atmospheric Research Satellite (UARS)', *Journal of Geophysical Research* **108**, doi: 10.1029/2003JD003748.

Clark, H. L., Billingham, A., Harwood, R. and Pumphrey, H. [2001], 'Water vapour in the tropical lower stratosphere during the driest phase of the atmospheric tape recorder', *Journal of Geophysical Research* **106**, 22695–22705.

Clark, H. L., Harwood, R., Mote, P. and Read, W. [1998], 'Variability of water vapour in the tropical upper troposphere as measured by the Microwave Limb Sounder on UARS', *Journal of Geophysical Research* **103**, 31695– 31707.

Clough, S. A., Kneizys, F. and Davies, R. [1989], 'Line shapes and water vapour continuum', *Atmospheric Research* **23**, 229–241.

Cooper, O. R., Stohl, A., Hubler, G., Hsie, E. Y., Parrish, D. D., Tuck, A., Kiladis, G. N., Oltmans, S., Johnson, B., Shapiro, M., Moody, J. L. and Lefohn, A. [2005], 'Direct transport of midlatitude stratospheric ozone into the lower troposphere

and marine boundary layer of the tropical Pacific Ocean', *Journal of Geophysical Research* **110**, doi: 10.1029/2005JD005783.

Cortesi, U., Lambert, J. C., De Clercq, C., Bianchini, G., Blumenstock, T., Bracher, A., Castelli, E., Catoire, V., Chance, K. V., De Maziere, M., Demoulin, P., Godin-Beekmann, S., Jones, N., Jucks, K., Keim, C., Kerzenmacher, T., Kuellmann, H., Kuttippurath, J., Ialori, M., Liu, G. Y., Liu, Y., McDermid, S., Meijer, Y. J., Mencaraglia, F., Mikuteit, S., Oelalf, H., Piccolo, C., Pirre, M., Raspollini, P., Ravegnani, F., Reburn, W. G. R., Remedios, J., Sembhi, H., Smale, D., Steck, T., Taddai, A., Varotsos, C., Vigouroux, C., Waterfall, A., Wetzol, G. and Wood, S. [2007], 'Geophysical validation of MIPAS ENVISAT operational ozone data', *Atmospheric Chemistry and Physics* **7**, 4807–4867.

Danielsen, E. [1982], 'A dehydration mechanism for the stratosphere', *Geophysical Research Letters* **9**, 605–608.

Dessler, A. and Kim, H. [1999], 'Determination of the amount of the water vapour entering the stratosphere based on Halogen Occultation Experiment (HALOE) data', *Journal of Geophysical Research* **104**, 30605–30607.

Diab, R., Raghunandhan, A., Thompson, A. and Thouret, V. [2003], 'Classification of tropospheric ozone profiles over Johannesburg based on MOZAIC aircraft data', *Atmospheric Chemistry and Physics* pp. 713–723.

Dickerson, R., Huffman, G., Luke, W., Nunnermacker, L., Pickering, K., Leslie, A., Lindsey, C., Slinn, W., Kelly, T., Daum, P., Delany, A., Greenberg, J., Zimmerman, P., Boatman, J., Ray, J. and Stedman, D. [1987], 'Thunderstorms: An important mechanism in the transport of air pollutants', *Science* **235**(4787), 460–465.

Dudhia, A. [1997], Software User's Manual: Michelson Interferometer for Passive Atmospheric Sounding (MIPAS) Reference Forward Model (RFM), Technical report, ESA ESTEC, Contract No: 11886/NL/GS.

URL: www.atm.ox.ac.uk/RFM/

Dudhia, A., Jay, V. and Rodgers, C. [2002a], 'Microwindow selection for high-spectral-resolution sounders', *Applied Optics* **41**, 3665–3673.

- Dudhia, A., Morris, P. and Wells, R. [2002b], ‘Fast monochromatic radiative transfer calculations for limb sounding’, *Journal of Quantitative Spectroscopy & Radiative Transfer* **74**, 745–756.
- Dunkerton, T, J. [1995], ‘Evidence of meridional motion in the summer lower stratosphere adjacent to the monsoon regions’, *Journal of Geophysical Research* **100**, 16675 – 16688.
- Edwards, D. [1996], High Level Algorithm Definition Document: Development of a Reference Forward Algorithm for the simulation of MIPAS atmospheric limb emission spectra, Technical report, ESA ESTEC: Contract No: 118i86/NL/GS.
- Edwards, D., Lamarque, J.-F., Attie, J.-L., Emmons, L., Richter, A., Cammas, J.-P., Gille, J., Francis, G., Deeter, M., Warner, J., Ziskin, D., Lyjak, L., Drummond, J. and Burrows, J. [2003], ‘Tropospheric ozone over the tropical Atlantic: A satellite perspective’, *Journal of Geophysical Research* **108**, doi: 10.1029/2002JD002927.
- Endemann, E. [1999], Mipas instrument concept and performance, in ‘European Symposium on Atmospheric Measurements from Space’, Noordwijk.
- Endemann, E., Gare, P., Langent, J., Nett, H. and Readings, C. [2000], MIPAS - An Envisat Instrument for Atmospheric Chemistry and Climate Research, in ‘European Space Agency Bulletin’, number 101.
- ESA [2007], MIPAS Product Handbook (Version 2.2), Technical report, European Space Agency.
- Ewen, G., Grainger, R., Lambert, A. and Baran, A. [2005], ‘Infrared radiative transfer modelling in a 3D scattering cloudy atmosphere: Application to limb sounding measurements of cirrus’, *Journal of Quantitative Spectroscopy & Radiative Transfer* **96**, 45–74.
- Fischer, H., Birk, M., Blom, C., Carli, B., Carlotti, M., von Clarmann, T., Delbouille, L., Dudhia, A., Ehhalt, D., Endemann, M., Flaud, J., Gessner, R., Kleinert, A., Koopmann, R., Langen, J., Lopez-Puertas, M., Mosner, P., Nett, H., Oelalf, H., Perron, G., Remedios, J., Ridolfi, M., Stiller, G. and Zander, R. [2008], ‘MIPAS: An instrument for atmospheric and climate research’, *Atmospheric Chemistry and Physics* **8**, 2151–2188.

- Fischer, H. and Oelhaf, H. [1996], 'Remote sensing of vertical profiles of atmospheric trace constituents with MIPAS limb-emission spectrometers', *Applied Optics* **35**(16), 2787 – 2796.
- Fishman, J. and Brackett, V. G. [1997], 'The climatological distribution of tropospheric ozone derived from satellite measurements using version 7 Total Ozone Mapping Spectrometer and Stratospheric Aerosol and Gas Experiment data sets', *Journal of Geophysical Research* **102**, 19275 – 19278.
- Fishman, J., Watson, C. E., Larsen, J. and Logan, J. [1990], 'Distribution of tropospheric ozone determined from satellite data', *Journal of Geophysical Research* **95**, 3599–3617.
- Fitz, D. [1998], 'Performing ozonesonde measurements for the southern California ozone study', *Centre for Environmental Research and Technology* .
- Folkins, I., Bernath, P. F., Boone, C. D., Lesins, G., Livesey, N., Thompson, A., Walker, K. and Witte, J. [2006], 'Seasonal cycles of O₃, CO and convective outflow at the tropical tropopause', *Geophysical Research Letters* **33**, doi: 10.1029/2006GL026602.
- Folkins, I., Braun, C., Thompson, A. and Witte, J. [2002], 'Tropical ozone as an indicator of deep convection', *Journal of Geophysical Research* **107**, doi: 10.1029/2001JD001178.
- Folkins, I., Loewenstein, M., Podolske, J., Oltmans, S. and Proffitt, M. [1999], 'A barrier to vertical mixing at 14 km in the tropics: Evidence from ozonesondes and aircraft measurements', *Journal of Geophysical Research* **104**, 22,095–22,102.
- Forster, P. d. F. and Shine, K. [1997], 'Radiative forcing and temperature trends from stratospheric ozone changes', *Geophysical Research Letters* **26**, 3309–3312.
- Fueglistaler, S., Wernli, H. and Peter, T. [2004], 'Tropical troposphere-to-stratosphere transport inferred from trajectory calculations', *Journal of Geophysical Research* **109**, doi: 10.1029/2003JD004069.

- Fujiwara, M., Hasebe, F., Shiotani, M., Nishi, N., Vomel, H. and Oltmans, S. [2001], 'Water vapour control at the tropopause by equatorial Kelvin waves observed over Galapagos', *Geophysical Research Letters* **28**, 3143–3146.
- Gettelman, A. and de Forster, P. [2002a], 'Definition and climatology of the tropical tropopause layer', *Journal of the Meteorological Society of Japan* **80:4B**, 911–924.
- Gettelman, A., Kinnison, D., Dunkerton, T. and Brasseur, G. P. [2004b], 'Impact of monsoon circulations on the upper troposphere and lower stratosphere', *Journal of Geophysical Research* **109**, doi: 10.1029/2004JD004878.
- Gettelman, A., Randel, W., Fu, W. and Massie, S. [2002c], 'Transport of water vapour in the tropical tropopause layer', *Geophysical Research Letters* **29**(1), doi: 10.1029/2001GL013818.
- Gettelman, A., Salby, M. and Sassi, F. [2002b], 'Distribution and influence of convection in the tropical tropopause region', *Journal of Geophysical Research* **107**(D10), doi: 10.1029/2001JD001048.
- Glatthor, N., von Clarmann, T., Fisher, H., Funke, B., Gil-Lopez, S., Grabowski, U., Hopfner, M., Kellmann, S., Linden, A., Lopez-Puertas, M., Mengistu Tsidu, G., Milz, M., Steck, T., Stiller, G. and Wang, D. [2006], 'Retrieval of stratospheric ozone profiles from MIPAS/ENVISAT limb emission spectra: a sensitivity study', *Atmospheric Chemistry and Physics* **6**, 2767–2781.
- Goody, R. [1995], *Principles of Atmospheric Physics and Chemistry, Second Edition*, Oxford University Press.
- Goody, R. and Yung, Y. [1989], *Atmospheric Radiation: Theoretical Basis, Second Edition*, Oxford University Press.
- Greenhough, J., Remedios, J., Sembhi, H. and Kramer, L. J. [2005], 'Towards cloud detection and cloud frequency distributions from MIPAS infra-red observations', *Advances in Space Research* **36**, 800–806.
- Griffiths, P. [1975], *Chemical Infrared Fourier Transform Spectroscopy, (Series on Chemical Analysis: Vol 43.)*, John Wiley & Sons.

- Griffiths, P. and de Haseth, J. [1986], *Fourier Transform Infrared Spectroscopy*, John Wiley & Sons.
- Hao, W. M. and Liu, M.-H. [1994], 'Spatial and temporal distribution of tropical biomass burning', *Global Biogeochemical Cycles* **8**, 495-503.
- Harries, J., Russell III, J., Tuck, A., Gordley, L., Purcell, P., Stone, K., Bevilacqua, R., Gunson, M., Nedoluha, G. and Traub, W. [1996], 'Validation of measurements of water vapour from the Halogen Occultation Experiment (HALOE)', *Journal of Geophysical Research* **101**, 10,205-10,216.
- Hartmann, D., Holton, J. R. and Fu, Q. [2001], 'The heat balance of the tropical tropopause, cirrus, and stratospheric dehydration', *Geophysical Research Letters* **28**, 1969-1972.
- Hervig, M. and McHugh, M. [1999], 'Cirrus detection using HALOE measurements', *Geophysical Research Letters* **26**, 719-722.
- Highwood, E. and Hoskins, B. J. [1998], 'The Tropical Tropopause', *The Quarterly Journal of the Royal Meteorological Society* **124**, 1579-1604.
- Hofmann, D., Rodgers, C., Russell III, J., Smit, H., Storz, R. and Randel, W. [1998], SPARC/IO3C/GAW: Assessment of Trends in the Vertical Distribution of Ozone, Technical report, World Meteorological Organisation (WMO), Global Ozone Research and Monitoring Project, Report No. 43, WCRP-SPARC Report No. 1.
- Holton, J. and Gettleman, A. [2001], 'Horizontal transport and the dehydration of the stratosphere', *Geophysical Research Letters* **23**, 2799-2802.
- Holton, J., Haynes, P., McIntyre, M., Douglass, A., Rood, R. and Pfister, L. [1995], 'Stratosphere-Troposphere Exchange', *Reviews of Geophysics* **33**, 403-439.
- Hopfner, M. and Emde, C. [2005], 'Comparison of single and multiple scattering approaches for the simulation of limb-emission observations in the mid-IR', *Journal of Quantitative Spectroscopy & Radiative Transfer* **91**, 275-285.
- Hopfner, M., Oelhaf, H., Wetzell, G., Friedl-Vallon, F., Kleinert, A., Lenglé, A., Maucher, G., Nordmeyer, H., Glatthor, N., Stiller, G., v. Clarmann, T., Fisher, H.,

- Kroger, C. and Deshler, T. [2002], 'Evidence of scattering of tropospheric radiation by PSCs in mid-IR limb emission spectra: MIPAS-B observations and KOPRA simulations', *Geophysical Research Letters* **29**, doi: 10.1029/2001GL014443.
- Houghton, J.T, D. Y., Griggs, D., Noguier, M., van der Linden, P., Dai, X., Maskell, K. and Johnson, C. [2001], *Intergovernmental Panel on Climate Change: Climate Change 2001: The Scientific Basis*, Cambridge University Press.
- Jensen, E. and Pfister, L. [2004], 'Transport and freeze-drying in the tropical tropopause layer', *Journal of Geophysical Research* **109**(D02207), doi: 10.1029/2003JD004022.
- Jensen, E., Toon, O., Selkirk, H. B., J.D, S. and Schoerberl, M. R. [1996], 'On the formation and persistence of subvisible cirrus clouds near the tropical tropopause', *Journal of Geophysical Research* **101**, 21361-21375.
- Jiang, J., Wang, B., Goya, K., Hocke, K., Eckerman, S., Ma, J., Wu, D. and W.G, R. [2004], 'Geographical distribution and intraseasonal variability of tropical deep convection: UARS MLS observations and analyses', *Journal of Geophysical Research* **109**, doi: 10.1029/2003JD003756.
- Johnson, B., Oltmans, S., Vomel, H., Smit, H., Deshler, T. and Kroger, C. [2002], 'Electrochemical concentration cell (ECC) ozonesonde pump efficiency measurements and tests on the sensitivity to ozone of buffered and unbuffered ECC sensor cathode solutions', *Journal of Geophysical Research* **107**, doi:10.1029/2001JD00055.
- Kerridge, B., Goutail, F., Bazureau, A., Wang, D., Bracher, A., Weber, M., Brandstedt, K., Siddans, R., Latter, B., Reburn, W., Jay, V., Detof, A. and Payne, V. [2004a], MIPAS ozone validation by satellite intercomparisons, in 'Proceedings of the Second Workshop on the Atmospheric Chemistry Validation of ENVISAT (ACVE-2), 3-7 May, ESA Esrin, Frascati, Italy'.
- Kerridge, B., Jay, V., Reburn, J., Siddans, R., Latter, B., Lama, F., Dudhia, A., Grainger, R., Burgess, A., Hopfner, M., Steck, T., Stiller, G., von Clarmann, T., Grabowksi, U., Buehler, S., Emde, C., Eriksson, P., Ekstrom, M., Baran, A. and

- Wickett, M. [2004b], ‘Task 2 Report: Consideration of mission studying the chemistry of the UTLS’, *ESA ESTEC, Contract No: 15457/01/NL/MM* .
- Kiefer, M., von Clarmann, T., Grabowksi, U., De Laurentis, M., Mantovani, R. and Ridolfi, M. [2007], ‘Characterization of MIPAS elevation pointing’, *Atmospheric Chemistry and Physics* **7**, 1615–16228.
- Kiehl, J. and Trenberth, K. E. [1997], ‘Earth’s Annual Global Mean Energy Budget’, *Bulletin of the American Meteorological Society* **78**, 197–208.
- Kirchhoff, V., Alves, da Silva, F. and Fishman, J. [1996], ‘Observations of ozone concentrations in the Brazillian Cerrado’, *Journal of Geophysical Research* **101**, 24029–24042.
- Kleinert, A., Aubertin, G., Perron, G., Birk, M., W. G., Hase, F., Nett, H. and Poulin, R. [2007], ‘MIPAS Level 1B algorithms overview: operational processing and characterization’, *Atmospheric Chemistry and Physics* **7**, 1395–1406.
- Kley, D., Russell, J. I., Phillips, C., Remsberg, E., Schiller, C., Oltmans, S. A., Rosenlof, K., Gettelman, A., Harries, J. and Mote, P. W. [2000], SPARC assessment of Upper Tropospheric and Stratospheric Water Vapour, Technical report, WMO/ICSU/IOC, WCRP Report 113, SPARC Report No. 2.
- Kley, D., Stone, E., Henderson, W., Drummond, J., Harrop, W., Schmeltekopf, A. L., Thompson, T. L. and Winkler, R. [1979], ‘In situ measurements of the mixing ratio of water vapour in the stratosphere’, *Journal of the Atmospheric Sciences* **36**, 2513–2523.
- Komhyr, W., Barnes, R., Brothers, G., Lathrop, J. and Opperman, D. [1995], ‘Electrochemical concentration cell ozonesonde performance evaluation during STOIC 1989’, *Journal of Geophysical Research* **100**, 9231–9244.
- Lelieveld, J. and Dentener, F. [2000], ‘What controls tropospheric ozone?’, *Journal of Geophysical Research* **105**, 3531–3551.
- Lelieveld, J., Dentener, F., Peters, W. and Krohl, M. [2004], ‘On the role of hydroxyl radicals in the self-cleansing capacity of the troposphere’, *Atmospheric Chemistry and Physics* **4**, 2337–2344.

- Liou, K. [2002], *An Introduction to Atmospheric Radiation (International Geophysics), Second Edition*, Academic Press.
- Liu, C. and Zipser, E. [2005], 'Global distribution of convection penetrating the tropical tropopause', *Journal of Geophysical Research* **110**(D23104), doi: 10.1029/2005JD006063.
- Lopez-Puertas, M. [2001], *Non-LTE Radiative Transfer in the Atmosphere, (Series on Atmospheric, Oceanic and Planetary Physics, Vol 3.)*, World Scientific Publishing Co.
- Luo, B., Peter, T., Wernli, H., Fueglistaler, S., Wirth, M., Kiemle, C., Flentje, H., Yushkov, V., Khattatov, V., Rudakov, V., Thomas, A., Borrmann, S., Toci, G., Mazzinghi, P., Buermann, J., Schiller, C., Cairo, F., Di-Don-Francesco, G., Adriani, A., Volk, C., Strom, J., Noone, K., Mitev, V., MacKenzie, R., Carslaw, K., Trautman, T., Santeccesaria, V. and Stefanutti, L. [2003], 'Ultrathin Tropical Tropopause Clouds (UTTCs): II. Stabilization mechanisms', *Atmospheric Chemistry and Physics* **3**, 1093–1100.
- Ma, Q. and Tipping, R. [1999], 'The averaged density matrix in the coordinate representation: Application to the calculation of the far wing line shapes of H₂O', *The Journal of Chemical Physics* **111**, 5909–5921.
- Marengo, A., Thouret, V., Nedelec, P., Smit, H., Helten, M., Kley, D., Karcher, F., Simon, P., Law, K., Pyle, J., Poschmann, G., von Wrede, R., Hume, C. and Cook, T. [1998], 'Measurement of ozone and water vapour by Airbus in-service aircraft: The MOZAIC airborne program, An overview:', *Journal of Geophysical Research* **103**, 25631–25642.
- Martin, R., Jacob, D., Logan, J., Ziemke, J. and Washington, R. [2000], 'Detection of a lightning influence on tropical tropospheric ozone', *Geophysical Research Letters* **27**, 1639–1642.
- McHugh, M., Magill, B., Walker, K., Boone, C. D., Bernath, P. F. and Russell, J. I. [2005], 'Comparison of atmospheric retrievals from ACE and HALOE', *Geophysical Research Letters* **32**, doi: 10.1029/2005GL22403.

- Mendrok, J., Schreier, F. and Hopfner, M. [2007], 'Estimating cirrus cloud properties from MIPAS data', *Geophysical Research Letters* **34**, doi: 10.1029/2006GL028246.
- Michelsen, K. [2006], 'The 1st Vaisala Radiosonde', *Vaisala News* **171**, 11-13.
- Miloshevich, L., Paukkunen, A., Vomel, H. and Oltmans, S. [2004], 'Development and Validation of a Time-lag Correction for Vaisala Radiosonde Humidity Measurements', *Journal of Atmospheric and Oceanic Technology* **21**, 1305-1327.
- Miloshevich, L., Vomel, H., Paukkunen, A., Heysmfield, A. J. and Oltman, S. [2001], 'Characterization and correction of Relative Humidity Measurements from Vaisala RS80-A Radiosondes at cold temperatures', *Journal of Atmospheric and Oceanic Technology* **18**, 135-156.
- Miloshevich, L., Vomel, H., Whiteman, D., Lesht, B., Schmidlin, F. and Russo, F. [2006], 'Absolute accuracy of water vapour measurements from six operational radiosonde types launched during AWEX-G and implications for AIRS validation', *Journal of Geophysical Research* **111**, doi: 10.1029/2005JD006083.
- Milz, M., von Clarmann, T., Fischer, H., Glatthor, N., Grabowksi, U., Hopfner, M., Kellmann, S., Keifer, M., Linden, A., Mengistu Tsidu, G., Steck, T. and Stiller, G. [2005], 'Water vapour distributions measured with the Michelson Interferometer for Passive Atmospheric Sounding on board Envisat (MIPAS/Envisat)', *Journal of Geophysical Research* **110**, doi: 10.1029/2005JD005973.
- Montoux, N., Hauchecorne, A., Pommereau, J.-P., Durray, G., Morel, B., Jones, R., Lefevre, F. and Bencherif, H. [2007], 'Evaluation of balloon and satellite water vapour measurements in the Southern tropical UTLS during the HIBISCUS campaign', *Atmospheric Chemistry and Physics Discussions* **7**, 6037-6075.
- Moore, D. [2005], Measurements of HCHO-22 in the upper troposphere and lower stratosphere from the MIPAS-E instrument, PhD thesis, Department of Physics and Astronomy, University of Leicester.
- Morris, G. A., Gleason, J. F., Russell, J. I. and Schoerberl, M. R. [2002], 'A comparison of HALOE V19 with SAGE II V6.00 ozone observations using trajectory mapping', *Journal of Geophysical Research* **107**, doi: 10.1029/2001JD000847.

- Mote, P. W., Rosenlof, K., McIntyre, M., Carr, E., Gille, J., Holton, J., Kinnersley, J. S., Pumphrey, H., Russell, J. I. and Waters, J. [1996], ‘An atmospheric tape recorder: The imprint of tropical tropopause temperatures on stratospheric water vapour’, *Journal of Geophysical Research* **101**, 3989–4006.
- Newell, R. and Gould-Stewart, S. [1981], ‘A Stratospheric fountain?’, *Journal of the Atmospheric Sciences* **38**, 2789–2796.
- Oelhaf, H., Schiller, C., Chance, K., Gurlit, W., Ovarlez, J., Renard, J.-B., Rohs, S., G., W., Clarmann, T., Milz, M., Wang, D.-Y., Remedios, J. and Waterfall, A. [2004], Validation of MIPAS-ENVISAT version 4.61 operational data with balloon and aircraft measurements: H₂O, *in* ‘Proceedings of the Second Workshop on the Atmospheric Chemistry Validation of ENVISAT (ACVE-2), 3-7 May, ESA Esrin, Frascati, Italy’.
- Oltmans, S., Johnson, B., Harris, J. M., Vomel, H., Thompson, A., Koshy, K., Simon, P., Bendura, R., Logan, J., Hasebe, F., Shiotani, M., Kirchhoff, V., Maata, M., Sami, G., Samad, A., Tabuadruva, J., Enriquez, H., Agama, M., Cornejo, J. and Paredes, F. [2001], ‘Ozone in the Pacific tropical troposphere from ozonesonde observations’, *Journal of Geophysical Research* **106**, 32503–32525.
- Pappalardo, G., Colvitto, T., Congeduti, F., Cuomo, V., Deuber, B., Kampfer, N., Ialori, M., Mona, L. and Rizi, V. [2004], Validation of MIPAS H₂O vapour by ground based measurements, *in* ‘Proceedings of the Second Workshop on the Atmospheric Chemistry Validation of ENVISAT (ACVE-2), 3-7 May, ESA Esrin, Frascati, Italy’.
- Paynter, D., Ptashnik, I., Shine, K. and Smith, K. [2007], ‘Pure water vapour continuum measurements between 3100 and 4400 cm⁻¹: Evidence for water dimer absorption in near atmospheric conditions’, *Geophysical Research Letters* **34**, doi: 10.1029/2007GL029259.
- Pumphrey, H., Clark, H. L. and Harwood, R. [2000], ‘Lower stratospheric water vapour measured by UARS’, *Geophysical Research Letters* **27**, 1691–1694.
- Randel, C., Rusch, D., Bevilacqua, R., Hoppel, K., Lumpe, J., Shettle, E., Thompson, E., Deaver, L., Zawodny, J., Kyro, E., Johnson, B., Kelder, H., Dorokhov, V., Konig-Langlo, G. and Gil, M. [2003], ‘Validation of POAM III ozone: Comparison

- with ozonesonde and satellite data', *Journal of Geophysical Research* **108**, doi: 10.1029/2002JD002944.
- Randel, W., Wu, F., Gettelman, A., Russell, J. I., Zawodny, J. and Oltmans, S. [2001], 'Seasonal variation of water vapour in the lower stratosphere observed in Halogen Occultation Experiment Data', *Journal of Geophysical Research* **106**, 14313–14325.
- Randel, W., Wu, F., Vomel, H., Nedoluha, G. E. and Forster, P. [2006], 'Decreases in stratospheric water vapour after 2001: Links to changes in the tropical tropopause and Brewer- Dobson circulation', *Journal of Geophysical Research* **111**, doi: 10.1029/2005/JD006744.
- Raspollini, P., C.Belotti, A.Burgess, B.Carli, Carlotti, M., S.Ceccherini, Dinelli, B., A.Dudhia, J-M.Flaud, B.Funke, M.Hopfner, Lopez-Puertas, M., V.Payne, C.Piccolo, J.J.Remedios, M.Ridolfi and R.Spang [2006], 'MIPAS Level 2 Operational Analysis', *Atmospheric Chemistry and Physics* **6**, 5605–5630.
- Raspollini, P. and Ridolfi, M. [2000], 'Mapping of Temperature and Line-of-sight Errors in Constituent Retrievals for MIPAS/ENVISAT Measurements', *Atmospheric Environment* **34**, 5329–5336.
- Read, W., Wu, D., Waters, J. and Pumphrey, H. [2004], 'Dehydration in the Tropical Tropopause Layer', *Journal of Geophysical Research* **109**(D6), doi: 10.1029/2003JD004056.
- Read, W.G, W. J., Wu, D., Stone, E., Shippony, Z., Smedley, C., Smallcomb, C. . C., Oltmans, S., Smit, H., Mergenthaler, J. and Karki, M. [2001], 'UARS Microwave Limb Sounder upper tropospheric humidity measurements: method and validation', *Journal of Geophysical Research* **106**, 32207 – 32528.
- Reid, G. and Gage, K. S. [1981], 'On the annual variation in height of the tropical tropopause', *Journal of the Atmospheric Sciences* **38**, 1928–1938.
- Remedios, J., R.J, L., Waterfall, A., Moore, D., Sembhi, H., Parkes, I., Greenhough, J., Chipperfield, M. and D, H. [2007], 'MIPAS Reference Atmospheres and comparisons to V4.61/V4.62 MIPAS Level 2 geophysical data sets', *Atmospheric Chemistry and Physics Discussions* **7**, 9973–10017.

- Ridolfi, M., Blum, U., Carli, B., Catoire, V., Ceccherini, S., Claude, H., De Clercq, C., Fricke, K., Friedl Vallon, F., Ialori, M., Keckhut, P., Kerridge, B., Lambert, J., Meijer, Y. J., Mona, L., Oelalf, H., Pappalardo, G., Pirre, M., Rizi, V., Robert, C., Swart, D., von Clarmann, T., Waterfall, A. and Wetzel, G. [2007], ‘Geophysical validation of temperature retrieved by the ESA processor from MIPAS/ENVISAT atmospheric limb-emission measurements’, *Atmospheric Chemistry and Physics* **7**, 4459–4487.
- Ridolfi, M., Carli, B., Carlotti, M., von Clarmann, T., Dinelli, B., Dudhia, A., Flaud, J., Hopfner, M., Morris, P., Raspollini, P., Stiller, G. and Wells, R. [2000], ‘Optimized forward model and retrieval scheme for MIPAS near-real-time data processing’, *Applied Optics* **39**(8), 1323–1340.
- Rodgers, C. [2000], *Inverse Methods for Atmospheric Sounding: Theory and Practise*, (Series on Atmospheric, Oceanic and Planetary Physics, Vol 3.), World Scientific Publishing Co.
- Rodgers, C. and Conner, B. J. [2003], ‘Intercomparison of remote sensing instruments’, *Journal of Geophysical Research* **108**, doi: 10.1029/2002/JD002299.
- Roe, J. and Jasperson, W. [1980], A new tropopause definition from simultaneous ozone temperature profiles, Technical Report AFGL-TR-80-0289, Air Force Geophysics Laboratory Technical Report.
- Rosenlof, K., Oltzman, S., Kley, D., Russell, J. I., Chiou, E.-W., Johnson, D., Kelly, K., Michelsen, H., Nedoluha, G. E., Remsberg, E., Toon, G. and McCormick, M. [2001], ‘Stratospheric water vapour increases over the past half-century’, *Geophysical Research Letters* **28**, 1195–1198.
- Rothman, L., Jacquemart, D., A, B., Benner, C. D., Birk, M., Brown, L., Carleer, M., Chackerian, C., Chance, K., Coudert, L., Dana, V., Devi, V., Flaud, J., R.R., G., Goldman, A., Hartmann, J., Jucks, K., Maki, A., J.Y, M., Massie, S., J, O., Perrin, A., Rinsland, C., Smith M.A.H and Tennyson, J., R.N, T., Toth, R., J, V. A., P, V. and G, W. [2005], ‘The HITRAN 2004 molecular database’, *Journal of Quantitative Spectroscopy & Radiative Transfer* **96**, 139–204.

- Rozanov, V., Diebel, D., Spurr, R. and Burrows, J. [1997], ‘GOMETRAN: A radiative transfer model for the satellite project GOME, the plane-parallel version’, *Journal of Geophysical Research* **102**, 16683–16695.
- Sauvage, B., Thouret, V., Cammas, J.-P., Brioude, J., Nedelec, P. and Mari, C. [2007], ‘Meridional ozone gradients in the African upper troposphere’, *Geophysical Research Letters* **34**, doi: 10.1029/2006GL028542.
- Sembhi, H., Remedios, J. and Raspollini, P. [2007], Investigating the effect of upper tropospheric cirrus clouds on tropical MIPAS Level 2 water vapour and ozone retrievals, in ‘Proceedings of the ENVISAT Symposium, 23-27 April, Montreux, Switzerland’.
- Sherwood, S. [2000], ‘A Stratospheric ”Drain” over the Maritime Continent’, *Geophysical Research Letters* **27**, 677–680.
- Sherwood, S. and Dessler, A. [2000], ‘On the control of stratospheric humidity’, *Geophysical Research Letters* **27**, 2513–2516.
- Sherwood, S. and Dessler, A. [2001], ‘A model for transport across the tropical tropopause’, *Journal of the Atmospheric Sciences* **58**, 765–779.
- Sherwood, S. and Dessler, A. [2003], ‘Convective mixing near the tropical tropopause: insights from seasonal variations’, *Journal of the Atmospheric Sciences* **60**(21), 2674–2685.
- Shine, K. and Sinha, A. [1991], ‘Sensitivity of the Earth’s climate to height dependent changes in the water vapour mixing ratios’, *Nature* **354**, 382–384.
- Sinha, P., Jaegle, L., Hobbs, P. and Liang, Q. [2004], ‘Transport of biomass burning emissions from southern Africa’, *Journal of Geophysical Research* **109**, doi: 10.1029/2004JD005044.
- Solomon, S., Thompson, D. J., Portmann, R., Oltmans, S. and Thompson, A. [2005], ‘On the distribution and variability of ozone in the tropical upper troposphere: Implications for tropical deep convection and chemical-dynamical coupling’, *Geophysical Research Letters* **32**, doi: 10.1029/2005GL024323.

- Spang, R., Eidmann, G., Reise, M., Offerman, D., Preuse, P., Pfister, L. and Wang, P. [2002], 'CRISTA observations of cirrus clouds around the tropopause', *Journal of Geophysical Research* **107**, doi: 10.1029/2001JD000698.
- Spang, R. and Remedios, J. [2003], 'Observations of a distinctive infrared spectral feature in the atmospheric spectra of polar stratospheric clouds measured by the CRISTA instrument', *Geophysical Research Letters* **30**(16), 1875–1879.
- Spang, R., Remedios, J. and Barkley, M. [2004], 'Colour indices for the detection and differentiation of cloud types in infra-red limb emission spectra', *Advances in Space Research* **33**, 1041–1047.
- Stephens, G. L. [1994], *Remote Sensing of the Lower Atmosphere: An Introduction, First Edition*, Oxford University Press.
- Stohl, A., Bonasoni, P., Cristofanelli, P., Collins, W., Feichter, J., Frank, A., Forster, C., Gerasopoulos, E., Gaggeler, H., James, P., Kentarchos, T., Kromp-kolb, H., Kruger, B., Land, C., Meleon, J., Papayannis, A., Priller, A., Seibert, P., Spregner, M., Roelofs, G., Scheel, H., Schnabel, C., Siegmund, P., Tobler, L., Trickl, T., Wernli, H., Wirth, V., Zanis, P. and Zerferos, C. [2003], 'Stratosphere-troposphere exchange: A review, and what we have learned from STACCATO', *Journal of Geophysical Research* **108**, doi: 10.1029/2002JD002490.
- Stone, E., Pan, L., Sandor, B., Read, W. and Waters, J. [2000], 'Spatial distribution of upper tropospheric water vapour measurements from the UARS Microwave Limb Sounder', *Journal of Geophysical Research* **105**, 12149 – 12161.
- Suhre, K., Cammas, J.-P., Nedelec, P., Rosset, R., Marenco, A. and Smit, H. [1997], 'Ozone-rich transients in the upper equatorial Atlantic troposphere', *Nature* **388**, 661–663.
- Takashima, H. and Shiotani, M. [2007], 'Ozone variation in the tropical tropopause layer as seen from ozonesonde data', *Journal of Geophysical Research* **112**, doi: 1029/2006JD008322.
- Thompson, A., Tao, W.-K., Pickering, K., Scala, J. and Simpson, J. [1997], 'Tropical deep convection and ozone formation', *Bulletin of the American Meteorological Society* **78**, 1043 – 1054.

- Thompson, A., Witte, J., McPeters, R., Oltmans, S., Schmidlin, F., Logan, J., Fujiwara, M., Kirchhoff, V., Posny, F., Coetzee, G., Hoegger, B., Kawakami, S., Ogawa, T., Johanson, B., Vomel, H. and Labow, G. [2003], 'Southern Hemisphere Additional Ozonesonde (SHADOZ) 1998- 2000 tropical ozone climatology. i. Comparison with Total Ozone Mapping Spectrometer (TOMS) and ground based measurements', *Journal of Geophysical Research* **108**, doi: 10.1029/2003JD000967.
- Thompson, A., Witte, J., Oltmans, S. and Schmidlin, F. [2004], 'SHADOZ -A tropical ozonesonde-radiosonde network for the atmospheric community', *Bulletin of the American Meteorological Society* pp. 1549 – 1564.
- Thompson, A., Witte, J., Smit, H., Oltmans, S., Johnson, B., Kirchhoff, V. and Schmidlin, F. [2007], 'Southern Hemisphere Additional Ozonesonde (SHADOZ) 1998 - 2004 tropical ozone climatology', *Journal of Geophysical Research* **112**, doi: 10.1029/2005JD007042.
- Thompson, O., Dazlich, D. and Hou, Y.-T. [1986], 'The Ill-posed Nature of Satellite Temperature Retrieval Problem and the Limits of Retrievalability', *Journal of Atmospheric and Oceanic Technology* **3**, 643–649.
- Thuburn, J. and Craig, G. [2002], 'On the temperature structure of the tropical stratosphere', *Journal of Geophysical Research* **107**(D2), doi: 10.1029/2001JD000448.
- Valks, P., Koelemeijer, R., Weele, M. v., Velthoven, P. van, F. J. and Kelder, H. [2003], 'Variability in tropical tropopause layer: Analysis with Global Ozone Monitoring Experiment observations and a global model', *Journal of Geophysical Research* **108**, doi: 10. 1029/2002JD002894.
- Vomel, H. [2005], Saturation Vapour Pressure Formulations, Technical report, CIRES, University of Colorado, Boulder.
- Vomel, H., Oltman, S., Johnson, B., Hasebe, F., Shiotani, M., Fujiwara, M., Nishi, N., Agama, M., Cornejo, J., Paredes, F. and Enriquez, H. [2002], 'Balloon - borne observations of water vapour and ozone in the tropical upper troposphere and lower stratosphere', *Journal of Geophysical Research* **107**, doi: 10.1029/2001JD000707.

- Vomel, H., Selkirk, H., Miloshevich, L., Valverde-Canossam, J., Valdes, J., Kyro, E., Kivi, R., Stoltz, W., Peng, G. and Diaz, J. [2006], ‘Radiation dry bias of the Vaisala RS92 Humidity Sensor’, *Journal of Atmospheric and Oceanic Technology* .
- von Clarmann, T. [2006], ‘Validation of remotely sensed profiles of atmospheric state variables: strategies and terminology’, *Atmospheric Chemistry and Physics* **6**, 4311–4320.
- von Clarmann, T., G. N., Stiller, G., Grabowksi, U., Hopfner, M., Kellmann, S., Linden, A., Milz, M., Steck, T., Funke, B. and Koukouli, M. E. [2007], ‘MIPAS measurements of upper tropospheric C₂H₆ and O₃ during the Southern Hemisphere biomass burning season of 2003’, *Atmospheric Chemistry and Physics Discussions* **7**, 12067–12095.
- von Clarmann, T., Hopfner, M., Funke, B., Lopez-Puertas, M., Dudhia, A., Jay, V., Schreier, F., Ridolfi, M., Ceccherini, S., Kerridge, B., Reburn, J. and Siddans, R. [2003], ‘Modelling of atmospheric mid-infrared radiative transfer: the AMIL2DA algorithm intercomparison experiment’, *Journal of Quantitative Spectroscopy & Radiative Transfer* **78**, 381– 407.
- Wang, J., Cole, H., Carlson, D., Miller, E., Beierle, K., Paukkunen, A. and Laine, T. [2002], ‘Corrections of Humidity Measurement Errors from the Vaisala RS80 Radiosonde -Application to TOGA COARE Data’, *Journal of the Atmospheric Sciences* **19**, 981– 1002.
- Wang, P., Fishman, J., Harvey, V. and Hitchman, M. [2006], ‘Southern tropical upper tropospheric zonal ozone wave-1 from SAGE II observations (1985-2002)’, *Journal of Geophysical Research* **111**, doi: 10.1029/2005JD006221.
- Wang, P., Minnis, P., McCormick, M., Kent, G. and Skeens, K. [1994], ‘A 6-year climatology of cloud occurrence frequency from Stratospheric Aerosol and Gas Experiment’, *Journal of the Atmospheric Sciences* **51**, 3019–3026.
- Waugh, D. and Polvani, L. [2000], ‘Climatology or intrusions into the Tropical Upper Troposphere’, *Geophysical Research Letters* **27**, 3857–3860.
- Wayne, R. P. [2000], *Chemistry of the Atmospheres, Third Edition*, Oxford University Press.

Yang, P., Gao, B., Baum, B., Hu, Y., W.J, W., T.S-C., W, D. and Nasiri, S. [2001],
'Radiative properties of cirrus clouds in the infrared (8 - 13 micron) spectral region',
Journal of Quantitative Spectroscopy & Radiative Transfer **70**, 473-504.